Republic of Iraq
Ministry of Higher Education
and Scientific Research
University of Babylon
College of Materials Engineering
Department of Metallurgical Engineering

Surface Improvement of 705 Zr alloy by ZrO_2/HA coating using duplex processes of anodizing and micro-arc oxidation for medical application

A Dissertation

Submitted to the Council of The Department of The College of Materials Engineering/ University of Babylon in Partial Fulfillment of the Requirements for the Degree of Doctor of Philosophy in Materials Engineering/ Metallurgical.

By

Maysam Abbood Salman

B.Sc. In mechanical engineering (2012)

M.Sc. In mechanical engineering (2017)

Supervised by

Prof. Ali Hubi Haleem (Ph.D.)

Prof. Samir Hamid Awad (Ph.D.)

2022 A.D 1443 A.H

Supervisor Certificate

We certify that this thesis entitled **" Modification of Zirconium alloys for Biomedical Applications "** was prepared by (**Maysam Abbood Salman**) under our supervision at the department of Metallurgical Engineering / College of Materials Engineering / university of Babylon in partial fulfillment of the requirements for the degree of Philosophy-Doctorate in Materials Engineering / Metallurgical Engineering .

Signature:

Prof. Dr.	Prof. Dr.
Ali Hubi Haleem	Samir Hamid Awad
/ / 2022	/ / 2022

بِسمِ اللهِ الرحَمنِ الرَّحيمِ

"وَقُلِ اعمَلُواْ فَسَيَرَى اللَّهُ عَمَلَكُم وَرَسُولُهُ
وَالمُؤمِنُونَ وَستُرَدُّونَ إِلَى عَالِمِ الغَيبِ
وَالشَّهَادَةِ فَيُنَبِّئُكُمُ بِمَا
كُنتُم تَعمَلُونَ"

صدق الله العلي العظيم

سورة التوبة (أية ١٠٥)

Dedicate

This work is dedicated with all my Love and Respect to:

My Soul Father

My Dear Mother

My Lovely brother and Sister

My kides (Hussen and abbass)

Maysam Abbood Salman

2022

TABLE OF CONTENTS

Lest of Abbreviations

Abbreviations	Description	Units
AC	Alternating Current	
AFM	Atomic Force Microscopy	
AEO	Anodizing Electrolytic Oxidation	
BCC	Body Centered Cubic	
BM	Base Metals	
BG	Bio glass	
BFGF	Basic Fibroblast Growth Factor	
CA	Contact Angle	degree
CVD	Chemical Vaper Deposition	
DC	Direct Current	
EDS	Energy Dispersive Spectrometer	
EPD	Electrophoretic Deposition	
EW	Equivalent Weight	
FCC	Face Center Cubic	
FESEM	Field Emission Scanning Electron Microscopy	
HBSS	Hanks' Balanced Salt Solution	
HV	Hardness Vickers	Kg/cm^3

HCP	Hexagonal Crystal Structure	
LOM	Light Optical Microscope	
MAO	Micro-Arc Oxidation	
MFR	Mixed Fretting Regime	
OCP	Open Circuit Potential	mV
PBS	Phosphate Buffered Saline Solution	
PD	Plasma Discharging	
PEO	Plasma Electrolytic Oxidation	
PETP	Poly Ethylene Terephthalate	
PT	Prothrombin Time	
PP	PolyPropylene	
PPM	Part Per Million	Mg/l
PVD	Physical Vaper Deposition	
SAOS-2	Human Osteoblastic Cell Line	
SBF	Simulated Bodily Fluid	
SEM	Scanning Electron Microscopy	
SCE	Saturated Calomel Electrode	
SR	Slip Regime	
TF-XRD	Thin Film X-ray Diffraction	
THR	Total Hip Replacement	

TKR	Total Knee Replacement	
XRD	X-ray Diffraction	
XPS	X-Ray Photoelectron Spectroscopy	

Lest of symbols

Abbreviations	Description	Units
A	Anatase	
Ca, EDTA	Calcium, Ethylene Diamine Tetra Acetate	
C_R^o	Corrosion Rate of Master Sample (Before Coating)	mpy
C_R	Corrosion Rate of Master Sample (After Coating)	mpy
D	Displacement Amplitudes	mm
$E_{corr.}$	Corrosion Potential	mV
HA	Hydroxyapatite	
$i_{corr.}$	Corrosion Current Density	$\mu A/cm^2$
mpy	Mils Per Year	
R	Rutile	
TiO_2	Titania or Titanium Dioxide	
Y_2O_3	Yttrium	
ZrO_2	Zirconia	

α	Alpha	
β	Beta	
F_n	Normal load	N

Acknowledgements

All Praise is for **Allah**, The Almighty for granting me the bless of finishing this thesis.

First, I would like to express my thanks, respect and deepest appreciation to my supervisor **Prof. Dr.** ***Ali Hubi Haleem*** for his incessant advice, unlimited encouragement and endless help throughout the whole work.

Secondly, I would like to thank my **Prof. Dr. Samir Hamid Awad** (University of Babylon) for his effortless helps and scientific tips that helped to facilitate doing the project in the right path to success.

I wish to express my deep appreciation to the staff of laboratories of Material Engineering college/ University of Babylon for their help.

I would like to thank **Assi. Prof Dr. Haidar Akram Al-sabti** , **Assi. Prof Dr. Ahmed Al-Mukhtar, Dr. Munaf Salih Majeed** and **Dr. Ahmed Namah Hadi** for their help and supported .

The support and care of my family especially ***My uncle "Maan Salman Al-Abassli"*** are deeply appreciated. Their love has been for me a powerful source of inspiration and energy. I am enormously grateful and thankful to all persons who believed in me and provided me with the love, support and encouragement that have made all of this possible.

Maysam abbood salman

Abstract

Zirconium and its alloys give the highest degrees of biocompatibility, low toxicity, poor wear resistance and low hardness. Zirconia coatings are a good candidate for anti-wear applications. Various methods have been used to deposit zirconia coatings on zirconium and its alloys such as: anodizing, its useful treatment able to confer the zirconium alloys, high surface mechanical properties and corrosion resistance properties closely related to the nature of the ceramic layer, and Micro-arc oxidation (MAO) technology is an advanced and effective unconventional chemical-electrochemical method to form a thick and hard ceramic coating and corrosion resistance properties.

In this investigation, used anodizing process, MAO process, and duplex for the two previous processes where manufactured a locally coating system consisting of a power supply with a voltage of (0-500) Volts and a current of (0-8) Amperes. Several tests conducted to evaluate the efficiency of Zirconium 705, such as X-ray diffraction, field emission scanning electron microscopy, hardening test, wear test, adhesion test, coating thickness, wetting angle, corrosion test, and zirconium ion release test in Hank's solution and antibacterial test. During the experiments on Zirconium 705, the solution used in anodizing process was (1 mL/L phosphoric acid and 0.8 g/L of sodium fluoride) with/ without addition of hydroxyapatite HA (2.5, 5, and 8) g/L. The voltages are 10-30V, and times 4-60 minutes were used. Results are shown in anodizing high hardness (270HV) at (30V, 30min and, 8g/L HA), wear resistance which leads to decreases wear rate to (10.1×10^{-8} g/m), and corrosion rate equals (C_R= 0.743×10^{-6} mpy) in hank’s solution, with increased voltage and time increased thickness layer (18µm). For MAO, it was carried out under different conditions at voltages 100-200V, times 5-15 minutes.

The solution of 14 g / liter Potassium hydroxide, 14 g /liter sodium phosphate, 14 g /L sodium silicate, and 2 g /L sodium fluoride has been used with and without addition of hydroxyapatite (2.5, 5, and 8) g/l. Results are shown at (200V, 10min& ,8g/LHA) high hardness (347.59HV) and wear rate (4.5×10^{-8} g/m) and corrosion rate equals to (C_R= 0.454×10^{-6} mpy) in hank's solution with increased voltage thickness layer (44µm).

The actual improvement was done by duplex process under best conditions for anodizing and MAO processes. Results are shown increase in the hardness after coating from (164 to 483.6)HV , wear rate (2.5×10^{-8} g/m), corrosion rate equals to (C_R= 0.137×10^{-6} mpy) in hank's solution and the thickness layer (56.1µm).

The amount of ion released are less than that of the base alloy in Hank solution equal to (0.0229) ppm for uncoated specimens , the best specimens for anodizing and MAO equal to (0.0217, and 0.0209) ppm respectively , and for duplex coating reduced to (0.0193) ppm. The MAO and duplex coating has a strong antibacterial effect that could prevent the bacteria growth.

Chapter One
Introduction

1.1 Overview

Bone plays many roles such as supporting body weight, protecting the organs, assisting with movement, promoting mineral homeostasis, creating the blood supply, and storing triglycerides [1].

The various functions of bone tissue are strongly related to its hierarchical and anisotropic structure [2].

The bone may be an advanced tissue that unendingly undergoes dynamic biological reworking. This unique trait of bone underpins its ability to remodel itself to repair the damage. However, when a bone defect exceeds a critical non-healable size, external intervention is required to supplement self-healing if the defect is to be bridged. The optimal choice is to use autograft. Nevertheless, harvesting autograft tissue creates the morbidity associated with a second surgical site. An alternative choice is allograft tissue [1].

The insufficiencies of application of autograft and allograft tissue own lead up to greater research efforts to identify biomimetic materials and structures that are suitable for skeletal repair without the inherent problems. Metals and alloys own a long history of the application as bone implants, and are well established due to their good biocompatibility, satisfactory mechanical strength, and superior resistance of corrosion. However, implants made of these materials are usually have more hardness than natural bones, leading to stress shielding. If the Young's modulus of an implant is higher than that of the cortical bone, then the load is preferentially transferred to the implant.

This phenomenon is referred to as stress shielding, and it is especially true in the case of load-bearing implants, such as those used for replacing failed hard tissue (cortical bone). When stress shielding occurs, it results in bone resorption and poor bone remodeling, which are the leading causes of implant loosening and re fracture of the bone after implant extraction [1, 2].

1.2 Implant Properties

The property requirements of implant can broadly be categorized into three equally important features [3]:

1. The device must be relatively easy to fabricate, being reproducible, consistent, and conforming to all technical and biological requirements.
2. The body of human must be compatible with the material used in the prosthesis.
3. The implant must have the desired balance of physical and mechanical properties necessary to perform as expected.

1.3 Metals Used in Biomedical applications

The further commonly used metals for joint replacements are stainless steels, cobalt-chromium, and titanium-based alloy. Recently, alloys developed in the field of biomedicine have been used, including Nb alloys, zircon alloys and magnesium alloys. These three major alloys groups have a relatively long tradition in joint replacements [4]. Much types of these alloys have been standardized on the basis of international and national standards; for example, International Organization for Standardization (ISO), American Society for Testing and Materials (ASTM), and Japanese Industrial Standard (JIS) [5]. Types of metals used

in biomedical depend upon appointed implant applications. Table (1.1) shows the types of metals generally used for different implants division. Figure (1.1) shows a set of implants used in the human body.

Table (1.1):Types of Metals used for different implants [6].

Division	Example of implants	Types of metals
Cardiovascular	Stent Artificial valve	316L SS, CoCrMo, Ti, Ti6Al4V
Orthopaedic	Bone fixation (plate, screw, pin) Artificial joints	316L SS, Ti, Ti6Al4V CoCrMo,Ti6Al4V, Ti6Al7Nb,Zr and its alloy
Dentistry	Orthodontic wire Filling	316L SS, CoCrMo, TiNi, TiMo, AgSn(Cu) amalgam, Au
Craniofacial	Plate and screw	316LSS, CoCrMo, Ti, Ti6Al4V
Otorhinology	Artificial eardrum	316L SS

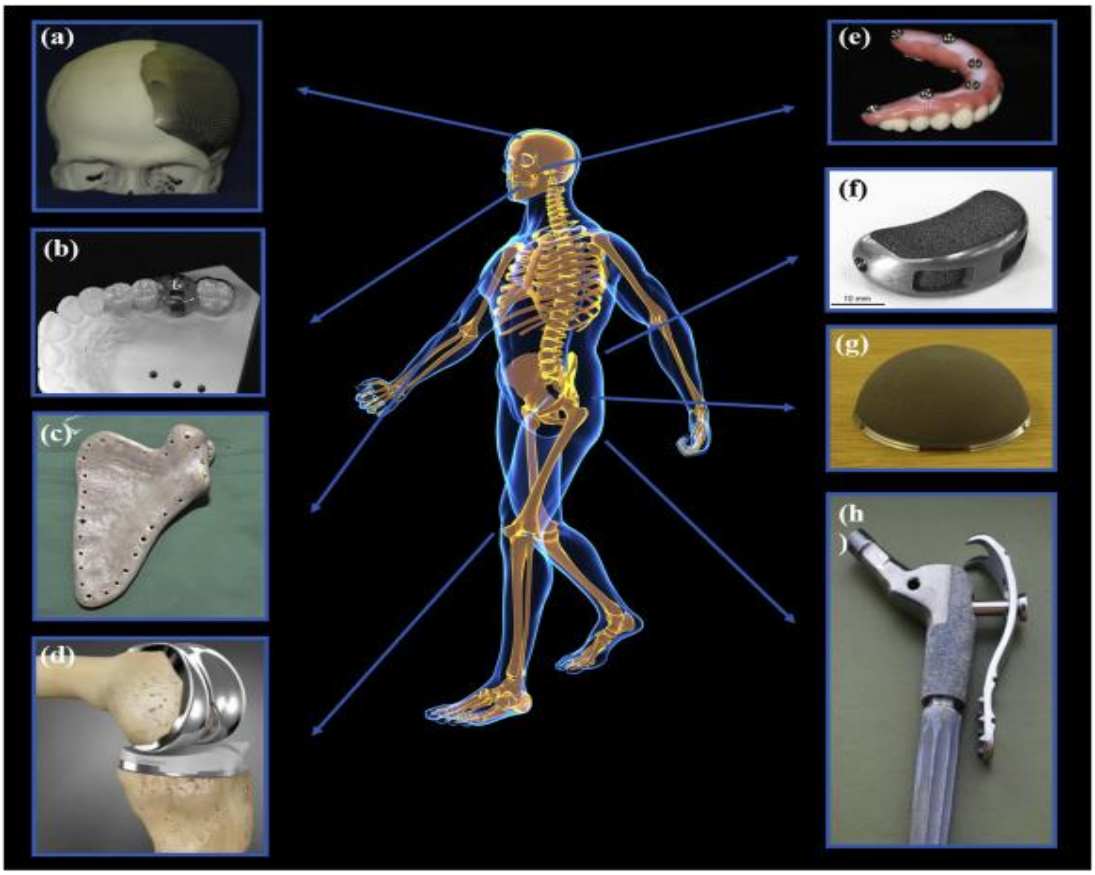

Figure (1.1): Set of Implants, (a) cranial prosthesis, (b) surgical guide, (c) scapula prosthesis, (d) knee prosthesis, (e) dental implants, (f) interbody fusion cage, (g) acetabular cup, and (h) hip prosthesis [7].

1.4 Zr properties and Bio applications

The atomic number of Zr is 40, and the atomic weight is 91.22. The density of pure Zr is 6.52 g/cm^3. Zr has a hexagonal close-packed crystal structure (hcp; alpha phase) at room temperature and is stable up to 862 ^{o}c. Allotropic transformation occurs at this temperature, and a body-centered cubic structure (Bcc; beta phase) is stable above that temperature to a melting point of approximately 1860 ^{o}c.

The lattice parameters of Zr are a = 0.3233 nm; and c = 0.5149 nm at room temperature, and a = 0.361 nm at 870 ċ [3].Tin (Sn), and oxygen (O) are added a stabilize α-phase. In addition, nickel and niobium are added a stabilize the β-phase. The amount of these added elements can be adjusted to improve the strength, and corrosion resistance [2].

Zr is a strong, ductile and malleable metal whose physical and chemical properties are similar to that of titanium. It has good corrosion and heat resistance. At elevated temperatures, the finely divided metal is capable of igniting spontaneously in air. It cannot be dissolved in acids or alkalis. Zirconium is used in oxide or zirconia form. Zirconium oxide has low thermal conductivity and high melting point [9]. The properties of Zr are notably different than those of Ti properties are density, thermal neutron cross section, and magnetic susceptibility. The density of Zr is about 1.4 times higher than that of Ti (4.51 g/cm^3), and the specific strength is disadvantageous as compared with Ti. However, the thermal neutron cross section of Zr is one-thirtieth that of Ti. Therefore, Zr has applications in the nuclear power industry. The magnetic susceptibility of Zr is almost half that of Ti, which a promising property for medical applications is. Details are given later. Zr is one of the active metals and it easily reacts with oxygen to form dense and continuous zirconium oxide at the surface. The black oxide layer forms in a steam at the temperature ranging from 260 to 400 ċ for the initial stage. With prolonging the reaction time, the oxide color gray, and the strong adhesion is lost at the interface between oxide and metal [2].The density of Zr is 6.53 g/cm³ and melting point is 1843°C [9].

And the mechanical properties for the pure Zr are excellent deformability at room temperature. The strength is insufficient and is improved by alloying and is one of the active metals and it easily reacts with oxygen to form dense and continuous zirconium oxide at the surface.

Table (1.2): Mechanical properties of Zr [10].

Properties	Metric
Tensile strength (annealed)	330 MPa
Yield strength (annealed)	230 MPa
Modulus of elasticity	94.5 GPa
Poissons ratio	0.34
Elongation at break (annealed)	32%
Hardness, Brinell (converted from Vickers for 3000 kg load/10 mm ball. Annealed sample)	145
Hardness, Rockwell A (converted from Vickers. annealed sample)	49
Hardness, Rockwell B (converted from Vickers. Annealed sample)	78
Hardness, Vickers (annealed sample)	150

1.5 Current issues in Zr surface modification

Poor tribological properties of Zr and its alloys, such as low wear resistance, have seriously restricted their extensive applications, especially in heavy load-bearing applications [11].The production of ceramic oxide coatings on metallic surface is a well-established process for protecting metals and alloys from oxidation at high temperature.

A wide variety of techniques are available for the deposition of ceramic oxide coatings namely, chemical vapor deposition (CVD), plasma spraying, sol-gel, and physical vapor deposition (PVD) processes [12]. Ceramic passive coatings one of the most significant ceramic substances due to its very appealing attributes such as electrical insulating, hardness, and chemical stable. These attributes make it favorable for very various applications [13].

Ceramic coatings have been extensively used in various industries such as power generation, automotive, aerospace for heat and wear resistance requirements. Coatings possess high stability to chemical attack, high hardness and refractoriness, which make them suitable for wear resistant applications, ZrO_2 are good candidates for anti-wear and anti-corrosion applications, due to their high hardness [14].

There are several methods have been used to deposit ZrO_2 coating on Zr alloys, which fabricating ZrO_2-based coatings with good mechanical properties, excellent wear resistance and corrosion resistance [15].

These techniques, however, suffer from constraints such as high processing temperatures, harder encountered in preparing ceramic oxide produces with high purity, and dominate microstructures [12].

Anodizing formation ceramic layer at Low voltage in acidic electrolytes. Plasma electrolyte oxidation (PEO), also known as Micro-arc oxidation (MAO), is an advanced anodizing process where ceramic coatings are formed at high voltages in low-concentrated eco-friendly alkaline electrolytes with visible short-lived micro discharges over the alloy surface [16].The coatings are formed above the dielectric breakdown voltage under AC and DC conditions [17]. MAO and Anodizing processes are treatment techniques used to convert the surfaces of suitable

metals to an oxide ceramic layer. It is featured by, high productivity, ecological friendliness, economic efficiency, good wear and corrosion resistance, high hardness and excellent bonding strength with the substrate [18].

1.6 Objective of the Present Study

The aim of the current work is focusing on the coating of the Zr705 (R60705) with (ZrO_2 and HA /ZrO_2) for the biomedical applications to improve the corrosion, wear performance and biocompatibility.

In this investigation , the anodizing, MAO and duplex anodizing with MAO techniques used to deposit a suitable layer of composite coating of HA/ ZrO_2 on the Zr705 substrate and investigate of the most essential variables (potential and deposition time) to obtain the best properties of coating layer in order to improve the performance of the biomedical implant. The study includes:

1. Enhancing of corrosion resistance and biocompatibility.
2. Lowering the amount of metallic ions released from the implant by exhibiting an efficacious chemical barrier against the metal ions release from the metallic implant.
3. Increases wear resistance and bioactivity. Produce an antibacterial coating layer safely used in the human body.

Chapter Two

Theoretical Part and Literature Review

2.1 Introduction

This chapter presents a general review about the types of Zr alloys, and its alloy that used in implants and about bone structure. There will be a focus on their chemical compositions which will include biomaterials, mechanical properties, biocompatible, and biology of wound healing following implant placement, corrosion behaviour and types of corrosion, wear properties.

2.2 Overview

Bone plays many roles such as supporting body weight, protecting the organs, assisting with movement, promoting mineral homeostasis, creating the blood supply, and storing triglycerides.

The various functions of bone tissue are strongly related to its hierarchical and anisotropic structure. Bone is often lost due to disease and trauma. Therefore, substitution with artificial medical devices and regenerative medicine is developing and becoming more common in clinical settings, but it is difficult to fully realize the complex role of complicated bony structure.

The first step toward this goal is developing a deep understanding of bone structure and function [19].

2.3 Bone Tissue

2.3.1 Bone Structure

Bones comes in a variety of sizes and shapes, including irregular, short, flat, and long, and the shapes and sizes [20]. The skeletal structure of an adult person is made up of around 206 bony components [20]. Bones have been arranged an isotropically and hierarchically at multiple levels due to its diverse tasks range from loading support to mineral control including phosphorus and calcium (see Figure2.1) [21].

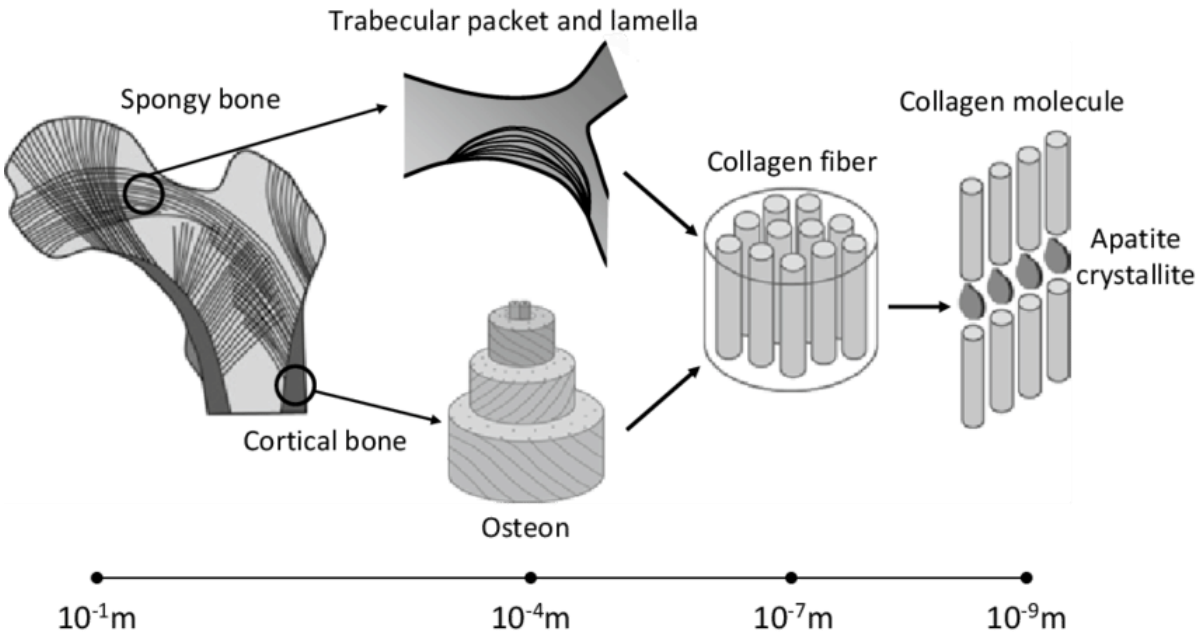

Figure (2.1) Schematic illustration of hierarchical structure of bone ranging from the atomic to organ level [21].Hormones, cytokines, and Protein are found in modest quantities in bone cells, which play a vital role [22]. Bones are classified into cortical and spongy types, which are responsible mainly for load support and turnover, respectively.The relative ratio of spongy bone surface area to volume is greater than that of cortical bone since it contributes to essential mineral homeostasis through the bone marrow [23,24]. Figure (2.2) shows the anatomical median section of the human proximal femoral bone [25].

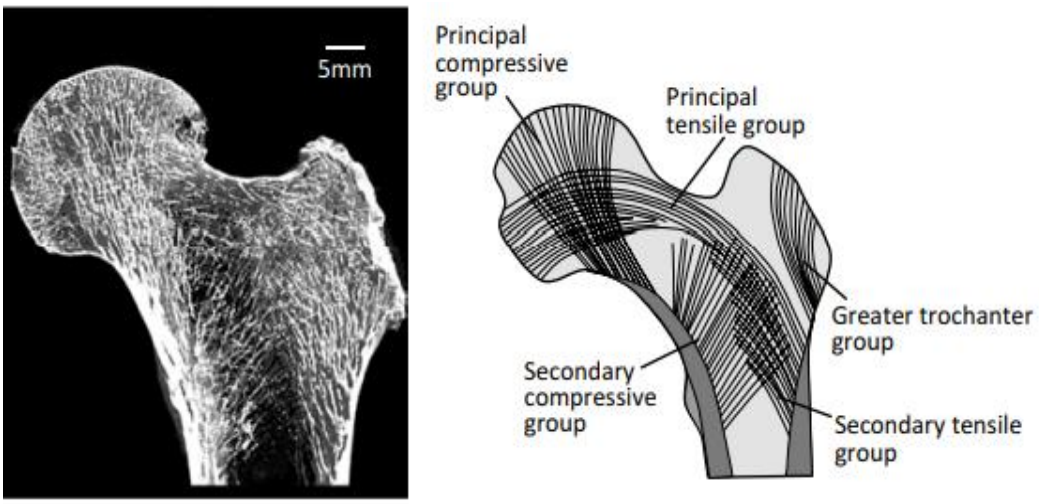

Figure (2.2) Schematic illustration of typical trabecular pattern in the proximal portion of a human femur. The directions of the trabecular extension are well correlated with the in vivo stress pattern [25]

Bone has a very complicated structure for its internal organ that is difficult to mimic artificially. Therefore, bone replacement materials or an artificial joint including metal is used to support functional degradation of bone or bony joints [25]. However, there is a significant difference in microstructure and related function between artificial materials and bone. Therefore, bone repair and artificial joint replacement must place great importance on mechanical safety and joint mobility. However, it may result in only partial bone function recovery. In addition, a bone regenerative technique is also being developed that can reconstruct original bone tissue [26].In orthopedic surgery, bones minerals density and bones masses have been utilized to diagnose and treat patients. As a result, innovative bio devices and biomaterials for bones formation and substitution must take into account the hierarchical and complex configuration of bones tissue with anisotropic microstructures [27, 28].The three dominant bone cell types, namely, osteoblasts, osteoclasts, and osteocytes, interact with other bone-related cells such as mesenchymal stem cells (see Figure 2.3).

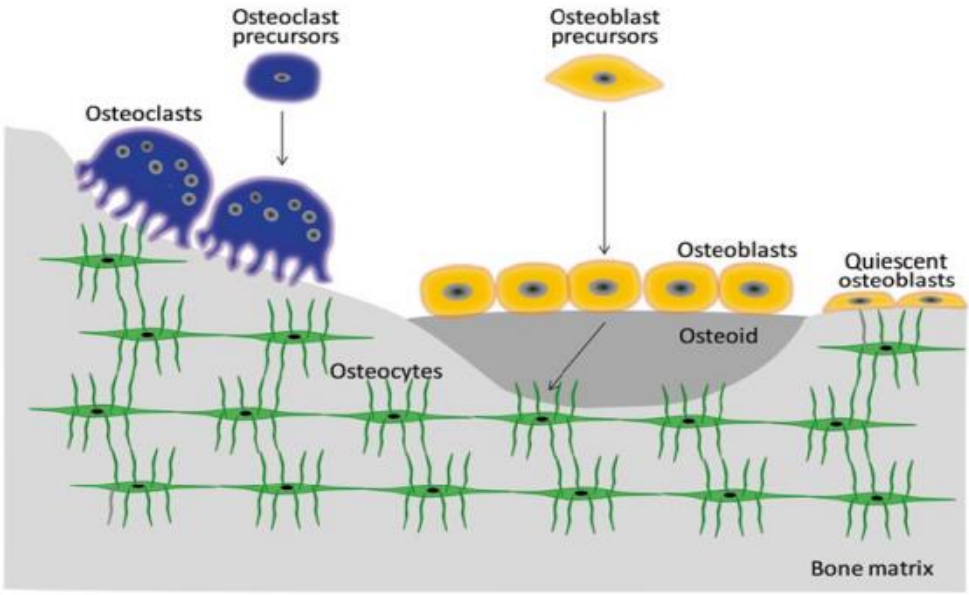

Figure 2.3 Bone cells involved in bone modeling [29, 30].

When a bone fracture occurs, small defects can be cured spontaneously. Figure 2.4 shows the repair process of general bone fractures in terms of the macroscopic changes. The bone fracture healing process is classified into three phases: inflammatory, reparative, and remodeling [31].

❖ The inflammatory phase, in addition to the bone damage of the periosteum and bone marrow, the fractured space is occupied by a hematoma, and osteonecrosis occurs due to osteocyte necrosis and extinction near the broken end of the bone (Figure 2.4(1)) [32].

❖ In the soft callus phase, capillary blood vessels invade and cells infiltrate the hematoma, the hematoma is removed, and granulation tissue is substituted [31,32].

❖ The remodeling phase, immature bone is substituted for lamellar bone due to remodeling, and the bone shape is gradually corrected to the original shape accompanied by marrow cavity formation (see Figure

2.4(3)). Bone union is finally achieved and the healing process is complete (Figure 2.4(4)) [32, 33].

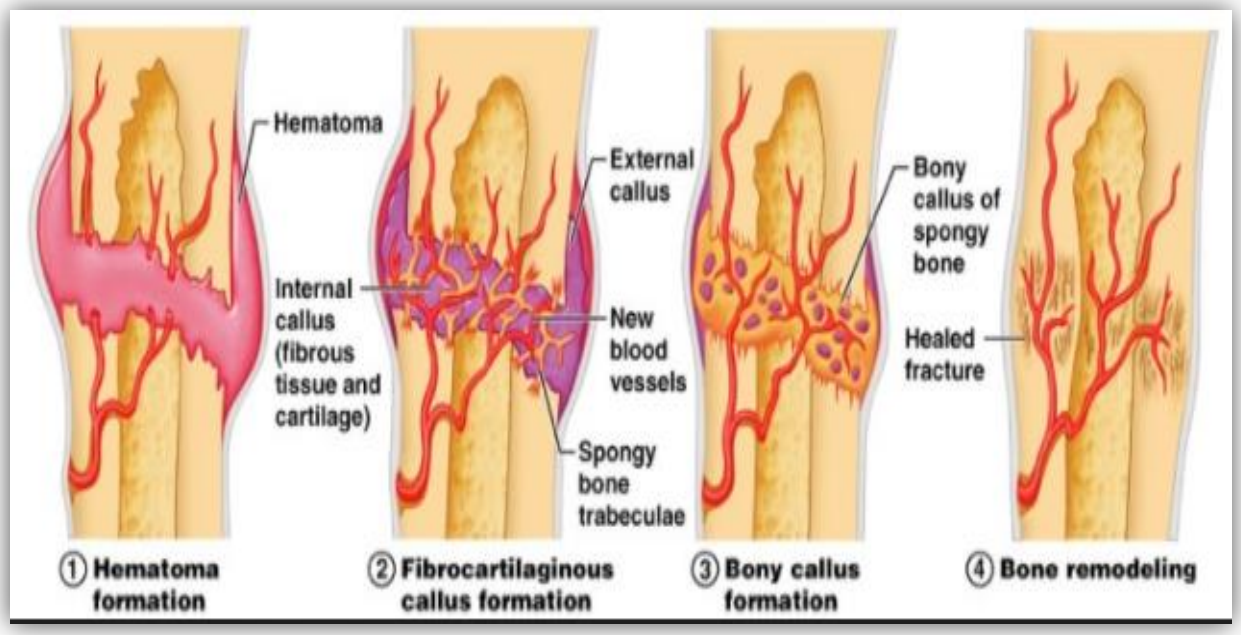

Figure 2.4 Typical fracture healing process [31]

2.4 Joint Structure

2.4.1 Anatomical Classification

The junction between adjacent bones is a joint. Gross type of joint is classified into three types: [34].

- Immovable joint is the fibrous synarthrosis which is filled with dense collagenized fibrous tissue, such as the skull structures. There is no mobility in this joint [34].
- Amphiarthrodial joint is the symphysis which is characterized by limited mobility, such as the intervertebral disc [35].
- The diarthrodial joint is the most common joint which is cavitated to form a freely movable connecting unit between two bones [36].

The diarthrodial joints are classified into four functional categories:

- ❖ Hinge motion shows angular motion on one plane, namely, flexion and extension, for example, knee joint [37].
- ❖ Pivot joint shows only uniaxial rolling motion, such as proximal radioulnar joint [38].
- ❖ Ball-and-socket joint. This joint shows a large range of motion because of triaxial motion. Hip joint is anatomically ball-and-socket joint and has a large range of motion, including flexion, extension, adduction, internal rotation, and external rotation. Hip joint has also an important role as a weight-bearing site [39].
- ❖ Saddle Joint shows large angular motion, not rolling motion, such as the carpometacarpal joint [40].

2.5 Bio metals and its Properties

Biocompatible is the essential requirement to choose a metal implant material that is, not exhibiting any toxicity to the surrounding biological system. Implantation of metals including magnesium, nickel, silver, and aluminum, copper, zinc, iron and carbon steels into the human body has been studied for over a century [41]. All of these were discarded as being too reactive in the body for long term implantation. When stainless steel was introduced into general engineering as a new corrosion resistant material in the early 1900s, it was soon used in surgical applications. However, the 18-8 stainless steel that was initially used was found to exhibit intergranular corrosion due to high (0.08%) carbon content and gross pitting due to low molybdenum content [42].The alloys of cobalt-chromium molybdenum and cobalt-chromium have been initially developed and utilized in dentistry and orthopedic uses around the same time period because to their resistant to corrosion.

Titanium alloys are the most corrosion-resistant implantation materials currently in use. Titanium alloys have been initially utilized in the 1960s, and their popularity has continued to expand since the mid of 1970s. Many titanium alloys give optimum strengths and corosion esistance, including Ti-6Al-7Nb, Ti-5Al-2.5Fe, and Ti-6Al-4V. The major advantage of titanium and its alloys is the non-reactivity of the passive film that is formed; the main disadvantages are its susceptibility to fretting as well as oxygen diffusion during fabrication, causing embrittlement [43, 44]. Zr is often utilized in biological applications. The femur knee surfac and the head of the hips joints are made of a Zr-2.5 alloy named Oxinium, that has been developed by Smith & Nephew in 1997 for TKR and in 2002 for THR [2]. The major metals and alloys that utilized in medical equipment and industrial alternatives are shown in Table 2-1. The mechanical properties for these alloys discussed here are presented in Table 2-2.

Table 2-1: Major biomedical metal and alloys and their application .

Material	***Major Application***
316L Stainless Steel	cranial plates, orthopedic fracture plates, dental implants, spinal rods, joint replacement prostheses, stents, catheters[44].
Cobalt-Chromium alloys	dental implants, orthopedic fracture plates, heart valves, spinal rods, joint replacement prostheses[45]
Titanium,Nitinol,Titanium alloys (Ti-6Al-4V, Ti-5AL-2.5 Fe, Ti-6Al -7Nb)	cranial plates, maxillofacial reconstruction, dental implants, dental wires, orthopedic fracture plates, joint replacement prostheses, stents.[45]

Zirconium alloy	Total knee replacement (TKR) and total hip replacement (THR)[2]

Table 2-2: Mechanical properties of implant alloys and human bone [2.45,46].

Material	***Tensile Strength $(MN/m)^2$***	***Yield Strength $(MN/m)^2$***	***Vickers Hardness (Hv)***	***Young's Modulus $(GN/m)^2$***	***Fatigue Limit $(GN/m)^2$***
316L SS	650	280	190	211	0.28
Wrought Co-Cr Alloy	1540	1050	450	541	0.49
Cast Co-Cr Alloy	690	490	300	241	0.30
Ti-6Al-4V	1000	970	---	121	---
zr	330	230	---	94.5	---
Human Bone	137.3	---	26.3	30	---

2.6 Failures of implant devices

2.6.1 Corrosion behavior

A patient had a primary total hip replacement with the insertion of a prosthesis. Seventy months postoperatively radiographs revealed a fractured prosthetic neck (Fig. 2.5a). A similar case was reported for the same type of prosthesis but 85 months postoperatively. The parts consisted of a wrought CoCrMo alloy head (ASTM F799) coupled to a

CoCrMo stem. The fractures happened right distal to the head-neck taper of the neck. Both sick people were overweight and active, but the mechanical strengths of the neck part ought to have been sufficient to support their weight [47]. A section through the taper showed the presence of corrosive penetration of fluid along the grain boundaries. It was also observed that the fracture followed the grain boundaries (Fig. 2.5a); (b) points to the onset of the fracture [47, 48].

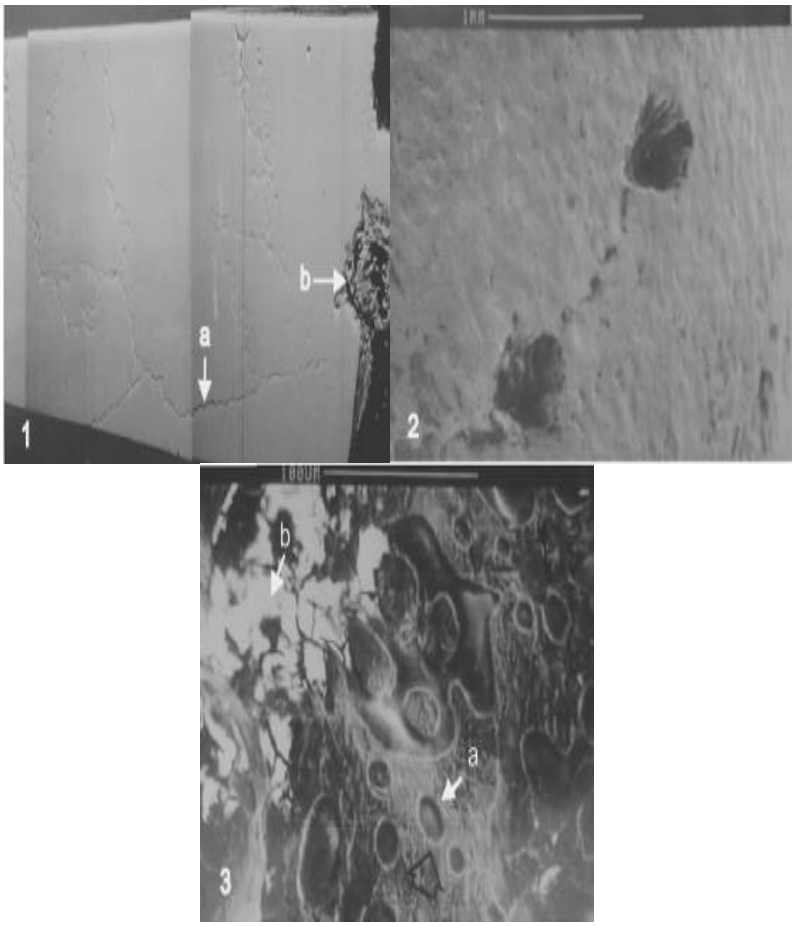

Figure 2.5 (1) The tapered neck of the prosthesis fractured 85 months postop.

The cross section clearly shows intergranular cracks (a) neck (b) onset site of the fracture,(2) Free fracture surface, showing pits (carbides),and (3) fracture surfaces: (a) pores; (b) non-conducting debris [47].

The free surface outside the taper junction showed pits as large as 500 µm and were connected through intergranular cracks (Fig. 2.6). Types of corrosion can be summarized in the table (2.2).

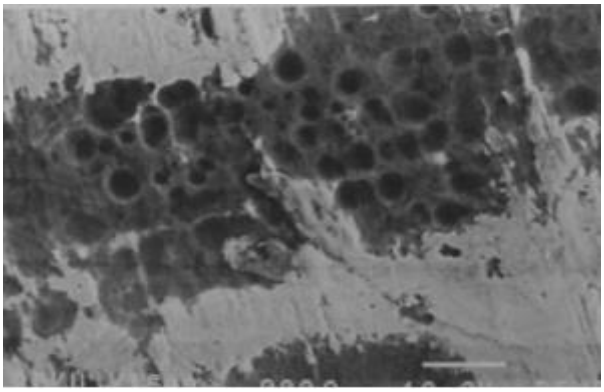

Figure 2.6 the severely pitted inner taper surface of a CoCr head [47].

Table (2.3): Types of Corrosion in the Conventional Materials Used for Biomaterial Implants [64].

Type of Corrosion	Material	Implant Location	Shape of the Implant
Pitting	304 SS, Cobalt based alloy	Orthopedic/ Dental alloy	
Crevice	316 L st.st	Bone plates and screws	
Stress Corrosion Cracking	C0CrMo, 316 LSS	Only in in vitro	
Corrosion Fatigue	316 SS, CoCrNiFe	Bone cement	

Fretting	Ti5Al2.5Fe, CoCrSS	Ball Joints	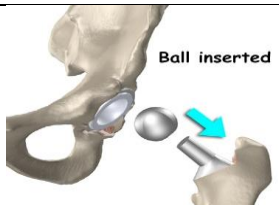
Galvanic	304 SS/316SS, CoCr+Ti5Al2.5Fe.‹ 316SS/Ti5Al2.5Fe or CoCrMo	Oral Implants Screws and nuts	
Selective Leaching	Mercury from gold	Oral implants	

2.6.1.1 Styles in Corrosion

When an unfortunate potential difference exists as driving force and when the reaction progresses at a detectable rate. The potential difference can be created along very odd ways, giving birth to different “styles” of corrosion. In the 1960s, the booming days of hip implantology, implant companies were violating basic rules of corrosion prevention by combining noncompatible metals. The next decades, due to some disastrous results, tremendous research efforts were dedicated to the subject and in general to degradation of biomaterials [49].

2.6.1.1 General or Uniform Attack and Galvanic Corrosion

In general, uniform corrosion is defined as a result of small spatially and temporarily randomly distributed anode and cathode zones on an otherwise macroscopically homogeneous metal substrate [50].

Uniform attack is happening for stainless steel, CoCr alloys but also Ti show small but sizeable attack, notwithstanding the dense protecting oxide layer. The process is definitely a combination of a chemical dissolution process of the protecting oxide films, followed by galvanic corrosion of the exposed or nearly exposed alloy substrate.

Both chemical and electrochemical reactions are heterogeneous processes: a solid and a liquid phase, with or without dissolved gases O_2 and/or any other agent from the biological soup potentially assisting the initiation of attack [51].

2.6.1.2 Localized Corrosion

Corrosion observed on one spot can simply be the result of a wrong environment at the distant end of a metal object. The term localized corrosion houses a few family members with eye-catching differences in appearance [52].

1. ***Crevice corrosion***. Differential aeration is easily occurring in crevices. The reaction partners produced or consumed at different locations are shown in Figure 2.7. Where is oxygen coming from? The partial pressure in human arterial blood is 12.6 kPa (94.2 mm Hg), in venous 5.1 kPa (38.0 mm Hg), interstitial 0.3–5.3 kPa (2–40 mm Hg) and intramedullary 1.6k Pa (12 mm Hg). The oxygen pressure outside the crevice will be about constant (homeostasis!) and the inflow of oxygen is diffusion controlled. The slower this diffusion, the higher the potential difference [53].

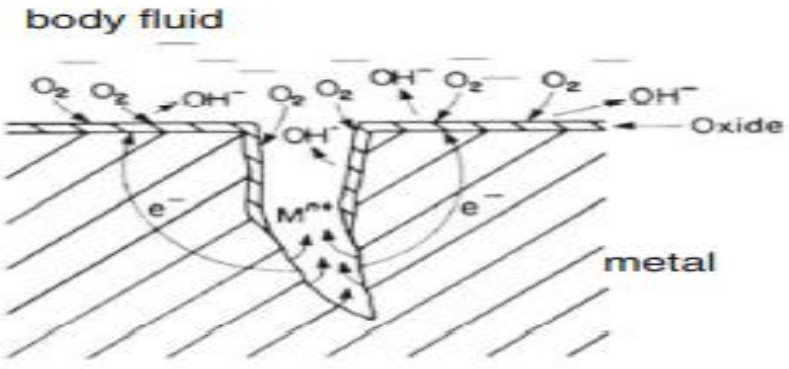

Figure 2.7 A crevice and reactions occurring in- and outside the crevice[53].

2. ***Fretting corrosion***. Fretting corrosion is a degradation process resulting from the combined action of small movements between contacting parts and the corrosivity of the environment. A special process that occurs at the contact area between two materials under load and subject to minute relative motion by vibration or some other force. This is a form of from erosion corrosion and considered as the more important form of corrosion for implantology. This can lead to tissues inflammation caused by degradation of metallic materials used in prosthetic implants which will lead to failure of orthopedic surgical operations corrosion exposes bare metal prone to corrosive attack and is caused by low-amplitude oscillatory displacement of one of the two pieces concerned. It is called fretting when the displacement is ranging from a few tens of nanometer to a few tens of micrometer. A classic biomedical example of fretting is the corrosion between the head of a screw fixing an osteosynthesis plate to bone. Oxygen is in all types the aggressive partner [54,55,56].

3. ***Pitting***. This member of the family is recognized by the formation of holes or pits on the metal surface. In terms of weight loss, pitting is negligible compared to general corrosion but not negligible in its potential harm. Pitting starts at the critical potential Ec, where the oxide layer is breaking down. The rate of penetration may be 10–100 times the one caused by general corrosion. The pits start modestly small and are in that stage hardly detectable, but they can grow to sizes macroscopically visible and generally in great number. The reason for the excessive fast growth rate is easily explained. The pits are generally anodic and their area is small compared to the rest of the corroding piece, for example the prosthesis stem, which acts as the cathode. The consequence is obvious: the anodic current density, the current per unit area, can be orders of magnitude higher than the cathodic one [58,59].

4. ***Corrosion fatigue***. Fatigue did not get that much attention till the Comet of BOAC, Flight 781, crashed off the Italian island of Elba on 10th January 1954 with the loss of everyone on board. High stresses in the corners of the window wrong engineering as would say now, causing metal fatigue were finally found to be the origin of the catastrophic blow of the fuselage. Fatigue was certainly not unknown as reason for failure, but the dramatic Comet crash (followed by a second one three months later near Naples) made the engineering community extra alert to the phenomenon. Here, only mechanical stresses were involved. The failure of the hip prosthesis was caused by corrosion-assisted fatigue crack growth. In fatigue cracks fresh unprotected metal is an easy prey to biofluids and, as mentioned in the case of stainless steel, sulfur compounds are diffusing into the cracks (and along the grain boundaries as well)[60,61]. A fracture failure of metal that happens due to the combined interaction of electrochemical reactions and cyclic loading. Corrosion fatigue resistance is an important factor of consideration for load-bearing surgical implant metals or for metals used in cyclicmotion applications. Normally, a failure may not happen, but cracks can initiate from hidden imperfections, minute flaws, surface damage, chemical attack and other causes [62]

5. ***Stress corrosion cracking***. The sudden failure of normally ductile metals when subjected to tensile stresses in a corrosive environment is called SCC. It is the result of typically subcritical crack growth, hence under conditions where failure should not occur. Although titanium alloys were recognized for their excellent corrosion resistance, Ti-6Al-4V is also sensitive to this phenomenon [63].

2.6.2 Intoxicated by Implants

2.6.2.1 Toxicity

By definition, essential elements do not have intrinsic toxicity. The supply and subsequent concentration in the body may, however, be deficient, optimal, in excess, or, beyond simple excess, harmful and toxic. Intrinsically, toxic elements show a negative response to any concentration, the end of the response curve being possible death [64, 65]. Tables are published for toxicity levels commonly expressed as Lethal Dose. LD50 is the administered amount of an element in a specified form (e.g., $CoCl_2$) for which 50% of the test animals die. Hercule Poirot, William of Baskerville, Sherlock Holmes and, of course, forensic investigators of today are well acquainted with deliberate administration of lethal doses. Acute poisoning is, however, only reported for accidental ingestion by children, intoxication during industrial accidents or in agriculture (thallium, arsenic, methylmercury) [66].

2.6.2.2 Trace and Essential Trace Elements

Except for iron, calcium, sodium, potassium and magnesium, all metal ions are present in the body as trace elements. The essential elements are listed in Table 2.4.

The second column lists the average total amount of the element present in an adult person. The third column lists the molar concentration in plasma and the fourth column the average daily amount an adult person takes in [67].

Table 2.4: Concentration of essential elements in humans [67]. The ions are listed as they are expected to occur at pH = 7

Element	Total	Plasma	Daily allowance
Na^+	100 g	141 mM	1–2 g
K^+	140 g	4 mM	2–5 g
Mg^{2+}	19 g	0.9 mM	0.7 g
Ca^{2+}	1000 g	2 mM	0.8 g
$Cr(OH)_2^+$	6 mg	0.5 µM	0.1 mg
MoO_4^{2-}	9 mg	0.05 µM	0.3 mg
Mn^{2+}	12 mg	0.2 µM	4 mg
Fe^{2+}	4.2 g	20 µM	10–20 mg
Co^{2+}	1 mg	0.1 µM	3 µg
Ni^{2+}	1 mg	0.1 µM	170 µg
$CuO\downarrow$	72 mg	18 µM	3 mg
Zn^{2+}	2.3 g	20 µM	15 mg
Si			10–26
HPO_4^{2-}	780 g	2 mM	1 g
SO_4^{2-}	140 g	1 mM	–
$HSeO_3^-$	5 mg	2 µM	0.1 g
F^-	2.6 g	10 µM	2 mg
Cl^-	95 g	103 mM	2–4 g
I^-	30 mg	0.5 µM	0.15 µg

A remark about silicon. This element is not taken up in current tables of essential elements. Its absence in the body should be quite strange as it is the second most abundant element in earth's crust (about 28%). silicon element is actively involved in bone formation sites of the body with Ca contents ranging from 0.1 to 2.0%, the Si content ranges from 0.08 to 1.0%. [67].

2.6.2.3 Sensitivity to Metal Implants

About 10–15% among the general population is sensitive to nickel, cobalt or chromium but with Ni having the highest sensitivity (>10%) as shown in fig (2.8) and fig (2.9).

The prevalence of metal sensitivities to one or combinations of Ni, Cr and Co is for patients with well-functioning implants roughly double that of

the general population (25 vs. 10%), and four to five times that for patients with poorly functioning implants as reported by 60%. Notice, however, that the association of patients to well- or poorly functioning prostheses is not proving causal effect and a number of parameters were not specified (preexisting sensitivity). The outcome is as such not unexpected; wear and corrosion provoke anyway more metal dissolution than well-fixed prostheses .

Figure 2.8 A patient with severe allergy to cobalt [68].

Figure 2.9 Allergy to chromium two months following implantation of a cobalt–chromium alloy[69].

2.6.3 Friction and wear failure

Wear is surface damage or material removal from surfaces in contact and in motion with respect to each other. Material may be damaged at the surface, broken loose as a wear particle, or it may be transferred from one

surface to another [70]. Wear properties of an implant material are important, especially for various joint replacements. Wear cannot be discussed without some understanding of friction between two materials. When two solid materials contact, they touch only at the tips of their highest asperities (microscopic protuberances). Therefore, the real contact area is much smaller than the apparent surface area. It is found that the true area of contact increases with applied load (P) for ductile materials. Ductile materials can be pressure welded due to the formation of plastic junctions, as shown in Figure 2-10 [71].

The plastic junctions are the main source of an adhesive friction when two materials are sliding over each other with or without a lubricating film. The resistance to the shear failure of the plastic junction results in a frictional force [70, 72].

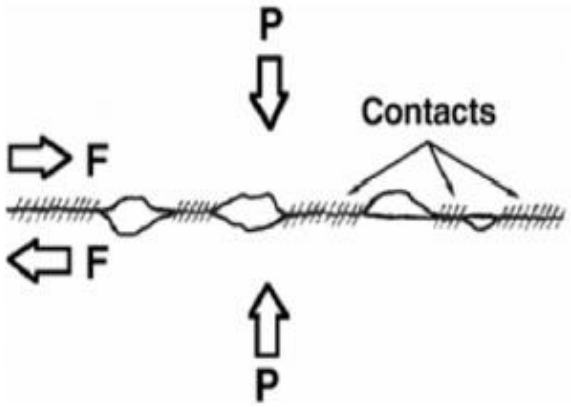

Figure 2-10 Schematic representation of two surfaces under pressure. Plastic junctions are formed when ductile materials are pressed together between asperities [71].

The wear rate is increasing in case of the similar metals are used in contact surfaces. Hence, dissimilar metals will decrease the wear. Specifically, the lower the mutual solid solubility of the metals, the lower the wear. Typical wear coefficients for various conditions [73].

In the context of biomaterials, dissimilar metals are problematic in view of the fact that corrosion occurs when dissimilar metals are placed in an aqueous, saline environment such as the body. Moreover, wear of metals in a corrosive environment is exacerbated. Polymer–metal interfaces can exhibit relatively low friction and wear, but low friction does not guarantee low wear.For example, (PTFE, polytetrafluoroethylene) offers a low coefficient of friction, but it undergoes severe wear. Was tried in early implants but was not successful due to excess wear. Currently, UHMWPE (ultrahigh-molecular-weight polyethylene) is favored for use in joint replacement implants. Polymers cannot withstand as much contact stress as metals, but they are adequate in this regard for use in joint replacements.

Wear debris in hip replacement implants can cause tissue reactions, including proliferation of local fibroblast-like cells and activated macrophages. While PMMA and UHMWPE are inert in the bulk, small particles of these materials act as cellular irritants. Tissue reaction to wear debris is a contributing factor to bone resorption and implant loosening, a major cause of joint implant failure [71, 73].In joint replacement implants, metal-on-metal designs offer reduced wear rates in comparison with metal-on-polymer ones, and are therefore considered an alternative. However, since the new designs and better congruent head and socket designs are relatively new, only early and midterm clinical results are available, and no long-term results.

Elevated levels of metal ions due to wear debris have been observed in patients with these implants, but it is not yet known if there is a health risk. Diamond coatings have been explored in the laboratory in an effort to achieve wear-free surfaces. Alumina ceramic surfaces have been used clinically to achieve low wear [73, 74].

2.7 Zirconium Alloys for Orthopedic Applications

2.7.1 Zirconium and Zirconium alloy

Highly pure Zr shows excellent deformability at room temperature because of dislocation slip as well as twining work as deformation modes, similar to Ti. However, the strength is insufficient and is improved by alloying. Tin (Sn) and oxygen (O) are added as alloying elements, which stabilize the α phase, the α stabilizer, and increase the allotropic temperature. On the other hand, iron, chromium, nickel, and niobium stabilize the β phase, the β stabilizer, decreasing the allotropic temperature. The phase equilibrium diagram of Zr alloy as shown in figure (2.11).To increase resistant to corrosion and strengths, the quantity of these components added may be changed. Zr alloy grades are classified into industrial and nuclear grades. Table 2.5 lists the chemical compositions and tensile properties of industrial and nuclear grades of Zr alloys [12, 14].

The clear difference between the grades is the hafnium (Hf) content. Industrial grades permit Hf content of up to 4.5 %, but the content is restricted below 0.01 % for the nuclear grade because of the relatively higher thermal neutron cross section.

The effects of Hf on the mechanical properties as well as corrosion resistance seem to be small; thus, the properties are quite similar between the two grades. Various microstructures appear, depending on the annealing temperature and the cooling condition. For example, after cold

rolling up to 20 % followed by stress-relief annealing at 673 K for 20 h, the network structure, consisting of the α phase surrounded by the β phase, is formed in the alloy [13].

Table 2.5 Compositions and tensile properties of industrial and nuclear grades of Zr alloys [12 – 14].

	(Mass%)			
Element	R60702	R60704	R60705	R60901
Zr+Hf, min	99.2	97.5	95.5	Balance
Hf, max	4.5	4.5	4.5	0.010
Fe+Cr	0.2, max	0.2–0.4	0.2, max	Fe:0.15, Cr:0.020
Sn	…	1.0–2.0	…	0.0050
H, max	0.005	0.005	0.005	0.0025
N, max	0.025	0.025	0.025	0.0080
C, max	0.05	0.05	0.05	0.027
Nb	…	…	2.0–3.0	2.40–2.80
O, max	0.16	0.18	0.18	0.13
Tensile properties	R60702	R60704	R60705	R60901
UTS, min (MPa)	379	413	552	450
Yield strength, min (MPa)	207	241	379	310
Elongation, min (%)	16	14	16	15

2.7.2 Current biomedical applications

Typical use of Zr for biomedical applications is in total knee replacement (TKR) and total hip replacement (THR). The Zr-2.5Nb alloy (UNS R60901) is provided for surgical implant applications and is regulated in ASTM F2384-10 [14]. The Zr-2.5 Nb alloy is used for the femoral knee surface and the head of the hip joints, which was called Oxinium and developed by Smith and Nephew in 1997 for TKR and in 2002 for THR. Although the wear resistance of Zr is low because of its

low hardness, thin zirconium oxides (ca. 5 μm) form when the Zr-2.5Nb alloy is heat-treated at approximately 500°c in air [15]. Relatively high compressive stress is generated in the oxide layer, and this contributes to the adherence to the base material [16].

Zircadyne alloys uses in biomedical applications are composed of 95.5% to 99.2% zirconium and hafnium with a maximum hafnium content of 4.5%. Zircadyne mill products are available in two chemical grades each sharing an excellent corrosion resistance and also having slightly different physical and mechanical properties. Zircadyne 702 Zirconium is commercially pure. Zircadyne 705 zirconium is alloyed with niobium to increase its strength and improve its formability. As table 2.5 shows [12-14-75].

The presence of hafnium in Zircadyne alloys does not significantly influence the physical, mechanical, or corrosion properties. Zirconium, a reactive metal, has a high affinity for oxygen that results in the formation of a protective oxide layer in air at room temperature.

This protective oxide gives Zircadyne alloys their superior corrosion resistance and this oxide layer can be enhanced through a heat treating process. A properly formed enhanced oxide layer serves as an excellent bearing surface against a variety of materials, imparts impressive erosion resistance in high velocity systems, and can improve the corrosion resistance in certain aggressive environments [76].

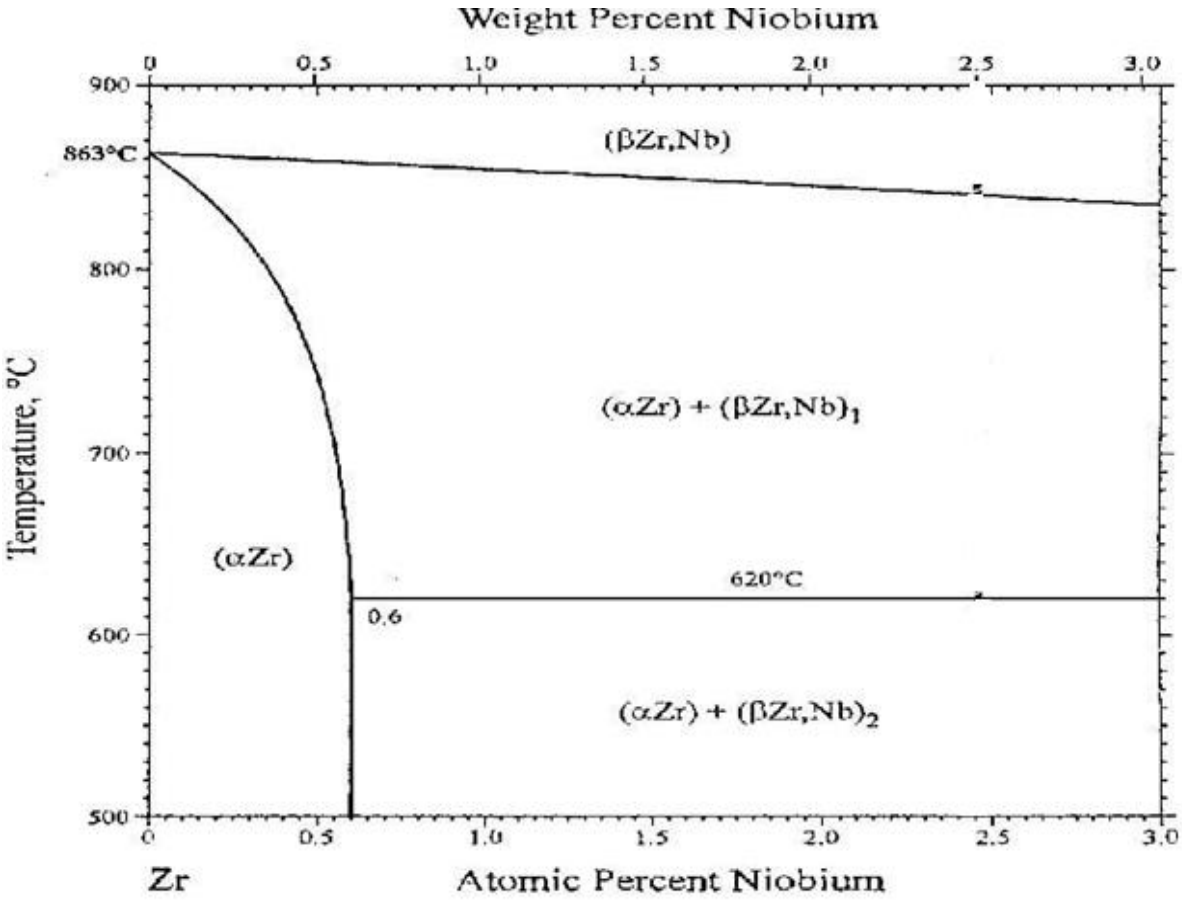

Figure (2.11) Phase equilibrium diagram of Zr alloy [27].

2.8 Surface properties of biomaterials

The exterior boundary or the outermost layer of atoms of the material. Surface is sometimes also defined as the shell that separates the object from the environment. Interface is the boundary region between two adjacent phases, such as between solid and liquid. Atoms and molecules forming the surface will govern the surface properties of that material, because they will be in contact with the host atoms and molecules or their immediate. Surfaces of the bulk materials are different because the number of dangling bonds is less as compared to the smaller particles of the same volume. Dangling bonds are the chemical bonds associated with atoms present on the surface layer of solids. Surface atoms are joined with the atoms from their interior side but do not join an atom with a

second atom from their exterior side and extend in the direction of the solid’s exterior or toward the vacuum. [77].

Biomaterials are artificial or natural materials that are designed to operate properly in biological environments where they are utilized to direct complement or substitute the function of the human body's living tissues [13]. Surface properties, to a large extent, define success or failure of a biomaterial. The surface properties of biomaterials that are important for acceptance in the host include chemical structure, hyrophilicity/hydrophobicity, the presence of ionic group, surface morphology and top graphy.

Surface modifications can be employed to tune surface properties for specific applications such as cell adhesion, biomimetics, and so on. Surface modifications can be performed by methods such as chemical modification using polymers, biopolymers, organic layers or by growing microbes on the surface of the material [12]. Biomaterials such as polyethylene and their composites titanium and titanium-based alloy that are used in different kind of implants such as in acetabular cup replace and hip joints replacement in human body need surface modification for long life of implant as well as host and for better performance .

Some of the required surface properties of biomaterials include the following:

1. protein adsorption,
2. cell adhesion ability,
3. biocompatibility,
4. biomimetics,
5. biodegradation,
6. hydrophobicity/hydrophilicity

2.9 Surface Engineering and modification

Furthermore/surface modification is the attachment of various ligands or molecules to bring forth distinct physical, chemical or biological properties [28].Surface modification is achieved by modifying the surface atoms/molecules via physical/chemical route, or by depositing a layer over the surface. The layer could be of polymer, organic layer, or a thin film of another material. Surface modification is employed in biomaterials to improve interfacial properties such as wettability, adsorption of proteins and ligands and improved roughness that will enhance the biomaterial's effectiveness [29].Several surface modification methods are shown in Figure (2.12, 2.13) and table 2.6. Particular methods can be applied according to the surface of the substrate and the requirement of the modification.

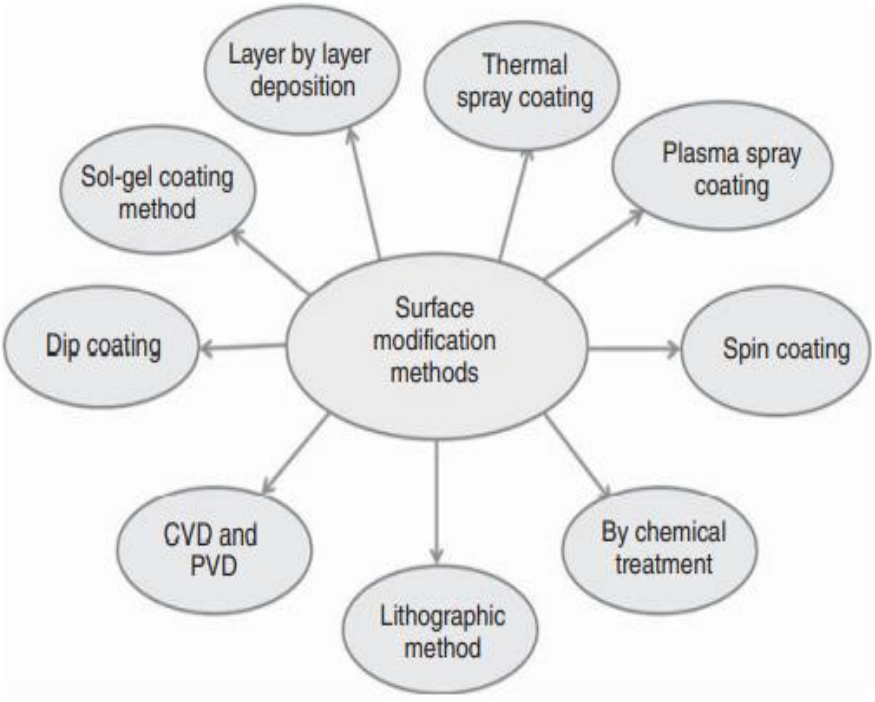

Figure 2.12 Schematic diagram showing different methods for the surface modifications [29].

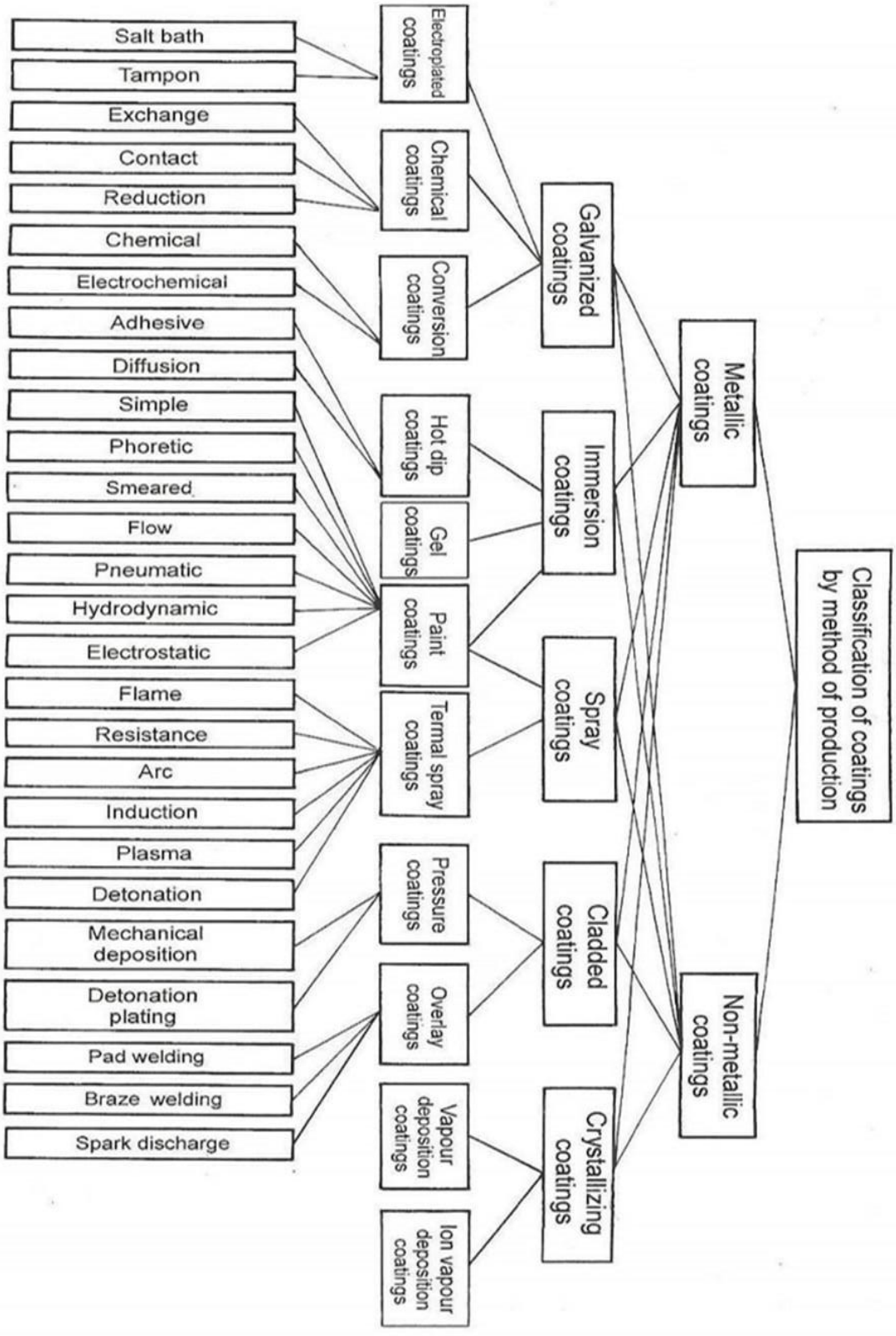

Figure 2.13 Schematic diagram showing classification of coatings[164].

Table (2.6) Different methods for the surface modifications.

Surface modification methods	Modified layer	Objective
Mechanical methods **Machining** **Grinding** **Polishing** **Blasting**	Rough or smooth surface formed by subtraction process	Produce specific surface topographies; clean and roughen surface; improve adhesion bonding
Chemical methods: Acidic treatment Alkaline treatment Hydrogen peroxide treatment Sol–gel Anodic oxidation CVD	 <10 nm of surface oxide layer. ~1 μm of sodium titanate gel. ~5 nm of dense inner oxide and porous outer layer. ~10 μm of thin film, such as calcium phosphate, TiO2. ~10 nm to 40 μm of TiO2 layer, ~1 μm of TiN, TiC, TiCN, diamond and diamond-like carbon thin film.	 Remove oxide scales Improving biocompatibility, bioactivity or bone conductivity Improve biocompatibility, bioactivity or bone conductivity. improve biocompatibility, bioactivity or bone conductivity Produce specific surface topographies; improved corrosion. Improve wear resistance, corrosion resistance and blood compatibility.
Biochemical methods	Modification through silanized titania, photochemistry, self-assembled monolayers, protein-resistance, etc.	Induce specific cell and tissue response by means of surface-immobilized peptides, proteins, or growth factors
Physical methods: Thermal spray Flame spray Plasma spray HVOF and DGUN	~30 to 200 μm of coatings, such as titanium, HA, calcium silicate, Al2O3, ZrO2, TiO2.	Improve wear resistance, corrosion resistance and biological properties
PVD Evaporation Ion plating Sputtering	~1μm of TiN, TiC, TiCN, diamond and diamond-like carbon thin film	Improve wear resistance, corrosion resistance and blood compatibility

Ion implantation and deposition Beam-line ion implantation PIII	~10 nm of surface modified layer and/or ~µm of thin film	Modify surface composition; improve wear, corrosion resistance, and biocompatibility
Glow discharge plasma treatment	~1 nm to ~100 nm of surface modified layer	Clean, sterilize, oxide, nitride surface; remove native oxide layer

2.9.1 Surface Modification of Biomaterials Objectives

Objectives of modifying a bio surface include the following:

1. reduce/eliminate protein adsorption (according to the need of application);
2. control cell adhesion ability;
3. reduce bacterial adhesion;
4. increase biocompatibility;
5. increase lubricity;
6. increase/decrease wettability;
7. increase hardness/softness;
8. enhance corrosion/degradation resistance (according to the need of application)

It is better for biomaterials to possess anti-microbial property so that the growth of bacteria can be avoided. A biofilm is a layer formed during the growth of bacteria through which they adhere to each other and also to the implanted surface. The bacterial growth on a biosurface can be prevented or reduced by modifying their surface chemistry [31].

2.10. Chemical/electrochemical Methods

Chemical reactions take place at the interface of metal products and the imposed media (solution or gas phase) in chemical methods. Surface-modified layers formed on the surfaces of alloys are produced based on redox reactions [78]

2.10.1Anodic oxidation

Anodic oxidation is a well-acknowledged method for preparing different oxide films on metallic materials [79]. In this process, metallic material is used as anode. In comparison to passivation, anodic oxidation reactions are driven by electric field which can promote the diffusion of metal ions and oxygen ions, resulting in the formation of oxide film on the surface of anode [80–81].

Anodization used to protective and dense oxide layers. Pure metals that can be anodized include aluminum, titanium, zinc, magnesium, zirconium, tantalum, and hafnium. Basically, anodization is the oxidation of these metals in certain electrolytes by generating an electrical field at metal/ electrolyte interface several electrolytes, such as sulfuric acid, phosphoric acid, acetic acid, chromic acid and others, have been used for electrolytic solutions in anodic oxidation[82].

The main advantages of anodic oxide films are the enhanced adhesion and wear resistance, which mainly aims to serve the electronics and aerospace industries [83, 84, 85]. Fortunately, the formed oxide films on metal and its alloys also have the functions of improving corrosion resistance and decreasing ions release [86].

Therefore, anodic oxidation can also be used for biomedicine. Although the formed oxide film has a high resistivity to the electrical circuit consisting of the electrolyte and the metallic part, the oxide film would continuously grow as long as the electric field is strong enough to drive the ions through the oxide film.

The final thickness of oxide film is approximately proportional to the applied potential. However, the formed oxide has a breakdown potential of about 100 V [87].

If anodic oxidation is conducted at a voltage above the breakdown limit, the oxide film would not be resistive enough. As a result, increased gas

evolution and frequent sparking would take place during such an anodic process. Typically, a nonuniform and porous oxide film is formed in this situation.

Such a process is also called as micro-arc oxidation (MAO) or plasma electrolytic oxidation [87].

Oxide films prepared on Ti and Ti alloys by anodic oxidation show complicated surface morphologies and microstructures[87].The morphologies of oxide films are dependent on their thickness (usually increase in roughness associated with increasing the thickness) and the topographies of the underlying substrates. Similar memory effects were observed between the microstructures of oxide films and metal substrates, which is attributed to the distinct growth rates of oxides on the different phases in metallic materials. For biomedical applications, calcium and phosphorus ions can be incorporated into anodic oxide films in an electrolytic solution containing dissolved calcium and phosphorus compounds [86, 88]. Figure 2.14 schematic indicates Ti6Al7Nb alloy as the anode, the mechanism of anodization is similar for all Titanium alloy.

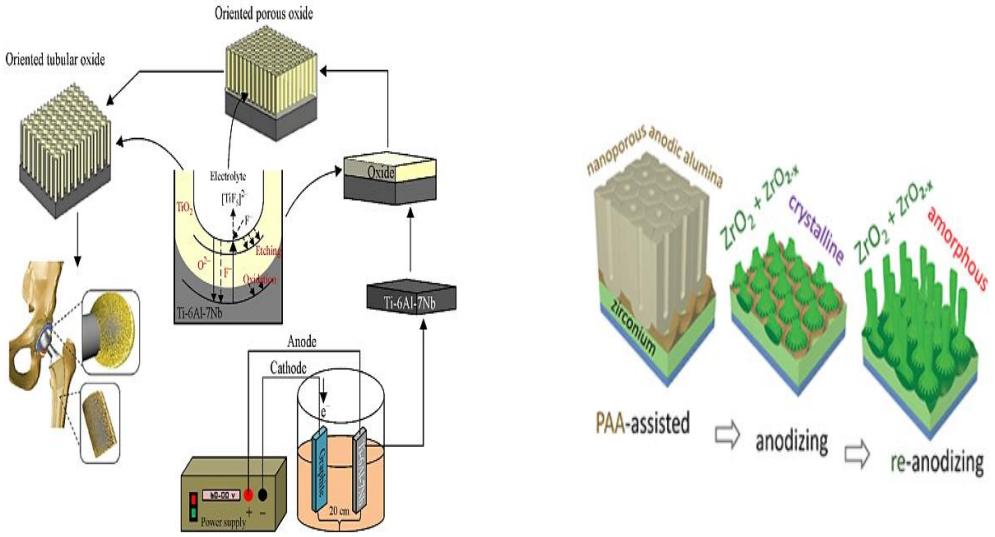

Figure 2.14 Schematic depicting the growth of nanostructured oxide film on Ti6Al7Nb alloys [89].

Anodization parameters:

- Electrolyte type
- electrolyte concentration,
- pH
- temperature
- Applied voltage
- time

It is possible to control physical and chemical properties of the oxide film forming on the metal alloys [89,90]. Anodization using various electrolytes, such as NH4F, CH3COOH, H2SO4, HF, Na2HPO4, NaF, NH4Cl [91]. In addition, it is well-established that different electrolytes have different ionic conductivities, and thus form different electrical fields inside an electrochemical cell.

2.10.2 Micro-Arc Oxidation

MAO can be regarded as a developed method from anodic oxidation, which is also named anodic spark oxidation or plasma electrolytic oxidation.[92,93]

This method can synthesize ceramic coatings on the surface of many metals, such as Ti, Al, Zr, Mg, and other metals [92, 94, and 95]. During the MAO process, the sample is used as anode and immersed in the aqueous solution associated with a relatively high voltage. This voltage must be above the breakdown limit of the formed oxides. Sparking, which leads to less uniform and more porous oxide films, frequently takes place on the surface of the processed samples. For TiO2, the breakdown limit is about 100 V [96]. Therefore, the voltage of MAO is often conducted above 150 V for Ti and Ti alloys.

After MAO treatment, porous coatings with high hardness, wear resistance, and adhesion could be produced. Such porous coatings improve the biocompatibility of metal and its alloys [97]. MAO method is primarily used for metal and its alloys in the biomedical applications.

The chemical compositions, morphologies, and microstructures of MAO-produced coatings strongly depend on the MAO parameters:

- alloy compositions
- electrolyte
- temperature
- time
- Voltage
- duty cycle (the ratio of the on-time to the total working time),
- current density .

The biocompatibility examinations show a highest proliferation rate on the sample treated at 190 V and exhibit a best alkaline phosphatase activity on the sample treated at 600 V [98].The parameters used during MAO should take the service environments into consideration. Similar to voltage, current density has a significant influence on the microstructures and properties of the MAO coatings. Constant-voltage mode results in a freely decreased current density during MAO, which finally leads to a relatively smooth surface with low porosity [99]. Conducted MAO on CP–Ti in a phosphate electrolyte for 300 s at different current densities and their results showed that the pore size decreases with decreasing the current density. Such morphology facilitates the formation of apatite and the proliferation of osteoblast cells [99,100]. Higher duty cycle results in a higher on-time of electricity during each cycle, leading to a higher energy of spark[101].Although there is no systematic investigation on the microstructure and properties of MAO-treated Ti and Ti alloys with

respect to duty cycle, some studies on other metals show that increase in duty cycle can slightly decrease the coatings thickness but increase their porosity [102]. Apart from these processing parameters, the choice of electrolyte is extremely important to MAO coatings as the concentration and composition of the electrolytes influence the metal passivation, therefore the morphologies, thicknesses, and properties of the MAO coatings. In general, NaOH/KOH is used as the base electrolyte [97].

The electrophoresis can be used as an auxiliary method for MAO [103]. Carried out MAO treatment on a Ti–6Al–4V alloy using a phosphate salt solution as electrolyte and followed by conducting electrophoresis using an HA powder aqueous suspension as electrolyte. Their results showed that a relatively thick TiO2 film is produced by MAO and an HA coating formed on the TiO2 film; the as-produced coating shows a porous appearance and better corrosion resistance in a buffered physiological solution compared with the untreated Ti sample. Some additives, such as phosphate, fluoride, silicate, sodium salt, and calcium salt, are frequently used as the primary additives in the base electrolyte [104].

Fluoride-containing electrolyte induces the formation of fluoridated HA in the MAO coatings, leading to a favorable bone response and interface adhesion [104, 105,106]. Prepared Si-incorporated MAO coating on CP–Ti using simple electrolyte composed of NaOH and $NaSiO_3$; the Si-incorporated MAO coating shows better adhesion and proliferation of rat bone mesenchymal stem cells compared with the Si-free counterpart. Some other ions, such as strontium, manganese and copper, have been also considered to be incorporated in the electrolytes to improve the bioactivity or antimicrobial property of implant materials [107–108]. Ionic substitutions easily take place in apatite structure, hence multiple elements can be considered to modify the electrolyte, which may result in better biocompatibility and closer composition of the MAO coatings to

human bone [109].As a very popular method for surface modifications, MAO has a promising future in the biomedical applications . As the produced in the micro-arc oxide film has good dielectric properties and photocatalytic performances, MAO technology is also used in electronics and environment protection industries [104, 110]. However, there are still some questions needed to be solved. Meanwhile, although MAO can also conduct on the work pieces with complex shapes [111,112].

The thickness of the MAO layer is not homogeneous due to the limitation of geometry [111]. Conducted MAO on the porous metal alloys and found that the MAO coating formed on the outer pore walls has a larger thickness and larger pore size compared with the MAO coating formed on the inner pore walls. Such a difference also causes the different compositions [112]. The schematic diagram is shown in figure 2.16. The detailed mechanism of MAO process has not yet been revealed; however, most investigators agree that during each alternating current (AC) period several principal stages occur [162]:

Stage I: The voltage approaches the breakdown voltage, it increases rapidly and linearly as shown in Figure 2.15 (a) [162] some small oxygen bubbles and an oxide layer on the sample surface, which corresponds to the conventional anodizing step.

Stage II: Dielectric breakdown occurs when the applied voltage surpasses a certain point, leading in the production of spark discharges. The current flow focuses exclusively in regions of breakdown at this step, resulting in localized oxide layer thickening. The newly created coating can restore current flow resistance, whereas other areas with lower resistance are more prone to collapse as shown in Figure 2.15 (b) [162]. It’s showing a stage when a shrill sound is accompanied by a large number of tiny white sparks that are randomly dispersed and rapidly traveling across the whole anode surface.

Stage III: The cell potential fluctuates due to the continual production and breakdown of the oxide layer. The immediate production of ceramic oxide coating is enabled by gasification of both the valve metals and the electrolyte. The coating breaks down at a susceptible location in the developing oxide sheet. The discharge sparks become larger as the processing time increases, and their hue changes from white to orange or red. It shows how the micro-arcs convert into strong arcs in this location as shown in Figure 2.15 (c) [162].

Stage IV: The huge pores and thermal breaking of the film are caused by the strong sparking and gas release. The voltage drops fast together with the absence of sparks and gas bubbles, indicating the conclusion of the MAO process. The MAO coating has a two-layered design, with a barrier inner layer and a porous outer layer with many fine and coarse cavities. The coating thickness ranges from 1 to 100 meters as shown in Figure 2.15(d) [162].

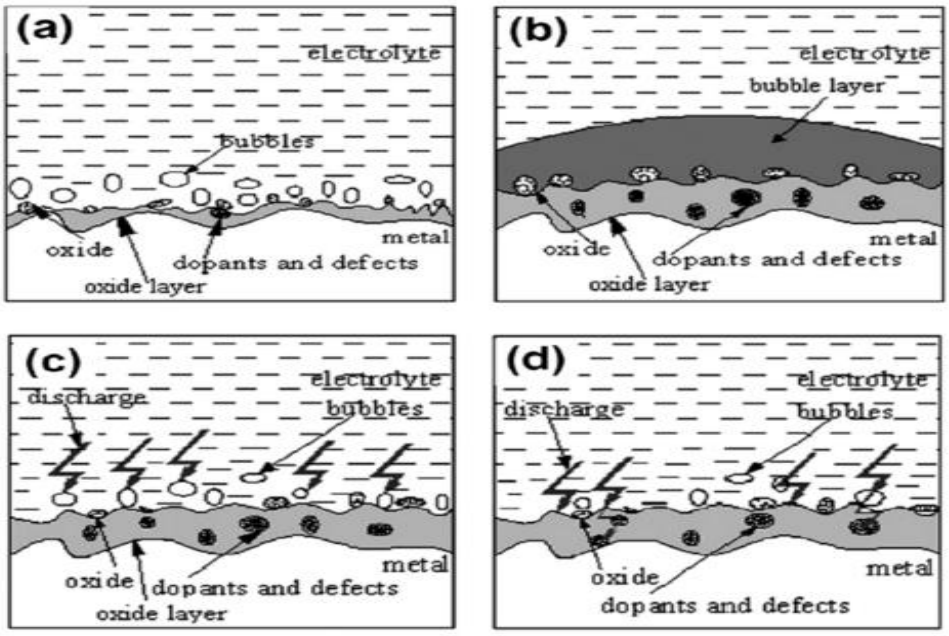

Figure (2.15): Schematic illustration of the plasma discharge during different stages of the MAO process. (a) Stage I, (b) stage II, (c) stage III, and (d) stage IV [162].

So far, the mechanism of MAO has remained a mystery, making it impossible to develop a precise theory to guide the functioning. The presence of an electrical breakdown throughout the operation is acknowledged, and the breakdown mechanism is based on the solid liquid contact. A thermal electron emission process was proposed as the cause of the discharge along the dielectric surface. believed that an electron current forms along the dielectric's surface as a result of the tunnel effect and impurity ionization [163].

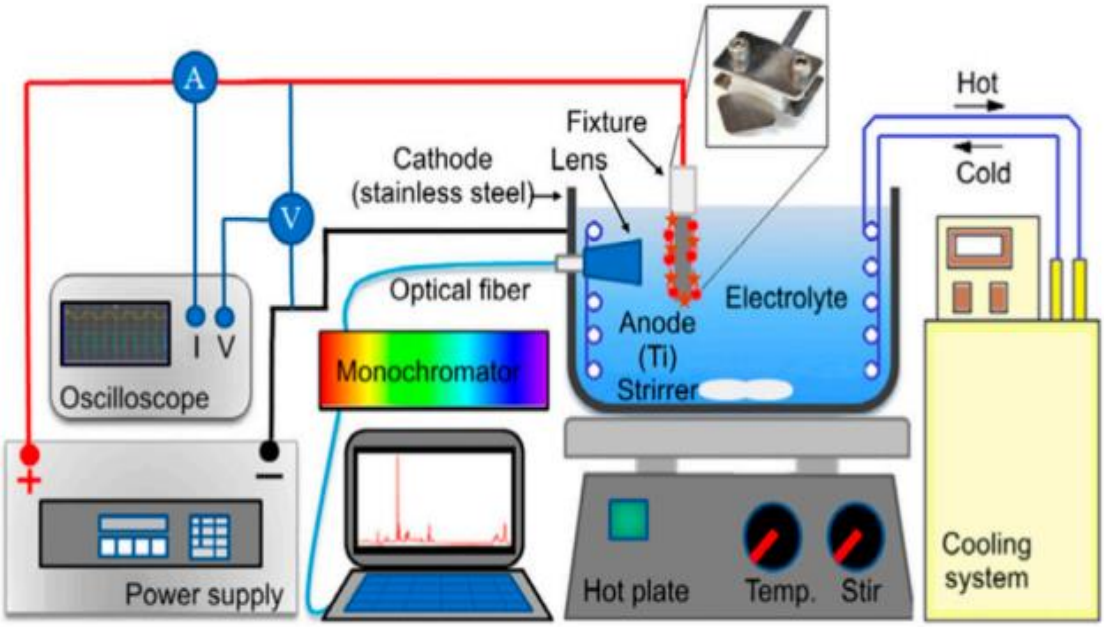

Figure 2.16 Schematic diagram of the micro-arc oxidation (MAO) [113].

Different thickness values may provide an evidence to specify their different properties. Furthermore, there is a lack of investigations on the design of electrolyte as well as the influence of substrate on the compositions of MAO film. Therefore, the detailed mechanism for MAO is not well understood. These questions draw forth the future development of MAO technology. First, increasing the utilization of energy by optimizing MAO facility should be significantly considered. Second, to complete the discharge model and film growth model of MAO is necessary in the further development of this technology Third, combining some other methods (such as heat treatment and electrophoresis) to further enhance the performance metal alloys may be a trend for MAO technology targeting broad applications.

2.11 Hydroxyapatite (HA)

Hydroxyapatite (HA) is calcium phosphate ceramic material that has been used for manufacturing various forms of implants. morphology and composition very similar to the inorganic parts of the human bone and

teeth. HA was commonly utilized in biomedical applications due to its excellent osteoconductivity, biocompatibility and bioactivity [114].

2.11.1 Crystal structure and phase of HA

Calcium phosphate can be crystallized into salts such as hydroxyapatite [$Ca_{10}(PO_4)6(OH)_2$] depending on the Ca:P ratio of HA is 10:6. The atomic structure of hydroxyapatite projected down the *c*-axis onto the basal plane is shown in Figure 2.17 [115].

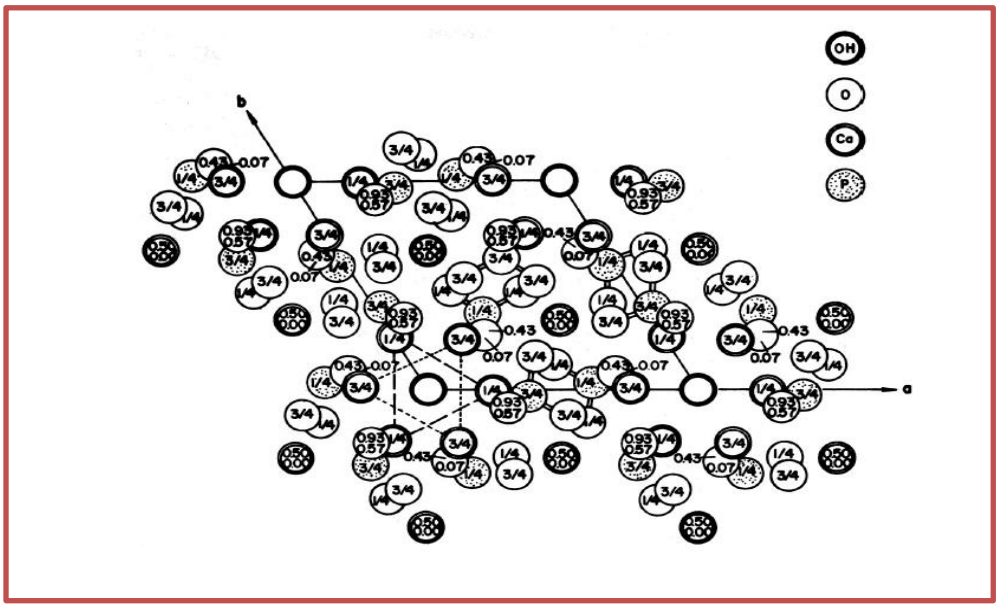

Figure 2.17 Hydroxyapatite structure projected down the *c*-axis onto the basal plane [115].

2.11.2 Properties of HA

Attractive properties of HA such as lack of toxicity and high elastic modulus (40 to 117 GPa) as shown in Table 2.7 [116]. The large gradient in the elastic modulus between implant and the bone, where this lead to stress-shielding phenomenon. During stress shielding, the load put on the implant during movement is not transmitted by the bone but through the stiff implant leading to atrophic loss of the cortical bone [117]. Excellent biocompatibility of HA so that used biomaterial. HA appears to forma direct chemical bond with hard tissues [116]. The lower fracture

toughness is the main constraints of HA as compared to the compact cortical bone, which means that HA behaves as a relatively brittle material [118].

Table 2.7: Mechanical properties of bone VS. HA [116].

Mechanical properties	Cortical bone	HA
Compressive strength, MPa	100-230	120-900
Tensile strength, MPa	50-150	38-300
Fracture toughness, MPa.m1/2	2-12	1
Young's/Elastic modulus, GPa	18-22	35-120
Density, g/cm3	2.9-3.88	3.156

2.11.3 The HA coating

This coating of HA enhances the bone/implant bonding properties, and increases the corrosion resistance of the substrate. HA coatings have a close composition match with that of the bones as the components are the major inorganic portion of the bone composition. these coatings allow fast and selective bone ingrowth and enhanced osseointegration. HA shows a high increase in biocompatibility and bone/implant interface formation [119].The bioactivity of the HA make it an outstanding material for the metallic implants coating since it has the ability to form and grow to the surrounding tissues of the bones [120]. An intimate contact between the surface of metallic implant and the adjacent bone tissue required for posterior bone growth. However, coating of the metallic implant with the HA results in a fast bonding between them. Using of the HA as coating on the metallic implant combine the strength

and toughness of the implant material with the bioactive properties of the HA coating layer that can promote the surrounding bone tissue growths and future chemical bonding formations. Moreover, the existence of the HA can enhance the corrosion resistance of the implant in the human body, thus reducing the release of metallic ions and promoting fixation through chemical bonding [119].

3.11.4 Advantages of HA

A list of advantages includes [121]:

1. High biocompatibility.
2. High bioactivity.
3. Faster and improved osseointegration.
4. No formation of fibrillar connective tissue surrounding the implant and thus separating it from the bone.
5. Osseointegration even in the presence of micromotion between implant and bone.
6. Formation of a strong bond between implant and bone with tensile strengths.
7. Reduction of pain after operation.
8. Earlier implant loading after healing phase possible.
9. Variable metallic substrates possible.
10. Variable surface structures possible, including mesh, artificial spongiosa, porous coatings and roughened surfaces.
11. Thickness of HA coating depending on application.
12. Rarely problems with delamination and spalling in vivo.
13. Reduced or even completely alleviated release on metallic ions to the surrounding tissue.
14. High dissolution/resorption resistance in contact with body fluid.
15. Quality control and standard according to ASTM.

2.11.5 Applications of the HA

HA has been widely used in medicine and dentistry because it is biocompatible, osteoconductive, excellent chemical, biological affinity with bony tissue , support the growth of bone over its surface, increased bone-to-implant contact, improve the implant fixation, and facilitate the bridging of small gaps between implant and surrounding bone [119]. The HA has a broad range of applications in bone and tooth repairing as shown in Figure 2.18 [119].

Because of its resemblance to the human bone and teeth, HA regard a perfect candidate for [115]:

a. Hard tissue repair, such as:

1. Powders or granules for bone and tooth defect filling.
2. Particles as the component for toothpastes and bone cements.
3. Small and unloaded implants, such as in the middle ear.
4. Biocompatible and bioactive coatings on metal components.
5. Femoral plugs in total hip replacement.

b. Soft tissue repairs, such as:

1. Support the healing of skin wounds.
2. Therapy or prevention of nerve injury.
3. HA bio ceramics contact tightly and adhere strongly with skin tissue to prevent exit-site and tunnel bacterial infection.

Figure 2.18 Micro-textured and HA-coated acetabulum cups and femoral stem of hip surgery implants [119].

2.12 Zirconia (ZrO_2)

Zirconia is inert bioceramics materials. High density ZrO_2 showed excellent compatibility with autogenous bone and was completely nonreactive [122]. ZrO_2 has shown excellent biocompatibility and good wear and friction so that used in biomedical materials [115]. ZrO_2 is ceramics have several advantages over other ceramic materials due to the transformation toughening mechanisms operating in their microstructure that can be manifested in components made out of them [122].

2.12.1 Crystal structure and phase of ZrO_2

ZrO_2 is an extremely capable ceramic exists in three polymorphic forms at ambient pressure: monoclinic at <1,170 ºC, tetragonal at 1,170–2,370 ºC temperature range; and cubic at >2,370 ºC, until it melts at 2,706 ºC [123]. Pure ZrO_2 can be obtained from chemical conversion of (ZrSiO4), which is an abundant mineral deposit. a = 5.145 Å, b = 0.521 Å, c = 5.311 Å, and β = 99◦14.

It undergoes a large volume change during phase changes at high temperature in pure form; therefore, a dopant oxide such as Y2O3 is used to stabilize the high temperature (cubic) phase. Have used 6 mole% Y2O3 as dopant to make ZrO_2 for implantation in bone [121]. ZrO_2 produced in this manner is referred to as partially stabilized ZrO_2 as shown in Figure 2.19 [121].

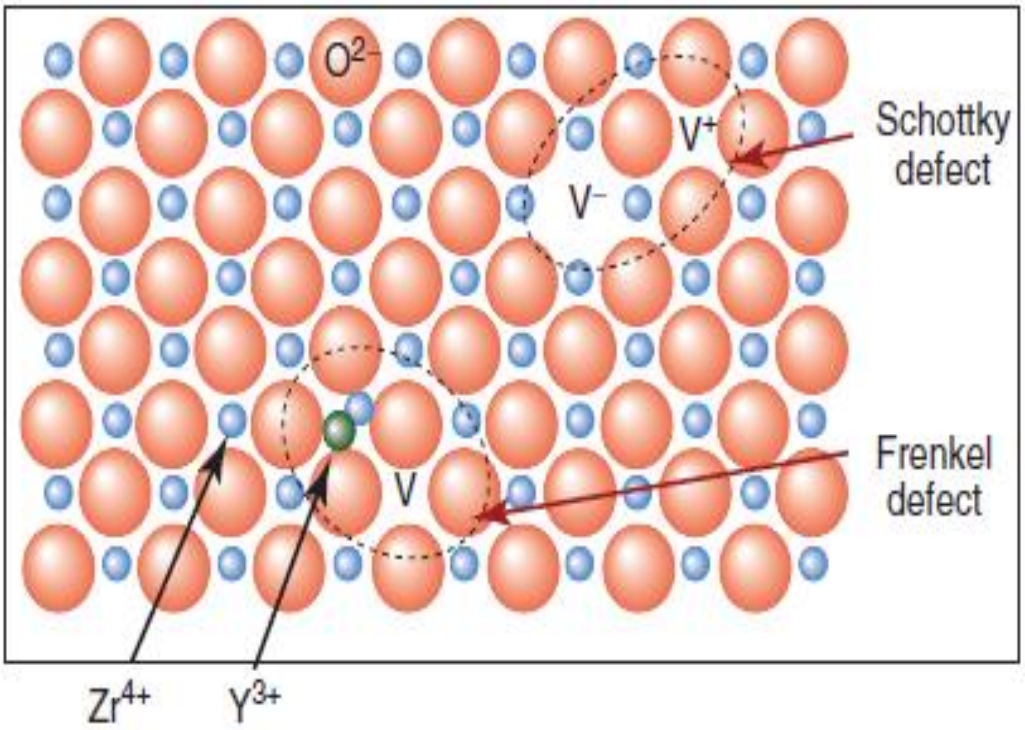

Figure 2.19 Vacancy V in the oxygen sub-lattice of zirconia and interstitial yttrium atom (Frenkel-type defect) and two matching vacancies with opposite charges in the oxygen sublattice and the cation sub-lattice (Schottky-type defect) [121].

2.12.2 Properties of ZrO_2

ZrO_2 possesses a unique combination of physicochemical characteristics such as [122]:

1. Biocompatibility and bioactivity: zirconia is biocompatible and promotes cell proliferation and differentiation in osteogenic pathways.

2. Osseointegration: bone attachment on ZrO_2 surface and the formation of a direct interface between bone and zirconia has been demonstrated in several studies, that is often comparable to or even better than titania implants.
3. Radiopaqueness: that makes it clearly visible in radiographs, thus making it possible to monitor its function.
4. Its mechanical strength and toughness: that is ascribed to the transformation toughening mechanism of ZrO_2 ceramics. The properties of ZrO_2 in Table 2.8 [121].

Table 2.8 Mechanical properties of commercially available zirconia [121].

Properties	**Range**
Density (Mg/m3)	6.05-6.09
Vickers hardness(HV)	1200-1300
Young's Moduluos	150-210
Compressive strength (MPa)	>2000
Tensile strength (MPa)	>650
Flexural strength (Mpa)	900-1300
Fracture toughness(MN/m-3/2)	7-9

2.12.3 The ZrO_2 coating

Various zirconia ceramics in modern bone replacement and repair applications as orthopaedic implants, thin films and coatings on other metallic implants, porous bone scaffolds and bone graft materials, and bone cements and spinal stabilisation devices [122]. ZrO_2 are usually

encapsulated with a thick fibrous tissue after their in vivo implantation, leading to possible aseptic loosening of the implants. It has been accepted that no foreign material placed within a living body is completely compatible [121].

2.12.4 Application of the ZrO2

ZrO_2 is one of the ceramic materials with the highest strength suitable for medical use. has been reported for zirconia femoral balls articulated for hip prostheses under normal laboratory hip simulation conditions [115].

In addition, zirconia is extremely hard with excellent mechanical properties for hip replacements, knees, teeth, tendons and ligaments, repair for periodontal disease, bone fillers after tumor surgery as shown in figure 2.20 [122]. Various applications in ZrO_2 are [122]:

1. In reconstruction of acetabular cavities
2. As bone plates and screws Zimmermann et al.
3. As drug delivery devices.
4. As femoral heads.
5. As middle ear.
6. In the reconstruction of orbital rims.
7. As components of total and partial hips.
8. In the repair of the cardiovascular area.

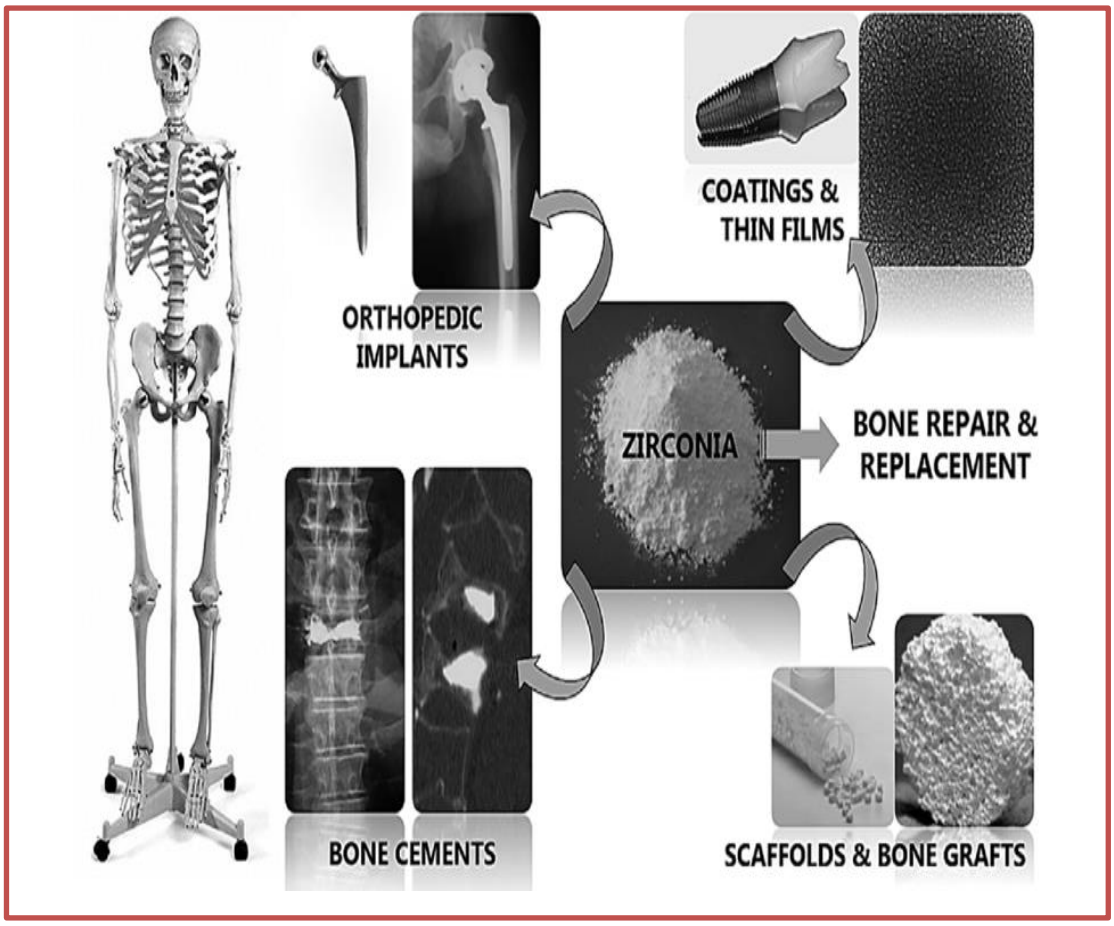

Figure 2.20 Biomedical uses of zirconia ceramics in modern bone replacement and repair applications [122].

2.13 Literature review

According to our knowledge until this time, there are no works have used the additives in the electrolyte of anodizing, and MAO. Hence, merging the two processes to improve the properties of Zr alloy. Therefore, will focus on the latest studies that have used the Anodizing and micro to improve the different properties of Zr alloys.

1. **Anodizing**

In 2014 Michał Stępień et al. studied the electrochemical growth of self-ordered zirconia nanotubes formed in aqueous Na2SO4+HF and nonaqueous electrolytes with glycerol addition. Anodizing process was carried out in this inorganic water-based mixture with constant pH=2.5 and in the voltage range from 5 to 60 V. Similar experiments were

repeated in an organic glycerol-based electrolyte with the voltage equal to 20 V and with variable glycerol concentration. All experiments were conducted at constant room temperature. The tube diameter dependence on the voltage of anodizing process in an inorganic electrolyte was derived. It was found that when glycerol addition to water electrolyte was used, it takes more time to produce long zirconia nanotubes. However, they do not collapse as the similar structure of the same length formed in aqueous electrolyte [124].

In 2018 Yang Jeong Park et al showed that the zirconium oxide layer is formed on the surface of zirconium alloy by anodizing using platinum as a counter electrode and the zirconium alloy plate as a working electrode. The anode and cathode were separated by 20 mm. Ethylene glycol (EG, 95 % purity) containing a small amount of ammonium fluoride (NH4F) and DI water were used as an electrolyte. All chemicals and materials were utilized without any modifications. A direct-current power supply with a maximum capacity of 1 A and 1,000 V was used at a temperature of 15 ℃. Zirconium alloy with the nanoporous oxide layer exhibits improvement in the oxidation resistance compared to bare zirconium alloy without the nanoporous oxide layer. Analysis using several characterization tools reveals that large single-crystalline columnar zirconium oxide grains are formed beneath the nanoporous oxide layer and these grains prevent further oxidation [125].

In 2020 Viktoriia Korniienko et al. has assessed the biocompatibility and antibacterial properties of a PEO (plasma electrolytic oxidation) coating incorporated with CuNPs (Cu nanoparticles). The structural and chemical parameters of the CuNP and PEO coating were studied with TEM/SEM (Transmission Electron Microscopy/Scanning Electron Microscopy), EDX (Energy-Dispersive X-ray Dpectroscopy), and XRD (X-ray Diffraction) methods. Cell

toxicity and bacteria adhesion tests were used to prove the surface safety and antibacterial properties. can conclude that PEO on a ZrNb alloy in Ca–P solution with CuNPs formed a stable ceramic layer incorporated with Cu nanoparticles. The new surface provided better
osteoblast adhesion in all time-points compared with the nontreated metal and showed medium grade antibacterial activities. PEO at 450 V provided better antibacterial properties that are recommended for further investigation [126].

In **2020 Aida Pantazi et al**. investigated the preparation of anodized zirconium in a mixture of electrolytes with fluoride ions, 1 M (NH4)2SO4 + 0.15 M NH4F + distilled water, at 20 V. The obtained nanostructures were investigated by SEM, EDX, XRD and AFM techniques. The SEM - EDX longitudinal and cross sectional analysis revealed the morphology of the formed oxide layers and their thicknesses, which were found to be 7.45 ± 0.18 μm. The mean nanopores' diameter was calculated as 15.8 ± 3.3 nm. The AFM revealed that the nano-porous Zr has similar hardness parameter as the uncoated Zr. However, the lower surface adhesion force that could be translated into improved properties in terms of antimicrobial effects, as confirmed by its inhibition index, which makes it a very promising material for bio-medical applications [127].

In **2021 Alexander Mozalev et al**. showed that the zirconium-oxide nanostructures highly was aligned on substrates via the self-organized anodizing and subsequent re-anodizing of pure Zr (99.99%) layers, following the initial formation of a porous anodic alumina (PAA) overlayer, at voltages ranging 50 to 500 V. The films formed after the dissolution of PAA consist of upright-standing zirconium-oxide nano-protrusions shaped like 'polyps' (anodized samples) or pillars and rods (re-anodized samples) anchored by tiny widespread nanoroots to the

bottom oxide layer. The arrays synthesized in 0.2 M H_3PO_4, which was chosen as a model electrolyte, consist of stoichiometric ZrO_2, the suboxides Zr_2O_3 and ZrO, a minor amount of Al_2O_3, and traces of PO43−species. Unexpectedly, all the anodic zirconium oxide in the re-anodized sample forms in an amorphous and perfectly flawless manner. The oxide grows due to the cross-migration of oxygen and zirconium ions with nearly equal transport numbers, which is a unique situation for anodic films on pure Zr metal. Annealing the films at 600 °C in air increases the oxidation state of the zirconium ions and induces an amorphous-to-crystalline transition, with the formation of highly textured monoclinic ZrO_2 (P21/c) nano crystallites, without generating destructive stresses or physical defects. Annealing under vacuum (10−4 Pa) partly reduces the oxide to Zr metal, with the concurrent growth of a ZrO_2 phase of the same structure and texture but in substantially larger amounts. The impact of these new findings, with detailed understanding of the abnormal ionic transport, paradoxical oxide growth, and phase-transition effects, is considered, focusing on specific applications relating to surface finishing, electronics, optics, and biomedicine [128].

2. MAO technique

In 2016 Shimin Liua et.al., deposited the hydroxyapatite (HA)/ TiO_2 composite coating on a titanium surface by one-step (MAO). The formation mechanism of the composite coating was investigated and the adhesion of the coating to the substrate was also measured. The results showed that flocculent structures could be obtained during the early stages of treatment. As the treatment period extended, increasing amounts of Ca–P precipitate appeared on the surface, and the flocculent morphology transformed into a plate-like morphology.

Then the plate-like calcium and phosphate salt self. This study shows that it is a promising method to prepare bioactive coating on a titanium surface [129].

In **2017 Salih Durdu et al** have coated the pure zirconium(Zr) by micro arc oxidation (MAO) technique in solution,consistig of calcium acetate and β-calcium glycerophosphate salt. Then, silver (Ag) thin film layer deposited on the MAO coated bioceramic surface by thermal evaporation (TE) technique. Ag coated and uncoated MAO coatings were characterized by XRD and, SEM, EDX-mapping and contact angle goniometer, respectively. Zirconia, calcium zirconate and hydroxyapatite were detected on the surface after MAO and MAO+TE processes. Both coating surfaces were rough and porous. After TE process, Ag was homogeneously distributed on the surface. The Ag-based coated surface was hydrophobic compared to MAO surface. In vitro properties such as bioactivity and anti-bacterial tests of both coatings were investigated by soaking test in simulated body fluid (SBF) and bacterial formation, respectively. The apatite-forming abilities of both coatings were evaluated after soaking in SBF up to 10 days. After soaking process, secondary apatite layer formed on the Ag-based MAO coatings was more homogenous and denser than one on the MAO surface, whereas secondary apatite structure was completely formed on both surfaces. Therefore, the bioactivity of the Ag-based MAO surfaces was significantly improved compared to the uncoated MAO coatings under SBF conditions. The bacterial adhesion of the Ag-based MAO coatings was considerably reduced compared to plain MAO surface [130].

In **2017 Sezgin Cengiz et al.** conducted the coating by using MAO in an electrolyte containing Na_2SiO_3, $Ca(CH_3COO)_2$ and $C_3H7Na_2O_6P$, for different durations of 2.5, 5, 15, and 30 mins. The effect of the process duration on the different model types and bioactivity of the coatings were

investigated by using X-ray Diffractometry (XRD), Scanning Electron Microscopy-Energy Dispersive X-ray spectroscopy measurements (SEM-EDS) and Optical Surface Profilometry (OSP). It was found that the increasing MAO duration resulted in thicker and rougher coatings. The XRD data revealed that all the samples prepared at different process durations contained the ZrO_2 (zirconia). During the MAO process, non-crystalline hydroxyapatite (HA) formed. The surface morphology, the amount and distribution of the features of the coating surface were modified by increasing the voltage. The simulated body fluid (SBF) tests showed the more bioactive surface with more HA crystals formed owing to chemical composition and high surface roughness of the coating. The pore, crack and discharge structures played a key role in apatite nucleation and growth, and provided ingrowth of apatite into discharge channels on the coating surface [131].

In **2018 R G Farrakhov, et al**. have improved the corrosion properties for Zr-1Nb alloy via plasma electrolytic oxidation (PEO). The coatings obtained in DC, were assessed using SEM, and XRD techniques. It was shown mode provides the PEO coatings having promising combination of the coating thickness, surface roughness, porosity, corrosion potential and current density, all contributing to corrosion protection of the zirconium alloy for advanced fuel cladding applications [132].

In 2018 Alexander Sobolev et.al., found that the MAO is an electrochemical surface treatment process to produce oxide protective coatings on some metals. MAO is usually conducted in an aqueous electrolyte, which requires an intensive bath cooling and leads to the formation of a coating containing impurities that originate in the electrolyte. They were applied an alternative ceramic coating to the Ti-6Al-4V alloy using the MAO process in molten nitrate salt. The obtained

coating morphology, chemical and phase composition, and corrosion resistance were investigated and described. The obtained results showed that a coating of 2.5 μm was formed after 10 min of treatment, containing titanium oxide and titanium-aluminum intermetallic phases. Morphological examination indicated that the coating is free of cracks and contains round, homogeneously distributed pores. Corrosion resistance testing indicated that the protective oxide coating on Ti alloy is 20 times more resistive than the untreated alloy [133].

In **2020 Na Li, et al**., investigated the effects of silicate concentration at the range of (16 g/L to 56 g/L) on the plasma electrolytic oxidation of Zircaloy-2 in potassium hydroxide/sodium silicate electrolytes in detail, including the growth behavior, wear and corrosion resistance of as-obtained ZrO_2/SiO_2 alloyed coatings. It was found that the coating thickness increased continuously on increasing the silicate concentration in electrolyte compositions (1 g/L KOH + c g/L) $Na2SiO_3 \cdot 9H_2O$ (c = 16, 32, 48 or 56). Besides, the amount of t-ZrO_2 in the coatings increased with increase of silicate concentration in electrolyte, while the amount of m-ZrO_2 decreased. Comparative studies have shown that the coatings formed in electrolyte with high silicate concentration possessed superior wear and corrosion performance, which could be ascribed to heavy silica deposition associated with the presence of t-ZrO_2 stabilized by SiO_2. These results may provide guidance for obtaining high performance of ZrO_2/SiO_2 alloyed coatings. Besides, it's believed that the presence of Si species in zirconia endows the coatings with enhanced bioactivity like bioactive glasses and ceramics coatings and envision that the as-prepared ZrO_2/SiO_2 alloyed coatings have great potential for biological applications. [134].

In 2020 Yajie Chu et.al., enhanced the surface wettability for biological application by carrying out the micro-arc oxidation (MAO) treatment with various voltages on Ti alloys in 10% H_2SO_4 aqueous solution. The effects of applied voltage on the surface morphology, phase constituents, functional group, roughness and wettability of the MAO coatings were investigated comprehensively. The results showed that the increasing of the applied voltages significantly change phase constituents, surface morphology and wettability of the MAO coatings. Furthermore higher applied voltages are favorable to form higher fraction of rutile phase, with larger micro-pores and higher surface roughness [135].

In **2020 J. Martin, et al**. investigated the producing particles by carrying out PEO treatments on two different grade of aluminum alloy (Al1050,Al2024) and a low-alloyed zirconium grade (Zr-M5). The samples were PEO-processed in 4 L beaker containing a low concentrated solution of potassium hydroxide ([KOH] = 1 g/L ≅ 0.018 mol/L) diluted in deionised water. Results showed that particles exhibit a hollow spherical shape with outer diameter ranging from 100 nm to 10 μm. They consist of polycrystalline alumina for the PEO of aluminum alloys and zirconia (m-ZrO_2) for the zirconium alloy. A correlation has been presented between the microstructure of the produced particles and the "pancake"-like structure that usually develops over PEO coatings [136].

In **2021 Salim Levent Aktug, et al**., used the MAO that operated with AC (alternating current) power supply. Zr substrates were served as an anode (working electrode) as stainless steel container was served as a cathode through the MAO process. The MAO electrolyte consisted of 0.25 M calcium acetate and 0.06 M β-calcium glycerol phosphate. The electrolyte was prepared by dissolving of all chemicals into de-ionized water. The MAO coating productions was carried out at 0.292 A/cm^2 for 10 min. The electrolyte temperature could not exceed 40°C during MAO

process by a water-cooling circulator system. After the MAO treatment, they were dried with hot air. Result The cubic-ZrO_2, meta-stable Ca0.15Zr0.85O1.85, and $Ca_3(PO_4)_2$ were detected on the MAO surface by powder-XRD. The existence of chitosan on the MAO-coated, the MAO surface is porous and rough, surfaces indicated hydrophobic properties. In vitro bioactivity was significantly enhanced on the chitosan-based MAO [137].

2.14 Summary of literatures

From the review of literatures, it is clear that many researchers have studied about anodizing and MAO. Were studied the effect of their method on the mechanical properties, corrosion behavior and improve alloys for bio application. Table (2.9) Summary of these researchers.

Table (2.9) Summary the review of literatures.

Ref.	Year	Method and condition's	Result
[124]	2014	Anodizing process, PH = 2.5 and volt.(5-60)V at room temp. with variable glycerol concentration.	When glycerol addition, it takes more time to produce long zirconia nanotubes.
[125]	2018	Anodizing for zirconium alloy, A direct-current power supply with a maximum capacity of 1 Aand 1,000 V was used at a temp. 15 ℃.	improvement in the oxidation resistance compared to bare zirconium alloy without the nanoporous oxide layer.
[126]	2020	PEO on a ZrNb alloy in Ca–P solution with CuNPs.	Formed a stable ceramic layer incorporated with Cu nanoparticles. Showed medium grade antibacterial activities. PEO at 450 Vprovided better antibacterial properties.

[127]	2020	Anodized at 20 V	the nano-porous Zr has similar hardness parameter as the uncoated Zr, the lower surface adhesion force that could be translated into improved properties in terms of antimicrobial effects.
[128]	2021	anodizing and subsequent re-anodizing of pure Zr (99.99%) at voltages (50 – 500) V	Improve the applications relating to surface finishing, electronics, optics, and biomedicine.
[129]	2016	deposited (HA)/ TiO_2 composite coating on a titanium (MAO).	Bioactive coating on a titanium surface.
[130]	2017	pure zirconium(Zr) by (MAO)	. Zirconia, calcium zirconate and hydroxyapatite were detected on the surface after MAO. Improve the properties such as bioactivity and anti-bacterial tests of both coatings in (SBF) and bacterial formation
[131]	2017	coating by using MAO at different time (2.5, 5, 15, and 30)mins	More bioactive surface with more HA crystals formed owing to chemical composition and high surface roughness of the coating.
[132]	2018	Zr-1Nb alloy via (PEO)	Improve corrosion protection of the zirconium alloy for

			advanced fuel cladding applications
[133]	2018	Coating the Ti-6Al-4V alloy by MAO	Corrosion resistance testing indicated that the protective oxide coating on Ti alloy is 20 times more resistive than the untreated alloy
[134]	2020	Coating Zircaloy-2 by (PEO) at (16-56) g/L of silicate	Prepared ZrO_2/SiO_2 alloyed coatings have great potential for biological applications.
[135]	2020	(MAO) treatment with various voltages on Ti alloys	higher applied voltages are favorable to form higher fraction of rutile phase, with larger micro-pores and higher surface roughness
[136]	2020	PEO treatments of (Al1050,Al2024) and (Zr-M5)	Results showed that particles exhibit a hollow spherical shape. consist of polycrystalline alumina for the PEO of aluminium alloys and zirconia (m-ZrO_2) for the zirconium alloy
[137]	2021	MAO operated with AC to Zr substrates at 0.292 A/cm2 for 10 min and temp. could not exceed 40°C.	the MAO surface is porous and rough, surfaces indicated hydrophobic properties. In vitro bioactivity was significantly enhanced.

2.15 Concluding Remarks

The previous literature review that studied by researchers showed the effect of dispersant and the parameters of duplex like as applied potential, deposition time, suspension medium on the corrosion behavior and morphology of ZrO_2, and HA/ZrO_2 with coated on Zr705 substrate. The following remarks can be listed:

1. ZrO_2 coatings by anodizing, MAO, and duplex process suitable and high corrosion resistance than the uncoated sample.
2. Based on the type material, selecting of processes parameters depending on the optimum deposition voltage and time, which result in less porous and good strength coating layer.
3. The addition of enough amount of HA to Produced HA/ZrO_2 composite coatings result in bond strength accretion to Zr substrate and cause a reduction of corrosion rate in solution. Moreover, the morphology of the composite coatings was uniform and less porous structure.

What distinguishes the current work is that the using of Zr705 exclusively as the substrate for the HA/ZrO_2 composite deposition as utilized by the other researchers and investigations and thus it will give a high performance biomaterial used in bone fixation for orthopedic applications.

Chapter Three

Experimental work and Procedure

3.1 Introduction

This chapter deals with the main features of experimental procedures, which were required to achieve the aims of this investigation. This chapter presents the materials used in this work to produce a coating layer by means of the anodizing process, MAO process and duplex process, devices and tests used in this investigation. Thus including, preparation, chemical composition using X-Ray fluoresce (XRF), microstructure investigation using optical microscopy OM, Field Emission Scanning Electron Microscopy FESEM, energy dispersive X-ray spectrometer (EDX), and X-ray diffraction (XRD). In addition, it presents the mechanical tests such as micro – Vickers hardness (HV) and elastic modulus measurement. Finally, it presents in vitro tests conditions of electrochemical measurements and tribology test. Figure3.1 shows the summary of the overall experiments used in this investigation to give the reader an overview of everything that was used.

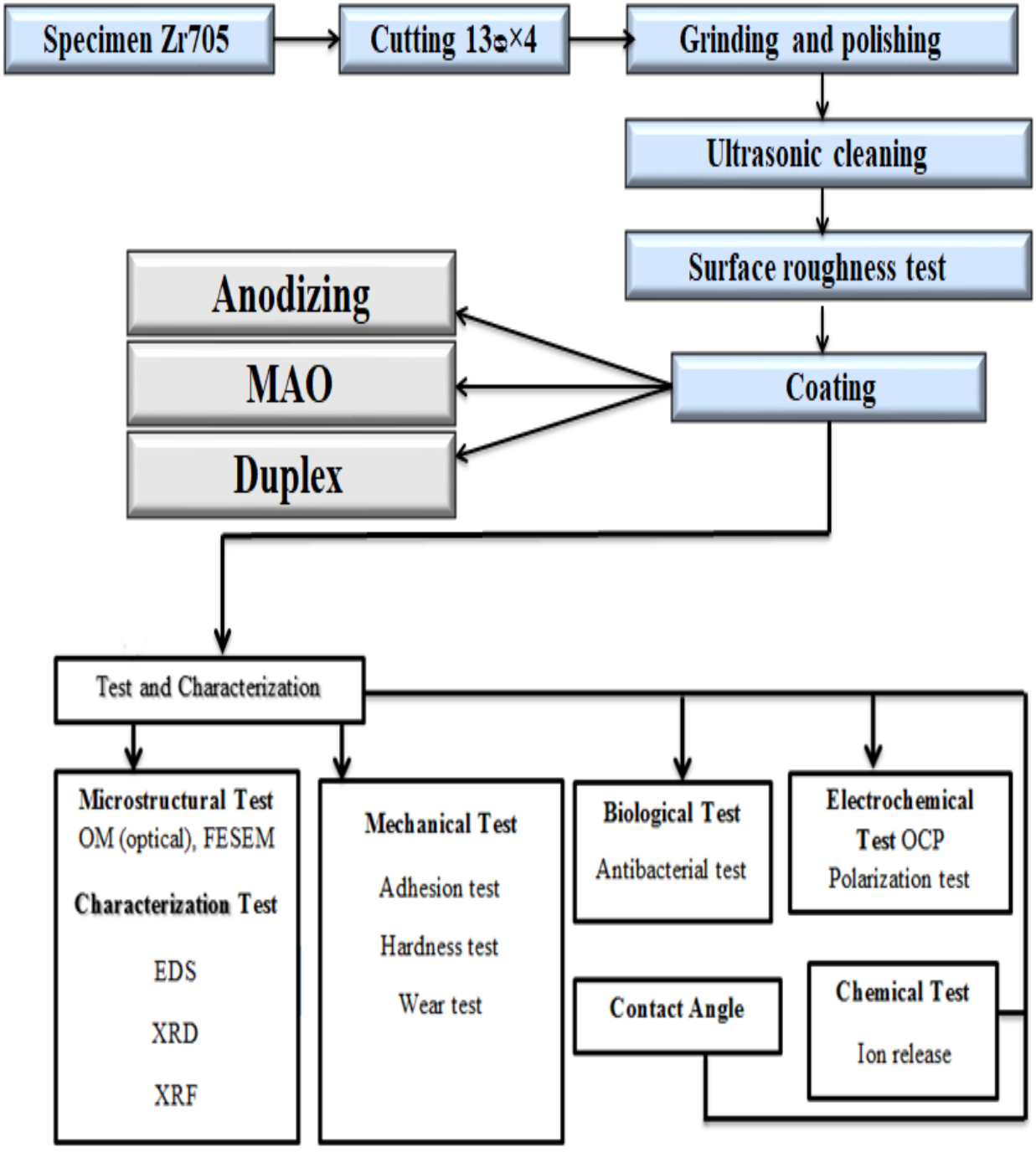
Specimen Zr705
Cutting 13ø×4
Grinding and polishing
Ultrasonic cleaning
Surface roughness test
Anodizing
MAO
Duplex
Coating
Test and Characterization
Microstructural Test
OM (optical), FESEM
Characterization Test
EDS
XRD
XRF
Mechanical Test
Adhesion test
Hardness test
Wear test
Biological Test
Antibacterial test
Contact Angle
Electrochemical Test OCP
Polarization test
Chemical Test
Ion release

Anodizing

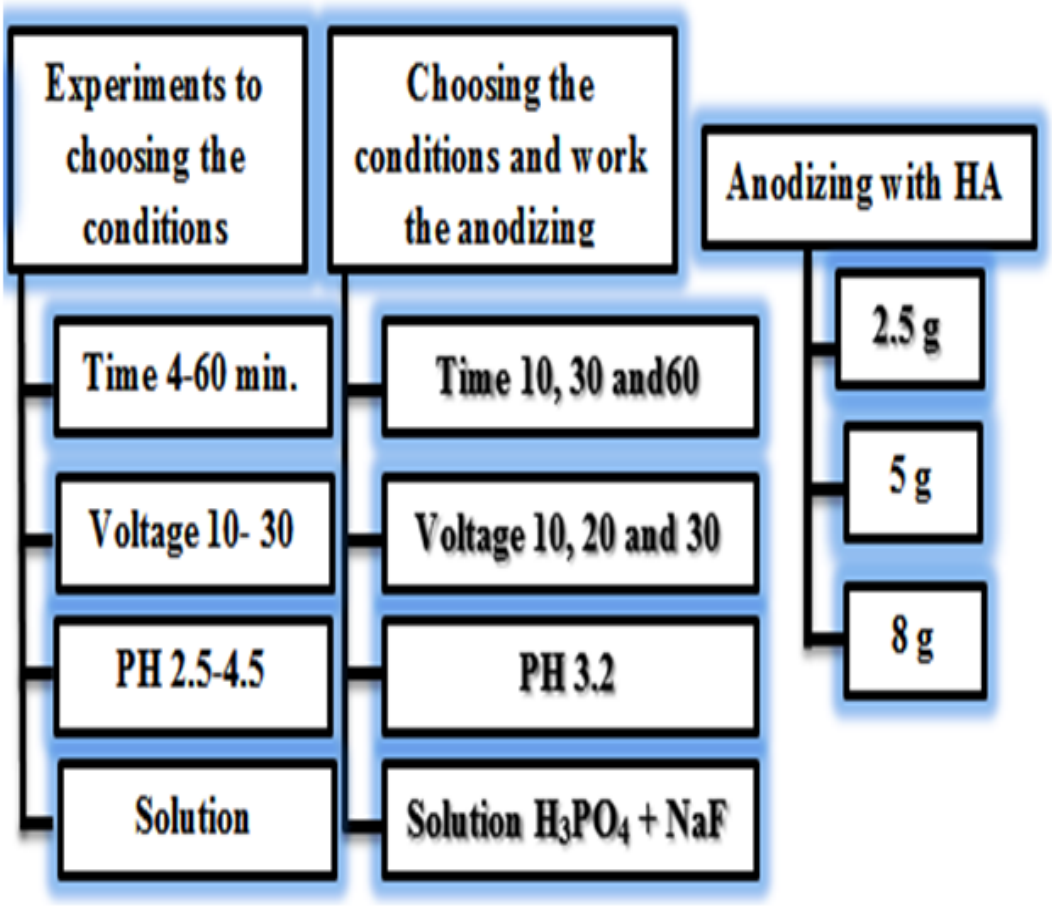
Experiments to choosing the conditions
Time 4-60 min.
Voltage 10- 30
PH 2.5-4.5
Solution
Choosing the conditions and work the anodizing
Time 10, 30 and60
Voltage 10, 20 and 30
PH 3.2
Solution H_3PO_4 + NaF
Anodizing with HA
2.5 g
5 g
8 g

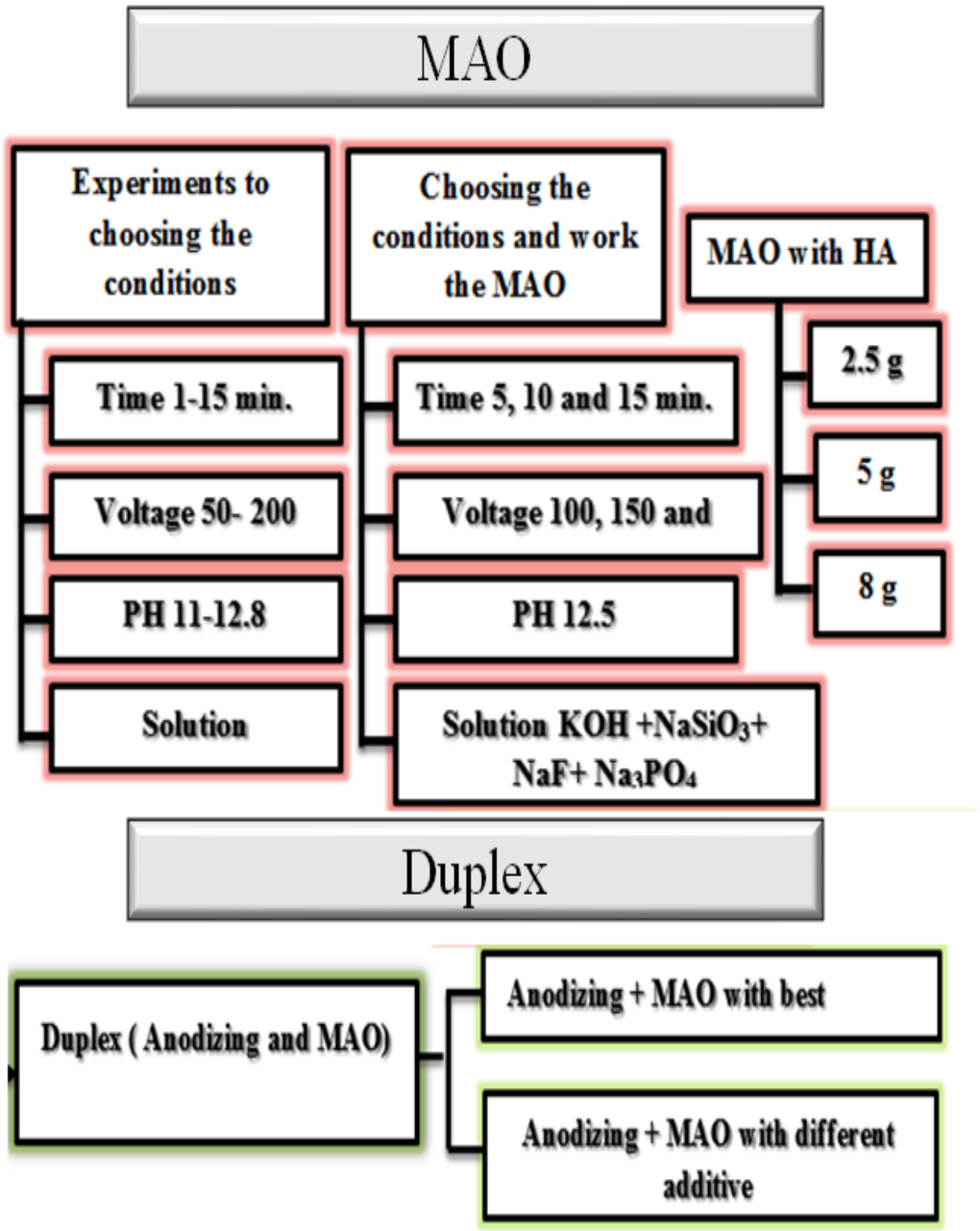

Figure (3-1): Flow chart of the experimental procedures

3.2 Equipment and Instruments

The following equipment and devices are used in this work:

1. Wire cut machine (Germany origin).
2. Grinding and polishing device (UNI POL-820, MTI Corporation, made in Toky).
3. Ultrasonic cleaner model (VGT-1860QTV) power 150Wmade in china.
4. Surface roughness tester (HSR210, made in china).
5. Light optical microscope, model (1280XEQ-MM300TUSB) (Metallurgical Department /materials engineering college/Babylon university).
6. XRD instrument type (XRD-6000) (Nanotechnology and Advanced Materials Research Center.
7. Field-Emission Scanning electron microscopy (FE-SEM) (ΣIGMA, JSM-7610F, Carl Zeiss, made in Germany (Tehran University).
8. Laser particle size analyzer, Better size 2000 (Ceramic Department / materials engineering college / Babylon university).
9. Digital, microprocessor CM- 8822, coating thickness meter)
10. pH meter (BP3001, made in Germany).
11. Sensitive Balance Type (L220S– D) with (± 0.0001% accuracy), made in Germany.
12. A Dc-Ac homemade MAO deposition unit.
13. Vickers Hardness (HV-1000) model Reicherter, Ut l250.
14. Digital Micro thickness test gauge model (CM- 8822) (Ceramic Department /materials engineering college/ Babylon university).
15. Corrosion potentiostats, model Digi-lvy,112609 (Metallurgical Department /materials engineering college/Babylon university).
16. Contact angle test, model SL 200KS (Ceramic Department /materials engineering college/ Babylon university).

17. Atomic force microscopy (AFM) Type was PHYWE/Nano Compact, made in UK (Department of Science/University of Baghdad).
18. Wear test Type (Pin-on-Disc), MT 4003, TRIBOMETER model (MT/60/H), made in U.S.A.
19. Adhesion Test model (ATM), (POSITEST AT, AT09377, made in U.S.A. (Metallurgical Department/materials engineering college/Babylon university).

3.3 Materials and chemicals

The material and chemicals that were employed to study the surface modification of Zr 705 for Bio applications are summarized in table (3-1).

Table (3-1)Material and chemicals in the study.

Material and chemical	Chemical formula	Purity %	source
Zirconium alloy	Zr 705	---	China
Potassium hydroxide	KOH	99	BDH/England
Sodium silicate	Na2SiO3	95	China
Sodium phosphate	Na3PO4	96	TAIZHOU ZHOUXING REFLECTIVE MATERIAL Co., LTD/ China
Sodium hydroxide	NaOH	99	HIMEDIA/India
Sodium fluoride	NaF	99	China
Phosphoric acid	H3Po4	99	India
Hydroxyapatite	$(Ca_{10}(PO_4)_6(OH)_2$	99	Epin Biotech Co, Ltd. China
Hank solution	Table 3-8	___	Iraq

3.3.1 Substrates and specimens preparation

Zr 705 was used for the substrates preparation in this study .Table (3-2) and (3-3) shows the chemical composition of Zr 705 (R60705) ASTM B550 used in the study and the code of uncoated specimen substrate was (US). The chemical analysis was performed using X-ray fluorescence (XRF) at the Ministry of Science and Technology, Materials Department / Baghdad - Iraq.

Table (3-2): Spectro chemical of analysis of Zr705 in wt%.

Elements	Zr	% C	%H	% O	% Hf	% N	% Nb	% Fe+Cr
Measured	95.6	0.05	0.003	0.17	4	0.025	0.054	0.2

Table (3-3): Standard Chemical composition of Zr705 in wt% according ASTM B550 [138].

Elements	Zr	% C	%H	% O	% Hf	% N	% Nb	% Fe+Cr
Standard	95.5	0.05	0.005	0.18	4.5	0.025	0.0 - 3.0	0.2

The specimens were cut into dimension of (13 diameter * 4 mm^2 thickness) by wire cutting machine at University of Technology/Baghdad as shown figure (3-2).

Figure (3-2): Wire cut machine

After that, the specimens were ground with emery paper (400, 600 and 1000) and washed well, cleaned by Ultrasonic cleaner (UTS) using acetone for 20 minutes, and kept in disc cater to be ready for coating.

3.3.2 Additive

Powder HA was used as coating additives. The average particle size of HA used in this study was (3.854μm). The HA powder was XRD tested at the Nano Center-University of Technology/Baghdad.

3.4 Preparation of Electrolytes

To choose the appropriate electrolytes for anodizing and MAO processes, many experiments were done as shown in tables (3-4) and (3-5).

3.4.1 Electrolyte for anodizing

Several acidc based electrolytes were tested to perform the anodizing process. The experiments were stabilized 1mL/L, and 0.8 g/L concentrations of H_3PO_4, and NaF in distilled water, respectively. The electrolytes were stirred using magnetic stirrer for (1-8) hour. Also, the pH of the electrolytes was measured by a pH meter show in figure (3-3).

3.4.2 Electrolyte for MAO

Several acidc based electrolytes were tested to perform the MAO process. The experiments were stabilized 14 g /L of Na_2SiO_3, KOH and Na_3PO_4 with 2 g/L NaF in distilled water. The electrolytes were stirred using magnetic stirrer for (1-8) hour. Also, the pH of the electrolytes were measured by a pH meter .

Where ,(electrolyte B) The best selection for anodizing process and (electrolyte D) for MAO process.

Table (3-4): Electrolytes used in the anodizing .

Specimens / **Compositions and conditions**	A	B	C
H_3PO_4	0.5g/L	1 g/L	1 g/L
NaF	---	0.8 g/L	---
Time (min)	4-60	4-60	4-60
PH	4.5	3.2	2.2
Temp.(C^o)	19-24	19-24	19-24

Table (3-5): Electrolytes used in the MAO.

Specimens / **Compositions and conditions**	A	B	C	D	E	F
KOH	1g/L	7.5g/L	15g/L	14g/L	1g/L	1g/L
Na_2SiO_3	1g/L	7.5g/L	15g/L	14g/L	---	---
Na_3PO_4	1g/L	7.5g/L	15g/L	14g/L	3g/L	---
NaOH	---	---	---	---	---	3g/L
EDTA	---	---	---	---	---	3g/L
NaF	---	1.5g/L	3g/L	2g/L	---	---
Time (min)	5-15	5-15	5-15	5-15	5-15	5-15
PH	11.85	12.27	12.8	12.6	11.8	12.2
Temp.(C^o)	20-30	20-30	20-40	20-30	20-30	20-30

3.5 Coating processes

3.5.1 Coating unit

A home – made coating unit shown in figures (3-3), and (3-4) was used for the deposition of ceramic coating by MAO and anodizing processes, and duplex processes. Coating equipment, cathode, anode, ventilation unit, stirrer, outer Plastic tank, cooling bath container, electrolyte container, cooling system and power supply unit. In this study designed the coating system with high current and voltage and specifications are high.

The power supply was AC-DC with variable voltage (0-500) v, and variables current density (0-8) mA/cm^2, home-made unit as shown in figure (3-5). It was designed and manufactured to meet the requirements of the coating processes in this study.

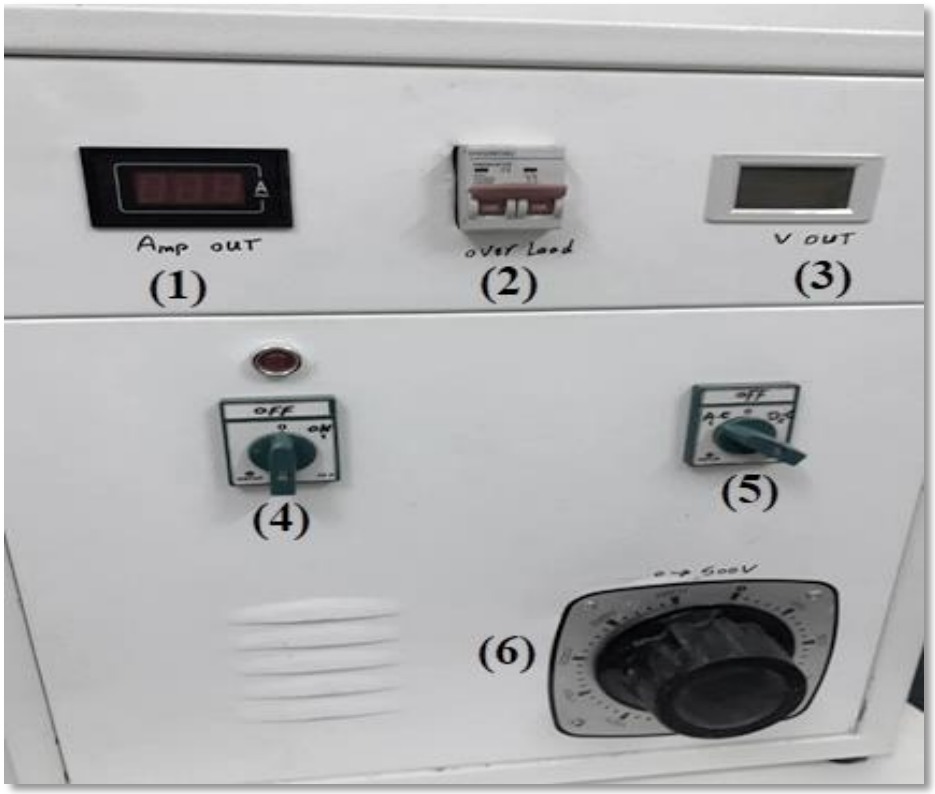

Figure (3-3): power supply ; (1).current gauge ;(2) over load; (3) voltage gauge;(4) on-off switch; (5) DC-AC current ;(6) voltage control. Zr 705 is the substrate used as (anode) and used stainless steel 316L as electrode (cathode). The electrodes were immersed vertically in a 1 liter container containing the solution. The electrodes were immersed in the electrolyte and the distance between the electrodes was 3 cm. Mixer was used to maintain the homogeneity of the electrolyte, cooling was used for the processes used ice containing salt and alum to keep it frozen for as long as possible. Thermo meter was used to constantly monitor the temperature.

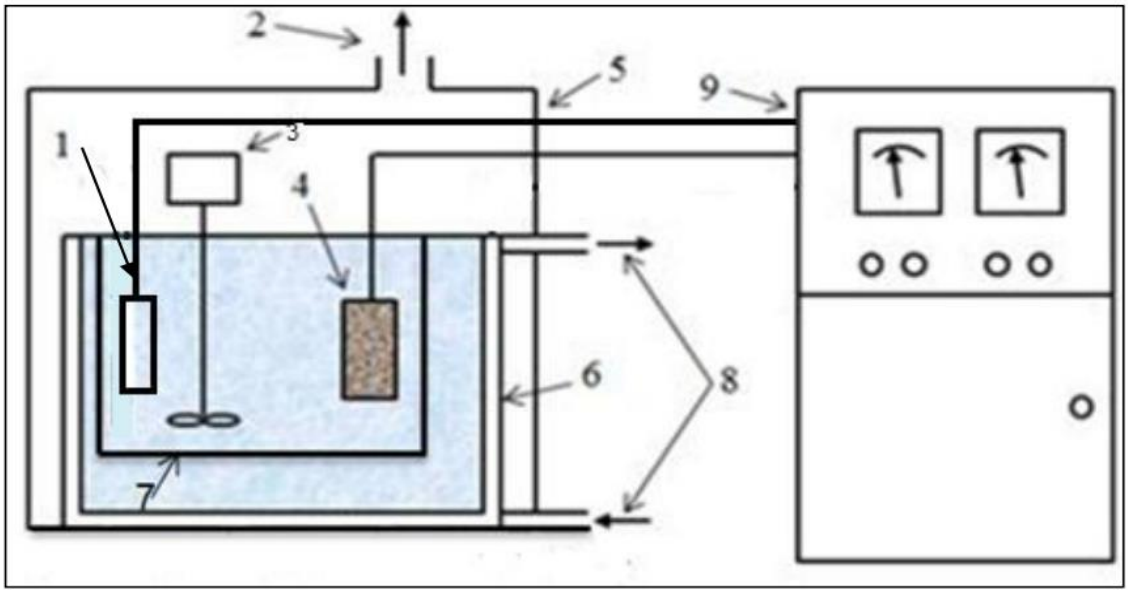

Figure (3-4): coating equipment: (1) cathode, (2) ventilation unit, (3) stirrer, (4) anode, (5) outer Plastic tank, (6) cooling bath container, (7) electrolyte container, (8) cooling system (9) power supply unit [139].

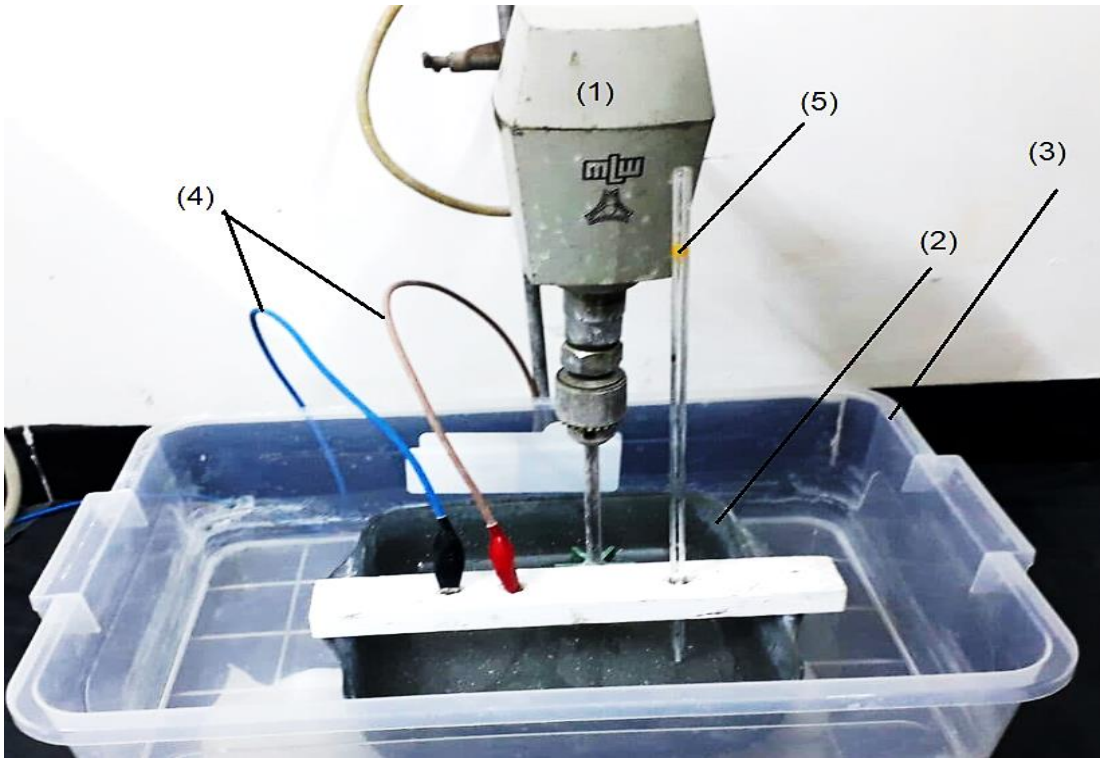

Figure (3-5) : Photographs of coating unit; (1) mixer; (2) coating container; (3) cooling container; (4) electrodes; (5) thermometer.

3.5.2 Anodizing process

Anodizing process was carried on Zr705 substrates at different DC voltages, deposition time, and HA additives as shown in table (3-6). The electrolyte was cooled to keep constant temp. (19-24c°).

In the anodizing process, it was observed that no spark occurred when coating, and mixer of the electrolyte was used during the process, which works to homogenize the electrolyte and makes the electrolyte more effective, especially when adding HA, where the additives are weighed with an accuracy of 0.0001g .

Table (3-6): Specimens of the anodizing process in B electrolyte at PH (3.2)

Specimen code	DC Voltage(v)	Time(min)	(HA)g/L
AN1	10	10	-
AN2	20	10	-
AN3	30	10	-
AN4	10	30	-
AN5	20	30	-
AN6	30	30	-
AN7	10	60	-
AN8	20	60	-
AN9	30	60	-
AN10	30	30	2.5
AN11	30	30	5
AN12	30	30	8

3.5.3 MAO process

MAO process was carried on Zr705 substrates at different AC voltages, deposition time, and HA additives as shown in table (3-6). The electrolyte was cooled to keep constant temp. (20-30^{o}c).In the MAO process, it was observed that spark occurred when coating shown in figure (3-6).

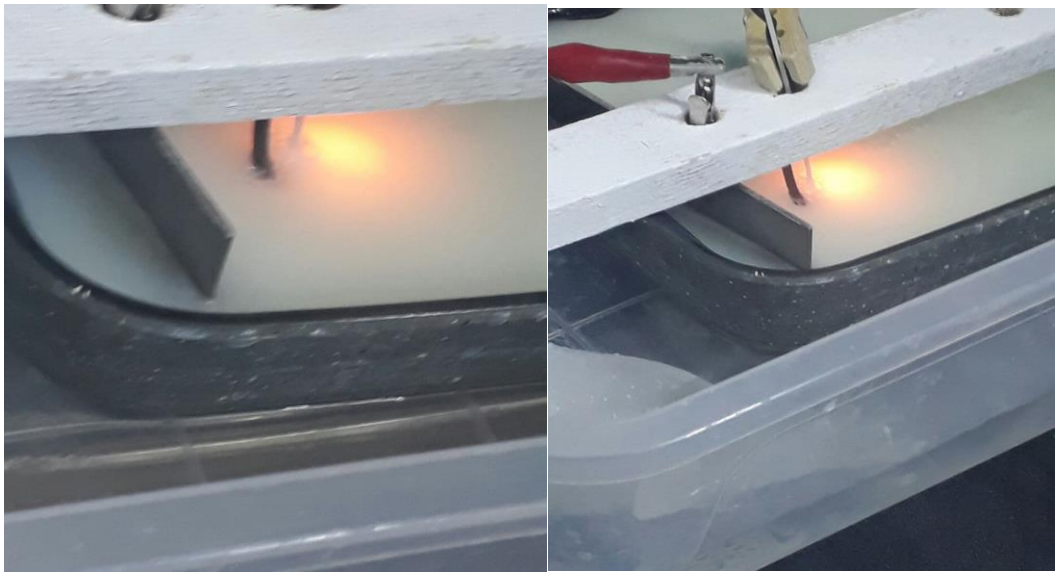

Figure (3-6): The spark in MAO process

Table (3-7): Specimens of the MAO process in D electrolyte at PH(12.6).

Specimens	Voltage(v)	Time(min)	Additive(HA)g
MAO1	100	5	-
MAO 2	150	5	-
MAO 3	200	5	-
MAO 4	100	10	-
MAO 5	150	10	-
MAO 6	200	10	-
MAO 7	100	15	-
MAO 8	150	15	-
MAO 9	200	15	-
MAO 10	200	10	2.5
MAO 11	200	10	5
MAO 12	200	10	8

3.5.4 Duplex processes of anodizing and MAO

In this step, duplex processes of anodizing and MAO were combined to modify the ZrO_2 /HA composite coating as mentioned in the objectives

of the study in chapter 1.Table (3-8) shows the basic rules and conditions that were taken into consideration in selection of duplex processes. Furthermore, best word is devoted to those specimens can exhibited the best results of hardness, wear resistance, corrosion resistance, antibacterial resistance and ion release. Figure (3.7) shows different types of coated Specimens in duplex process.

Table (3-8): Specimens of duplex processes DP

Specimen Code	Description of duplex processes	
	Anodizing	**MAO**
DP1	Best of AN specimens coated using HA additives (AN12)	Best of MAO specimens coated using HA additives (MAO12)
DP2	Best of AN specimens coated without HA additives (AN6)	Best of MAO specimens coated without HA additives (MAO6)
DP3	Best of AN specimens coated without HA additives (AN6)	Best of MAO10 specimens (2.5 g/L)HA (MAO10)
DP4	Best of AN specimens coated without HA additives (AN6)	Best of MAO10 specimens (5 g/L)HA (MAO11)

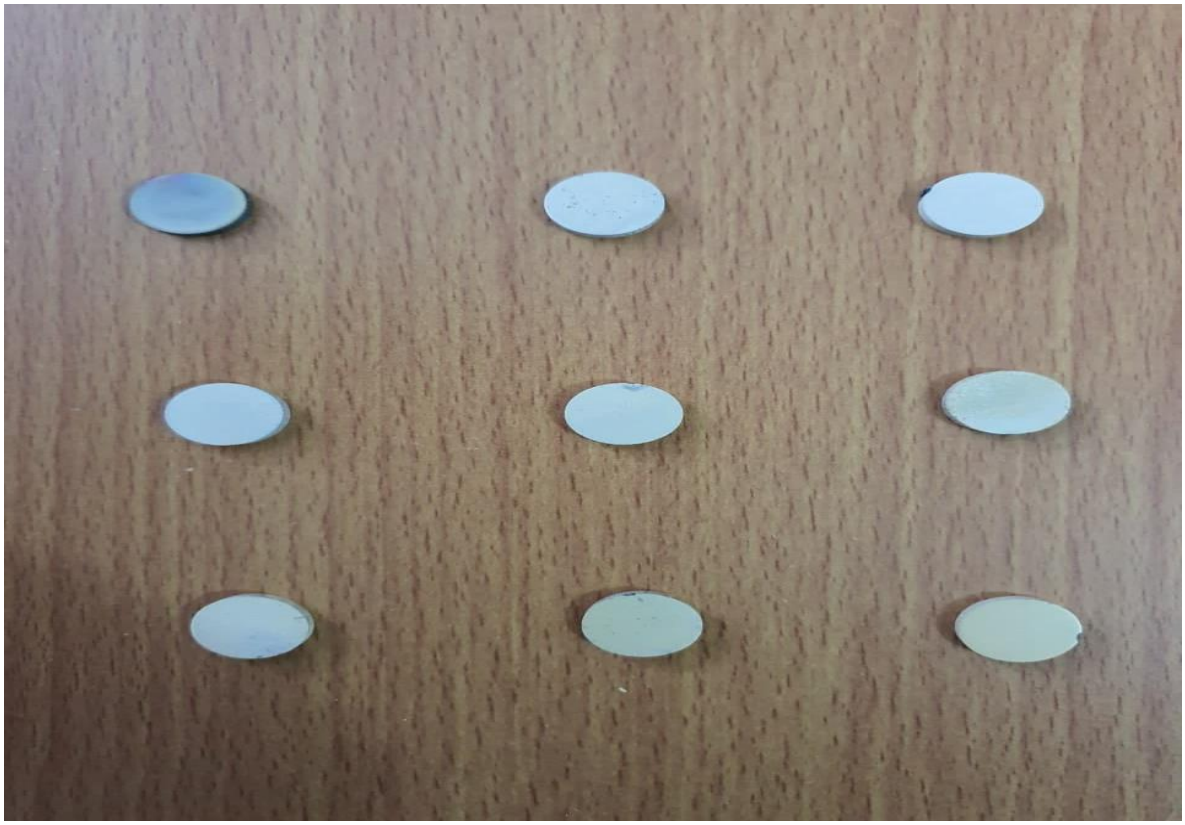

Figure (3-7): specimens coated of duplex process.

3. 6 Tests and Characterization

3.6.1 Light Optical Microscope (LOM)

After the coating process is completed, visual observation is a very serious and important step for evaluating the layer resulting from the coating process. The initial evaluation was also considered and checked by (LOM). All specimens that did not result in satisfactory coatings were discarded and work continued on those specimens. The surfaces of the etched specimens were observed using an optical microscope as well as the cross-section of the coated specimens, and the magnification powers were 100 X , 400 X, 600 X and 800 X. The etching solution to clarify the microstructure of the substrate surface was (100) ml of distilled water and (5 to 10) ml of fluoric acid for (1 to 5) seconds [145].

3.6.2 Field Emission Scanning Electron Microscopy (FESEM)

Field emission scanning electron microscopy (FESEM) provides topographical and elemental information at magnifications of (10x - 300,000x) with virtually unlimited depth of field. Compared with convention scanning electron microscopy (SEM), field emission SEM (FESEM) produces clearer, less electrostatically distorted images with spatial resolution down to 11/2 nanometers which is three to six times better. Energy dispersive spectroscopy (EDS) connected to the FESEM machine was also used. The FESEM test was done at University of Tehran (Amirabad) Iran.

3.6.3 X-Ray Diffraction

To discover the structure and phase distinguishing of all specimens, XRD test was conducted at Nanotechnology Laboratory- University of Technology by utilizing, Shimadzu diffract meter of X-ray (kind XRD-6000).

3.6.4 Liner polarization test

Due to the importance of Zr and its alloys and their uses as implants within the human body, corrosion tests should be performed on specimens to determine the corrosion behavior of specimens in the human body. The electrochemical evaluation of the corrosion behavior of Zr 705 was carried out before and after coating, and this test was carried out in the corrosion laboratory of the laboratories of the Metallurgical Engineering Department - University of Babylon. In this test Hank's solutions shown in Table (3-9) were used. The pH of Hank's solution at 37 ± 1 °C was (7.4).

Table (3-9): Chemical Composition of Hank's Solutions [140]

No.	Constituents	(g/L)
1	KCl	0.4
2	$CaCl_2$	0.14
3	$NaHCO_3$	0.35
4	NaCl	8
5	$MgCl_2.6H_2O$	0.1
6	Glucose	1
7	$Na_2HPO_4.2H_2O$	0.06
8	KH_2PO_4	0.06
9	$MgSO_4.7H_2O$	0.06

The test was carried out as shown: OCP (Open Circuit potential) calculation, the experimental arrangement of the open circuit potential measurement.A500ml glass electrolysis cell is used. Tests are performed with specimens immersed in Hank's solution. With a standard calomel electrode (SCE). Open circuit potential measurements were performed for each specimen from (0 to 160min).

Liner polarization electrochemical tests were carried out in three-electrodes cell and containing electrolytes similar to nature Hank's solution. The counter electrode was Auxiliary electrode and the reference electrode was SCE and working electrode specimen according to the American Society for Testing and Materials (ASTM). The polarization curves were plotted and both corrosion current density

($I_{corr.}$)and corrosion potential ($E_{corr.}$) were estimated by Tafel extrapolation by using anodic and cathodic branches

The test started using the output potentail of (OCP) after addition and subtraction to get the start and end point. The following equation was used calculate the wear rate [141]:

$$\textbf{\textit{Corrosion rate(mpy)}} = \frac{\mathbf{0.13}\ \boldsymbol{Icorr(Ew)}}{\boldsymbol{A.\rho}} \qquad \text{..... (3. 1)}$$

Where:

0.13 = metric and time conversion factor.

$I_{corr.}$= corrosion current density (μA/cm²).

E.W= equivalent weight (9.2g/eq.).

A= area ($1.32cm^2$)

ρ= density (g/cm³) measured by equation (3.2)…… [142]

$$\rho = \frac{m}{v} \quad \text{.....(3.2)}$$

mpy = Corrosion rate (mils per year).

The improvement percentage was calculated for specimens with coating,

using the following equation [143]:

improvement percentage =(CR0 _ CR / CR0)^x 100 ……(3.3)

Where:

CR° =the corrosion rate of master specimen (without coated).

CR =the corrosion rate of coated specimen (with coated).

3.6.5 Sliding Wear test

Pin on disc wear test was applied to coated and uncoated substrates in order to evaluate the wear resistance. This test was performed using alumina pin (hardness according to ASTM F603 (1500HV), the wear test machine was (Micro test-28021) at Metallurgical Department/College of Materials engineering/Babylon University as shown in figure (3-8). Also, table (3-10) shows the test parameters. Before starting the test, the specimen was weighed using a sensitive balance (0.0001). After the time (5, 10, 15, 20, 25 and 30 min), the specimen test was weighted and the wear rates were determined according to equation (3.4).

$$\textbf{\textit{Wear rate}} = \frac{\Delta W}{\pi D N t} \textbf{\textit{(g /cm) -----Eq.(3.4)}}$$

Where:

ΔW (g)= Weight loss after(5,10,15, 20,25 and 30)min.

D=Diameter of the sliding circle (4mm)

N=speed of rotation disk(rpm)

t= wear test time (30)min

Table (3-10): Test parameters of pin on disc wear test.

Applied load	**5 N,10N,15N**
Duration of Test	30 min
Sliding speed	350 rpm
Sliding distance	264mm
Pin Diameter	6 mm
Pin Material	alumina ball

Figure (3-8): Pin–on–disk Wear test Instrument.

3.6.6 Hardness Test

All specimens hardness values were obtained using the digital hardness analyzer (HBRVS-187.5) Micro hardness Vickers's tester at load of (100 g) as for (10 sec). The average of five measurements was adopted to evaluate the hardness of each specimen.

3.6.7 The Wettability

For OH contained films, the OH content and morphology of these films are different after treated at various voltages and times .Investigated the effect of oxygen concentration in films on the formed phases, crystallinity and wettability [156]. Their results showed the wettability is mainly determined by surface roughness. As such, the sharp variation of contact angle at various parameters may result from multiple influencing factor including roughness, morphology and OH content. Therefore, two models reported in the literature are used to explain the sharp variation in apparent contact angle obtained in the present work. For the MAO coatings with smaller pores, roughness and lower content of OH prepared

at higher contact angle, solutions cannot wet the smaller pores of the MAO coating surface, which forms a solutions MAO coating interface presented in figure (4-9a).

In other words, such a morphology and solutions surface tension lead to the capture of ambient gas in the interface between the MAO coating surface and solution used for the contact angle test. For the MAO coatings prepared at larger pores, roughness and higher content of OH, which promote the absorption of solutions on the MAO surface.

These effects of surface morphology and OH content on contact angle can be evaluated by Wenzel's model [150], as presented in figure (4-9 b). In this model, solutions drop sticks to the MAO coating surface, when the area value of interface of the liquid/solid increases, the apparent contact angle decreases [157].

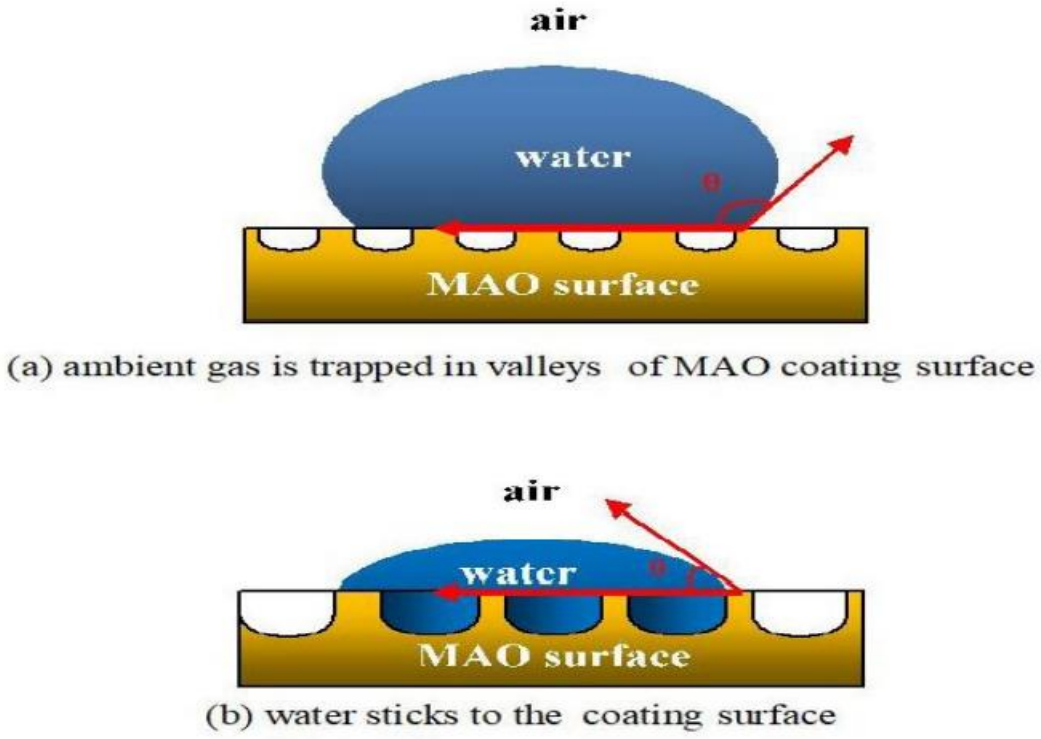

Figure (4-9): Two interface models used to describe the contact angle of the MAO coatings prepared at various voltages (a) ambient gas is trapped

in valleys of MAO coating surface. (b) Solutions stick to the coating surface.

The wettability between the substrate and coating was measured using contact angle device type KRUSS DSA30, Hamburg2009. The contact angle was used to scale by the Hanks solution drop contact angle measurements on substrates. Drop Contact Angle (DCA) measurements were produced by utilizing an automated machine as shown in figure (3-10). By utilizing the CCD camera, the drop was imaged, and the figure of the drop was calculated via image analysis software to determine the contact point of view. Models with a high porosity degree were kept out from these measurements as high soaking up rates engage with the measurement. Utilizing a computer programmed from a measurement of the width and height of the droplet at 1.0, 5.0 and 10.0 seconds, therefore the contact angle was calculated. Figure (3-11) shows the contact angle measurement device.

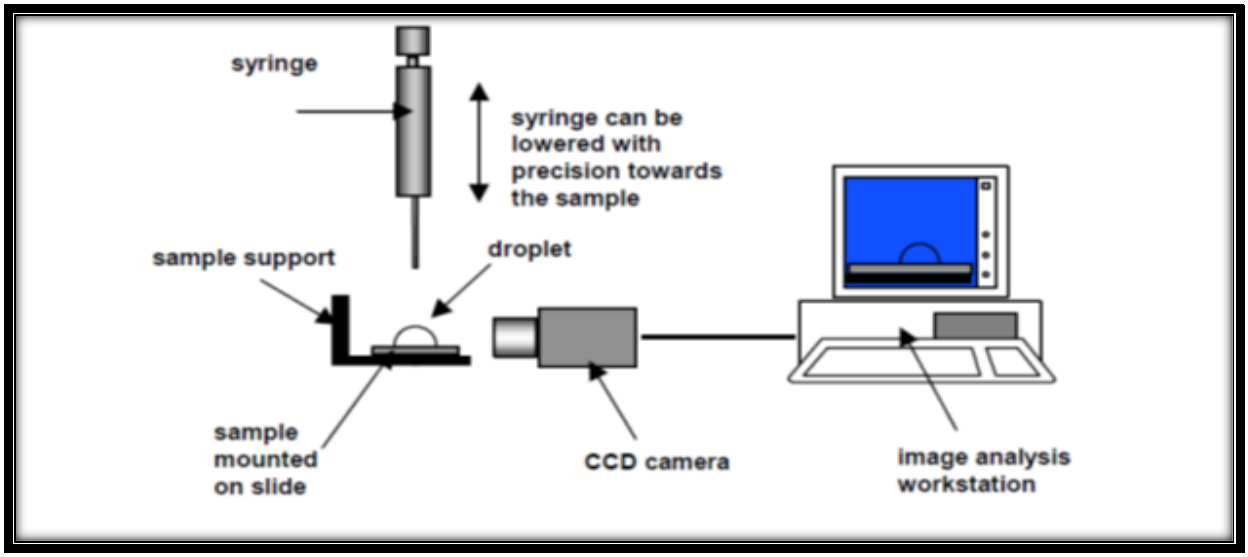

Figure (3-10): Contact angle by automated drop analysis methods**.**

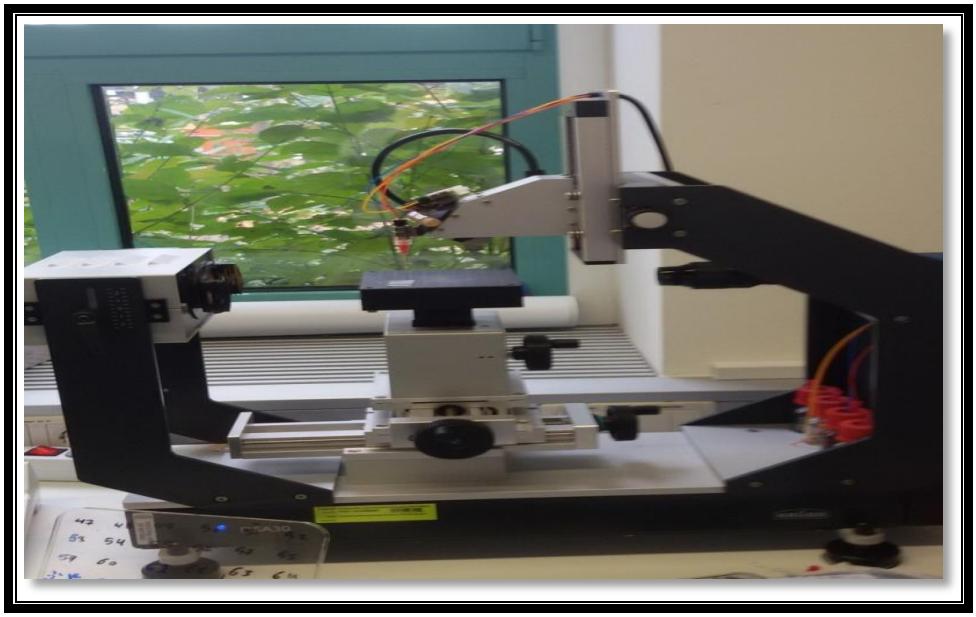

Figure (3-11): Contact angle measurement device.

3.6.8 Adhesion-Test

ASTM D 3359-B Tope adhesion test as shown in figure (3-12), using an Elcometer 107 cross-slot cutter (Manchester, UK) Quality, was employed to evaluate the adhesion strength between coatings and Zr substrates. It was done using a tool located on the substrate at a 90 degree angle to create a series of parallel cuts by applying pressure and pulling the tool in the direction of the actuator. After making the cuts, clean the film with a soft brush to remove the separated chips or paint tape, and a suitable adhesive material has been selected and carefully placed over the grid. The difficulty with this test is that the maximum strength that can be measured is the maximum strength of adhesive that can be obtained. High-performance adhesives typically have a tensile strength of less than 100 MPa. Achieving this level of stress in a practical test requires careful techniques to promote adhesion to the coating and for maintaining the force direction perpendicular to the specimen. Even slight angular deviations from the perpendicular can result in a premature ‘peeling-mode’ failure.

Figure (3-12): Adhesion test device

3.6.9 Thickness test

The thickness of coatings was measured by Digital Micro thickness test gauge model (CM- 8822) at Ceramic Department /materials engineering college/ Babylon university and in LOM. The center point of measurement was considered as a thickness value of the coating**.**

3.6.10 Surface Roughness Investigation

In order to identify the topographic change after surface treatments as well as the amount of roughness that has been produced before and after deposition process surface roughness investigation was done. The test was carried out using Atomic Force Microscope (AFM) at the Department of Science - University of Baghdad (PHYWE /Nano Compact AFM, UK) .

3.6.11 Ions release

This test was achieved by using atomic absorption spectroscopy device. To determine the amount of Zr ions leached from the coated and uncoated specimens into Hank's solution .The solubility test was used to measure the ions present in Hank's solution. Specimens were immersed for 3 weeks at 37°C, and pH 7. Specimen of each type, HA/ZrO_2 composite coated and uncoated specimens were immersed in 50 ml Hank's solution in Propylene (PP). The (PP) bottles were tightly closed and incubated in heat chambers at 37 °C for 3 weeks. All bottles were gently shaken for a few seconds every 2 days.

3.6.12 Antibacterial -Test

In this test, specimens were immersed in 5 ml of phosphate-buffered saline (PBS) shown in table 3-11 for 24 hours, after which specimens were taken from PBS to a conductive agar disc with E-Coil and S.aureus. Each series were formulated with different concentrations and the antibacterial activity of the specimens was considered [144].

The method of work**:**

1. Selected bacteria, were activated by adding 100 µL of cultured bacteria, incubation period of 5 minutes then 24 hours at 37
2. 100µL of activated bacteria were included or transported to alarm nutrients to all areas.
3. A few numbers of wells were prepared using the correk borer for an equal number of specimens.
4. The specimens were loaded to the wells then 24 hours incubation at 37C was applied.
5. After the incubation, the inhibition zones were measured using normal ruler.

Table (3-11): shows the composition of PBS solution[144].

Order	*Reagent*	*Amount(g) for 1L SBF*
1	NaCl	8.0754
2	$NaHCO_3$	0.3557
3	KCl	0.2250
4	$K_2HPO_4.3H_2O$	0.2310
5	$MgCl_2.6H_2O$	0.3180
6	1M HCl	39
7	$CaCl_2.2H_2O$	0.03725
8	Na_2SO_4	0.0720
9	Tris	6.1860
10	1M HCl	0-5ml

Chapter Four

Results & Discussion

4.1 Introduction

In this chapter, the results obtained in each parts of this investigation will be presented and followed by discussion of results. The results of alloys characterization including, particle size, optical microscopy, Filed Emission scanning electron microscopy, and X-ray diffraction, mechanical testing (wear and micro– hardness) results will be discussed. The results of electrochemical behaviour of Zr705 used in this investigation including open circuit potential, liner potential test and ion release will be discussed. The results of tribological behaviour of Zr705 used in this investigation including dry sliding wear, track characteristics (roughness), and total removed wear weight loss will be discussed.

4.2 Particles Size Analysis (PSA) results

The particles size of HA powder were analyzed. The results are shown in Figure (4-1). It is clear that the HA powder had an average particle size of about (3.854μm). The red curve shows the normal distribution for particles size and the blue curve shows accumulated distribution for particles size.

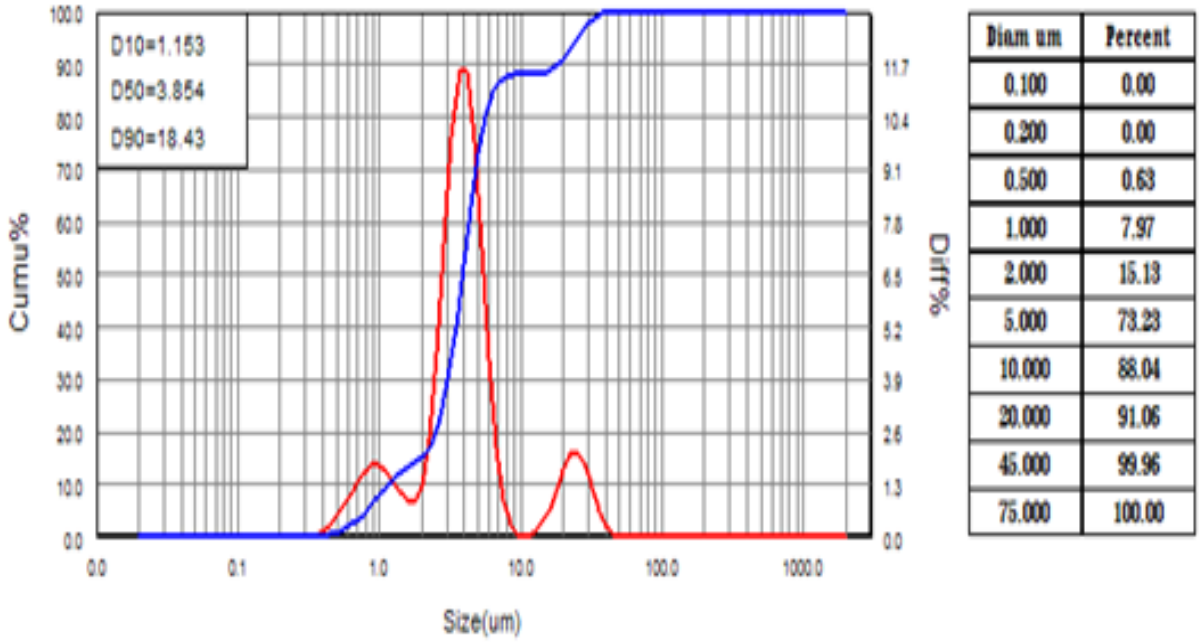

Diam um	Percent
0.100	0.00
0.200	0.00
0.500	0.63
1.000	7.97
2.000	15.13
5.000	73.23
10.000	88.04
20.000	91.06
45.000	99.96
75.000	100.00

Figure (4-1): PSA of HA Powder .

4.3 XRD Test results

X-ray diffraction tests were performed for Zr705 specimen before and after the coating process and for the additive of (HA). The diffraction patterns obtained for the specimens were the phases that developed as a result of coating.

4.3.1 XRD Pattern for HA Powder

Figure (4-2) represents the XRD patterns of HA Calcium phosphate Hydroxide. It is obvious that the HA powder is compos of HA peaks after comparison with standard card (JCPDS card No.09-0432).

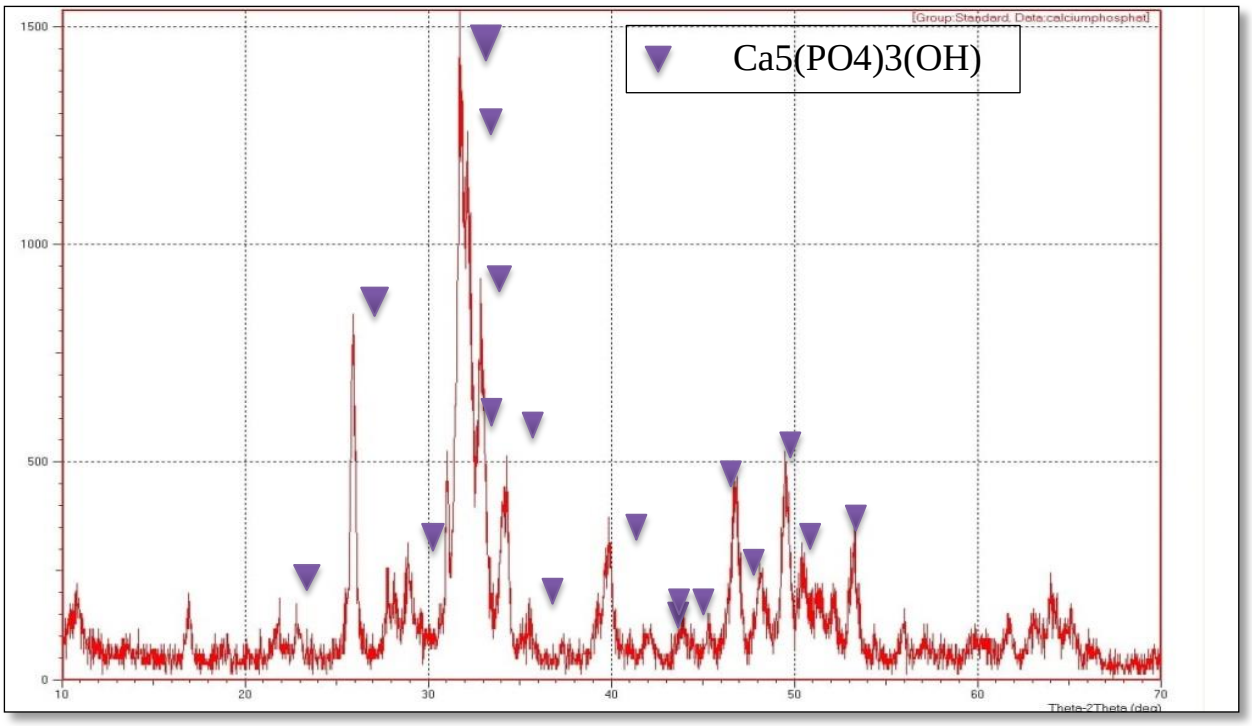

Figure (4-2): XRD Patterns of HA Powder.

4.3.2 XRD Patterns for the specimens

Figure (4-3) shows the XRD patterns of US. The observed positions of the diffraction lines (2Θ and corresponding d) for the patterns are in full agreement with corresponding values reported for Zr in the standard card (JCPDS cards No.05-0665 , 26-1399 and 34-0657).

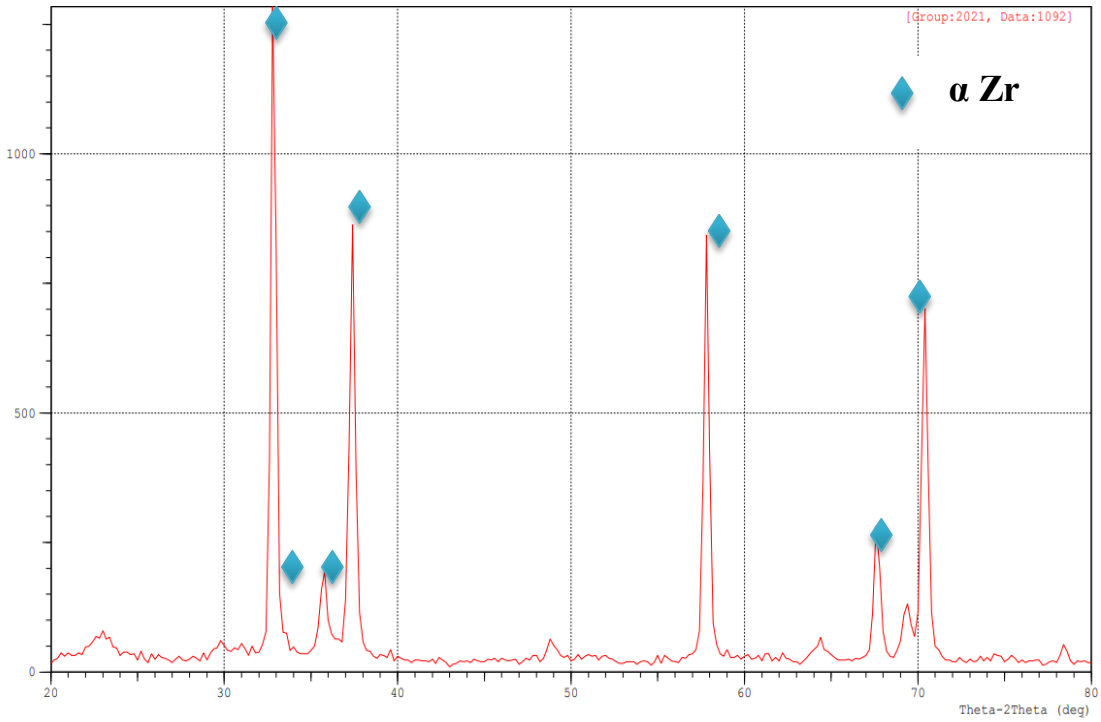

Figure (4-3): XRD Patterns of US.

Figures (4-4) to (4-6) show the XRD results of some coated specimens with different conditions. The XRD results proved the deposition of ZrO_2 on the surface of the substrates in accordance with the standard card (JCPDS cards No.05-0665, 26-1399 and 34-0657). This is agreed with the aim of this study in modification of Zr705 alloy surfaces by anodizing and MAO processes.

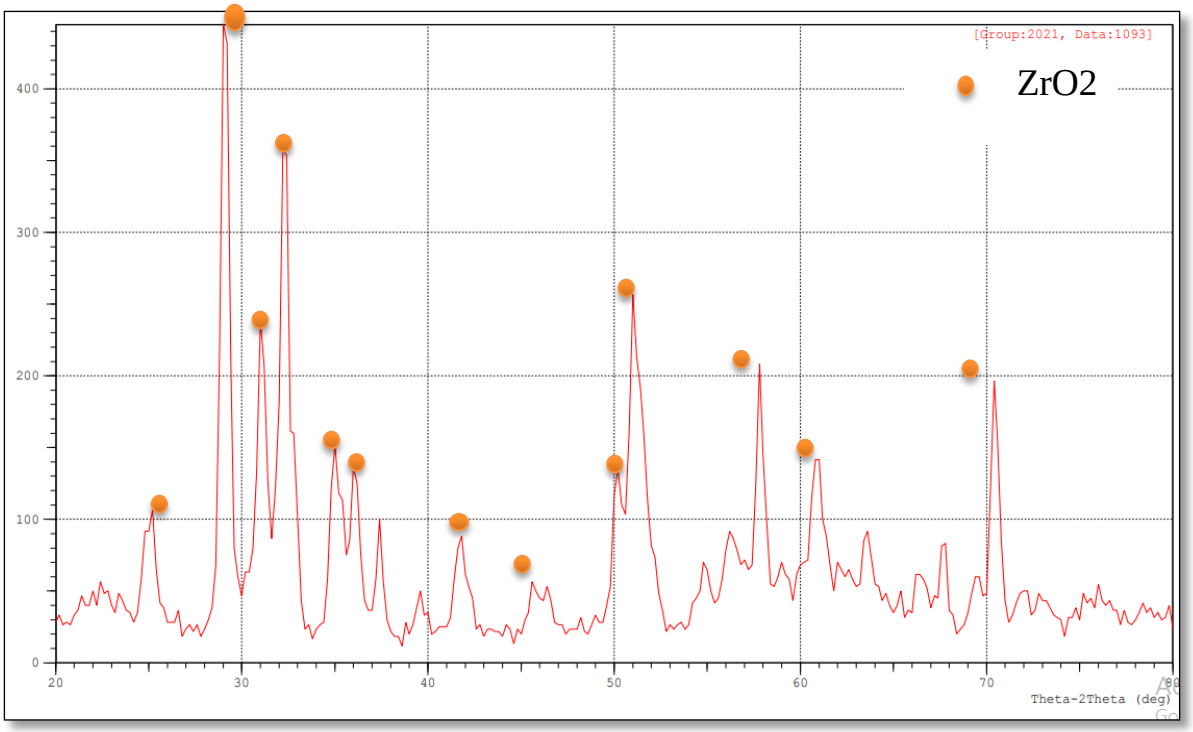

Figure (4-4): XRD Patterns of AN6 specimen.

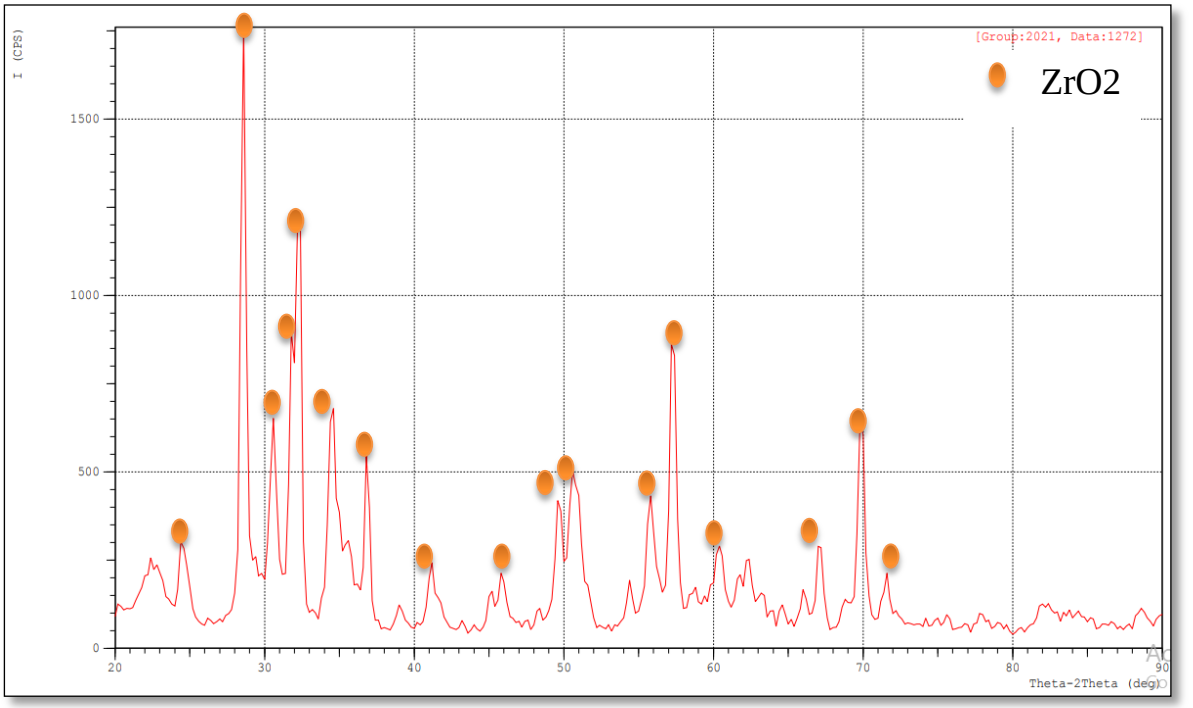

Figure (4-5): XRD Patterns of MAO6 specimen.

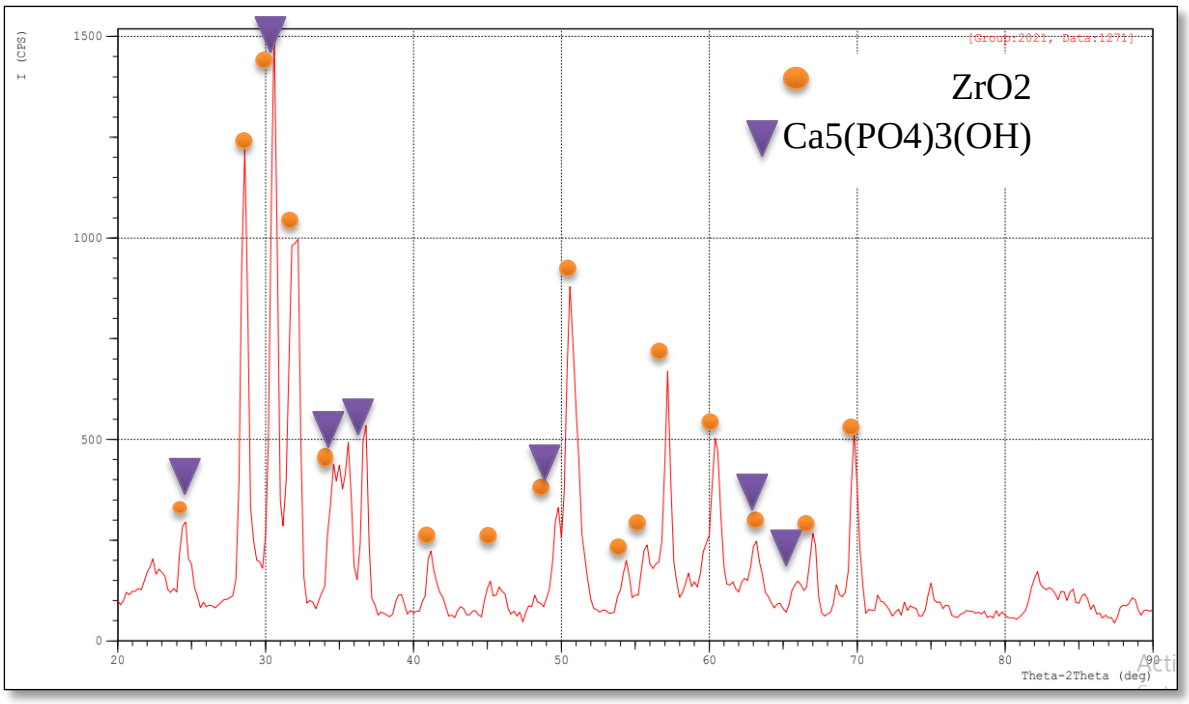

Figure (4-6): XRD Patterns of specimen DP1.

4.4 Microstructure and EDS Test results

(LOM) and (FESEM) were used to observe the microstructure of the etched specimens. The specimens were etched to reveal the grain boundaries in the microstructure [145]. Figure (4-7) shows LOM images US, grain structure was observed for Zr, and The Zr 705 had which contained the phase of α. Pores of different size are irregular but have been rounded. The metallography can give a simplified idea about the relationships between the microstructure of the material and the microscopic properties because the size and the shape of grains have a direct effect on the behaviour of the material [146].

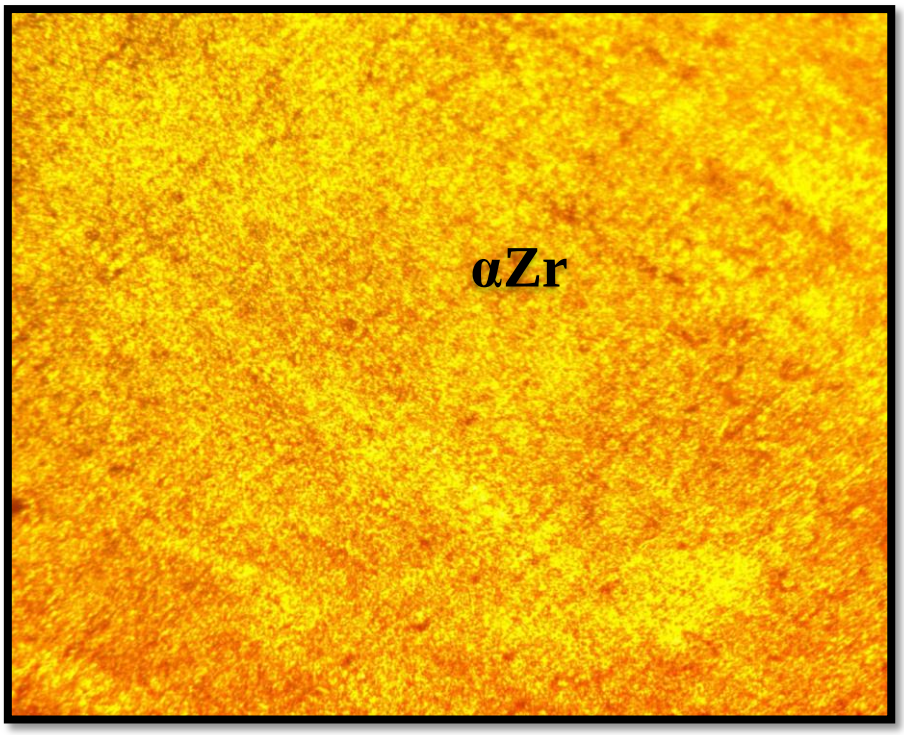

Figure (4-7): LOM image for US after Etching (100X).

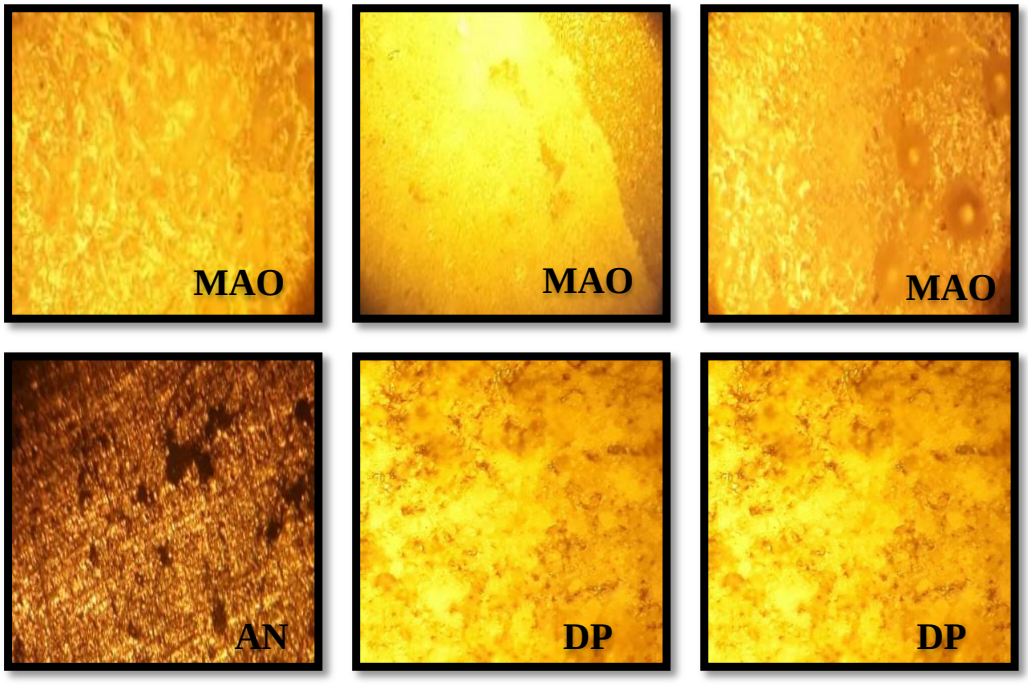

Figure (4-8): LOM image for specimens coated in different processes (600X).

FESEM images (Figure 4-9) the microstructure of specimens shows a multiphase structure, the images showed two phases (α Zr), which are confirming the XRD results.

FESEM images of specimens showed grain boundaries and pores in different sizes as indicated in figures (4-10) to (4-14). The surface of Zr705 is covered by ZrO2 or HA/ ZrO2 composite scale. It also can be noticed the disappearance of the phases in specimens due to the covering of surface with a scale.

Figure (4-10) and (4-11) shows the surface morphologies of the anodized coatings for 30min, and 60min, respectively. A uniform scale was prepared after 60min of anodizing. The porosity of the anodized Zr705 reduced after addition of HA but the bonding of layers seems to be unfavourable [147].

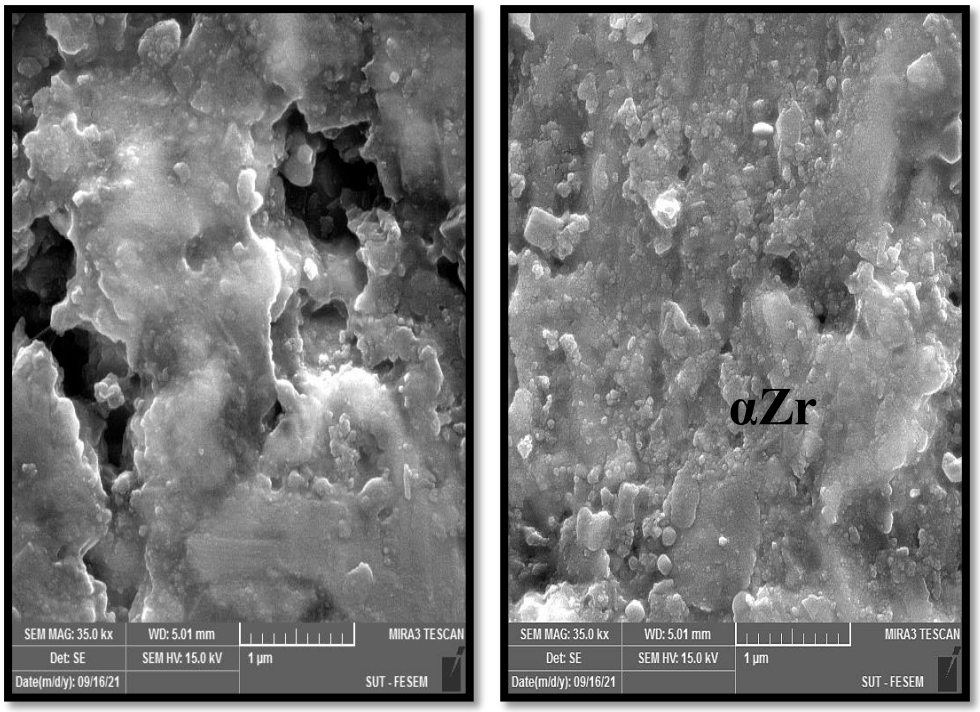

Figure (4-9): FESEM Images for US .

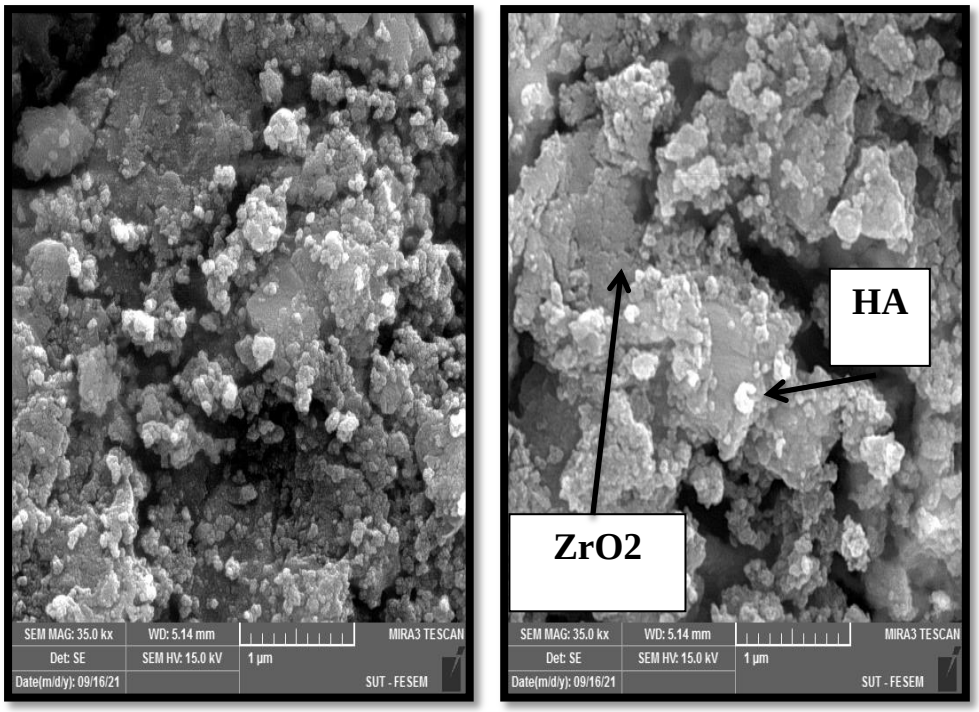

Figure (4-10): FESEM Images for AN12 specimens.

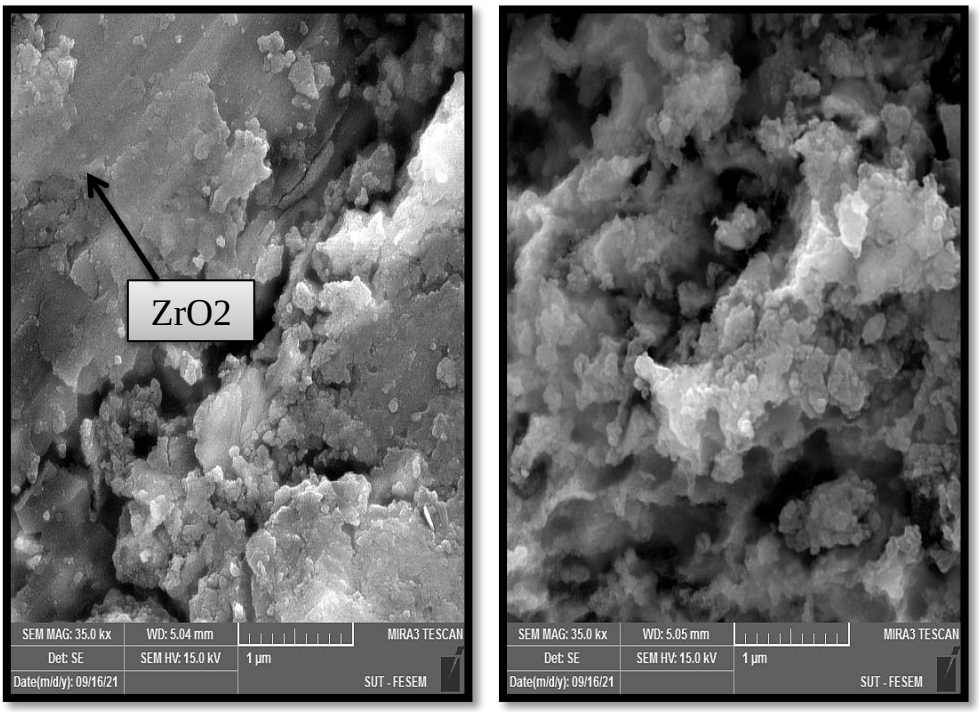

Figure (4-11): FESEM Images for AN6 specimens

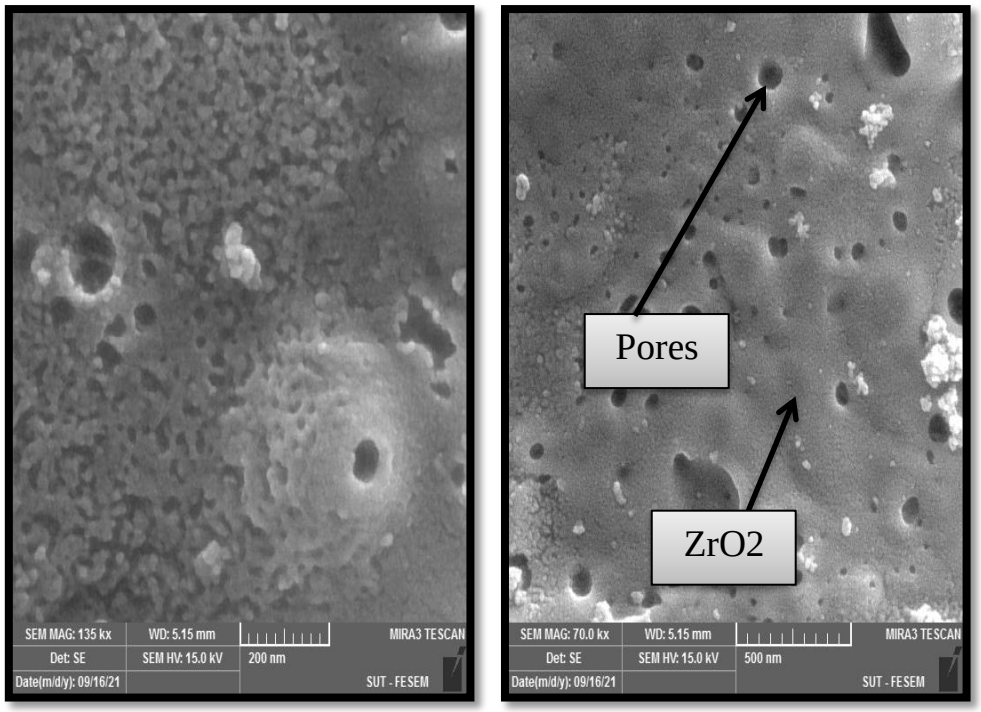

Figure (4-12): FESEM Images for MAO6 specimens

Figures (4-12)and(4-13) show the surface morphologies of MAO6,and MAO12 specimens ,respectively.

In obseration of the surface morphologies of the MAO coatings on MAO12 specimens modified by HA additives, HA precipitates could assist in closing the porous compared with figure (4-12).The morphology of the surface coating exhibited a flower-like structure due to the occurrence of self-assembly because of the long time of precipitation[148].The homogenous precipitates led to decrease pore ratio significantly

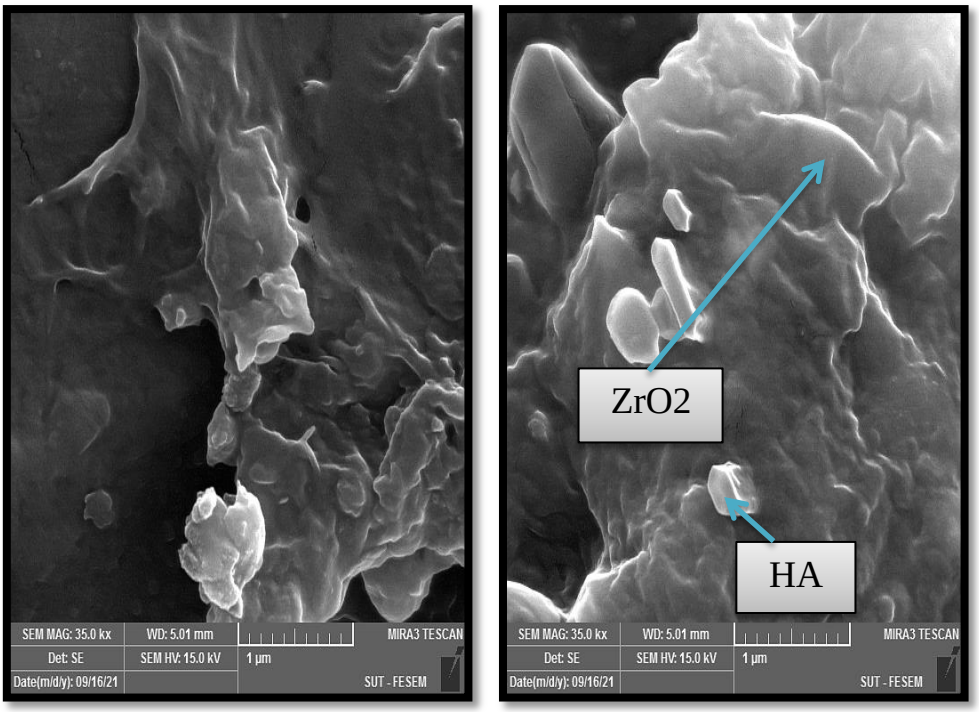

Figure (4-13): FESEM Images for MAO12 specimens.

Figure (4-14) show the surface morphologies of DP1 specimens. In observation of the surface morphologies of the duplex coatings on DP1 specimens modified by HA additives.

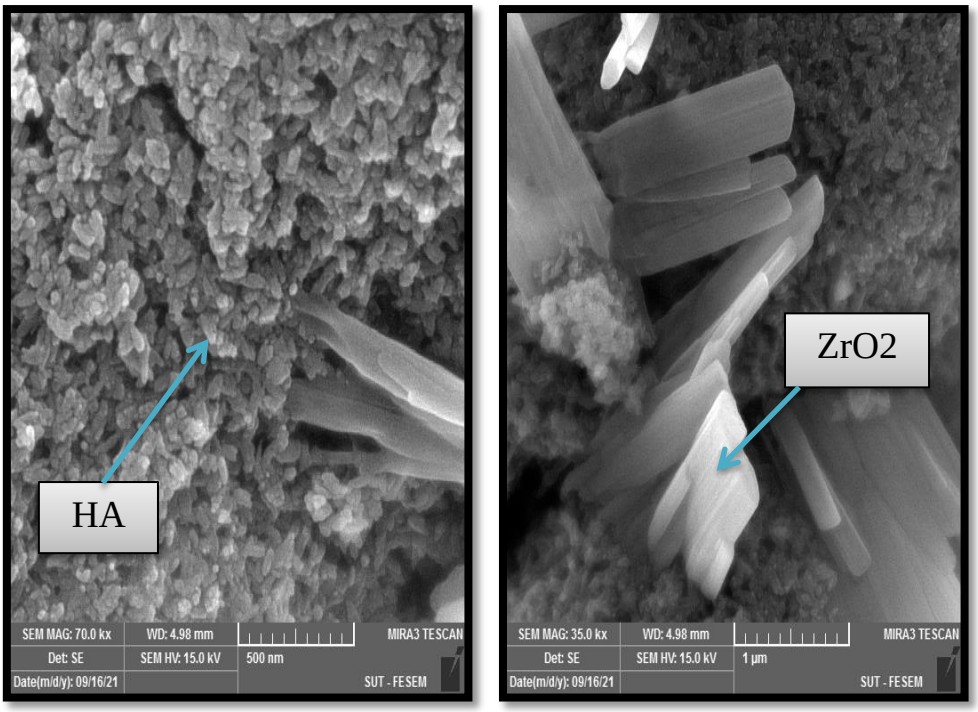

Figure (4-14): FESEM Images for DP1 specimens.

Figures from (4-15) to (4-20) show the EDS results for US and some coated specimens. As can be seen, the results of EDS analysis were relatively close from the percentage of addition, because the values gained from EDS analysis do not cover the total area, only the spot where the electron stroke[149].In general, EDS results in figures 4-16 and 4-18 proved the deposition of ZrO2 coatings on the coated substrates in comparison to those uncoated substrates. Also, EDS results for ZrO2/HA coatings (figures 4-17 and 4-19) could show the modification of ZrO2 coating with HA particles by means of existence of Ca element in EDS results. Anyhow, MAO recolored more modification of ZrO2 coatings by HA than that of anodizing. Such significant modification is expected due the fact that in the MAO, when the voltage is sufficient for causing dielectric breakdown variation with the Zr anode , a micro - arc discharge result in thick and porous film, where by , the HA components in the electrolyte are incorporated into the oxide films by the discharges.

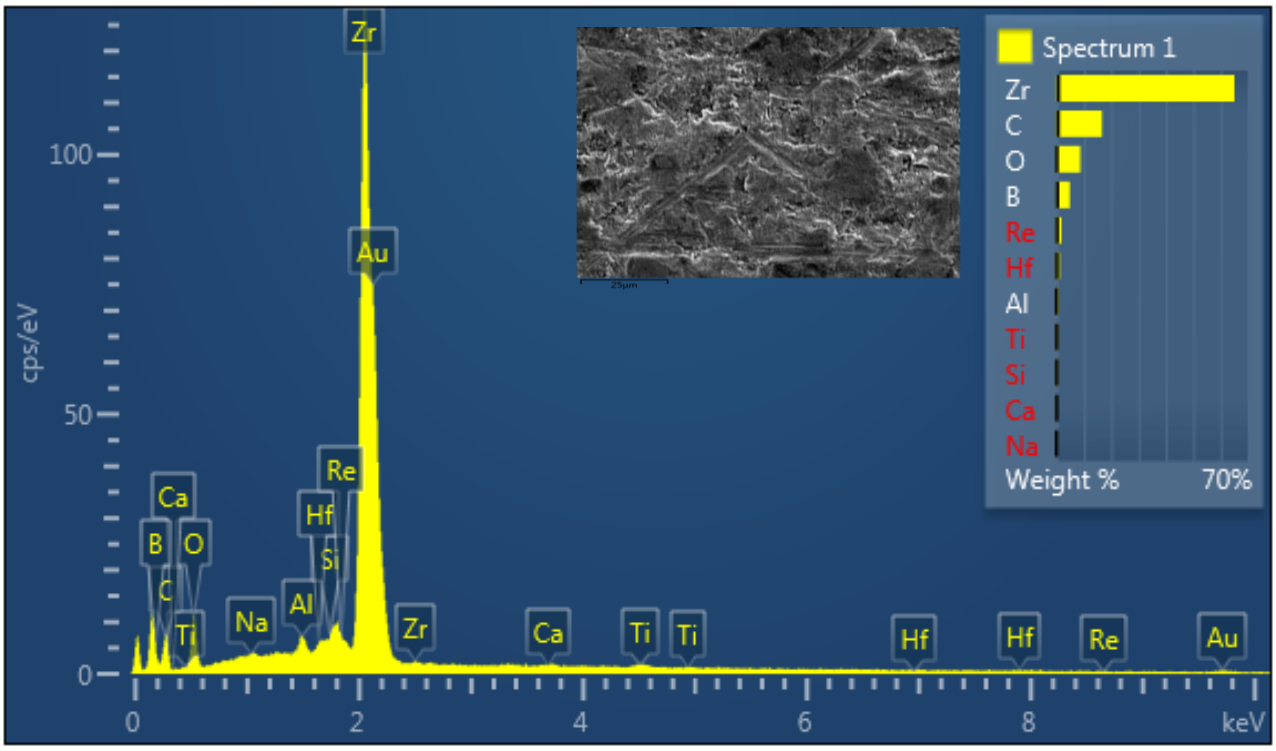

Figure (4.15): EDS Spectrum for uncoated US substrates.

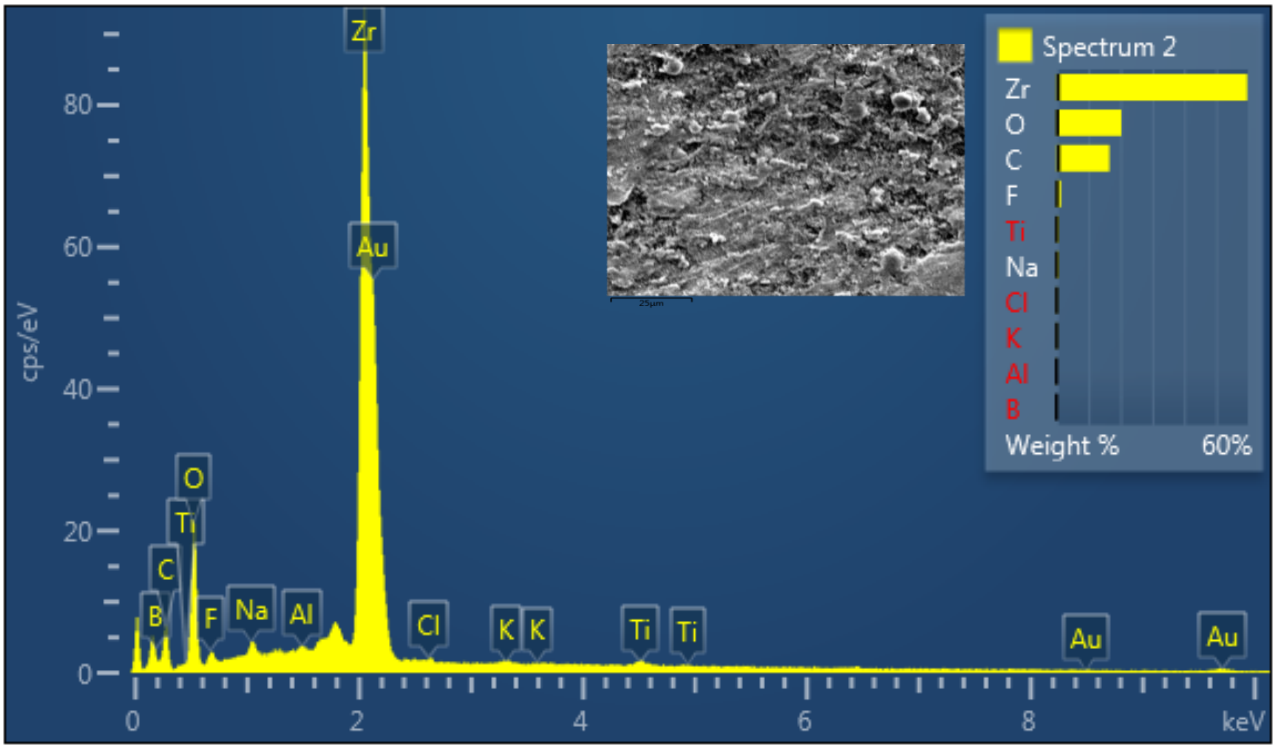

Figure (4.16): EDS Spectrum for AN6 specimens.

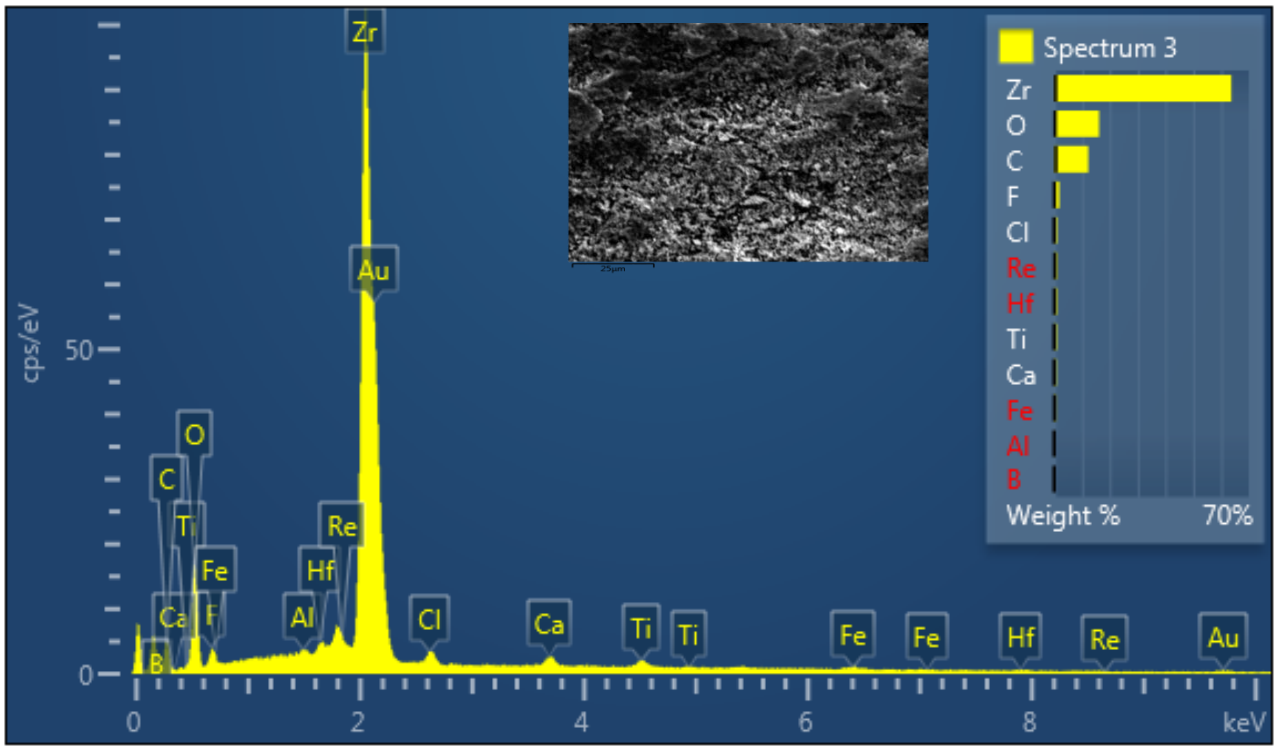

Figure (4-17): EDS Spectrum for AN12 specimens.

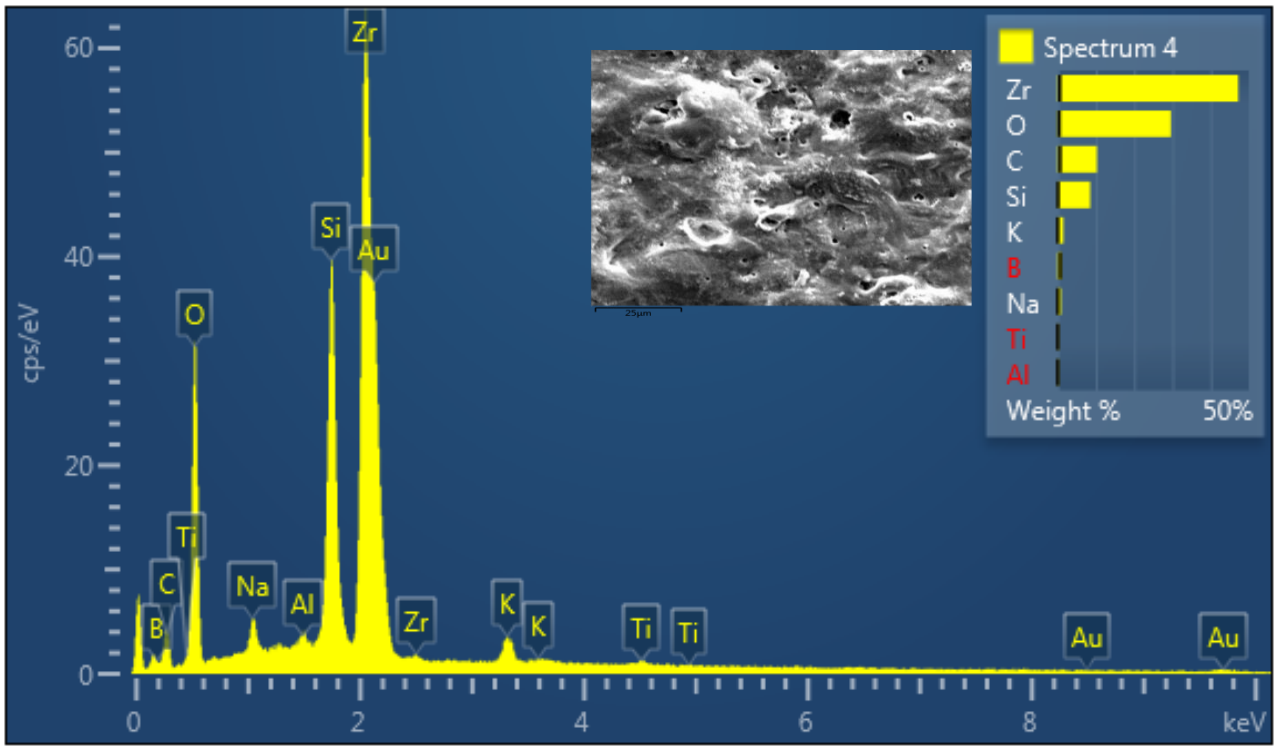

Figure (4-18): EDS Spectrum for MAO6 specimens.

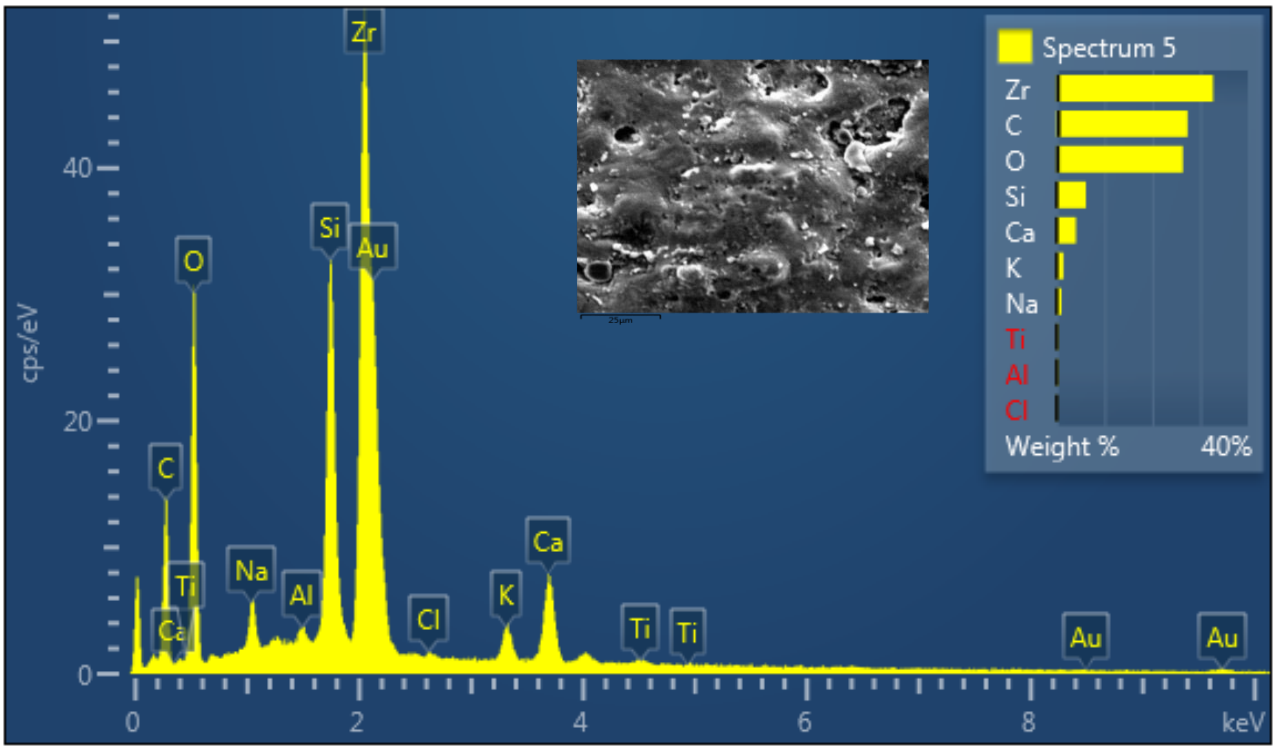

Figure (4.19): EDS Spectrum for MAO12 specimens.

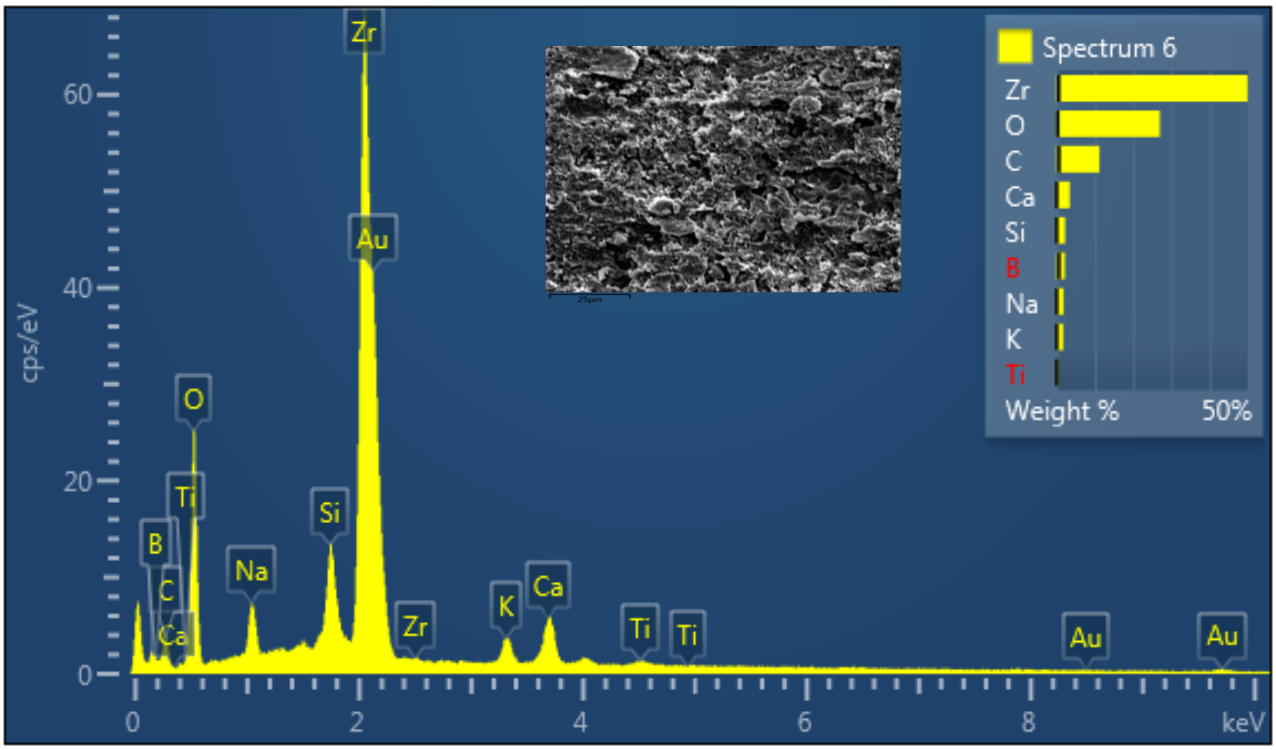

Figure (4.20): EDS Spectrum for DP1 specimens.

4.4 AFM Test Results

Figures (4-21 to 4-26) and Table (4-2) show the AFM results of different specimens. In general, it can be concluded that the topographic structures of the coating are uniform and dense.

Also, it can be concluded that the addition of HA to the electrolytes has less effects on increasing the surface roughness.

Most likely, the HA incorporation in coating layers is expected to have its significant effects on mechanical properties (hardness, wear), and corrosion behavior in comparison to other properties such as (Ra) [150].

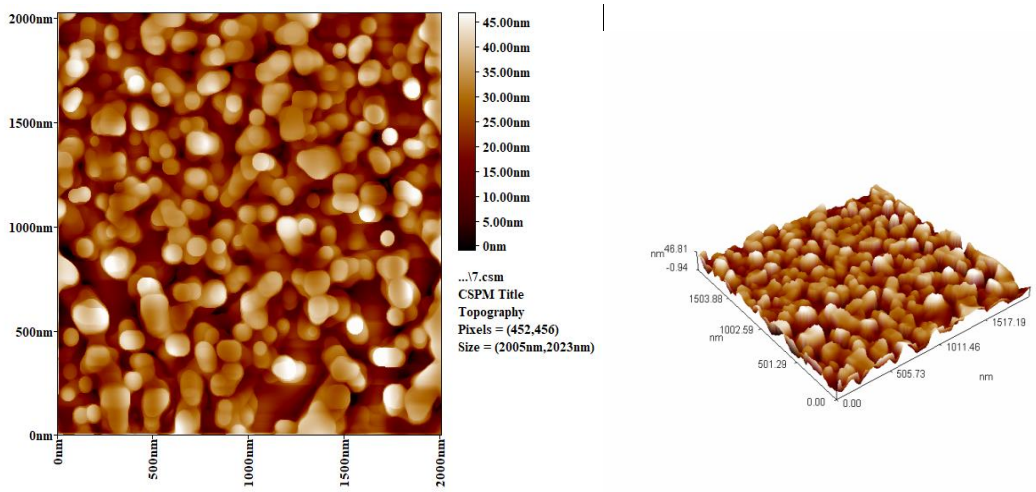

Figure (4-21): AFM of US.

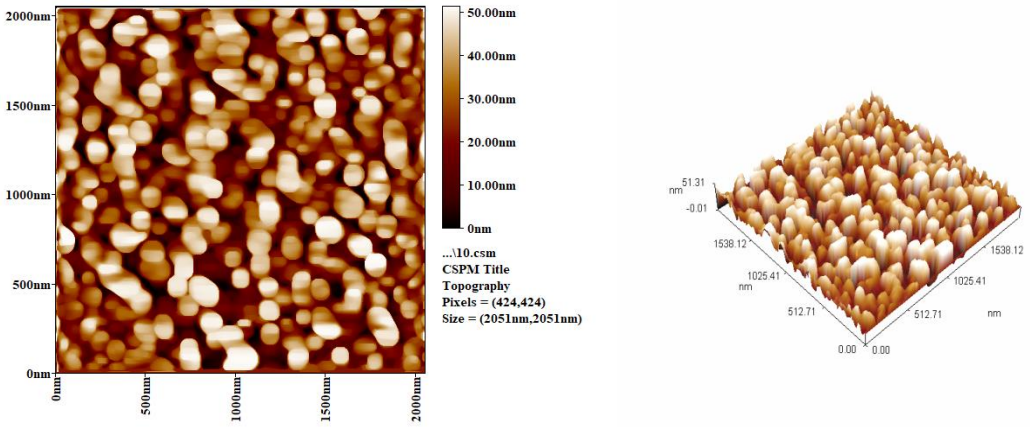

Figure (4-22): AFM results of AN6 specimens.

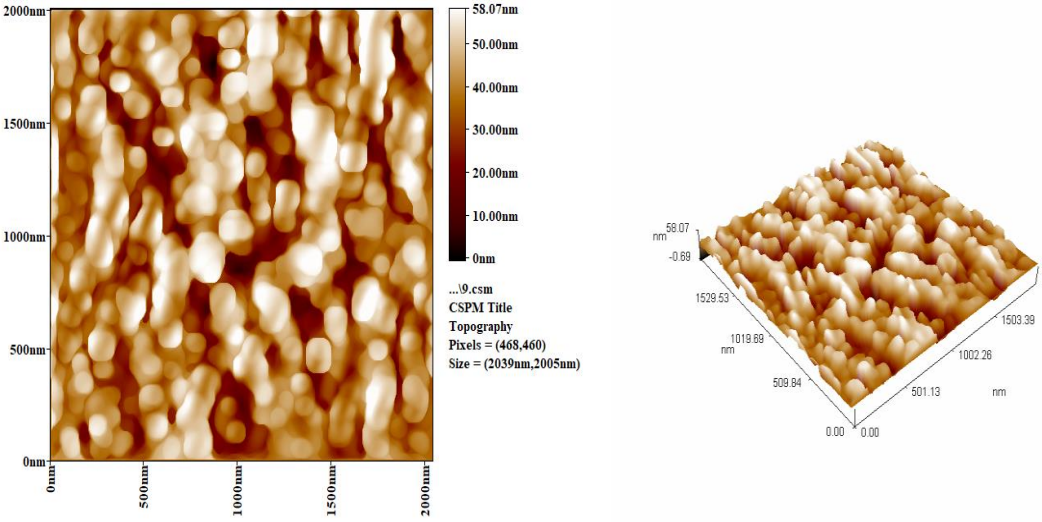

Figure (4-23): AFM results of AN12 specimens.

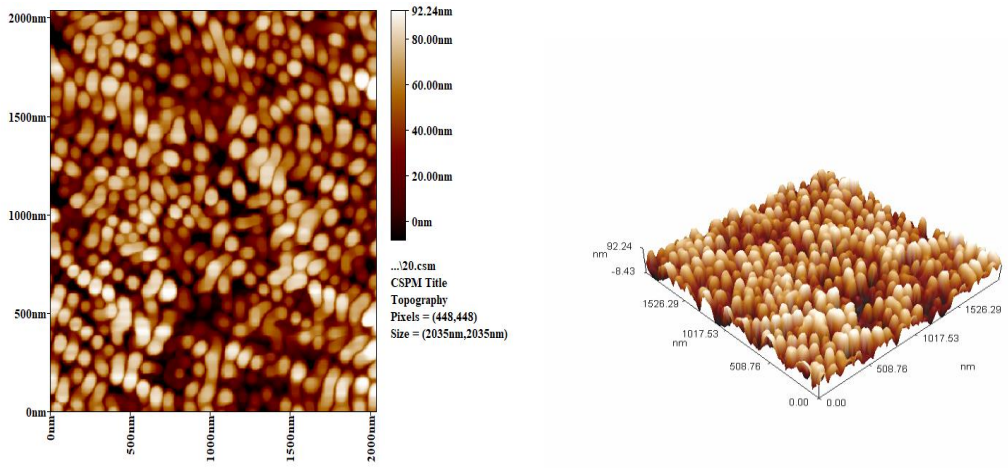

Figure (4-24): AFM results of MAO6 specimens.

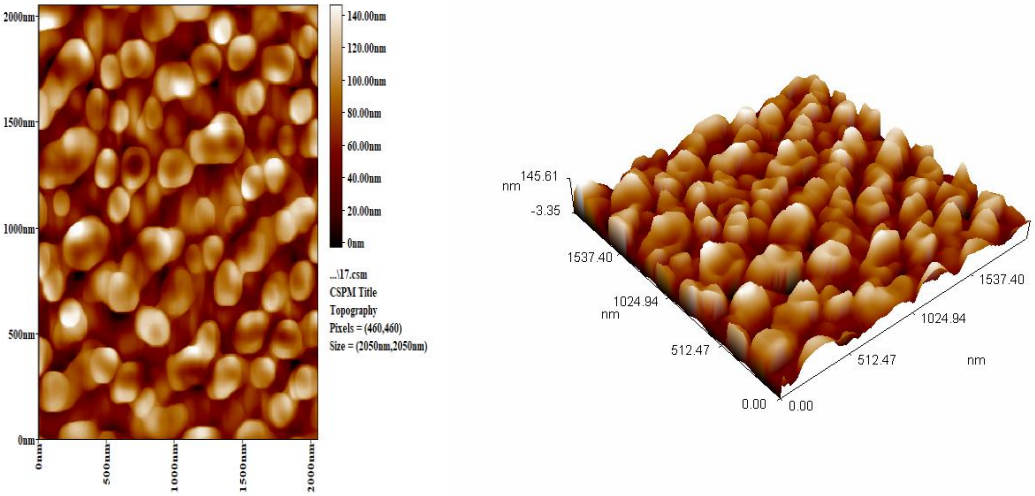

Figure (4-25): AFM results of MAO12 specimens.

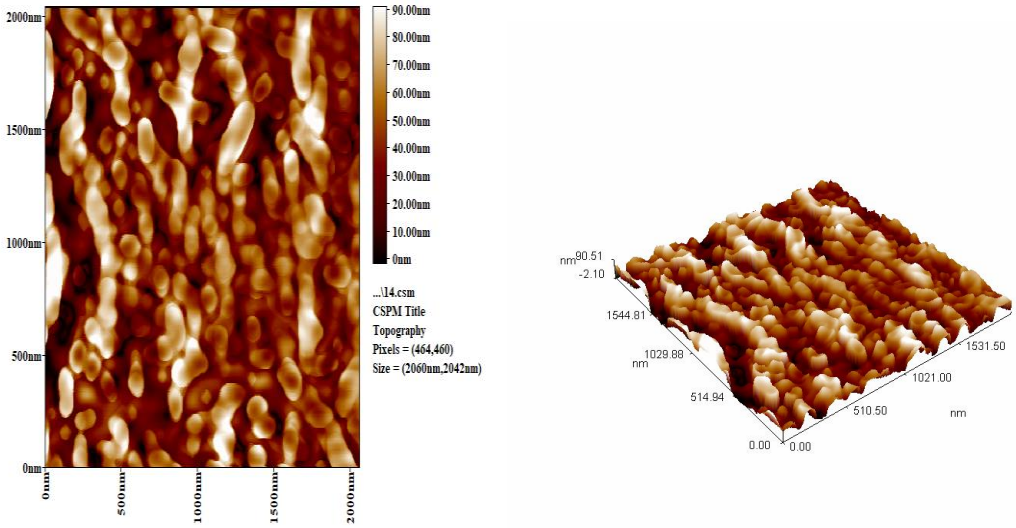

Figure (4-26): AFM results of DP1 specimens.

Table (4-2): Surface roughness values.

Specimen code	Surface roughness Ra (nm)
US	8.23
AN6	12.6
AN12	11.8
MAO6	24.3
MAO12	18.8
DP1	22.2

From the AFM results shown in figures, it is interested to decl are that the MAO6 specimen recorded the highest Ra among the other specimens because of the coating grown on the surface have a rough surface depending on the phenomenon of micro discharge resulting from the nature of MAO process [148].

Furthermore, resulting from melting, plenty of micro-volcano like formations and plenty of circular micro pores at the end of some of these formations have been encountered in different sizes [149]. Local melting occurring during the coating process followed by solidification led to the formation of pores in a circular pattern [151].

4.5 Mechanical Properties

4.5.1 Hardness Test

Figures (4-27) to (4.29) represent the Vickers hardness. Showed the obtained results. The test of hardness was done by taking the average of 5 readings. Hardness tests have been performed on a master specimen and these values will be compared before and after modification, that there is a significant increase in hardness .The value of the hardness is increase, may be due to pore filling by depositing materials, the hardness became close to the value that it means that the deposition on the surface is homogeneous. The other reason for the increased hardness can be attributed to the fact that the precipitated material (Exceptional Vickers hardness of zirconia about 1500 HV) and Ceramic has a higher hardness than metal [152].

Generally, the value of the hardness in this study was improved via coating by anodizing, MAO and duplex processes. Results reveal an increasing in the hardness for DP specimens comparing with anodizing and MAO. Results showed that the specimen DP1has the highest value of hardness, while the specimen AN9 has the lowest (438.6, 120.9) HV respectively.

Increasing the amount of HA in the coating would increase the hardness values in all kinds of coating.

With the increasing the amount of HA, the experiments observed an improve in the hardness values in MAO specimens comparing with the anodizing.

For anodizing results:

Experiments showed that the specimen AN12 has the highest hardness (270HV), while the specimen AN9 has the lowest (120.9HV), Voltage factor influences the hardness values more than anodizing time. At 30V the hardness increases with the anodizing time from 10 min to 30min and then decreasing at time of 60 min. At time of 10 min to 30min the hardness increases with increasing of voltage from 10V to30V. At time 60min, the hardness decreases with increasing of voltage from 10V to 30V.

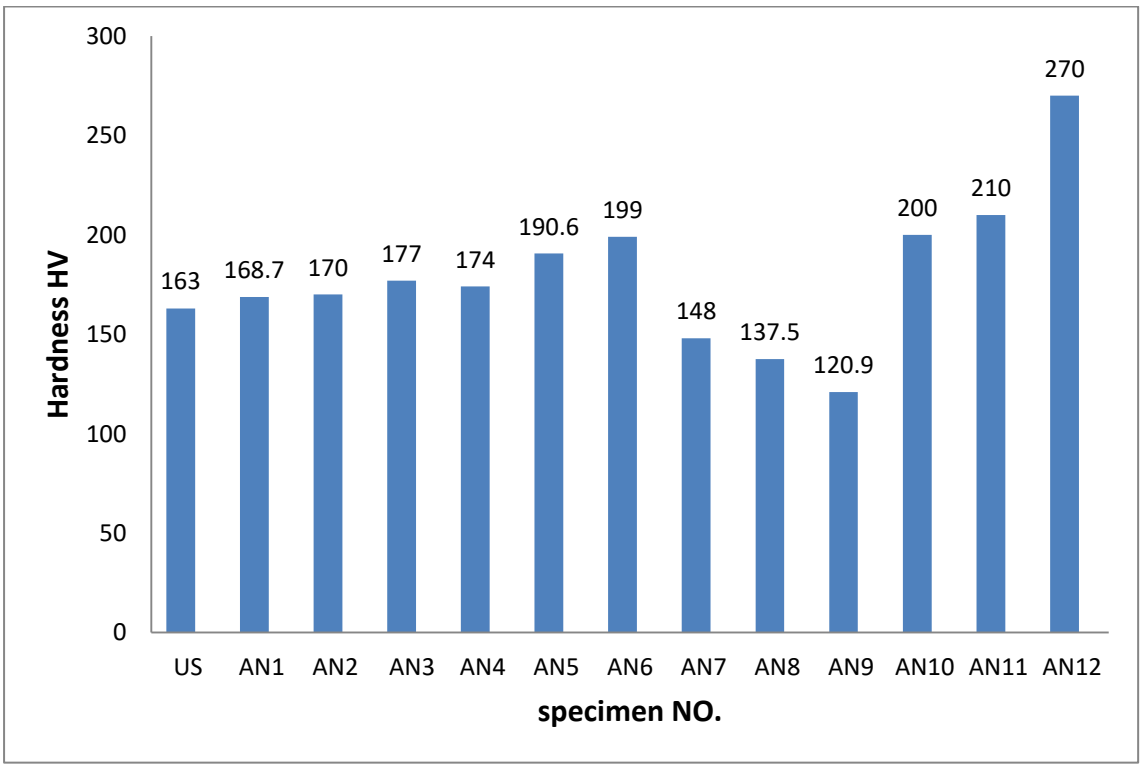

Figure (4-27): Effect of anodizing on the Hardness (HV).

For MAO results:

The experiments showed that specimen MAO12 has the highest value of hardness (347.59 HV), while the specimen MAO1 has the lowest hardness (243.5HV). Voltage factor affected the hardness values more than the MAO time. At 200 V, the hardness increase with MAO time from 5min to 10min and then decreasing at 15min. At time of 10 min, the hardness increases with the increasing of the voltage.

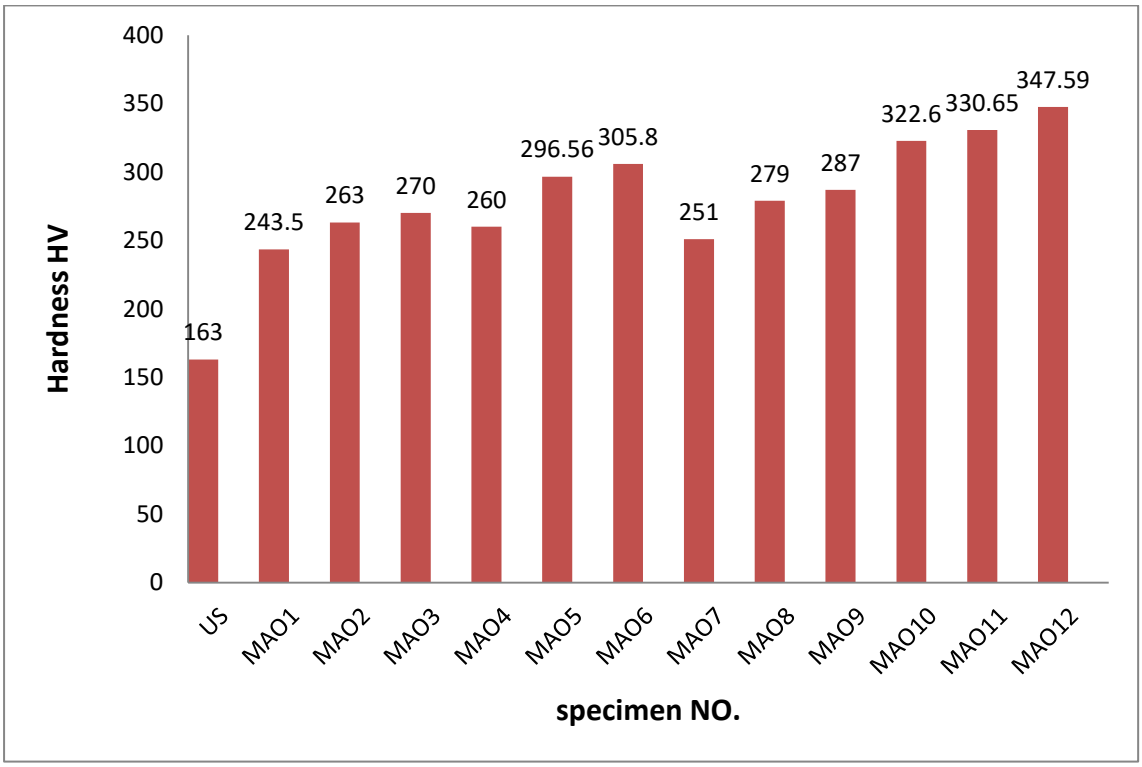

Figure (4-28): Effect of MAO on the Hardness (HV)

For duplex results:

The experiments showed that the specimen DP1 has the highest value of hardness (438.6HV), while the specimen DP2 has the lowest hardness (360HV).The hardness increases with the increasing of HA amount. Increases HA amount in MAO effected the hardness values more than the anodizing in duplex process.

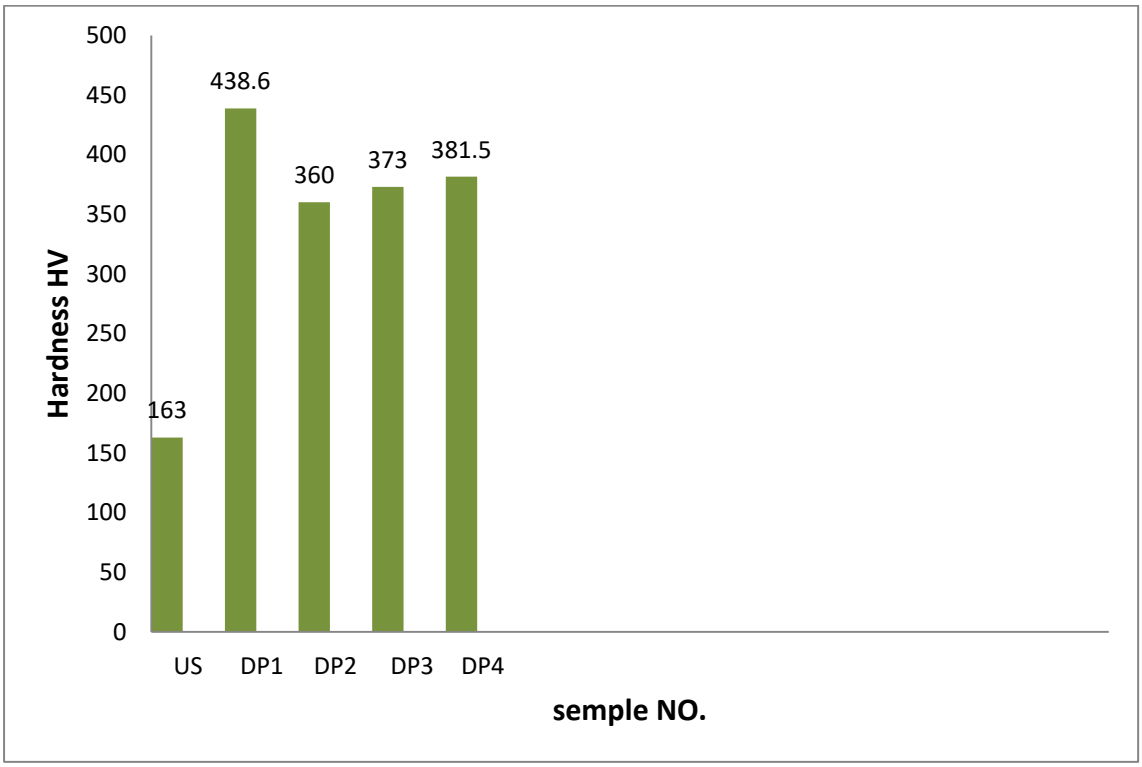

Figure (4-29): Effect of duplex on the Hardness (HV).

4.5.2 Dry Sliding Wear Test Results

Specimens with (13) mm diameter subjected wear test under various loads (5, 10 and 15) N and for several times (5, 10, 15, 20, 25 and 30) minutes. The loads and times were chosen according to [144,145 and146].

Where (5, 10 and 15) N and different times (5, 10, 15, 20, 25 and 30) minutes were tested. Generally, it can be concluded that the weight losses increased with increasing of loading time. Ceramic coating of ZrO_2 and ZrO_2/HA deposited by MAO, anodizing and duplex processes recorded significant low weight losses in comparison with uncoated Zr705 substrates (18×10^{-4}) g.

Furthermore, the aforementioned decreasing in weight losses is attributed to the improvement hardness (199HV-389.68HV) due to deposition of ZrO_2 ceramic coatings and incorporation of HA in those coatings. The variation in the weigh loss of Zr705 specimens used in this investigation as a function of test time at a normal loads of 5, 10 and 15 N are shown in figure 4.30 . The weigh loss values of Zr705 specimens used in this investigation at a normal loads . The weigh loss as a function of time could be divided into more than one zone. There are three main friction zone, the first zone run – in period zone, depasivation zone, and repasivation zone. However, the number of friction zone depended on the type of modifaction to Zr705 .

Before start rubbing it would be expected that the ZrO2 or HA/ ZrO2 layers would generate on the surface of specimens used in this investigation, and the compostion of oxide film depended on the types of processes .

During the first zone I from 5min to15min rubbing was started and the oxide film breack up due to the mechanical contact between the counter face and the surface of specimens used in this investigation . In the second zone II from 15 to 25 min, during rubbing the weigh loss increase, thus, could be related to the depassivation mechanism, which leading to remove the the layer in the contact zone during rubbing and exposing the fresh surface of Zr705 used in this investigation.

As rubbing continued, zone III from 25 min to 30 min, the weigh loss reach the steady state indicating occurrence of repassavation and the passive state regained. The behaviour between zone II and zone III could related to the dynamic equilibrium betwwen recoverable the oxide and removal of oxide film (depasavation and repassivation). The three main zones can clearlly seen in figure(4.30).

The higher weigh loss was obtained from in DP1 at normal loads as you can seen in figure 4.30. The higher weigh loss of DP1 may be related to the wear debris result from the remove of the passive film and metal during rubbing, leading to interaction between the wear debris, thus the friction force will increase as a result of an increase in the ploughing action.The chemical constituents of the passive oxide layes also has influnce in the friction behaviour of the Zr705 specimens used in this investigation[165].

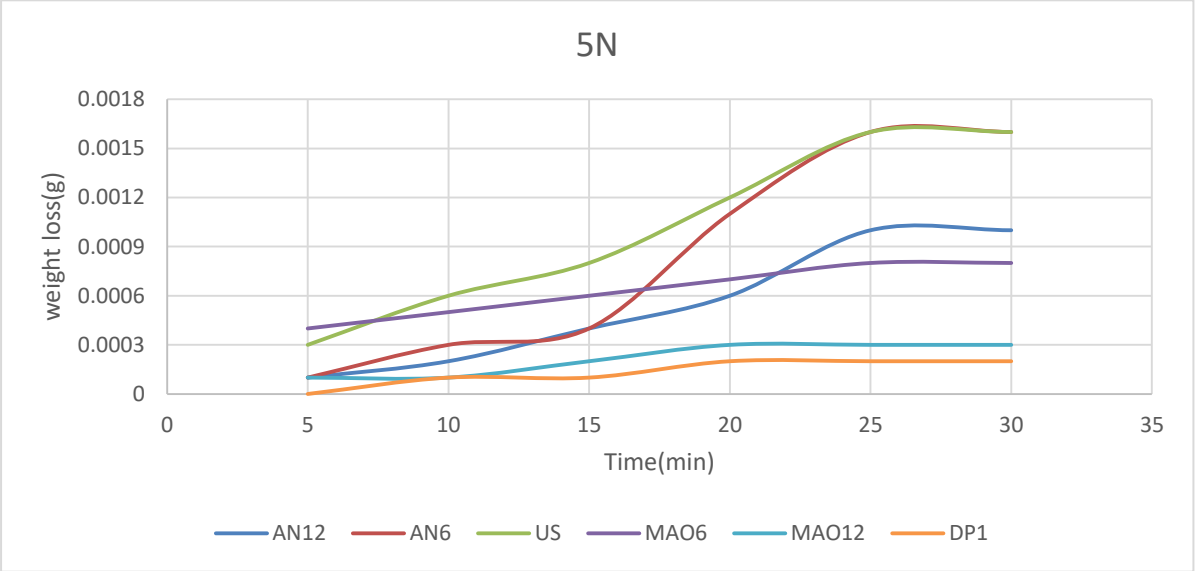

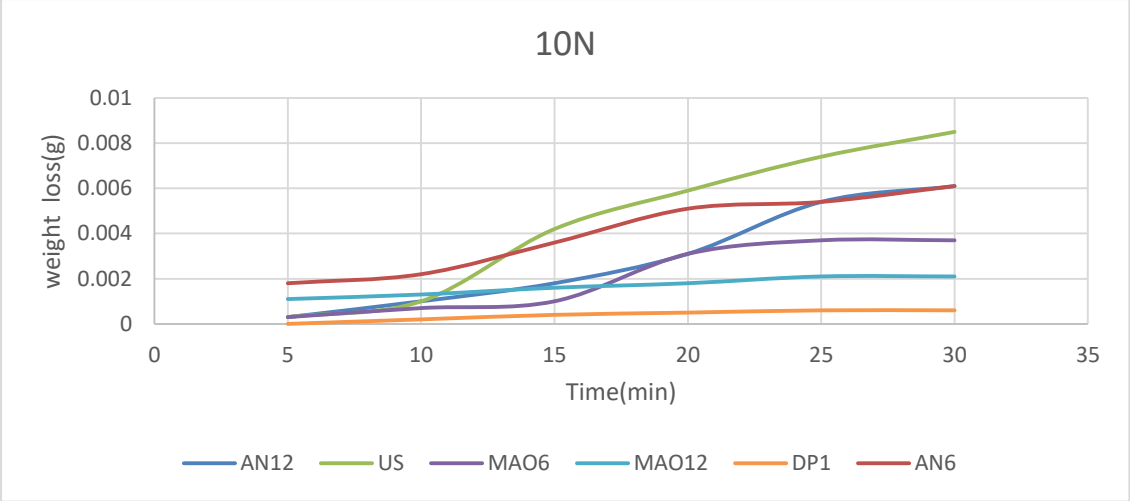

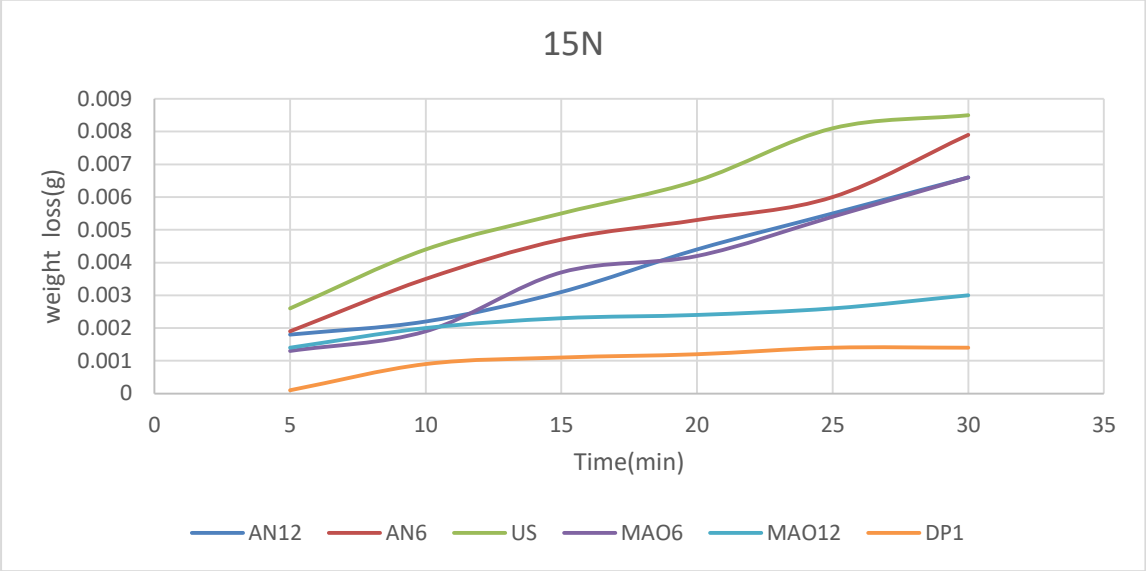

Figure (4-30): weight Losses vs. Time for (US, AN6, AN12, MAO6, MAO12, and DP1) under (5, 10 and 15N) Loads.

Despite the observed increasing of weight losses with increasing of load there is clear stability of weight losses for some specimens with increasing time, especially at 5N figure (4-30) It is possible to note the lower weight loss of DP1 and MAO12(for all loads) compared to the AN6,AN12and MAO6 .

This is Attributable to the hardness of this specimen, so, it is subjected to the Archard's law which States "weight loss for materials that is inversely proportional to the material hardness value", In addition, the thickness of the oxide film formed on the surface of the specimen due to high hardness which is difficult to remove during time [153].

The figures above show weight losses as a function of time. The losses in the weight of specimens (before or after adjustment) increase with the increase in the loads used, but there is a clear stability in the weight loss for some specimens with increasing time, especially in the specimens (MAO12, DP1). It can be observed that the increased losses in the weight of specimens (US, AN6) are higher than the rest of the specimens.

Tables (4-3) to (4-5) present values of weight losses, wear rate, coefficient of friction(μ) percentages of development in μ and wear rates at 30 minutes and under different loads (5, 10 and 15)N. The rotational speed is 350 rpm. Also, figure (4-30) and (4-31) show the effects of load on the μ and wear rates.

Table (4-3): Wear results at load 5N.

Specimens	**ΔW(g)×10^{-4}**	**Wear rate×10^{-8} (g/m)**	**Coefficient of friction(μ)**	**Wear rate reduction %**	**Coefficient of friction reduction%**	**Hardness(HA)**
US	18	2.7	0.67	-	-	163
AN6	17	2.5	0.44	8%	34%	199
AN12	13	1.9	0.42	29.6%	37%	270
MAO6	12	1.8	0.22	33%	67%	305
MAO12	4	0.6	0.21	77.7%	68%	347
DP1	2	0.3	0.07	88.8%	89.5%	438

Table (4-4): Wear results at 10N

Specimens	**ΔW(g)×10^{-4}**	**Wear rate×10^{-8} (g/m)**	**Coefficient of friction(μ)**	**Wear rate reduction %**	**Coefficient of friction reduction %**	**Hardness(HA)**
US	85	12.8	0.85	-	-	163
AN6	61	9.2	0.72	28%	15%	199
AN12	61	9.2	0.66	28%	22%	270
MAO6	59	8.9	0.51	30%	40%	305
MAO12	23	3.4	0.47	73%	44.7%	347
DP1	12	1.8	0.23	86%	72.9%	438

Table (4-5) : Wear results at 15N

Specimens	**ΔW(g)×10^{-4}**	**Wear rate ×10^{-8} (g/m)**	**Coefficient of friction(μ)**	**Wear rate reduction %**	**Coefficient of friction reduction %**	**Hardness(HA)**
US	85	12.8	0.96	-	-	163
AN6	79	11.8	0.92	7%	4%	199
AN12	67	10.1	0.89	21%	7%	270
MAO6	66	10.004	0.82	21.8%	14%	305
MAO12	30	4.5	0.73	65%	23%	347
DP1	17	2.5	0.69	80.4%	28%	438

The total weight removed due to wear of Zr705 used in this investigation after the wear tests are shown in the tables (4.3, 4.4, and 4.5).As you can see from the tables the total removed wear weight was relatively insensitive to the normal applied loads during the wear tests. Increase in the total removed wear weight with load. The smallest removed wear weight was obtained with DP1 normal loads

While, the second generation MAO12showed the smallest total removed wear weight. The secound generation US,and AN6 showed the highest total removed wear weight. At higher loads, 15 N in this investigation, the wear behaviour (total removed wear weight) could be explanied by the influnce of the mechanical characteristics, such as hardness (H) . It was reported that the wear ressistance may be better investigated using the ration between hardness and wear resistance [166].The alloy has a good wear resistance with higher values of (H).The main factors influnce the phenomenon of passiviting under rubbing are the critical pressure required to depassivation mechanism, the thickness of the passive oxide developed on the alloy's surface, and the chemical compostion of the oxide [167].This phenomenon is very benficial to biomdeical applicatipons since the phenomenon of passivity will play a key role to decrease the material loss and reduce the amount of debris during wear, also decrease the release of metal inos. Figures (4-3 1and 4-32) shows effect of the loads on the coefficient of friction and the wear rate, where with increased in the loads, the rate of wear and coefficient of friction increased.

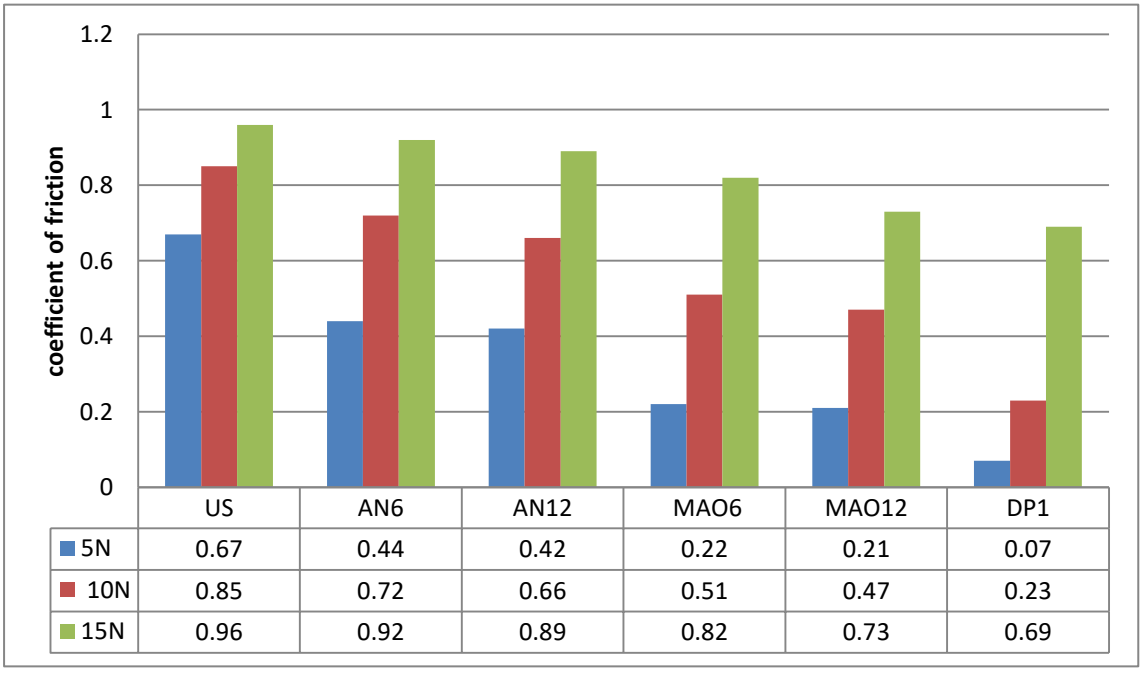

	US	AN6	AN12	MAO6	MAO12	DP1
5N	0.67	0.44	0.42	0.22	0.21	0.07
10N	0.85	0.72	0.66	0.51	0.47	0.23
15N	0.96	0.92	0.89	0.82	0.73	0.69

Figure (4-31): The effect of a variable loads on the coefficients of friction.

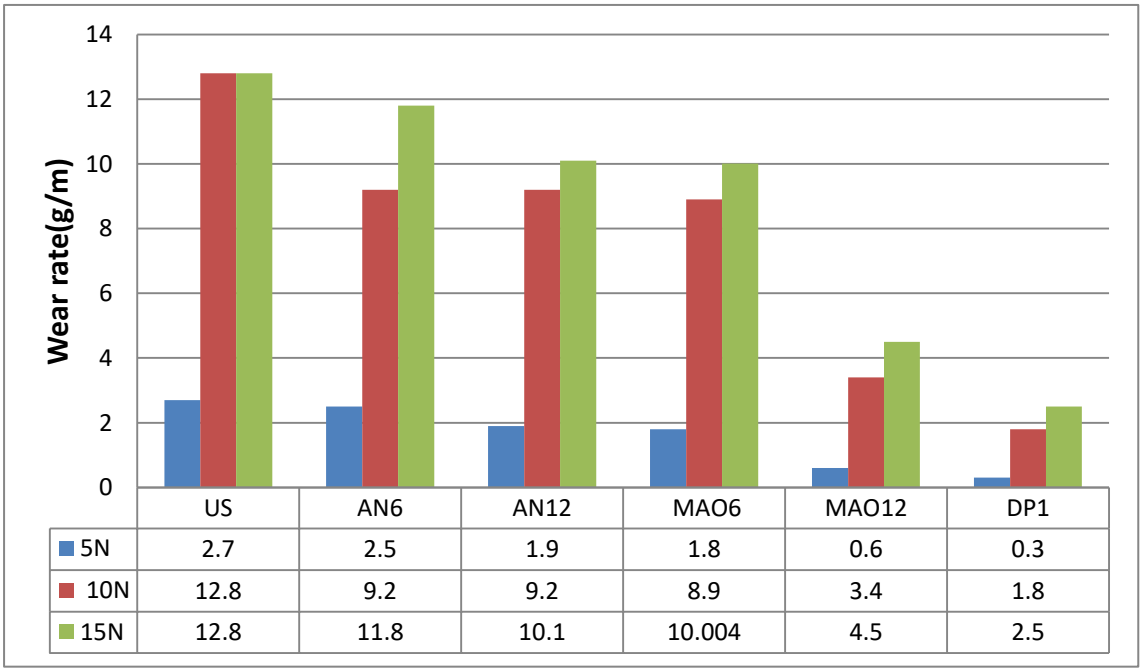

	US	AN6	AN12	MAO6	MAO12	DP1
5N	2.7	2.5	1.9	1.8	0.6	0.3
10N	12.8	9.2	9.2	8.9	3.4	1.8
15N	12.8	11.8	10.1	10.004	4.5	2.5

Figure (4-32): The effect of a variable loads on the wear rate.

Figures 4.33 and 4.38 display optical images of wear tracks and lines on Zr705 used in this investigation and on the alumina ball at 15N normal loads. There is evidence of isolated debris particles, scratching, track's surface and grooves. It is interesting to note that, on the surface .These results are in a good agreement with what reported by [168] Equally, no evidence of transfer from all Zr705 used in this investigation to the alumina ball surface, and transfer to the alumina ball surface from all specimens surface used in this investigation during rubbing at normal load of 15N. The mechanisms of wear for specimens under rubbing were primarily related to abrasive ploughing wear.

higher average roughnees at normal loads of 15N. Thus, might related to that the US ,and AN6had higher COF. No surprising that, the average roughness increased with increase the load. The increase in roughness with load indicates that the US and AN6, as well as deep scratches and grooves on a large scale with increase the load.

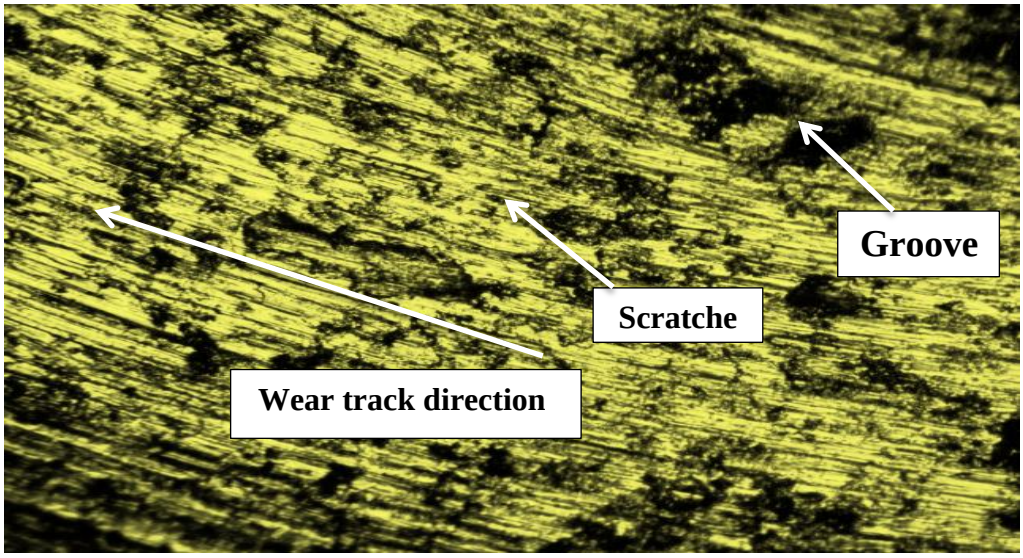

Figure (4-33): LOM images of US specimen worn surface at 100X Magnification after Wear Test (15N, 30min).

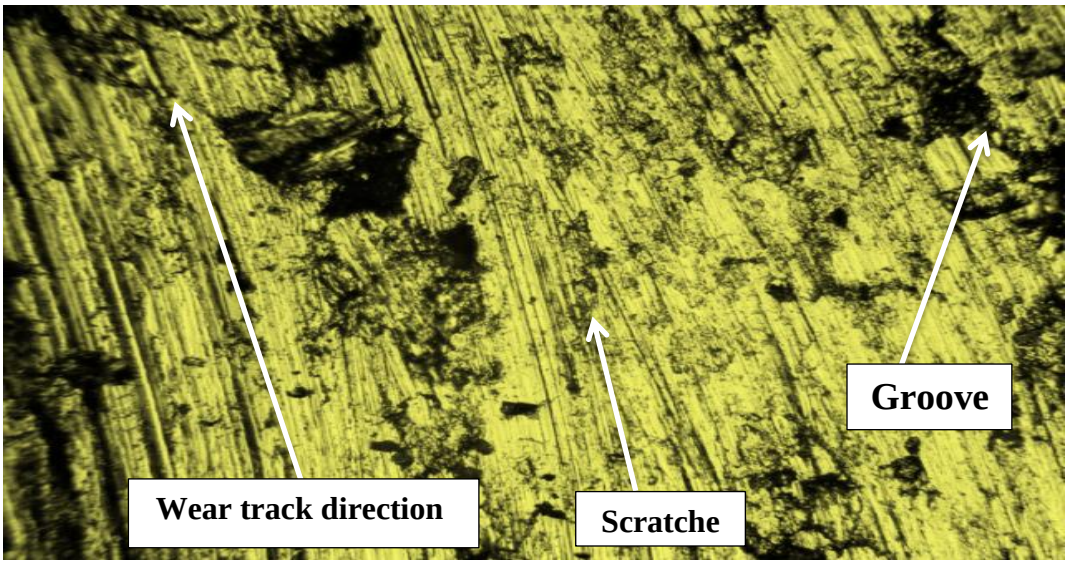

Figure (4-34): LOM images of AN6 specimen worn surface at 200X Magnification after Wear Test (15N, 30min).

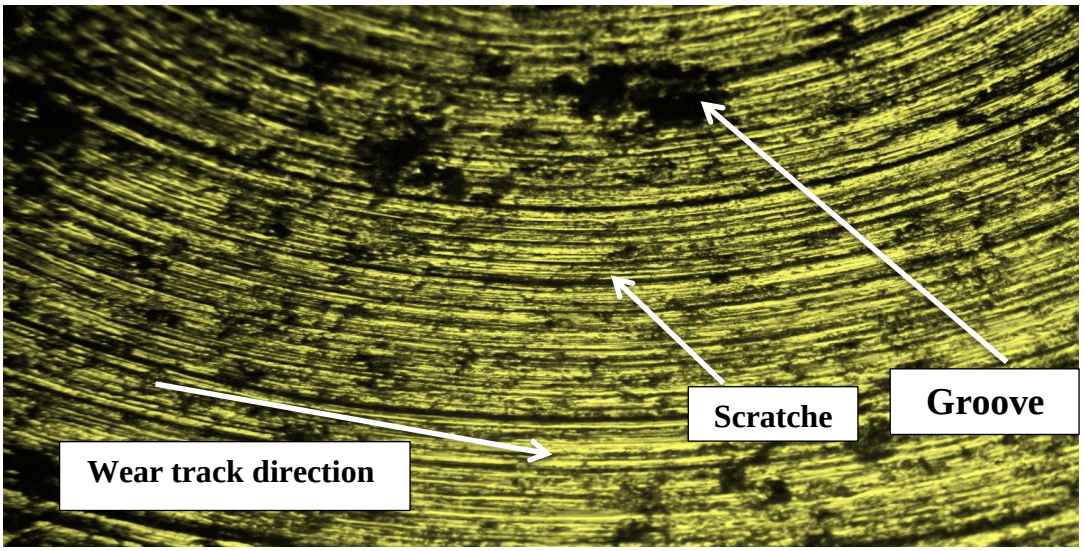

Figure (4-35): LOM images of AN12 specimen worn surface at 100X Magnification after Wear Test (15N, 30min).

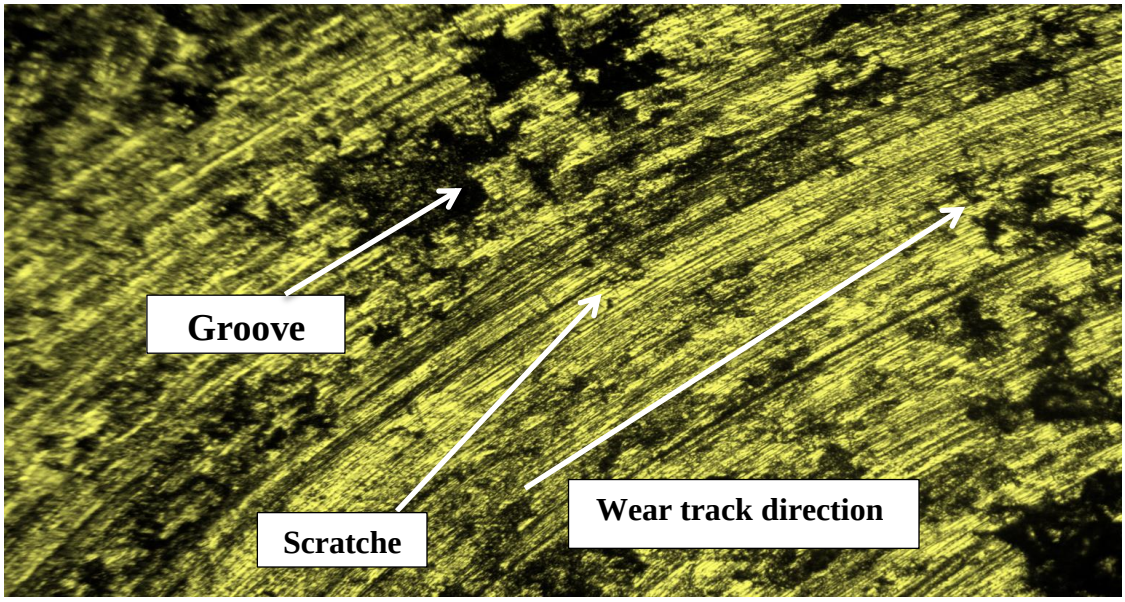

Figure (4-36): LOM images of MAO6 specimen worn surface at 100X Magnification after Wear Test (15N, 30min).

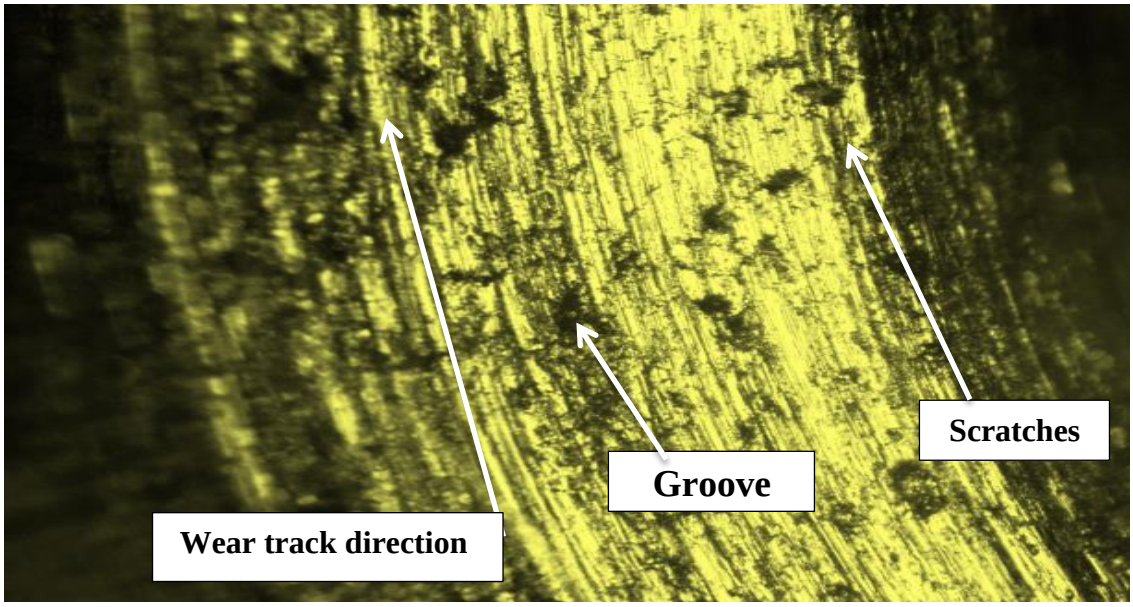

Figure (4-37): LOM images of MAO12 specimen worn surface at 100X Magnification after Wear Test (15N, 30min).

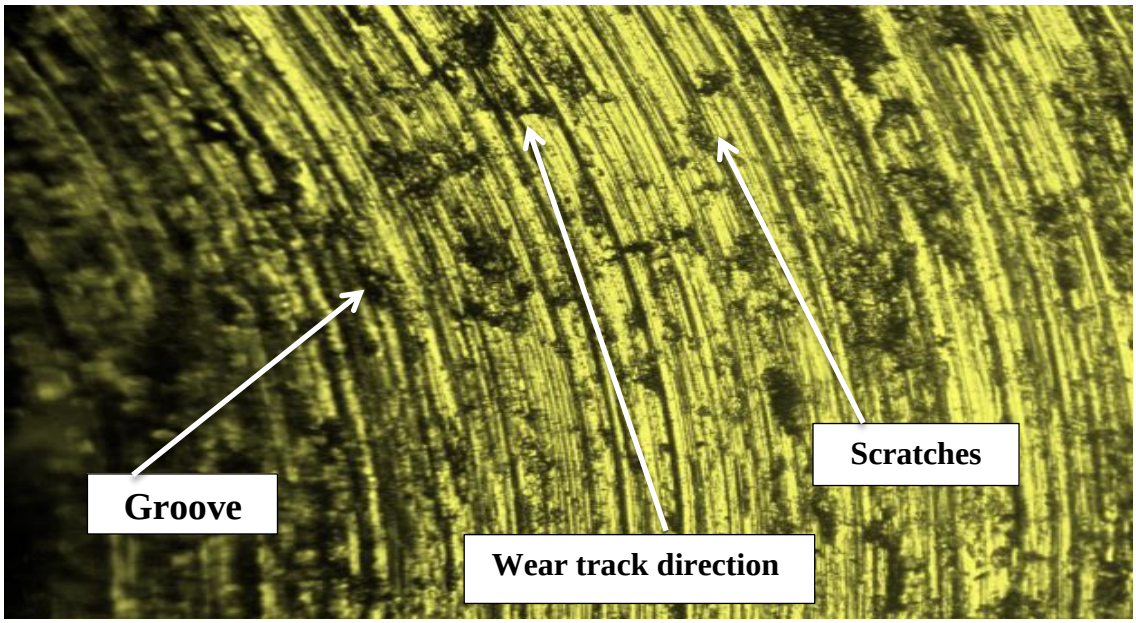

Figure (4-38): LOM images of DP1 specimen worn surface at 100X Magnification after Wear Test (15N, 30min).

4.6 Electrochemical Tests

4.6.1 Open Circuit Potential (OCP)-Time Measurement

The OCP-time was measured with respect to SCE Hank's solutions at (37)℃ ±1 for tested specimens. Figures (4-39) displays the evolution of corrosion potential of the alloys throughout time. The time period from (0 and stabilized at 160 min) and with interval of 5 min were potentially reported. The average of two specimens was adopted to evaluate the OCP of each measurement.

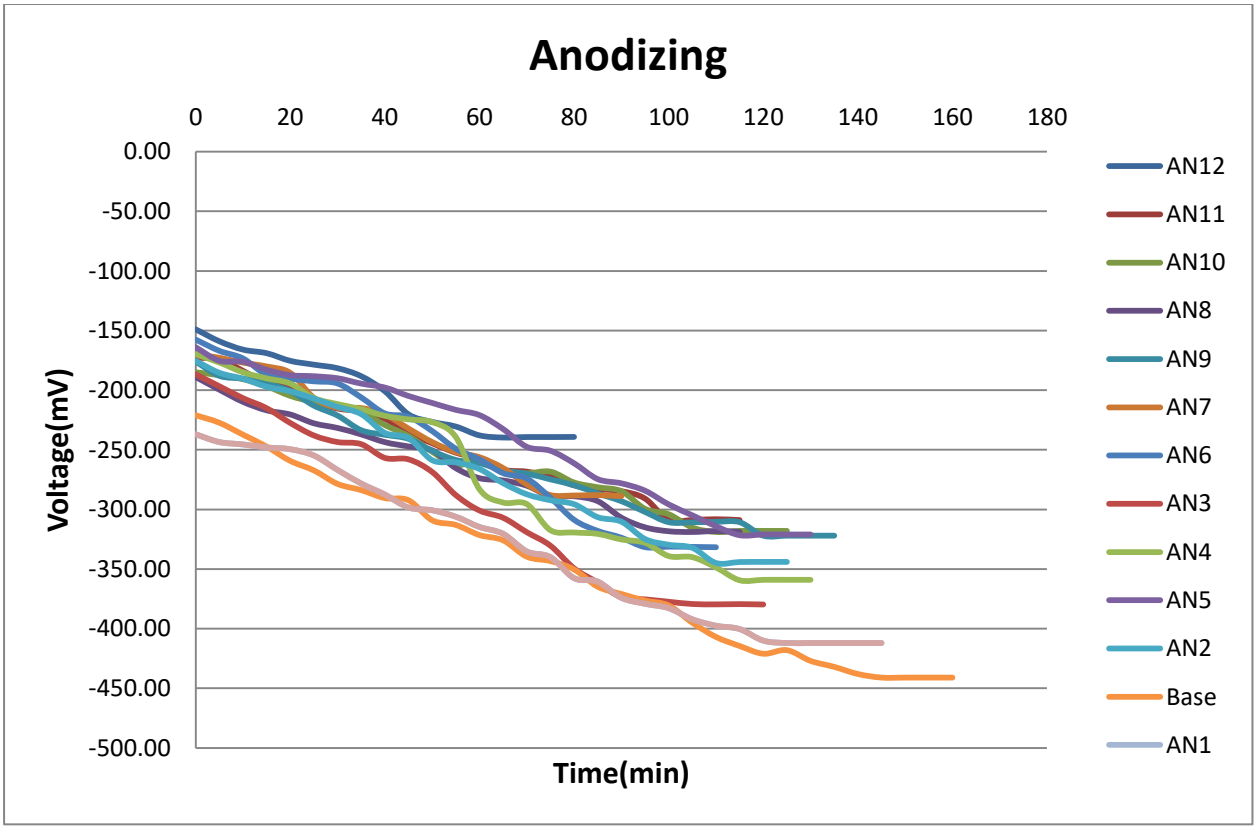

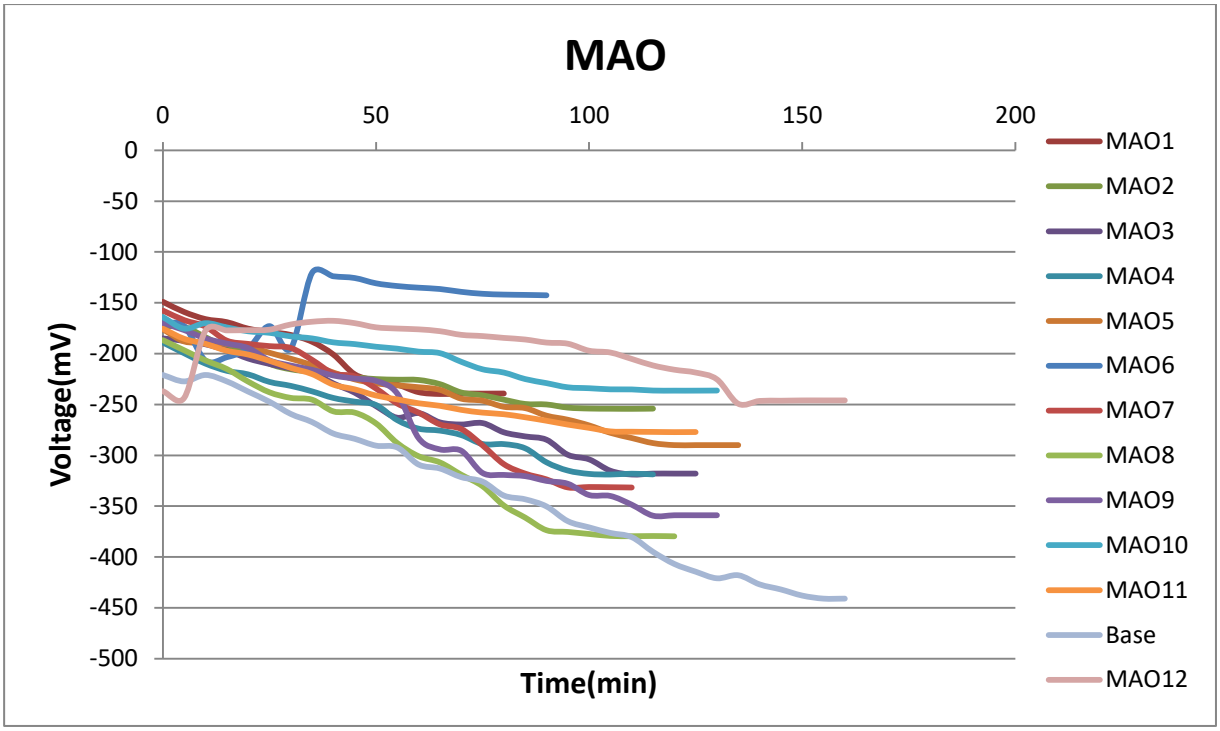

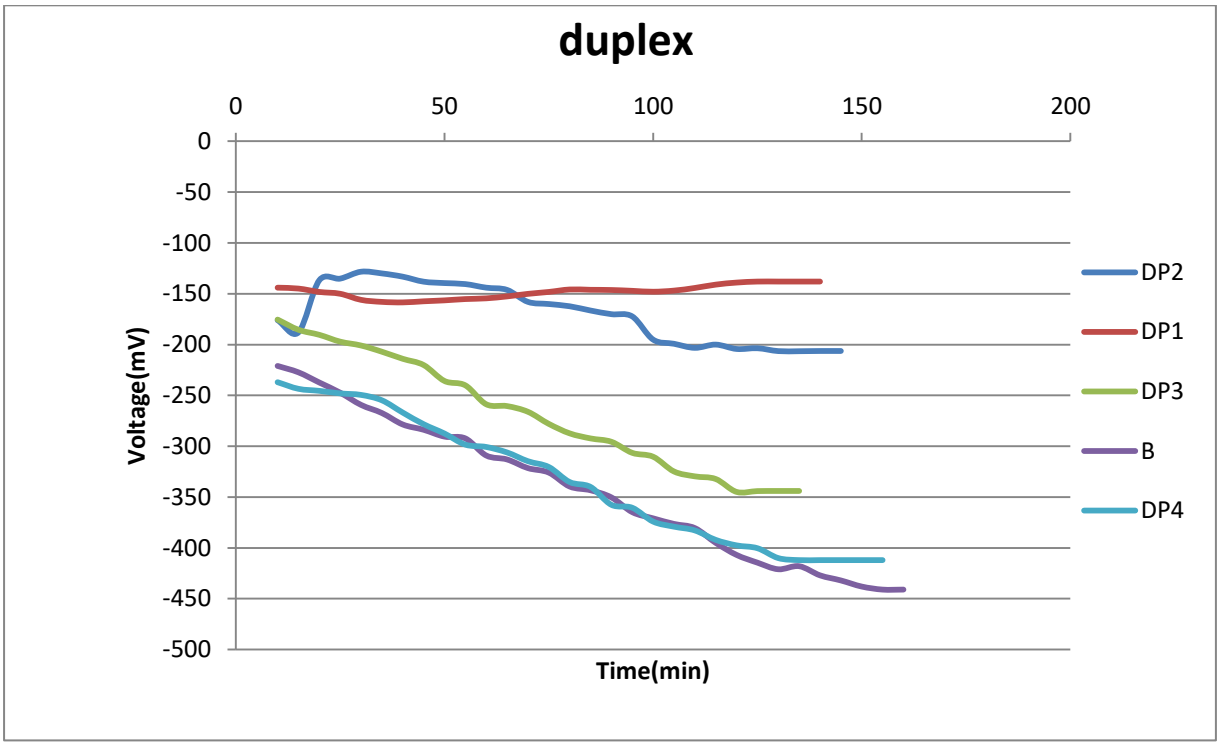

Figures (4-39): The OCP-Time in Hank's Solution at(37±1)℃.

Table (4-6): The values of OCP in Hank's Solution for anodizing process at(37±1)℃.

Specimens	Voltage(mV)
US	- 441
AN1	- 412
AN2	- 344
AN3	- 379.7
AN4	- 359
AN5	- 321
AN6	- 331.7
AN7	- 288.9
AN8	- 318.8
AN9	- 322
AN10	- 318
AN11	- 308.9
AN12	- 239.2

Table (4-7): The values of OCP in Hank's Solution for MAO process at(37±1)℃.

Specimens	Voltage(mV)
US	- 441
MAO1	- 412
MAO2	- 344
MAO3	- 379.7
MAO4	- 359
MAO5	- 321
MAO6	- 331.7

MAO7	- 288.9
MAO8	- 318.8
MAO9	- 322
MAO10	- 318
MAO11	- 308.9
MAO12	- 239.2

Table (4-8): The values of OCP in Hank's Solution for duplex processes at(37±1)℃.

Specimens	Voltage(mV)
US	- 441
DP1	- 138
DP2	- 206.3
DP3	- 344
DP4	- 412

In order to understand the stability of an alloy Zr in the solutions of the human body, it is necessary to know its behavior in the environment of body fluids, this is done by the open-circuit potential as time which is considered one of the specimen ways to study the formation of a protective layer and passivation of implants in Hank's solution. The above figures indicate a rising of potential towards the positive direction where the surface of the implant is covered with a protective scale.

4.6.2 Liner polarization Test

Anticorrosion properties of uncoated along with MAO coated substrates were verified on the basis of the results of liner polarization, where such test is valuable for estimating the electrochemical. Liner

polarization tests clarify the possibility of determining the values of corrosion parameters for example corrosion current density (Icorr.) corrosion potential (Ecorr.) and corrosion rate (CR) as shown in table (4-9) figures from (4-40) to (4-47) demonstrated the liner polarization curves of uncoated specimen ,coated specimen in mentioned solutions at 37±1 ℃ were illustrated in Tables (4-9) to (4-11). From figures (4-40), (4-414) and (4-42) which belong to (US), (AN) and (MAO) specimens respectively. There is a significant shift toward lower current densities with HA/ZiO_2 Composite coating .The liner polarization curves of specimen which coated by ZrO_2 only in solution .The corrosion resistance of treated Zr705 was significantly improved due to processes.

From Table (4.9), there is a significant improvement in corrosion resistance and $I_{corr.}$ for anodizing specimen graded from 5.972×10^{-6} (μA) for AN1 to 0.54×10^{-6} (μA) for AN12 which are lower than $I_{corr.}$ For B alloy which is 17.9×10^{-6} (μA). However the $E_{corr.}$ values for AN is graded from -277mV for AN1 to -73 mv for AN12 which are less than $E_{corr.}$ for B alloy which is -585 mV. The data listed in Table (4.9) shows significant an excellent improvement in corrosion resistance of AN and the $I_{corr.}$ of these specimen ranged between 0.82×10^{-6} (μA) for AN6 alloy and 0.54×10^{-6} (μA) for AN12. It can be noted that the $I_{corr.}$ of AN with HA additives is lower than that for each specimens.

Table (4-9): The values of Corrosion Current Density ($I_{corr.}$), Corrosion Potential ($E_{corr.}$) and Corrosion Rate for AN specimens in Hank's Solution at 37℃ ±1.

specimens	$I_{corr.}$ (μA)×10^{-6}	$E_{corr.}$ (mV)	Corrosion Rate(mpy)×10^{-6}	Improvement percentage%
US	17.9	-585	3.26	-
AN1	5.972	-277	1.089	66%
AN2	5.128	-450	0.935	71%
AN3	4.998	-379	0.9116	72%
AN4	1.222	-219	0.2228	93%
AN5	0.907	-100	0.1654	94%
AN6	0.82	-312	0.1495	95%
AN7	2.075	-461	0.3784	88%
AN8	1.785	-241	0.3255	90%
AN9	1.483	-140	0.270	91%
AN10	0.819	-165	0.1493	95%
AN11	0.78	-190	0.1422	95%
AN12	0.54	-73	0.98496	96.7%

From Table (4-10), it can be noted that the improvements of corrosion resistance for AN specimens are lower than those of MAO specimens. Also there is a noteworthy improvement in corrosion resistance for MAO with HA additives as compared with base alloy. An excellent improvement in corrosion resistant (MAO6-93%, MAO12-98%) as compared with the US specimen.

$I_{corr.}$ For specimen are graded from 6.843×10^{-6} (μA) for MAO1 to 0.33×10^{-6} (μA/cm²) for MAO12 which are more lower than $I_{corr.}$ for US which is around 17.9 (μA).However the $E_{corr.}$ values for MAO are graded from -386 mV for MAO1 to -34mv which are significantly lower than $E_{corr.}$ for US which is around -585 mV.

Table (4-10): The values of ($I_{corr.}$), Corrosion Potential ($E_{corr.}$) and Corrosion Rate for MAO specimens in Hank at 37℃ ±1.

specimens	$I_{corr.}$ (μA)×10^{-6}	$E_{corr.}$ (mV)	Corrosion Rate(mpy)×10^{-6}	Improvement percentage%
US	17.9	-585	3.26	-
MAO1	6.843	-386	1.248	61%
MAO 2	4.908	-94	0.895	72%
MAO 3	4.304	-150	0.785	75%
MAO 4	2.133	-92	0.389	88%
MAO 5	1.21	-84	0.220	93%
MAO 6	1.057	-82	0.192	93%
MAO 7	4.229	-431	0.771	76%

MAO 8	2.14	-135	0.390	88%
MAO 9	1.891	-4	0.344	88%
MAO 10	0.395	-288	0.072	97%
MAO 11	0.310	-129	0.056	98%
MAO 12	0.33	-34	0.0601	98%

Table (4-11): The value of ($I_{corr.}$), ($E_{corr.}$) and Corrosion Rate for Dp specimens in Hank at 37℃ ±1

specimens	$I_{corr.}$ (μA)×10^{-6}	$E_{corr.}$ (mV)	Corrosion Rate(mpy)×10^{-6}	Improvement percentage%
US	17.9	-585	3.26	-
DP1	0.109	-260	0.198	99.4%
DP2	0.35	-296	0.063	98%
DP3	0.44	-329	0.08	97.5%
DP4	0.18	-270	0.032	99%

The current result in this study are in a good agreement with those in literature [154, 155]. It was found that the corrosion rate is closely related to the voltage, the corrosion rate decreases with the increase in the voltage, that is, an inverse relationship. In our study, from the above tables, it can be seen that there is an obvious decrease in the corrosion current density and corrosion rate for specimens AN6, AN12, MAO6, MAO12, DP1 in Hank's solution.These results indicate stability behavior

of HA/ ZrO_2 composite coating layer , so with increase of concentration of coating material the corrosion resistance increase.

Also, it can be noticed the improvement of corrosion resistance due to increase of surface roughness because the presence of HA precipitates closed the porous and prevent harmful ions to pass through it [154]. Along with an improvement of corrosion resistance, this HA/ ZrO_2 coating is able to change the properties of the surface on the materials without affecting the properties of the bulk [155].

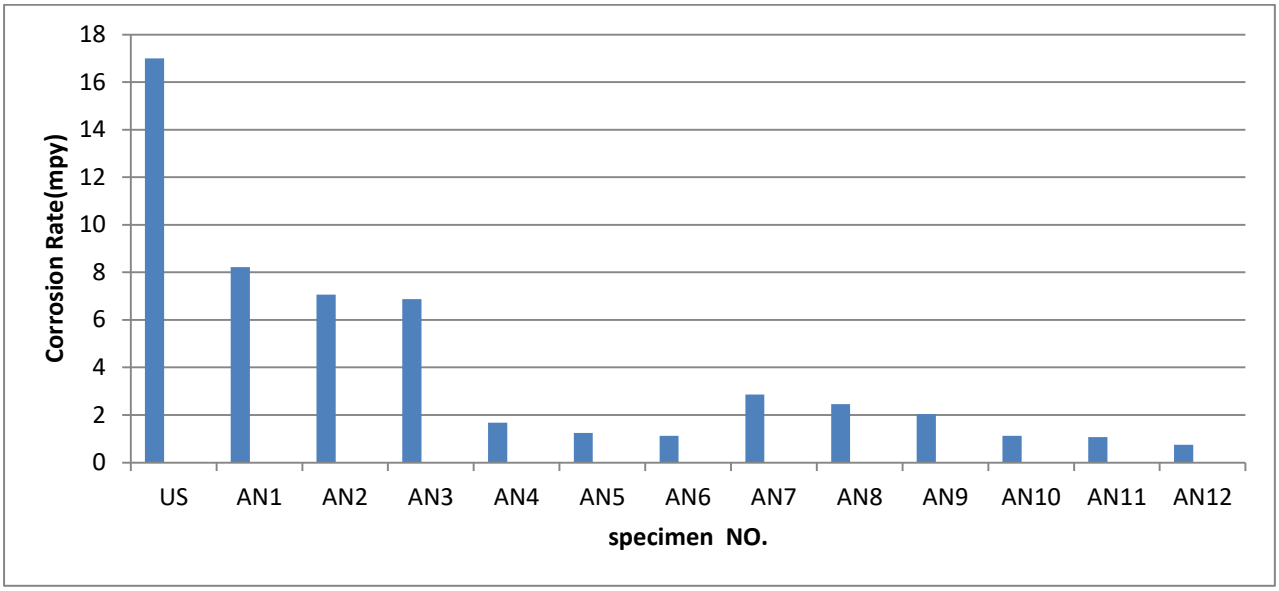

Figure (4-40): Corrosion Rate for all specimens Used in Anodizing in Hank at 37℃ ±1.

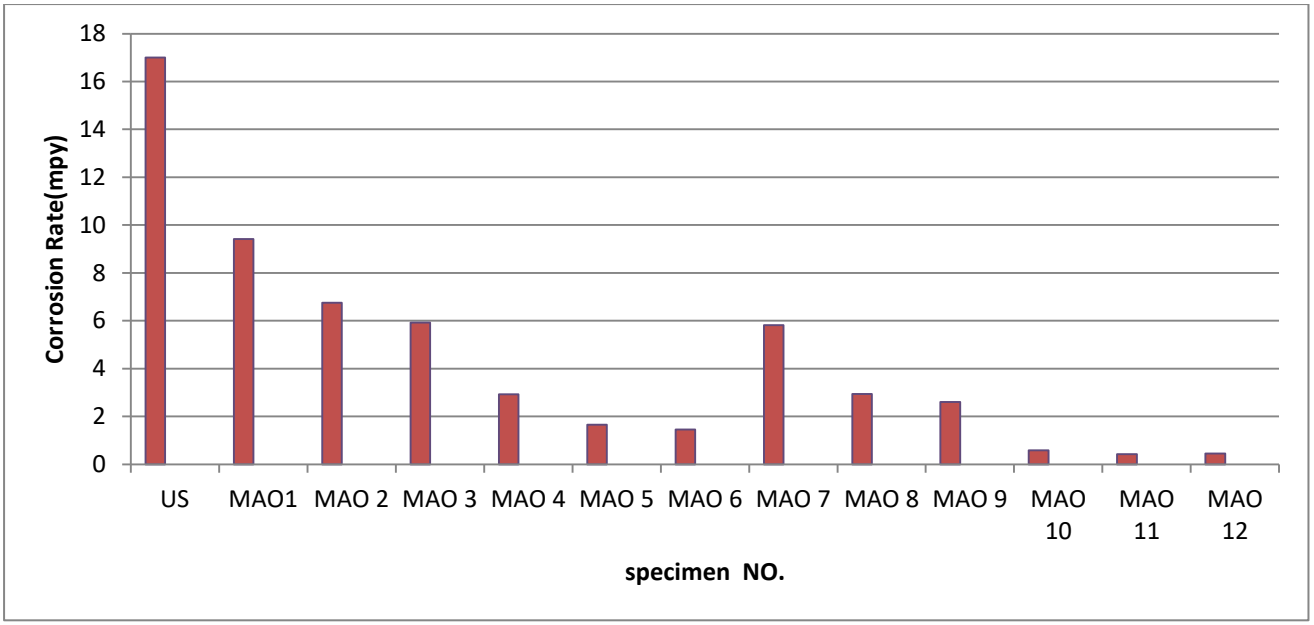

Figure (4-41): Corrosion Rate for all specimens Used in MAO in Hank at 37℃ ±1.

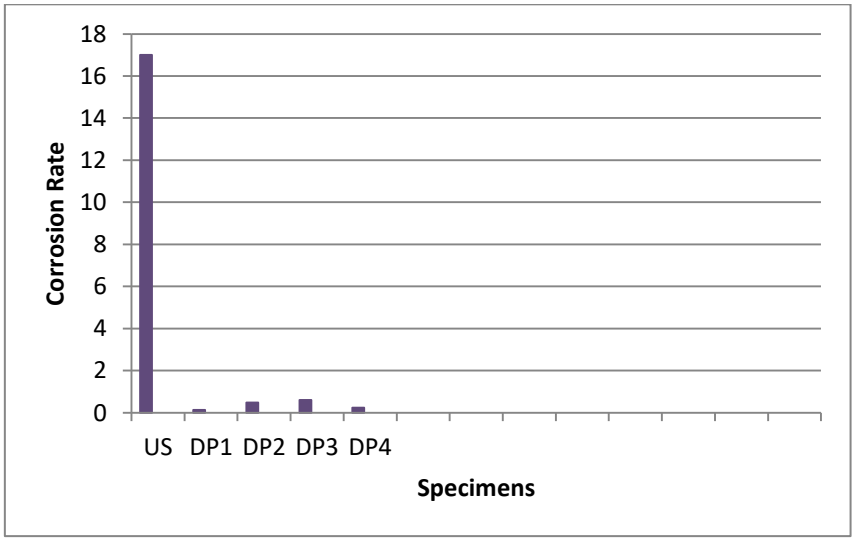

Figure(4-42): Corrosion Rate for all specimens Used in duplex in Hank at 37℃ ±1.

Tables (4-12), (4.13) and (4.14) show an improvement in the corrosion resistance of the Zr705 in Hank's solution. The corrosion current and calculated corrosion rate are relatively measures of corrosion and illustrate how much material is lost during the corrosion process .Hence, the higher current density and calculated corrosion rate cause more materials lost . HA/ ZrO_2 composite coating can reduce corrosion rate of the coating implant in human body, hence reduce the metallic ions release .Properties of HA gave a useful application in coating of porous metallic implants. After implantation of prostheses, a close surface contact between the metallic prosthesis and the surrounding bone tissue is needed for subsequent bone ingrowths. The presence of HA in the coating of the metallic implant leads to a rapid bonding between HA and surrounding bone tissue. Its application in coating implants combines the strength and toughness of the substrate with bioactive characteristics of HA which can induce the surrounding bone tissue ingrowths and future formation of chemical bonding.

The improvement percentage of HA/ ZrO_2 composite coating for (Dp1)specimen in Hanks solution are increased than the other coating specimens in different parameters .The best improvement percentage for specimen is (99.4%) for (DP1) specimen.

Figures (4.43-4.47) shows the liner polarization curves for the Zr705 substrate and ZrO_2 coated by anodizing, and MAO processes samples in the Hank's solution at 37°C±1 for a different applied voltages and time. The decreases corrosion potential of the specimens is obtained and this result has the corrosion rate improvement equal to (95% for sample AN6 and 93% for MAO6). Porosity affected the corrosion behavior of highly porous with high voltage where decreased corrosion resistance because increased $i_{corr.}$ and C_R .

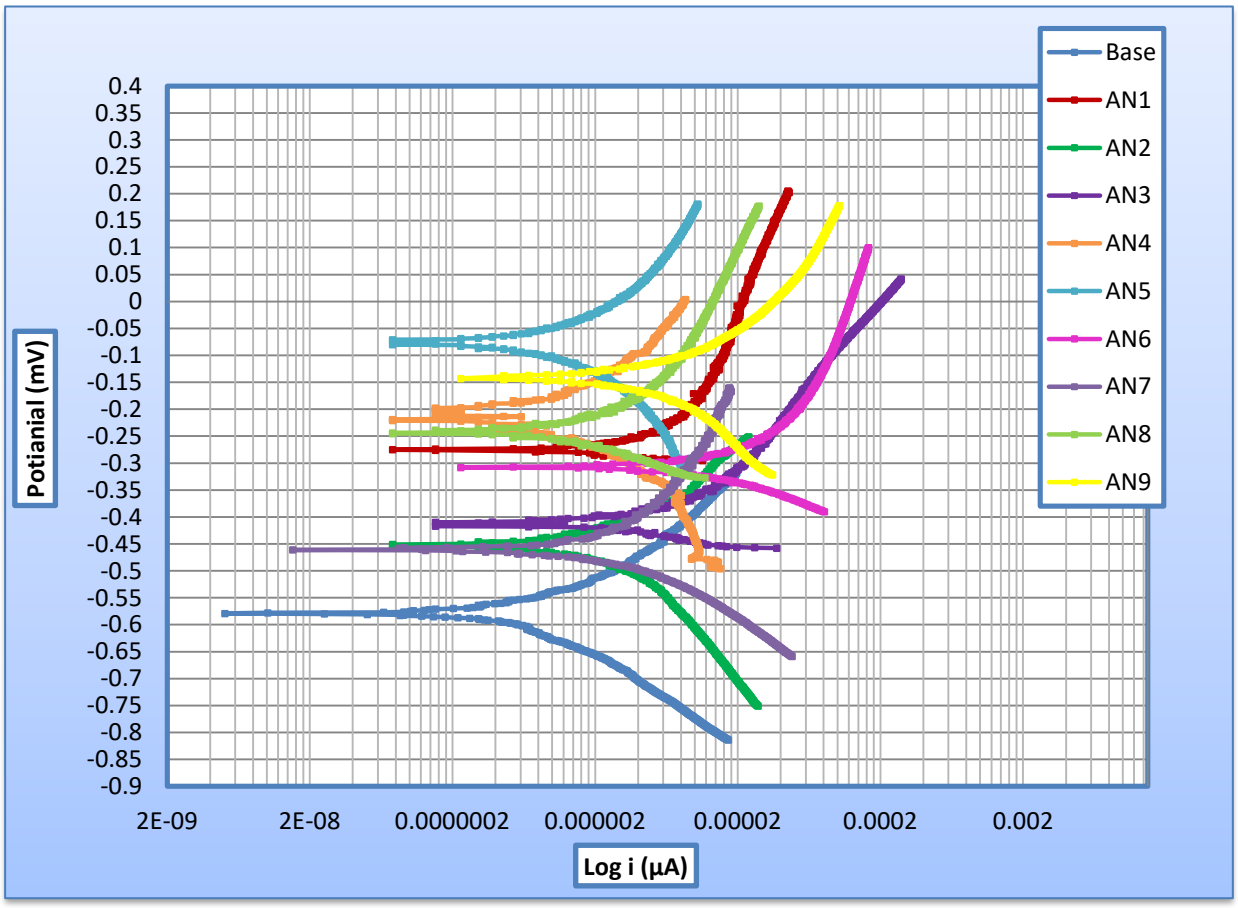

Figure (4.43) : Liner polarization curves of ZrO_2 coated by anodizing process

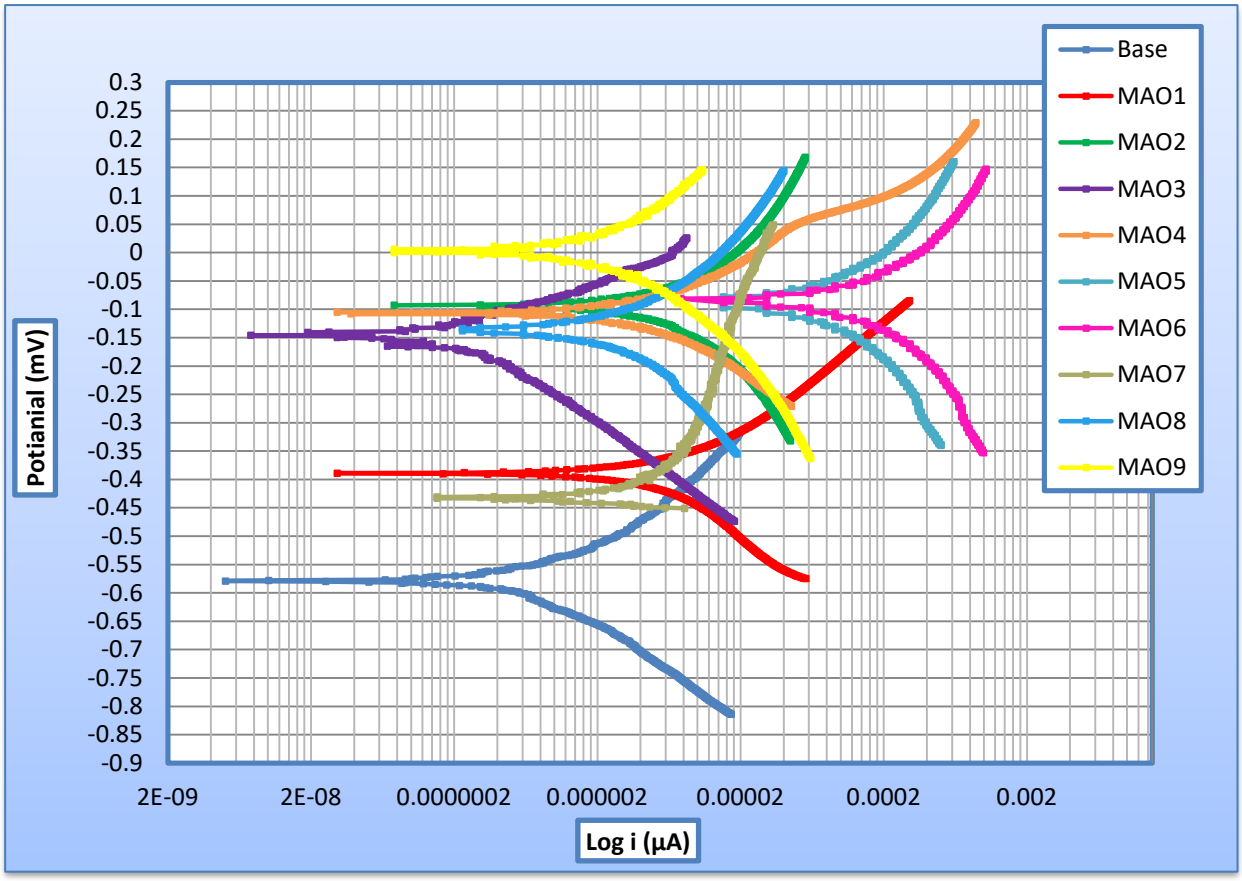

Figure (4.44) : Liner polarization curves of ZrO_2 coated by MAO process.

The liner polarization curves of the composite ceramics HA/ZrO_2 coating by anodizing and MAO processes with different content of additive in the Hank's solution in Figures (4.45-4.47) respectively, and showed coating provides a protective layer on the substrate surface that would reduce the corrosion rate (C_R) and current density ($i_{corr.}$) and increased corrosion potential ($E_{corr.}$).These results indicate stability behavior of HA/ZrO_2 composite coating layer, so with increase of concentration of coating material the corrosion resistance increases. Along with an improvement of corrosion resistance, this HA/ZrO_2 coating is able to change the properties of the surface on the materials without affecting the properties of the bulk [160].HA/ ZrO_2 composite coating can reduce corrosion rate of the coating implant in human body, hence reduce the metallic ions release .

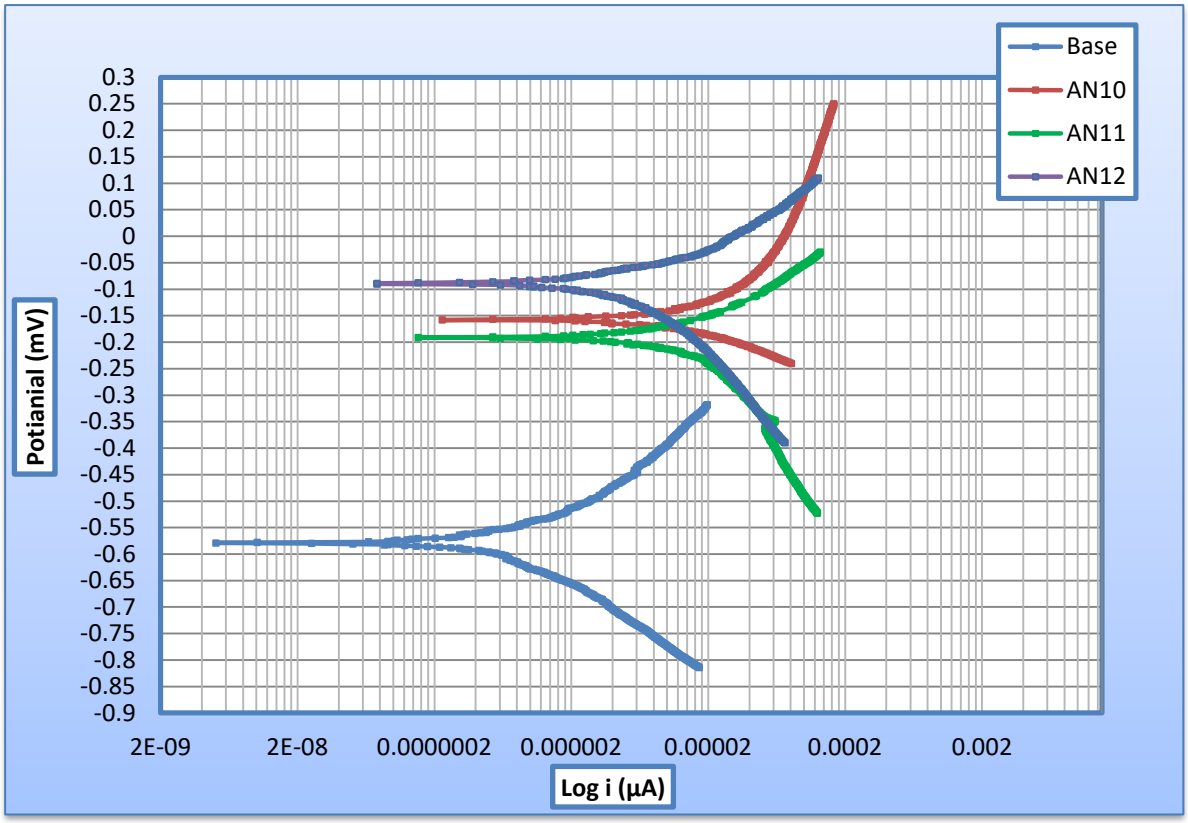

Figure (4.45) : Liner polarization curves of HA/ZrO_2 coated by anodizing process.

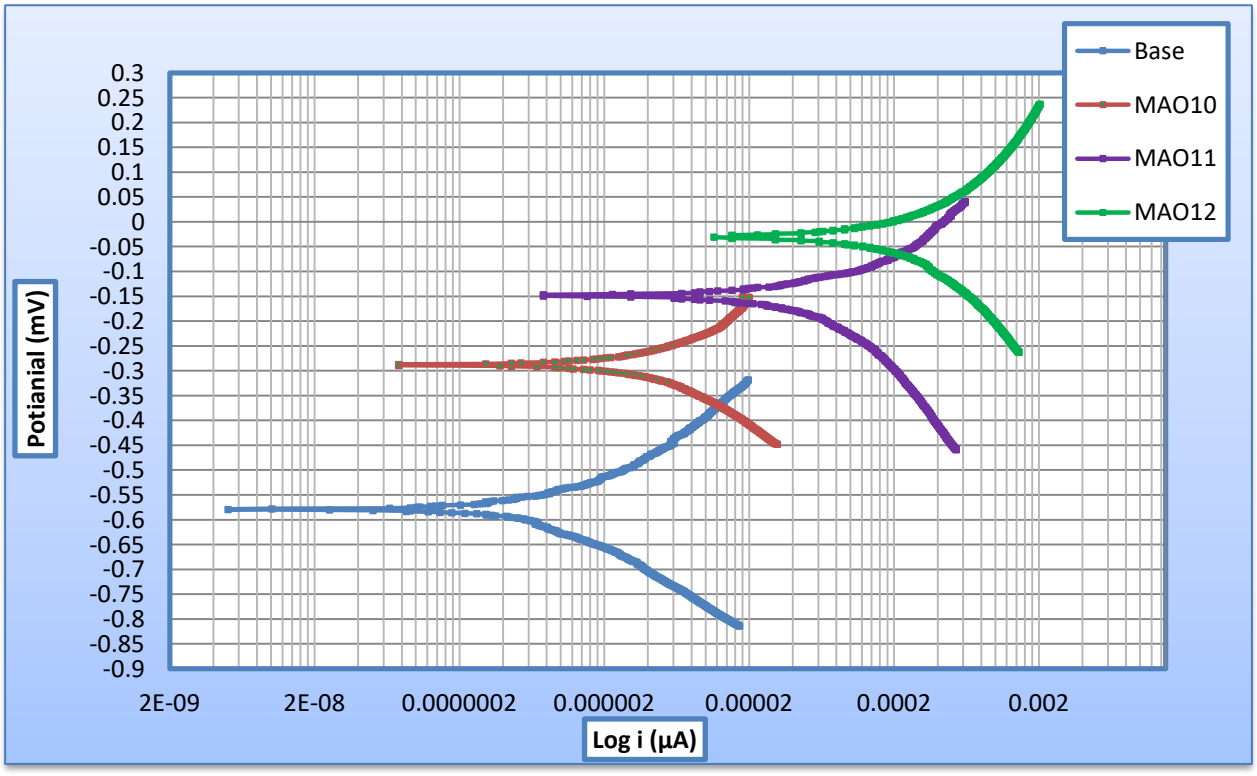

Figure (4.46) : Liner polarization curves of HA/ZrO_2 coated by MAO process.

Figure (4.47) illustrate the liner polarization curves for duplex process specimens in Hank's solution for a different deposition conditions. There are a clear improvement in the polarization behavior after coating in the values of $E_{corr.}$, $i_{corr.}$ and C_R.

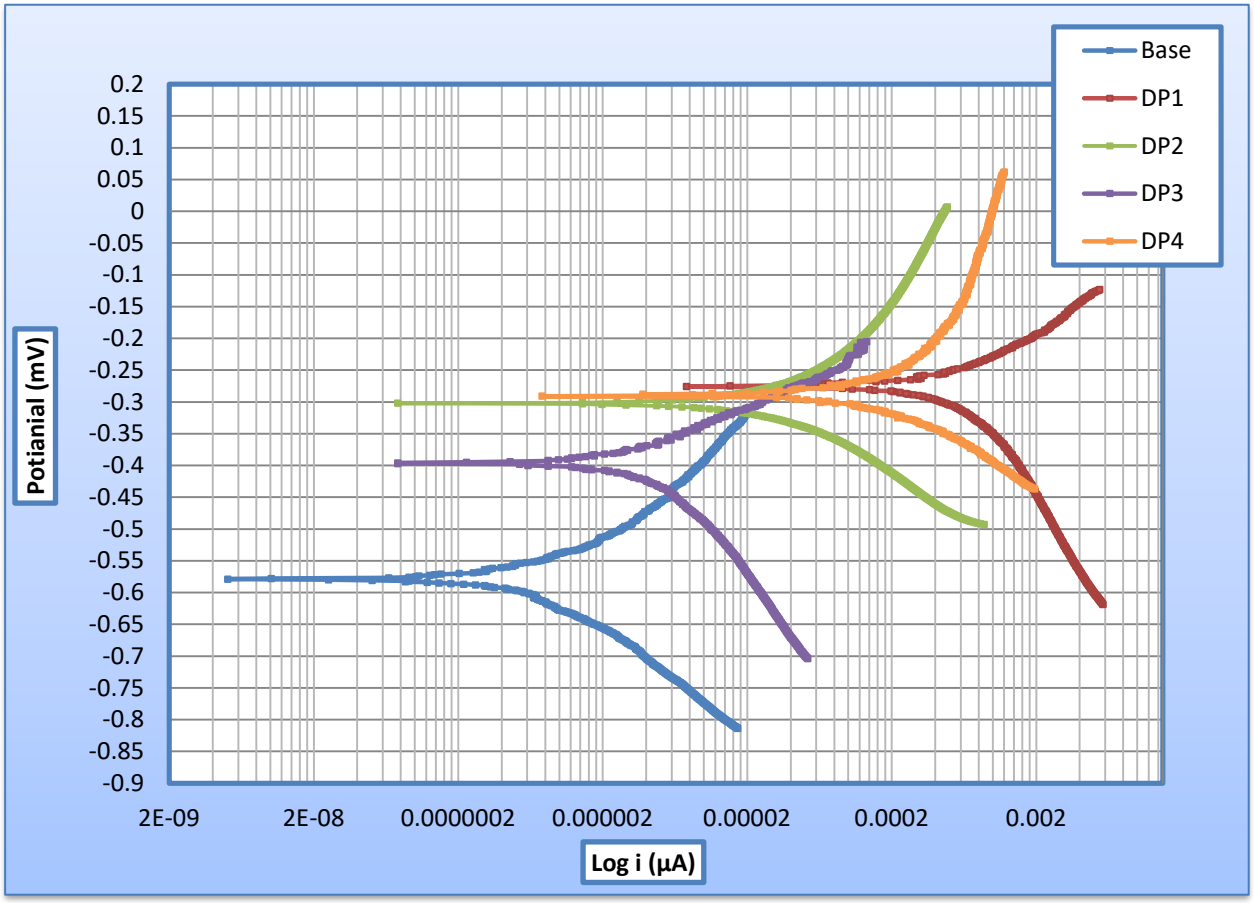

Figure (4.47): Liner polarization curves of duplex process and base at different conditions.

Finally, composite ceramic coating HA/ZrO_2 prepared by duplex process is to increasing the biocompatibility whereas anodizing and MAO processes are to enhance the corrosion behavior of the base metal. The corrosion progressed in the passive regain for the specimen coated with single layer more than uncoated one while the specimen coated with composite layers was quite effective against further corrosion due to the formation of stable oxide layer.

It should be noted that in the medical applications, the presence of small amount of porosity is necessary for ingrowth the bone tissue toward the coating to produce efficient implant fixation.In the other word, the presence of porosity is advantageous as it enhances the osseointegration as a result of its bonding capability is improved to the metallic implants. However, the high porosity level will consider as a source for penetrating large amount of body fluid to the human body and become harmful. Increasing the porosity level also has a negative influence on the mechanical properties, especially on bond strength, which will in turn lead to an easy fracture. Therefore, it proposes that the porosity level of the coatings must be well balanced to achieve the optimum mechanical and biological performance [161].

4.6.3 Cycle Polarization Test

The increased ion release rate due to different forms of localized corrosion, may lead to a series of undesirable biological responses and eventually, implant loosening. Susceptibility to these forms of corrosion is evaluated by cyclic polarization. The parameters obtained from the current-voltage curve can be associated with the localized corrosion mechanism. Typically, the reading starts at the open circuit potential and scans upwards until breakdown is attained. Then the direction of scan is inverted after specific amount of localized corrosion is established and the passive film is damaged [169]. The potential at which stable pit formed is called breakdown potential (E_b) or pitting potential (E_p). Consequently, the E_p implies the potential over which the pits initiated and developed. If the E_p is high, the material has high resistance to the pitting corrosion. The difference (ΔE) between E_p and E_{prot} will give an indication to the corrosion resistance of the sample, where the smaller ΔE value mean the highest corrosion resistance.

Figures (4.48-4.50) show the polarization curves o for US and coating by MAO, and duplex processes in Hank's solution. Significant differences were observed between the curves obtained for each sample. For US, has the lowest E_p and E_{prot} value compared to the susceptibility to pitting corrosion of the ZrO_2/HA specimens treated by MAO duplex processes. The cyclic polarization curves obtained as noted in the Table (4.13), the extent of the hysteresis loop is highly reduced and therefore, the corrosion mechanism operating on the substrate surface is less active when coating.

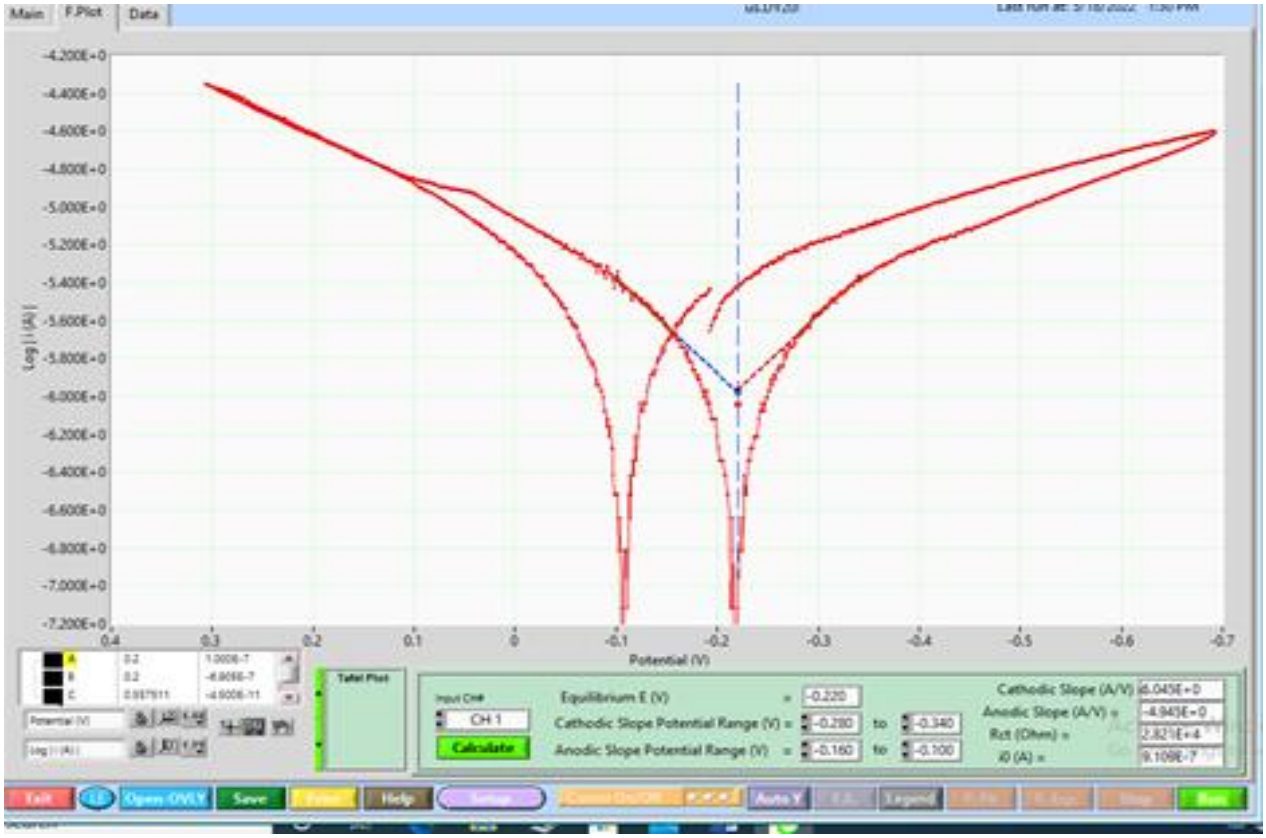

Figure (4.48): Cycle polarization curves of US of Zr705 .

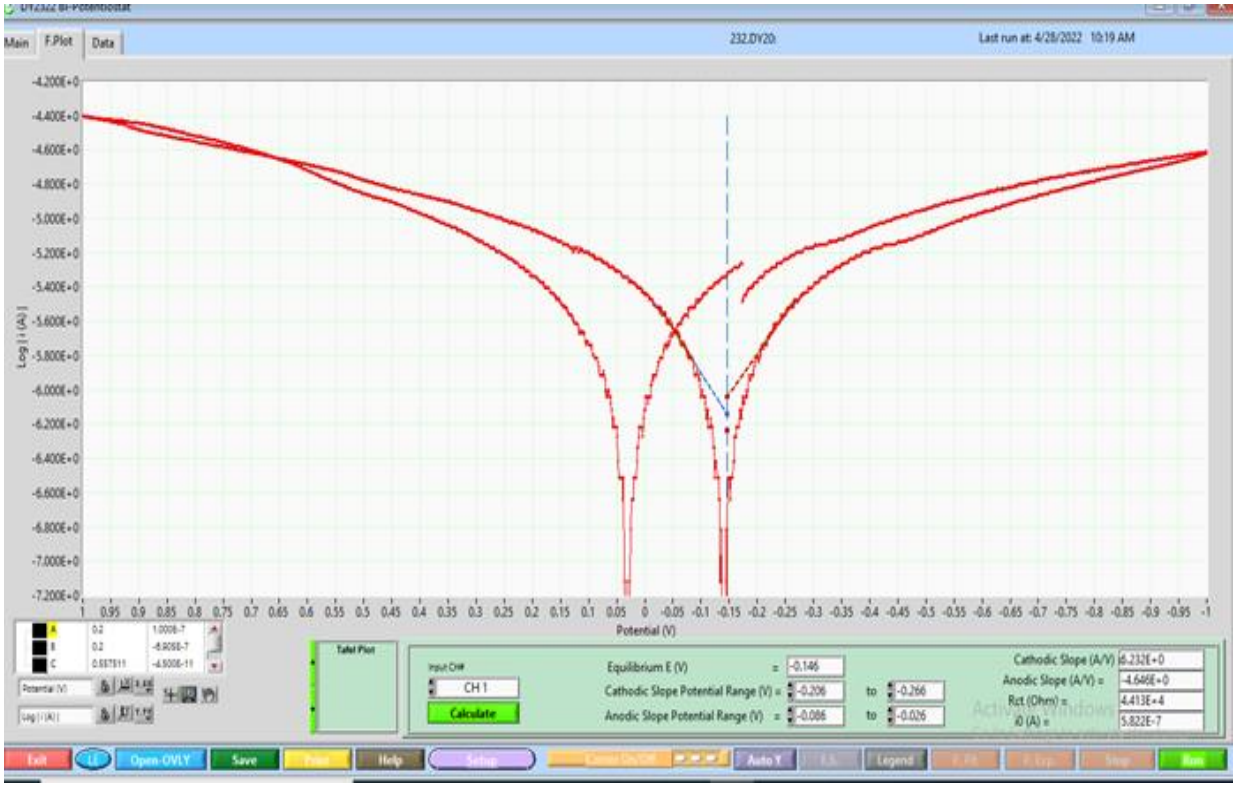

Figure (4.49): Cycle polarization curves of MAO12 on Zr705 by MAO process.

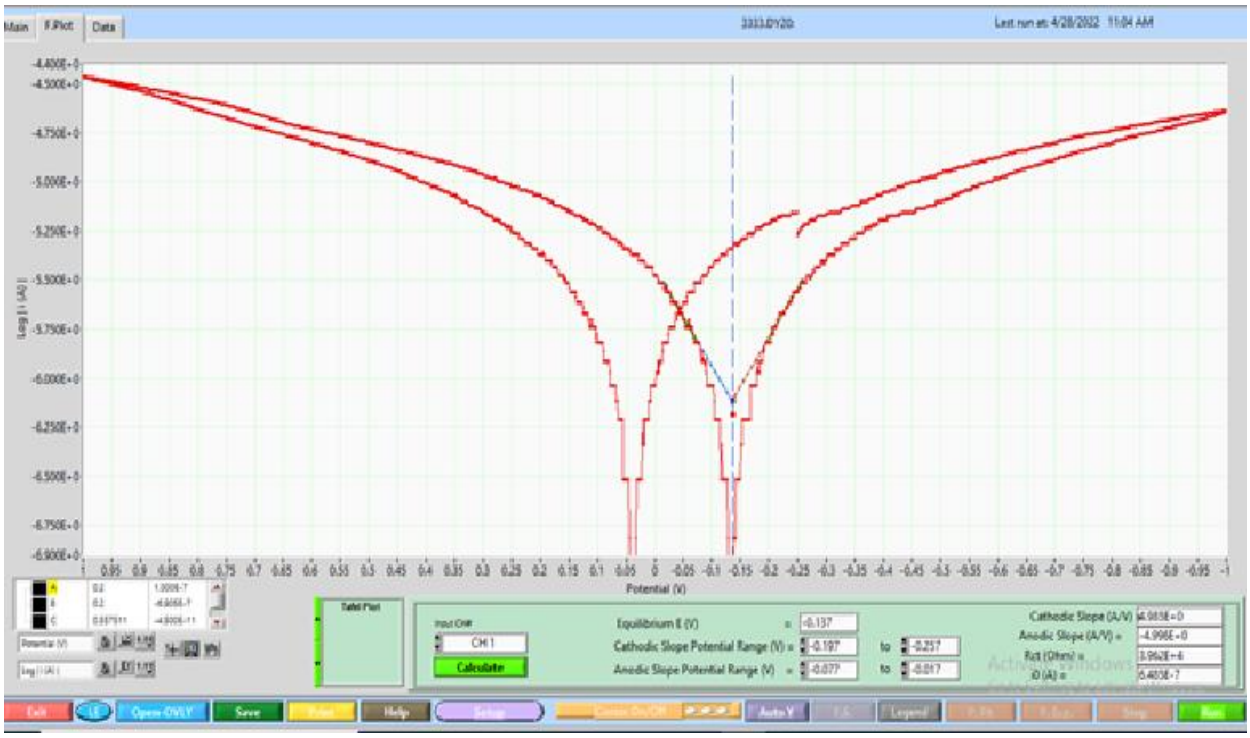

Figure (4.50): Cycle polarization curves of DP1 on Zr705 by duplex processes.

Table (4.13): Values of electrochemical parameters of Zr705 at different processes in Hank's solution from cyclic polarization.

Specimens Code	$E_{p.}$ (mV)	E_{prot} (mV)	$\Delta E = (E_p - E_{prot})$ (mV)	Improvement percentage (%)
US	100	-150	250	/
MAO12	650	-50	700	180
DP1	1000	-50	1050	320

4.7 Contact Angle Test Result

Contact angle is an important measurement method to evaluate material surface wettability, and materials with better wettability present lower contact angles in hank solution.

Table (4-14) and figures from (4-51) to (4-54) shows the results from contact angles for different specimens of ZrO_2 by anodizing, MAO, and duplex coatings prepared at various voltages and deposition times in hanks solution.

The contact angle of the specimens decreases dramatically after treatment with increase of surface roughness and porosity. The contact angle reached value to (77.8° for specimen US in Hank's solution) and decreased with increase voltage and deposition time reached to (0° for specimen MAO6, MAO11, and MAO12 in Hank solution). The increase wettability of the MAO treated because a large amount of pores formed on the oxidation coating surface caused its specific surface area to increase, which benefited water retention, MAO processing resulted in an uneven coating surface, increased roughness, increased absorbability, and decreased contact angles, all of which together affected the surface energy; and the OH and O_2 oxygen-containing groups formed on the

coating surface effectively introduced hydrophilic groups, changing the number of polar groups on the coating surface and causing surface polarity to increase, resulting in an increase in the surface energy [158].

Table (4- 14): Contact angle at Hank solution.

Code Specimen	CA/deg.
US	77.8
AN6	56.5
AN10	46.4
AN11	34.7
AN12	41.96
MAO6	0
MAO10	0
MAO11	0
MAO12	19.5
DP1	15.69

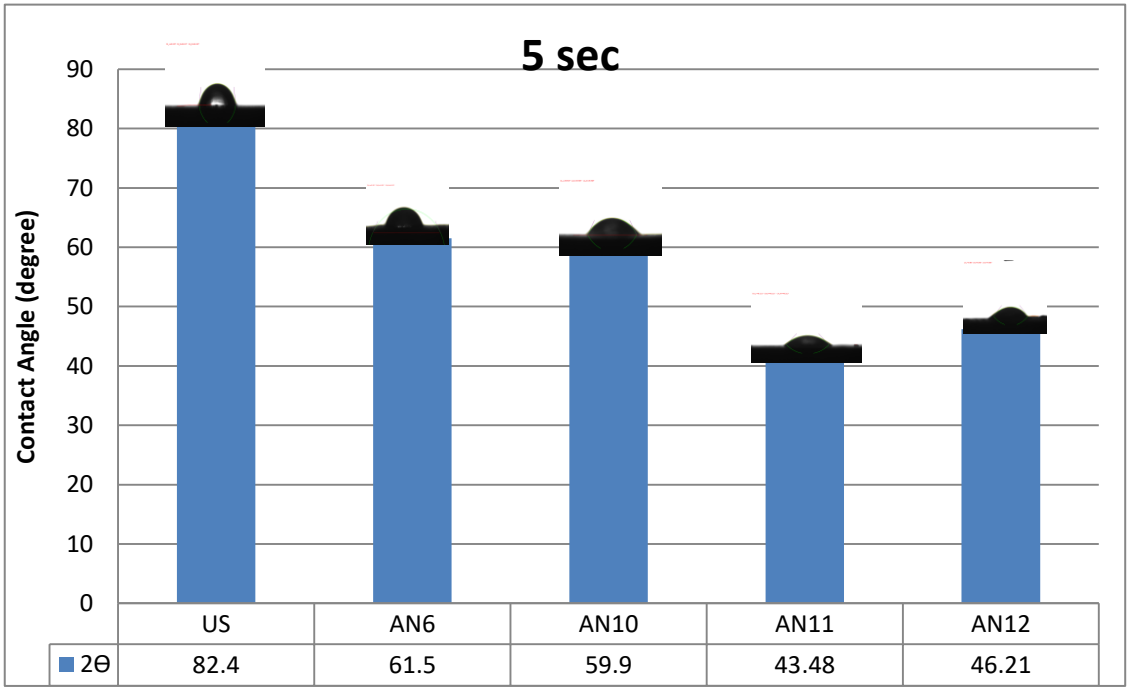

Figure (4-51): Results of contact angles after 5 sec anodizing.

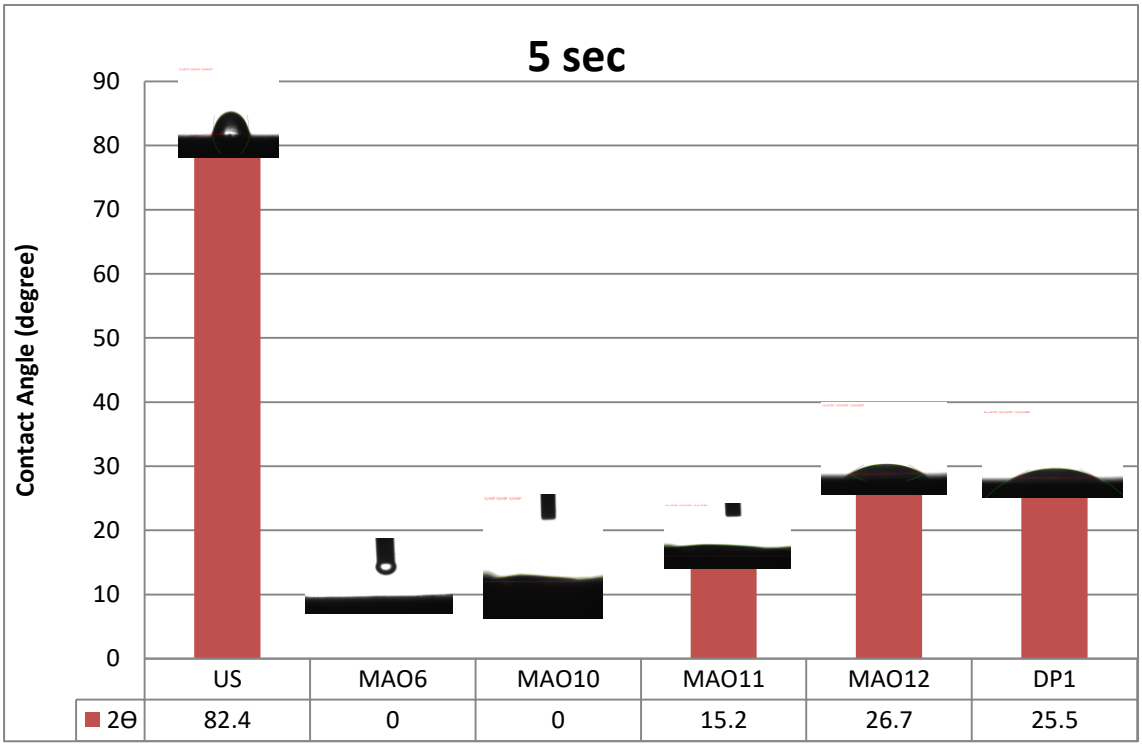

Figure (4-52): Results of contact angles after 5sec MAO and duplex process.

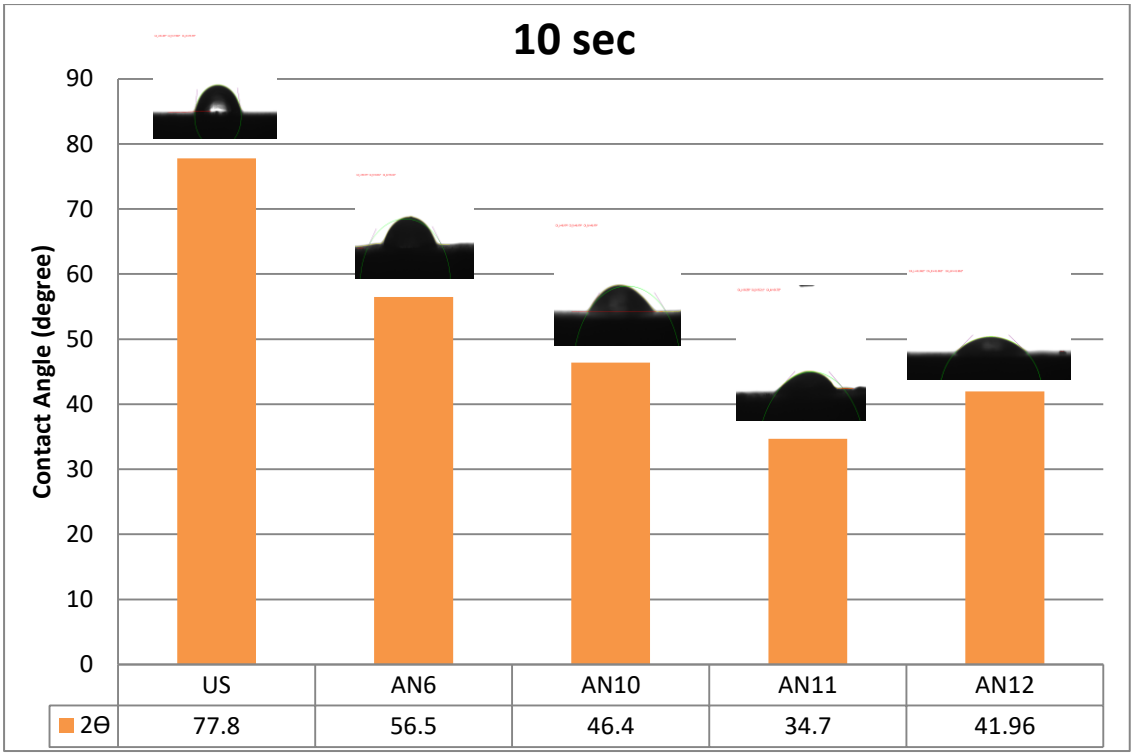

Figure (4-53): Results of contact angles after 10 sec anodizing processes.

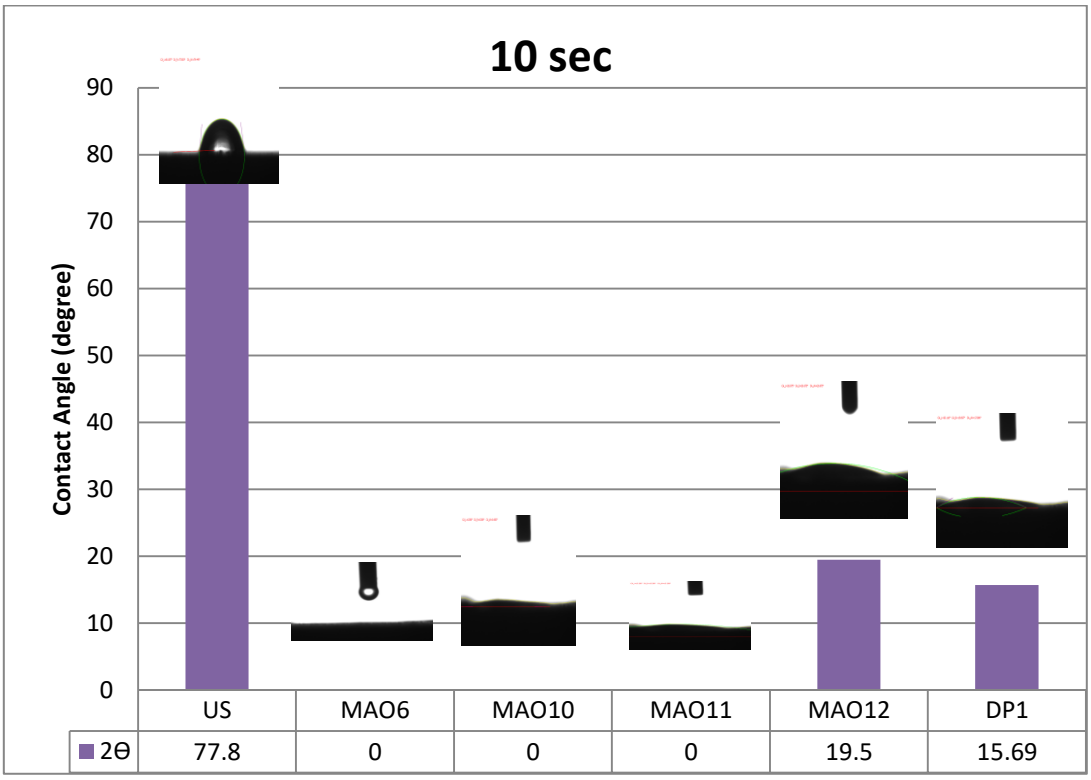

Figure (4-54): Results of contact angles after10 sec MAO and duplex processes.

4.8 Metals Ions Release Test Results

Releasing of metal ions from the orthopedic implant within surrounding tissue by a variety of mechanisms, involve wear and corrosion such as corrosion fatigue, stress corrosion, fretting corrosion, etc.Furthermore, the use of two solutions (Hank's solution) to perform the immersion tests of Zr705 is essential to get quantitative data necessary for selection appropriated materials in accordance with a variety of medical usage condition. Figure (4-55) show the amount of Zr ions released after immersion in Hank's solution for 3 weeks at 37℃ ±1.

Element of Zr705 was measured for coated and uncoated specimens by using atomic absorption spectrometry in Hank's solution at 37°C for 3 week. Zr ion release concentration in Hank’s solution, the US specimen is (0.0229ppm). The lowest corresponding numbers of AN12 (0.0217ppm) and at MAO12 equal (0.0209ppm) and finally DP1 reduced to (0.0193ppm).

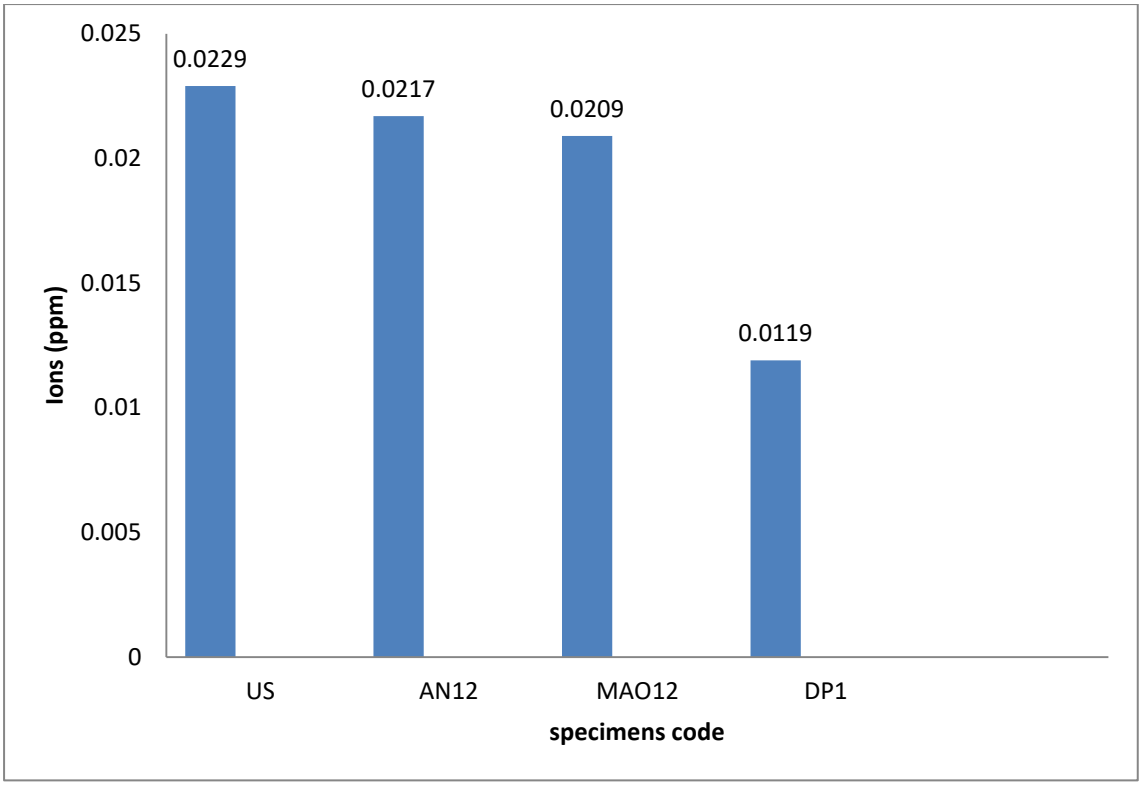

Figures (4.55): Amount of Zr ions released after immersion in Hank's solution for 3 week at 37℃ ±1.

4.9 Antibacterial

The antibacterial activities of the specimen surfaces were examined by agar diffusion .The test results are shown in figure (4-56) and (4-58). The minimum inhibition area was obtained for both strains with specimen surfaces. The surface of AN12, US showed regions of inhibition against E. coli and S. aureus, respectively. It has been observed that MAO12, DP1 the areas of inhibition obtained against bacteria increased.

In order to increase its solubility and usability, the ZrO_2 and HA is a straight-chain polymer. ZrO_2, which is physically, chemically and biologically compatible, is known to have medical activities such as antidiabetic, antimicrobial, antioxidant and antitumor. It is reported in the literature that many materials coated with ZrO_2 and HA exhibit different levels of antibacterial properties. Composite materials exhibit strong antimicrobial activity against E. coli, S. aureus [159].

E.Coli	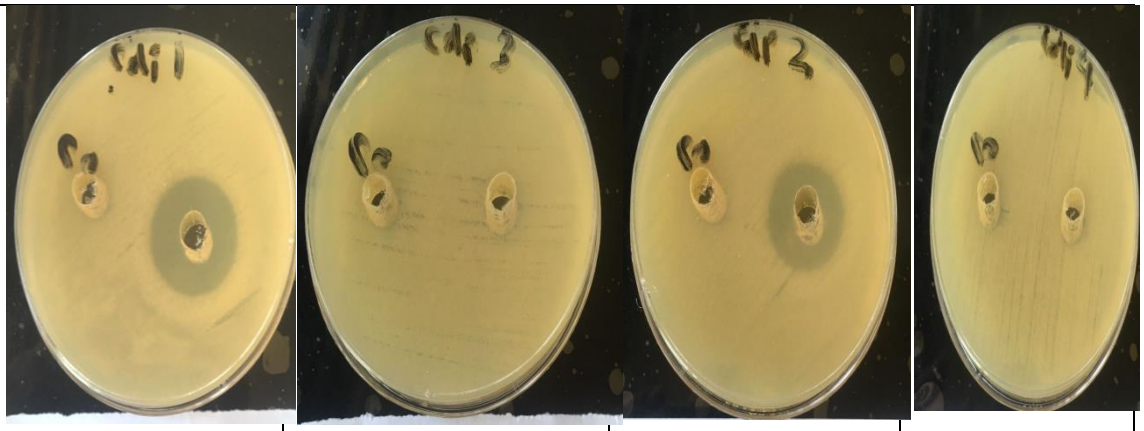			
	DP1	US	MAO12	AN12
Cont.	0	0	0	0
100%	22	0	19	0

Figure (4-56): The antibacterial activities of the specimen surfaces in E.Coli.

S. aureus	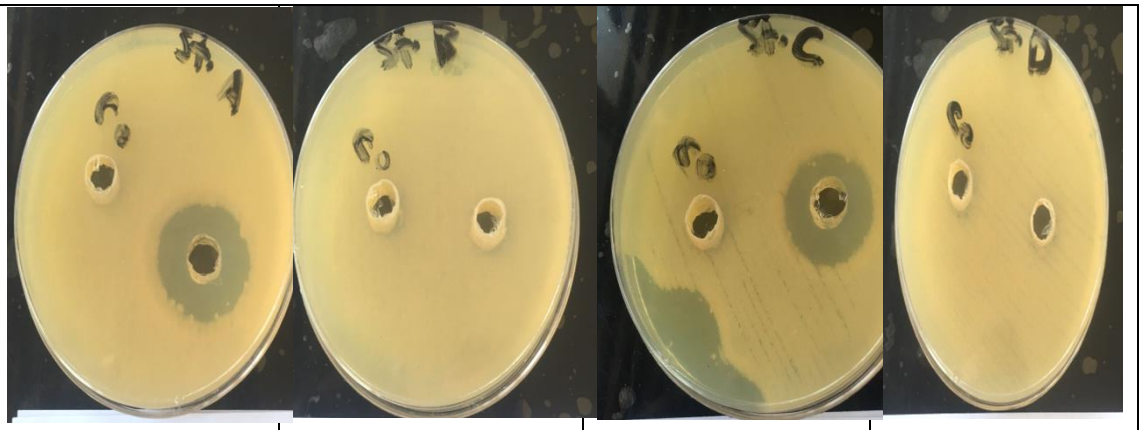			
	DP1	US	MAO12	AN12
Cont.	0	0	0	0
100%	24	0	20	0

Figure (4-57): The antibacterial activities of the specimen surfaces in *S. aureus*.

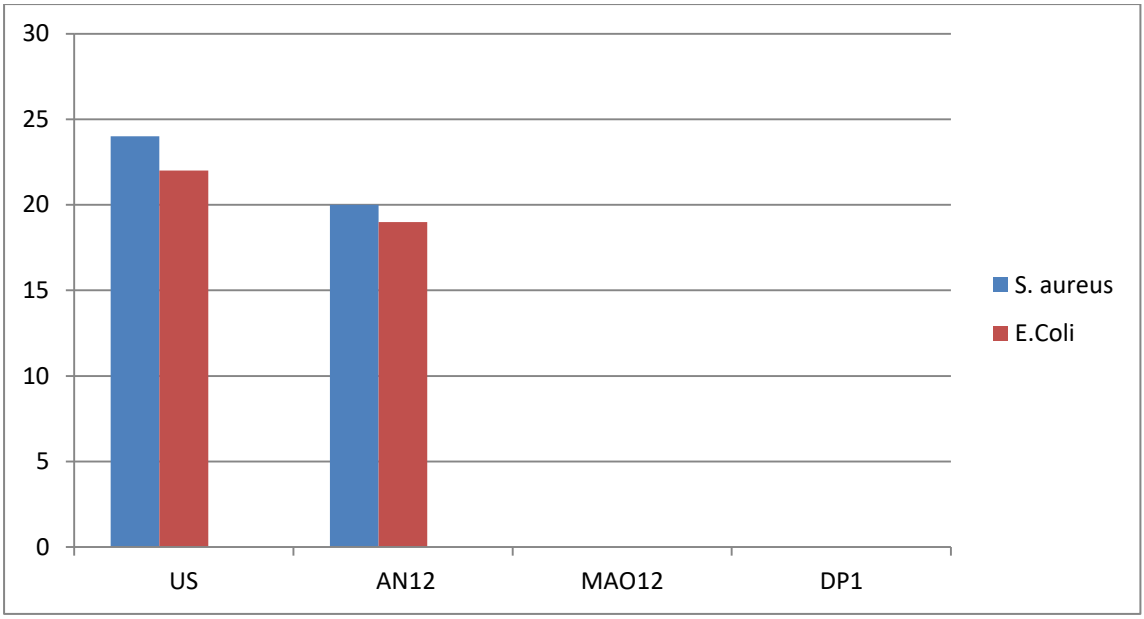

Figure (4-58): The antibacterial activities of the specimen surfaces.

4.10 Results of Coatings Thickness

The results of coating thickness and hardness at different processes are shown in figure (4-59). In the present study, the coatings thickness varied with the type of the processes, voltage, and deposition time. It can be observed that the coating thickness varied from (12 to 56.1 μm) and the highest thickness value could be recorded after the duplex process (56.1 μm for specimen DP1).

Generally, it can be seen that the coating thickness increased with increasing deposition time and increasing the voltage. Because the porosity of the coatings decreased, these results are good agreement with [154]. Such behavior is depend on the components of the electrolyte, the electrolyte resistance, PH for different electrolytes, sparks, and the chemical reactions. Most likely, during the early stage, the specimen geometrical dimensions, increase with oxidation, where after such dimensions will not increase.

The formation number of oxide is relatively, increased in a unit time, promoting the growth rate of ceramic coatings, but when the thickness increase to a certain limit, the cathodic voltage constrained to break down the coatings [155].

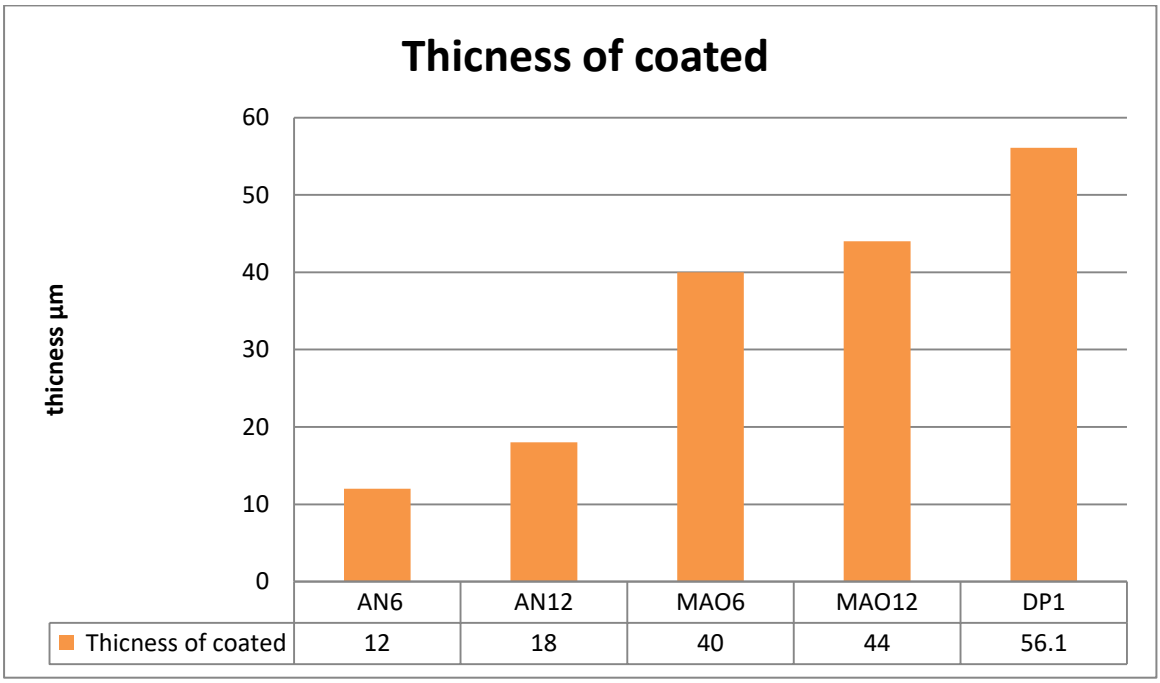

Figure (4-59): Coating thickness at different processes.

The AN6 and AN12 were lowest voltage (30V) have lowest thickness .The thickness increasing in MAO because increase the voltage (200V).The thickness results could prove the success of the present study in using duplex process with HA, in deposition of ceramic layers with thickness (56.1) µm. In general, it can be observed that the HA could recorded little increased thickness than without HA, due to the increasing of ceramic coated, which may be attributed to the merger of more HA into the coating structure, and promotes the production of HA on the coating surface. Also, the additives will has its effect in improving the hardness, further than the coating thickness.

In figure (4-60) illustrates the cross-sectional morphology by SEM of ZrO_2/HA coating on specimen DP1coating with duplex processes. The thickness of coating layer was estimated to be (2.5µm). The interface between the film and the matrix is not obvious and, there is observable HA inside the pores.

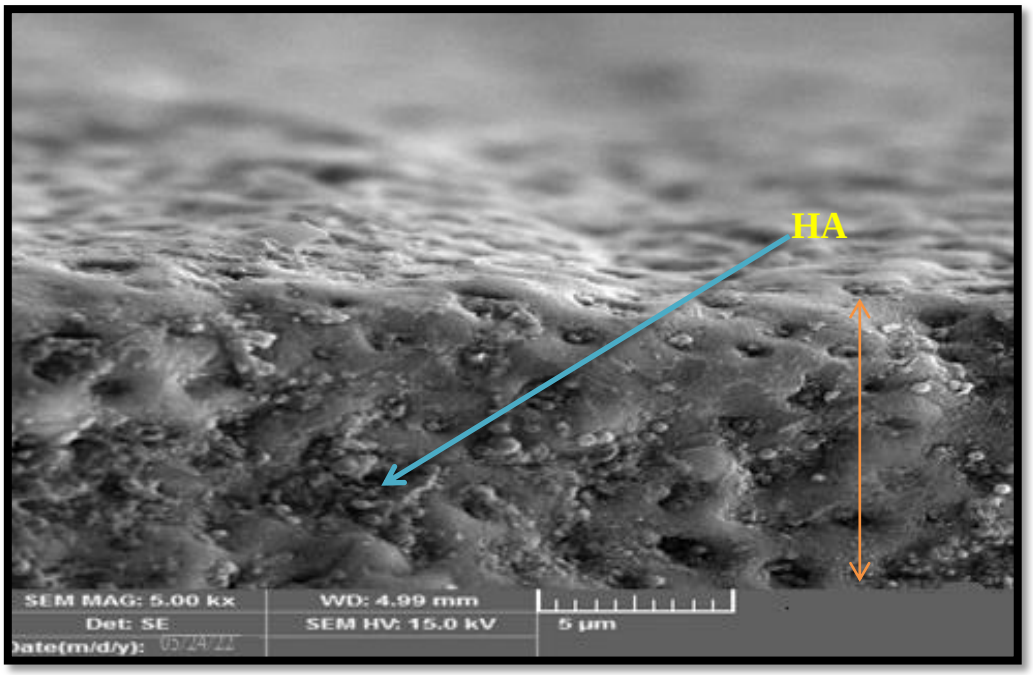

Figure (4.60): Cross section of DP1 specimen.

4.11 Adhesion results

Adhesion strengths of ZrO_2 coating by anodizing, MAO, and duplex processes with different parameters (voltage, time, and addition) used for the pull-off strength test. The maximum adhesion strengths of (59.2MPa) for specimen AN6. It is associated with the lowest thickness of such coatings increase of the oxidation voltage to 30V and time leads to the decrease of the coating adhesion strength to (48.13MPa) for specimen MAO6. In figure (4-61) adhesion strength of coating HA/ZrO2 in different processes with different voltage, and deposition time show that with increased thickness at high voltage and time

decrease adhesion strength at (36MPa) for specimen MAO12,and (22.14MPa) for DP1. HA is the most established bioactive material used in biomedical applications due to its excellent osteoconduction and chemical composition similar to that of the natural bone. However, HA has a poor mechanical property. Particularly for artificial joints and dental implants, the adhesion strength between HA or other biomaterial coatings and metallic implants is important to ensure long-term fixation [156].

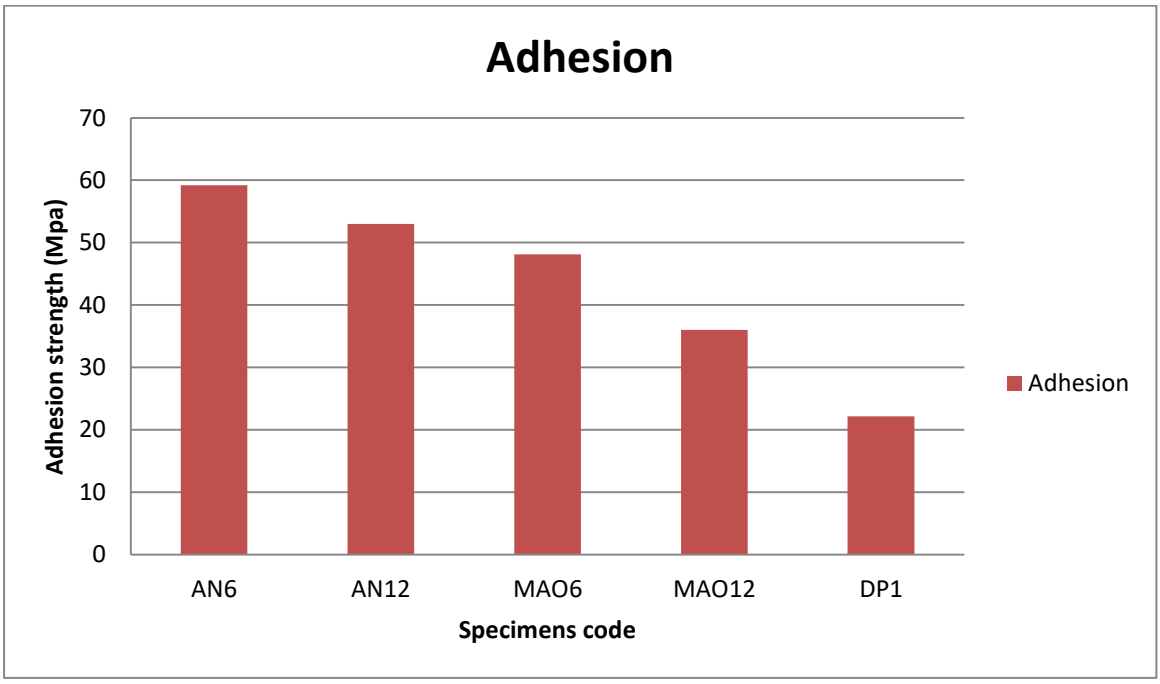

Figure (4-61): Adhesion strength of coating specimens.

5.1 Conclusions:

1. The research succeeded in deposition of ceramic layers with improved biological and mechanical properties by anodizing, MAO, and new duplex processes (DP) of anodizing and MAO on Zr705 alloys.
2. The research succeeded in confirmation that the "duplex process" of anodizing followed by MAO is a highly effective method in deposition of HA modified ZrO_2 ceramic layers with best properties in comparison of those commonly deposited by anodizing or MAO processes.
3. XRD and EDS results proved the deposition of ZrO2 ceramic layer with different contents and modification elements of (HA) on the Zr705 substrates
4. Ceramic coatings with thicknesses of (12-56.1) μm could significantly improve the Zr705 substrates hardness from (164) to (438.6 HV).
5. The addition of (8g/l) of HA modification elements provided the highest hardness (438.6 HV) in the duplex processes
6. Results of wear resistance proved the successes of duplex processes in providing ceramic coating with improved wear resistance (0.0002g) in comparison to that of Zr705 substrates (0.0023g).
7. The apparent contact angle was reduced from (77.8 º) to (15.69 º and 0 º) after being treated with different standards. The wettability of the prepared coating at lower roughness may be underestimated due to smaller pores and lower hydroxyl group content. However, the wettability of the prepared coating at higher roughness may be overestimated due to the lack of gas capture and the coarse liquid/solid interface.

8. Results from corrosion tests in Hank's solution proved that the samples DP1 (anodizing at 30 volt for 30 min. in 8g/ l HA containing electrolytes followed by MAO at 200 volt for 10 min. in 8g/ l HA containing electrolytes) showed the best results of corrosion rates (0.137×10^{-6} mpy) in comparison to those of the uncoated substrates (24.6×10^{-6} mpy) .
9. In addition, in corrosion test, it was found that the HA/ZrO2 composite coatings deposited by duplex processes increased the corrosion potential and reduced the current density.
10. The concentrations of Zr ions in Hank's solution decreased significantly for HA / ZrO2 composite coatings in comparison to those of ZrO2 coatings and uncoated substrates, wherein, the concentrations of ions reduced after being placed for 3 weeks in Hank's solution, to encourage values of 0.0209 ppm for MAO12 samples (MAO at 200 volt for 10 min. in 8g/ l HA containing electrolytes) and 0.0193 ppm for DP1 samples in comparison to 0.0229 ppm for uncoated substrates.
11. The aforementioned improvement in the reduction of Zr release can be attributed to the significant effects of the HA/ZrO2 composite coatings in providing a highly adhesive and protective layer that completely insulated the surface from its surroundings, thereby, inhibited the Zr ion releasing.
12. Depending on the superior properties of duplex processes coatings aforementioned, this study will promote the developments of future research works in surface engineering of Zr alloys and other light alloys for advanced bio applications by duplex processes of anodizing and MAO

5.2 Recommendations:

1- Study the effects of deposition parameters in the duplex processes such as voltage, PH, temperature and current density on the resulted modified coatings.

2- Investigate the effect of using other additives or the same additives used in this study with nano size on the properties of modified duplex processes coatings.

3- Examination of mechanical tests like tensile strength, compressive strength, and fatigue.

4- Applying the duplex processes to other light alloys such as Ti, Mg, and Al alloys.

References

[1] Wang, X., Xu, S., Zhou, S., Xu, W., Leary, M., Choong, P., Qian, M., Brandt, M. and Xie, Y.M. (2016) 'Topological design and additive manufacturing of porous metals for bone scaffolds and orthopaedic implants: a review', Biomaterials, Vol. 83, pp.127-141.

[2] Niinomi, M., Narushima, T., & Nakai, M. (Eds.). (2015). Advances in metallic Biomaterials: Tissues, materials and biological reactions (Vol. 3). Springer.

[3] Narayan, R. (2012) 'Fundamentals of medical implant materials', Materials for Medical Devices, Vol. 23, pp.6-17.

[4] Kunčická, L., Kocich, R. and Lowe, T.C. (2017) 'Advances in metals and alloys for joint replacement', Progress in Materials Science, Vol. 88, pp.232-280.

[5] Nagata, Y. (2007) 'National Institute of Advanced Industrial Science and Technology', Journal of Life Support Engineering, 19(Supplement), pp.65-65.

[6] Hermawan, H., Ramdan, D. and Djuansjah, J.R. (2011) 'Metals for biomedical applications', In Biomedical engineering-from theory to applications, InTech.

[7] Hansen, D.C. (2008) 'Metal corrosion in the human body: the ultimate bio-corrosion scenario', The Electrochemical Society Interface, Vol. 17, No. 2, p.31.

[8] Lai, P., Zhang, H., Zhang, L., Zeng, Q., Lu, J., & Guo, X. (2019). Effect of micro-arc oxidation on fretting wear behavior of zirconium alloy exposed to high temperature water. Wear, 424, 53-61.

[9] Tver, D. F. (2012). Encyclopedic Dictionary of Industrial Technology: Materials, Processes and Equipment. Springer Science & Business Media.

[10] Liu, C. T., Heatherly, L., Horton, J. A., Easton, D. S., Carmichael, C. A., Wright, J. L., ... & Inoue, A. (1998). Test environments and mechanical properties of Zr-base bulk amorphous alloys. Metallurgical and Materials Transactions A, 29(7), 1811-1820.

[11] Kaseem, M., Lee, Y. H., & KO, Y. G. Incorporation of MoO2 and ZrO2 particles into the oxide film formed on 7075 Al alloy via micro-arc oxidation. (2016). Materials Letters, 182, 260-263.

[12] Narayanan, T. S., & Seshadri, S. K. Cathodic electrosynthesis of alumina thin films and powders.(2000). Journal of materials science letters, 19(19), 1715-1718.

[13] Kumar, S., Kumar, A., Kumar, D., & Jain, J. Thermally sprayed alumina and ceria-doped-alumina coatings on AZ91 Mg alloy. (2017). Surface and Coatings Technology.

[14] Di Girolamo, G., Brentari, A., Blasi, C., & Serra, E. Microstructure and mechanical properties of plasma sprayed alumina-based coatings. (2014). Ceramics International, 40(8), 12861-12867.

[15] Hou, G., An, Y., Zhao, X., Zhou, H., Chen, J., Li, S., & Deng, W. Improving interfacial, mechanical and tribological properties of alumina coatings on Al alloy by plasma arc heat-treatment of substrate. (2017). Applied Surface Science, 411, 53-66.

[16] Arrabal, R., Mohedano, M., Matykina, E., Pardo, A., Mingo, B., & Merino, M. C. Characterization and wear behaviour of PEO coatings on 6082-T6 aluminium alloy with incorporated α-Al2O3 particles. (2015). Surface and Coatings Technology, 269, 64-73.

[17] Matykina, E., Arrabal, R., Monfort, F., Skeldon, P., & Thompson, G. E. Incorporation of zirconia into coatings formed by DC plasma electrolytic oxidation of aluminium in nanoparticle suspensions. (2008). Applied Surface Science, 255(5), 2830-2839.

[18] Wang, Y., Wei, D., Yu, J., & Di, S. Effects of Al2O3 nano additive on performance of micro-arc oxidation coatings formed on AZ91D Mg alloy. (2014). Journal of Materials Science & Technology, 30(10), 984-990.

[19] Kaseem, M., Lee, Y. H., & KO, Y. G. Incorporation of MoO2 and ZrO2 particles into the oxide film formed on 7075 Al alloy via micro-arc oxidation. (2016). Materials Letters, 182, 260-263.

[20] Narayanan, T. S., & Seshadri, S. K. Cathodic electrosynthesis of alumina thin films and powders.(2000). Journal of materials science letters, 19(19), 1715-1718.

[21] Kumar, S., Kumar, A., Kumar, D., & Jain, J. Thermally sprayed alumina and ceria-doped-alumina coatings on AZ91 Mg alloy. (2017). Surface and Coatings Technology.

[22] Di Girolamo, G., Brentari, A., Blasi, C., & Serra, E. Microstructure and mechanical properties of plasma sprayed alumina-based coatings. (2014). Ceramics International, 40(8), 12861-12867.

[23] Hou, G., An, Y., Zhao, X., Zhou, H., Chen, J., Li, S., & Deng, W. Improving interfacial, mechanical and tribological properties of alumina coatings on Al alloy by plasma arc heat-treatment of substrate. (2017). Applied Surface Science, 411, 53-66.

[24] Arrabal, R., Mohedano, M., Matykina, E., Pardo, A., Mingo, B., & Merino, M. C. Characterization and wear behaviour of PEO coatings on 6082-T6 aluminium alloy with incorporated α-Al2O3 particles. (2015). Surface and Coatings Technology, 269, 64-73.

[25] Matykina, E., Arrabal, R., Monfort, F., Skeldon, P., & Thompson, G. E. Incorporation of zirconia into coatings formed by DC plasma

electrolytic oxidation of aluminium in nanoparticle suspensions. (2008). Applied Surface Science, 255(5), 2830-2839.

[26] Wang, Y., Wei, D., Yu, J., & Di, S. Effects of Al2O3 nano additive on performance of micro-arc oxidation coatings formed on AZ91D Mg alloy. (2014). Journal of Materials Science & Technology, 30(10), 984-990.

[27] Burr DB, Allen MR (eds) (2014) Basic and applied bone biology. Academic, New York

[28] Christy, P. N., Basha, S. K., Kumari, V. S., Bashir, A. K. H., Maaza, M., Kaviyarasu, K., ... & Ignacimuthu, S. (2020). Biopolymeric nanocomposite scaffolds for bone tissue engineering applications–A review. Journal of Drug Delivery Science and Technology, 55, 101452.

[29] Hu, C., Ashok, D., Nisbet, D. R., & Gautam, V. (2019). Bioinspired surface modification of orthopedic implants for bone tissue engineering. Biomaterials, 219, 119366.

[30] Buikstra, J. E. (Ed.). (2019). Ortner's identification of pathological conditions in human skeletal remains.

[31] Kameo, Y., Sakano, N., & Adachi, T. (2020). Theoretical concept of cortical to cancellous bone transformation. Bone reports, 12, 100260.

[32] Boyle, C., & Kim, I. Y. (2011). Three-dimensional micro-level computational study of Wolff's law via trabecular bone remodeling in the human proximal femur using design space topology optimization. Journal of biomechanics, 44(5), 935-942.

[33] Guglielmi, G. (Ed.). (2013). Osteoporosis and bone densitometry measurements. Berlin: Springer

[34] Khan, M. U. A., Haider, S., Haider, A., Abd Razak, S. I., Kadir, M. R. A., Shah, S. A., ... & Al-Zahrani, A. A. (2021). Development of porous, antibacterial and biocompatible GO/n-HAp/bacterial cellulose/β-

glucan biocomposite scaffold for bone tissue engineering. Arabian Journal of Chemistry, 14(2), 102924.

[35] Li, X., Hung, V. W. Y., Yu, F. W. P., Hung, A. L. H., Ng, B. K. W., Cheng, J. C. Y., ... & Yip, B. H. K. (2020). Persistent low-normal bone mineral density in adolescent idiopathic scoliosis with different curve severity: a longitudinal study from presentation to beyond skeletal maturity and peak bone mass. Bone, 133, 115217.

[36] Maier, G. S., Kolbow, K., Lazovic, D., & Maus, U. (2016). The importance of bone mineral density in hip arthroplasty: results of a survey asking orthopaedic surgeons about their opinions and attitudes concerning osteoporosis and hip arthroplasty. Advances in orthopedics, 2016.

[37] Berridge MJ (2012) Cellular processes. In: Cell signalling biology. Portland Press, Cambridge,pp 7-1–7-136.

[38] Chocholata, P., Kulda, V., & Babuska, V. (2019). Fabrication of scaffolds for bone-tissue regeneration. Materials, 12(4), 568.

[39] Hasan, A., Byambaa, B., Morshed, M., Cheikh, M. I., Shakoor, R. A., Mustafy, T., & Marei, H. E. (2018). Advances in osteobiologic materials for bone substitutes. Journal of tissue engineering and regenerative medicine, 12(6), 1448-1468.

[40] Martinez-Zelaya, V. R., Archilha, N. L., Calasans-Maia, M., Farina, M., & Rossi, A. M. (2021). Trabecular architecture during the healing process of a tibial diaphysis defect. Acta Biomaterialia, 120, 181-193.

[41] Gittens, R. A., Olivares-Navarrete, R., Schwartz, Z., & Boyan, B. D. (2014). Implant osseointegration and the role of microroughness and nanostructures: lessons for spine implants. Acta biomaterialia, 10(8), 3363-3371.

[42] Sakai, T. (2015). Joint: Normal Anatomy, Function, and Pathological Condition. In Advances in Metallic Biomaterials (pp. 31-52). Springer, Berlin, Heidelberg.

[43] Wang, J. (2019). Small Joint Transplantation. In Microsurgical Orthopedics (pp. 175-183). Springer, Dordrecht.

[44] Tubbs, R. S., Shoja, M. M., & Loukas, M. (Eds.). (2016). Bergman's comprehensive encyclopedia of human anatomic variation. john Wiley & sons.

[45] Mow, V. C., Ratcliffe, A., & Poole, A. R. (1992). Cartilage and diarthrodial joints as paradigms for hierarchical materials and structures. Biomaterials, 13(2), 67-97.

[46] Aihaiti, Y., Tuerhong, X., Ye, J. T., Ren, X. Y., & Xu, P. (2020). Identification of pivotal genes and pathways in the synovial tissue of patients with rheumatoid arthritis and osteoarthritis through integrated bioinformatic analysis. Molecular Medicine Reports, 22(4), 3513-3524.

[47] Sapuan, S. M., Nukman, Y., Osman, N. A., & Ilyas, R. A. (Eds.). (2020). Composites in Biomedical Applications. CRC Press.

[48] Blue, C. M. (2015). Darby's Comprehensive Review of Dental Hygiene-E-Book.

[49] Nagay, B. E., Cordeiro, J. M., & Barão, V. A. R. (2020). Alloy Materials for Biomedical Applications. Alloy Materials and Their Allied Applications, 159-189.

[50] Bian, D., Zhou, X., Liu, J., Li, W., Shen, D., Zheng, Y., ... & Zhou, J. (2021). Degradation behaviors and in-vivo biocompatibility of a rare earth-and aluminum-free magnesium-based stent. Acta Biomaterialia, 124, 382-397.

[51] Zhang, X., Huang, Y., Wang, B., Chang, X., Yang, H., Lan, J., ... & Zhang, X. (2020). A functionalized Sm/Sr doped TiO2 nanotube array on titanium implant enables exceptional bone-implant integration and also self-antibacterial activity. Ceramics International, 46(10), 14796-14807.

[52] Quinn, J., McFadden, R., Chan, C. W., & Carson, L. (2020). Titanium for orthopaedic applications: an overview of surface

modification to improve biocompatibility and prevent bacterial biofilm formation. Iscience, 101745.

[53] Niinomi, M. (1998). Mechanical properties of biomedical titanium alloys. Materials Science and Engineering: A, 243(1-2), 231-236.

[54] Sotelo-Mazon, O., Henao, J., Giraldo-Betancur, A. L., Poblano-Salas, C. A., & Corona-Castuera, J. (2020). Corrosion of Biomaterials: Electrochemical Techniques, in Vitro Test, and Methods to Mitigate Corrosion. In New Challenges and Industrial Applications for Corrosion Prevention and Control (pp. 41-82). IGI Global.

[55] Aslankoohi, N., Mondal, D., Rizkalla, A. S., & Mequanint, K. (2019). Bone repair and regenerative biomaterials: Towards recapitulating the microenvironment. Polymers, 11(9), 1437.

[56] Papavinasam, S. (2021). Electrochemical polarization techniques for corrosion monitoring. In Techniques for corrosion monitoring (pp. 45-77). Woodhead Publishing

[57] Abdalla, M., Joplin, A., Elahinia, M., & Ibrahim, H. (2020). Corrosion Modeling of Magnesium and Its Alloys for Biomedical Applications. Corrosion and Materials Degradation, 1(2), 219-248.

[58] Manam, N. S., Harun, W. S. W., Shri, D. N. A., Ghani, S. A. C., Kurniawan, T., Ismail, M. H., & Ibrahim, M. H. I. (2017). Study of corrosion in biocompatible metals for implants: A review. Journal of Alloys and Compounds, 701, 698-715.

[59] Yan, K., Liu, H., Feng, N., Bai, J., Cheng, H., Liu, J., & Huang, F. (2019). Preparation of a single-phase Mg–6Zn alloy via ECAP-stimulated solution treatment. Journal of Magnesium and Alloys, 7(2), 305-314.

[60] Helsen, J. A., & Missirlis, Y. (2010). *Biomaterials: a Tantalus experience*. Springer Science & Business Media.

[61] Wu, H., Zhang, C., Lou, T., Chen, B., Yi, R., Wang, W., ... & Zhang, X. (2019). Crevice corrosion–A newly observed mechanism of degradation in biomedical magnesium. Acta biomaterialia, 98, 152-159.

[62] Corne, P., De March, P., Cleymand, F., & Geringer, J. (2019). Fretting-corrosion behavior on dental implant connection in human saliva. Journal of the mechanical behavior of biomedical materials, 94, 86-92

[63] Semetse, L., Obadele, B. A., Raganya, L., Geringer, J., & Olubambi, P. A. (2019). Fretting corrosion behaviour of Ti-6Al-4V reinforced with zirconia in foetal bovine serum. Journal of the mechanical behavior of biomedical materials, 100, 103392.

[64] Grabarczyk, J., Gaj, J., Pazik, B., Kaczorowski, W., & Januszewicz, B. (2021). Tribocorrosion behavior of Ti6Al4V alloy after thermo-chemical treatment and DLC deposition for biomedical applications. Tribology International, 153, 106560.

[65] Jafarzadeh, S., Chen, Z., & Bobaru, F. (2018). Peridynamic modeling of intergranular corrosion damage. Journal of The Electrochemical Society, 165(7), C362.

[66] Zhang, S., Jiang, Z., Li, H., Feng, H., & Zhang, B. (2017). Detection of susceptibility to intergranular corrosion of aged super austenitic stainless steel S32654 by a modified electrochemical potentiokinetic reactivation method. Journal of Alloys and Compounds, 695, 3083-3093.

[67] Hlinka, J., Kraus, M., Hajnys, J., Pagac, M., Petrů, J., Brytan, Z., & Tański, T. (2020). Complex corrosion properties of AISI 316L steel prepared by 3D printing technology for possible implant applications. Materials, 13(7), 1527

[68] Liu, M., Wang, J., Zhu, S., Zhang, Y., Sun, Y., Wang, L., & Guan, S. (2020). Corrosion fatigue of the extruded Mg–Zn–Y–Nd alloy in simulated body fluid. Journal of Magnesium and Alloys, 8(1), 231-240.

[69] Baragetti, S., & Arcieri, E. V. (2018). Corrosion fatigue behavior of Ti-6Al-4 V: Chemical and mechanical driving forces. International Journal of Fatigue, 112, 301-307.

[70] Antunes, R.A. and de Oliveira, M.C.L. (2012) 'Corrosion fatigue of biomedical metallic alloys: mechanisms and mitigation', Acta biomaterialia, Vol. 8, No. 3, pp.937-962.

[71] Jafari, S., Raman, R. S., Davies, C. H., Hofstetter, J., Uggowitzer, P. J., & Löffler, J. F. (2017). Stress corrosion cracking and corrosion fatigue characterisation of MgZn1Ca0. 3 (ZX10) in a simulated physiological environment. Journal of the mechanical behavior of biomedical materials, 65, 634-643.

[72] Manivasagam, G., Dhinasekaran, D. and Rajamanickam, A. (2010) 'Biomedical implants: corrosion and its prevention-a review', Recent patents on corrosion science, Vol. 2, pp.40-54.

[73] Hyson Jr, J. M. (2006). Amalgam: Its history and perils. Journal of the California Dental Association, 34(3), 215-229.

[74] Bermea, O. M., Castro-Larragoitia, J., Álvarez, Á. A. A., Perez-Rodriguez, R. J., Leura-Vicencio, A., Schiavo, B., ... & Álvarez, E. H. (2021). Mercury in Blood of Children Exposed to Historical Residues from Metallurgical Activity. Exposure and Health, 1-12.

[75] Pšenková, M., Toman, R., & Tančin, V. (2020). Concentrations of toxic metals and essential elements in raw cow milk from areas with potentially undisturbed and highly disturbed environment in Slovakia. Environmental Science and Pollution Research, 27, 26763-26772.

[76] Bouchard, M. E., Petrosyan, M., & Kane, T. D. (2021). Case series of metal allergy following Nuss procedure not only for stainless steel bars. Journal of Pediatric Surgery.

[77] Blom, L. H., Elrefaii, S. A., Zachariae, C., Thyssen, J. P., Poulsen, L. K., & Johansen, J. D. (2021). Memory T helper cells identify patients with nickel, cobalt, and chromium metal allergy. Contact Dermatitis.

[78] Liu, D., Nguyen, T., Wang, J., & Huang, C. (2020). Mechanisms of enhancing the machining performance in micro abrasive waterjet drilling of hard and brittle materials by vibration assistance. International Journal of Machine Tools and Manufacture, 151, 103528.

[79] Park, J., & Lakes, R. S. (2007). Biomaterials: an introduction. Springer Science & Business Media.

[80] Mekicha, M. A., de Rooij, M. B., Mishra, T., Matthews, D. T. A., Jacobs, L., & Schipper, D. J. (2021). Study of wear particles formation at single asperity contact: An experimental and numerical approach. Wear, 470, 203644.

[81] Li, Y., Pu, L., Xu, Y., Sun, Q., Xu, X., Fan, X., ... & Zhu, M. (2020). Experimental and modelling investigation on the fretting wear of PTFE with and without electron-beam irradiation. Wear, 460, 203459.

[82] Akay, C., Turan, N., Karakış, D., & Angurel, L. A. (2021). Improvement of flexural bond strength of zirconia-resin cement by surface patterning using sub nanosecond UV laser. International Journal of Applied Ceramic Technology, 18(1), 51-59.

[83] Yau, T. L. (1996). Performance of zirconium and zirconium alloys in organics. Journal of testing and evaluation, 24(2), 110-118.

[84] 16Holmes, D. R. (2010, March). Comparison of Zirconium 705 and Zirconium 702 in Sulfuric Acid. In CORROSION 2010. OnePetro.

[85] Balani, K., Verma, V., Agarwal, A., & Narayan, R. (2015). A Materials Science and Engineering Perspective. John Wiley & Sons, The American Ceramic Society.

[86] Zhang, L. C., Chen, L. Y., & Wang, L. (2020). Surface modification of titanium and titanium alloys: technologies, developments, and future interests. Advanced Engineering Materials, 22(5), 1901258.

[87] Zaraska, L., Gawlak, K., Gurgul, M., Gilek, D., Kozieł, M., Socha, R. P., & Sulka, G. D. (2019). Morphology of nanoporous anodic films formed on tin during anodic oxidation in less commonly used acidic and alkaline electrolytes. Surface and Coatings Technology, 362, 191-199.

[88] Chen, P., Liao, W. B., Liu, L. H., Luo, F., Wu, X. Y., Li, P. J., ... & Liu, Z. Y. (2018). Ultrafast consolidation of bulk nanocrystalline titanium alloy through ultrasonic vibration. Scientific reports, 8(1), 1-9

[89] Guan, L., Li, Y., Wang, G., Zhang, Y., & Zhang, L. C. (2018). pH dependent passivation behavior of niobium in acid fluoride-containing solutions. Electrochimica Acta, 285, 172-184

[90] İzmir, M., & Ercan, B. (2019). Anodization of titanium alloys for orthopedic applications. Frontiers of Chemical Science and Engineering, 13(1), 28-45.

[91] Rafieerad, A. R., Zalnezhad, E., Bushroa, A. R., Hamouda, A. M. S., Sarraf, M., & Nasiri-Tabrizi, B. (2015). Self-organized TiO2 nanotube layer on Ti–6Al–7Nb for biomedical application. Surface and Coatings Technology, 265, 24-31.

[92] Aladjem, A. (1973). Anodic oxidation of titanium and its alloys. Journal of Materials Science, 8(5), 688-704.

[93] Yetim, A. F. (2010). Investigation of wear behavior of titanium oxide films, produced by anodic oxidation, on commercially pure titanium in vacuum conditions. Surface and Coatings Technology, 205(6), 1757-1763.

[94] Zhu, X., Kim, K. H., & Jeong, Y. (2001). Anodic oxide films containing Ca and P of titanium biomaterial. Biomaterials, 22(16), 2199-2206.

[95] Song, H. J., Kim, M. K., Jung, G. C., Vang, M. S., & Park, Y. J. (2007). The effects of spark anodizing treatment of pure titanium metals and titanium alloys on corrosion characteristics. Surface and Coatings Technology, 201(21), 8738-8745.

[96] Ishizawa, H., & Ogino, M. (1995). Formation and characterization of anodic titanium oxide films containing Ca and P. Journal of biomedical materials research, 29(1), 65-72.

[97] Roy, P., Berger, S., & Schmuki, P. (2011). TiO2 nanotubes: synthesis and applications. Angewandte Chemie International Edition, 50(13), 2904-2939.

[98] Escada, A. L., Nakazato, R. Z., & Claro, A. P. R. A. (2017). Influence of anodization parameters in the TiO2 nanotubes formation on Ti-7.5 Mo alloy surface for biomedical application. Materials Research, 20(5), 1282-1290.

[99] Regonini, D., Bowen, C. R., Jaroenworaluck, A., & Stevens, R. (2013). A review of growth mechanism, structure and crystallinity of anodized TiO2 nanotubes. Materials Science and Engineering: R: Reports, 74(12), 377-406.

[100] Xu, G., & Shen, X. (2019). Fabrication of SiO2 nanoparticles incorporated coating onto titanium substrates by the micro arc oxidation to improve the wear resistance. Surface and Coatings Technology, 364, 180-186.

[101] Ding, Z. Y., Wang, Y. H., Ouyang, J. H., Liu, Z. G., Wang, Y. M., & Wang, Y. J. (2019). Influence of Al2O3 addition in NaAlO2 electrolyte on microstructure and high-temperature properties of plasma electrolytic oxidation ceramic coatings on Ti2AlNb alloy. Surface and Coatings Technology, 370, 187-195.

[102] Wang, Z. X., Chen, G. Q., Chen, L. Y., Xu, L., & Lu, S. (2018). Degradation behavior of micro-arc oxidized ZK60 magnesium alloy in a simulated body fluid. Metals, 8(9), 724.

[103] Gecu, R., Yurekturk, Y., Tekoglu, E., Muhaffel, F., & Karaaslan, A. (2019). Improving wear resistance of 304 stainless steel reinforced AA7075 aluminum matrix composite by micro-arc oxidation. Surface and Coatings Technology, 368, 15-24.

[104] Song, H. J., Kim, M. K., Jung, G. C., Vang, M. S., & Park, Y. J. (2007). The effects of spark anodizing treatment of pure titanium metals and titanium alloys on corrosion characteristics. Surface and Coatings Technology, 201(21), 8738-8745.

[105] Wang, Y., Yu, H., Chen, C., & Zhao, Z. (2015). Review of the biocompatibility of micro-arc oxidation coated titanium alloys. Materials & design, 85, 640-652.

[106] Ding, Z. Y., Wang, Y. H., Ouyang, J. H., Liu, Z. G., Wang, Y. M., & Wang, Y. J. (2019). Influence of Al2O3 addition in NaAlO2 electrolyte on microstructure and high-temperature properties of plasma electrolytic oxidation ceramic coatings on Ti2AlNb alloy. Surface and Coatings Technology, 370, 187-195.

[107] Shin, K. R., Kim, Y. S., Yang, H. W., Ko, Y. G., & Shin, D. H. (2014). In vitro biological response to the oxide layer in pure titanium formed at different current densities by plasma electrolytic oxidation. Applied surface science, 314, 221-227.

[108] Anselme, K. (2000). Osteoblast adhesion on biomaterials. Biomaterials, 21(7), 667-681.

[109] Dehnavi, V., Luan, B. L., Shoesmith, D. W., Liu, X. Y., & Rohani, S. (2013). Effect of duty cycle and applied current frequency on plasma electrolytic oxidation (PEO) coating growth behavior. Surface and Coatings Technology, 226, 100-107.

[110] Tang, Y., Zhao, X., Jiang, K., Chen, J., & Zuo, Y. (2010). The influences of duty cycle on the bonding strength of AZ31B magnesium alloy by microarc oxidation treatment. Surface and Coatings Technology, 205(6), 1789-1792.

[111] Nie, X., Leyland, A., & Matthews, A. (2000). Deposition of layered bioceramic hydroxyapatite/TiO2 coatings on titanium alloys using a hybrid technique of micro-arc oxidation and electrophoresis. Surface and coatings technology, 125(1-3), 407-414.

[112] Venkateswarlu, K., Rameshbabu, N., Sreekanth, D., Sandhyarani, M., Bose, A. C., Muthupandi, V., & Subramanian, S. (2013). Role of electrolyte chemistry on electronic and in vitro electrochemical properties of micro-arc oxidized titania films on Cp Ti. Electrochimica Acta, 105, 468-480.

[113] Wang, Y., Yu, H., Chen, C., & Zhao, Z. (2015). Review of the biocompatibility of micro-arc oxidation coated titanium alloys. Materials & design, 85, 640-652.

[114] Ding, Z. Y., Wang, Y. H., Ouyang, J. H., Liu, Z. G., Wang, Y. M., & Wang, Y. J. (2019). Influence of Al2O3 addition in NaAlO2 electrolyte on microstructure and high-temperature properties of plasma electrolytic oxidation ceramic coatings on Ti2AlNb alloy. Surface and Coatings Technology, 370, 187-195.

[115] Shin, K. R., Kim, Y. S., Yang, H. W., Ko, Y. G., & Shin, D. H. (2014). In vitro biological response to the oxide layer in pure titanium formed at different current densities by plasma electrolytic oxidation. Applied surface science, 314, 221-227.

[116] Anselme, K. (2000). Osteoblast adhesion on biomaterials. Biomaterials, 21(7), 667-681.

[117] Dehnavi, V., Luan, B. L., Shoesmith, D. W., Liu, X. Y., & Rohani, S. (2013). Effect of duty cycle and applied current frequency on plasma

electrolytic oxidation (PEO) coating growth behavior. Surface and Coatings Technology, 226, 100-107.

[118] Tang, Y., Zhao, X., Jiang, K., Chen, J., & Zuo, Y. (2010). The influences of duty cycle on the bonding strength of AZ31B magnesium alloy by microarc oxidation treatment. Surface and Coatings Technology, 205(6), 1789-1792.

[119] Nie, X., Leyland, A., & Matthews, A. (2000). Deposition of layered bioceramic hydroxyapatite/TiO2 coatings on titanium alloys using a hybrid technique of micro-arc oxidation and electrophoresis. Surface and coatings technology, 125(1-3), 407-414.

[120] Venkateswarlu, K., Rameshbabu, N., Sreekanth, D., Sandhyarani, M., Bose, A. C., Muthupandi, V., & Subramanian, S. (2013). Role of electrolyte chemistry on electronic and in vitro electrochemical properties of micro-arc oxidized titania films on Cp Ti. Electrochimica Acta, 105, 468-480.

[121] Venkateswarlu, K., Rameshbabu, N., Sreekanth, D., Bose, A. C., Muthupandi, V., Babu, N. K., & Subramanian, S. (2012). Role of electrolyte additives on in-vitro electrochemical behavior of micro arc oxidized titania films on Cp Ti. Applied surface science, 258(18), 6853-6863

[122] Wang, L., Shi, L., Chen, J., Shi, Z., Ren, L., & Wang, Y. (2014). Biocompatibility of Si-incorporated TiO2 film prepared by micro-arc oxidation. Materials Letters, 116, 35-38

[123] Kung, K. C., Lee, T. M., Chen, J. L., & Lui, T. S. (2010). Characteristics and biological responses of novel coatings containing strontium by micro-arc oxidation. Surface and Coatings Technology, 205(6), 1714-1722.

[124] Stępień, M., Handzlik, P., & Fitzner, K. (2014). Synthesis of ZrO 2 nanotubes in inorganic and organic electrolytes by anodic oxidation of zirconium. *Journal of Solid State Electrochemistry*, *18*(11), 3081-3090.

[125] Park, Y. J., Kim, J. W., Ali, G., & Cho, S. O. (2018). Enhancement of oxidation resistance of zirconium alloy with anodic nanoporous oxide layer in high-temperature air/steam environments. *Corrosion Science*, *140*, 217-222.

[126] Korniienko, V., Oleshko, O., Husak, Y., Deineka, V., Holubnycha, V., Mishchenko, O., ... & Pogorielov, M. (2020). Formation of a bacteriostatic surface on ZrNb alloy via anodization in a solution containing Cu nanoparticles. *Materials*, *13*(18), 3913.

[127] Pantazi, A., Vardaki, M., Mihai, G., Totea, G., Demetrescu, I., & Enachescu, M. (2020). Nanomechanical properties of zirconium anodized in a mixture of electrolytes with fluoride ions. *Journal of the Mechanical Behavior of Biomedical Materials*, *112*, 104084.

[128] Mozalev, A., Pytlicek, Z., Kamnev, K., Prasek, J., Gispert-Guirado, F., & Llobet, E. (2021). Zirconium oxide nanoarrays via the self-organized anodizing of Al/Zr bilayers on substrates. *Materials Chemistry Frontiers*, *5*(4), 1917-1931.

[129] Liu, S., Li, B., Liang, C., Wang, H., & Qiao, Z. (2016). Formation mechanism and adhesive strength of a hydroxyapatite/TiO2 composite coating on a titanium surface prepared by micro-arc oxidation. *Applied Surface Science*, *362*, 109-114.

[130] Durdu, S., Aktug, S. L., Aktas, S., Yalcin, E., Cavusoglu, K., Altinkok, A., & Usta, M. (2017). Characterization and in vitro properties of anti-bacterial Ag-based bioceramic coatings formed on zirconium by micro arc oxidation and thermal evaporation. *Surface and Coatings Technology*, *331*, 107-115.

[131] Cengiz, S., Azakli, Y., Yazici, M., Gayretli, B., Gencer, Y., & Tarakci, M. (2017). Effects of the addition of calcium acetate into silicate-based electrolytes on the properties of MAO coatings produced on zirconium. *Acta Physica Polonica A*, *129*(4), 504-508.

[132] Farrakhov, R. G., Mukaeva, V. R., Fatkullin, A. R., Gorbatkov, M. V., Tarasov, P. V., Lazarev, D. M., ... & Parfenov, E. V. (2018). Plasma electrolytic oxidation treatment mode influence on corrosion properties of coatings obtained on Zr-1Nb alloy in silicate-phosphate electrolyte. In *IOP Conference Series: Materials Science and Engineering* (Vol. 292, No. 1, p. 012006). IOP Publishing.

[133] Sobolev, A., Wolicki, I., Kossenko, A., Zinigrad, M., & Borodianskiy, K. (2018). Coating formation on Ti-6Al-4V alloy by micro arc oxidation in molten salt. *Materials*, *11*(9), 1611.

[134] Li, N., Yuan, K., Song, Y., Cao, J., & Xu, J. (2021). Plasma electrolytic oxidation of Zircaloy-2 alloy in potassium hydroxide/sodium silicate electrolytes: The effect of silicate concentration. *Boletín de la Sociedad Española de Cerámica y Vidrio*, *60*(5), 328-336.

[135] Chu, Y., Liu, P., Chen, Y., & Li, X. (2020). Influence of Applied Voltage on Surface Morphology and Wettability of Biological Coatings on Ti6-Al-4V by Micro-Arc Oxidation Treatment. *Materials Research*, *23*.

[136] Martin, J., Haraux, P., Ntomprougkidis, V., Migot, S., Bruyère, S., & Henrion, G. (2020). Characterization of metal oxide micro/nanoparticles elaborated by plasma electrolytic oxidation of aluminium and zirconium alloys. *Surface and Coatings Technology*, *397*, 125987.

[137] Aktug, S. L., Durdu, S., Kalkan, S., Cavusoglu, K., & Usta, M. (2021). In Vitro Biological and Antimicrobial Properties of Chitosan-based Bioceramic Coatings on Zirconium.

[138] Kind, A., Kind, B., & Kind, C. Standard Practice for Training a Land Search Tracker1.

[139] M. K. Sharma, Y. Jang, J. Kim, H. Kim, and J. P. Jung, "Plasma Electrolytic Oxidation in Surface Modification of Metals for Electronics" ,2014, Journal of Welding and Joining, Vol. 32, No. 3.

[140] Mutlu, I. and Oktay, E. (2013) 'Characterization of 17-4 PH stainless steel foam for biomedical applications in simulated body fluid and artificial saliva environments', Materials Science and Engineering: C, Vol. 33, No. 3, pp.1125-1131.

[141] Hanawa, T. (2004) 'Metal ion release from metal implants', Materials Science and Engineering: C, Vol. 24, No. 6-8, pp.745-752.

[142] Sarah Muhi Jawad, (2015) 'Effect of (Cu & Cr) Additives on112 Corrosion and Dry Sliding Wear of NiTi Shape Memory Alloy', MSC thesis, Submitted to the Council of the College of Materials engineering / University of Babylon.

[143] K. W.NG, H. C. Man and T.M.Yue(2011)'characterization and corrosion study of Ni Ti laser surface alloyed with Nb or Co',vol. 257,Isaue.8,32 G9.

[144] Li, X., Ren, Z., Wang, R., Liu, L., Zhang, J., Ma, F., ... & Liu, X. (2021). Characterization and antibacterial activity of edible films based on carboxymethyl cellulose, Dioscorea opposita mucilage, glycerol and ZnO nanoparticles. Food Chemistry, 349, 129208.

[145] S. Steel, "The Influence of Surface Wettability and Topography on the Bioactivity of TiO 2 / Epoxy Coatings on AISI" 2019.

[146] Ohring, M. Materials science of thin films. (2001), Academic press.

[147] M. Marciszko, "Diffraction study of mechanical properties and stresses resulting from surface processing of polycrystalline materials", 2013, AGH.

[148] Ogden, H.R. and Holden, F.C. (1958) 'Metallography of titanium alloys' (No. TML-103), Battelle Memorial Inst, Titanium Metallurgical Lab., Columbus, Ohio

[149] Lkhagvaa, T., Rehman, Z. U., & Choi, D. (2021). Post-anodization methods for improved anticorrosion properties: a review. Journal of Coatings Technology and Research, 18(1), 1-17.

[150] S. Liua, B. Lib, C. Langb, H. Wangb, Z. Qiao "Formation mechanism and adhesive strength of a hydroxyapatite/ TiO2 composite coating on a titanium surface prepared by micro-arc oxidation "Applied Surface Science 362 (2016) 109–114.

[151] A.A. Atiyah, A.K. Abid Ali,N.M. Dawood "Characterization of NiTi and NiTiCu Porous Shape Memory Alloys Prepared by Powder Metallurgy (Part I) , Arab J Sci Eng (2014

[152] Lin, Z., Liu, K., Zhang, Y. C., Yue, X. J., Song, G. Q., & Ba, D. C. (2009). The microstructure and wettability of the TiOx films synthesized by reactive DC magnetron sputtering. Materials Science and Engineering: B, 156(1-3), 79-83.

[153] E. E. Sukuroglu, S. S., Kubra Akar, Y. Totik, I. Efeoglu and E. Arslan "The effect of TiO2 coating on biological NiTi alloys after micro-arc oxidation treatment for corrosion resistance "DOI: 10.1177/0954411917705909, IMechE(2017).

[154] Zhang Z, Zhang Y, Chang L,. Effects of frequency on growth process of plasma electrolytic oxidation coating. Mater Chem Phys 2012; 132: 909–915.

[155] M. B. Sedelnikova et al., "Modification of titanium surface via Ag-, Sr- and Si-containing micro-arc calcium phosphate coating" Bioact. Mater., vol. 4, no. July, pp. 224–235, 2019, doi: 10.1016/j.bioactmat.2019.07.001.

[156] Lin, J. D., & Duh, J. G. (2003). Fracture toughness and hardness of ceria-and yttria-doped tetragonal zirconia ceramics. Materials Chemistry and Physics, 78(1), 253-261.

[157] S. Holmberg "Functionalizing C-MEMS: From Surface Modification to Structural Modification" 2018,

[158] M.Geetha, A.Singh, and R. Asokamani "Ti based biomaterials, the ultimate choice for orthopaedic implants- Areview" vol.54, no. 3, pp. 397-425, doi: 10.1016/j.pmatsci.2008.06.004.

[159] W.Lei, K.Mittal, and Z.Yu "Adhesion measurement of coatings on biodevices/implants: A critical review" Reviews of Adhesion and Adhesives, vol. 4, no. 4, pp. 367-396, 2016 , doi: 10.7569/RAA.2016.09713.

[160] M. H. Hong, D. H. Lee, K. M. Kim, and Y. K. Lee, "Study on bioactivity and bonding strength between Ti alloy substrate and TiO2 film by micro-arc oxidation" Thin Solid Films, vol. 519, no. 20, pp. 7065–7070, 2011, doi: 10.1016/j.tsf.2011.01.223.

[161] L. Lara Rodriguez and P. A. Sundaram, "Corrosion behavior of plasma electrolytically oxidized gamma titanium aluminide alloy in simulated body fluid" Mater. Chem. Phys., vol. 181, no. September, pp. 67–77, 2016, doi: 10.1016/j.matchemphys.2016.06.034.

[162] Y. Wang, H. Yu, C. Chen, and Z. Zhao, "Review of the biocompatibility of micro-arc oxidation coated titanium alloys" Mater. Des., vol. 85, pp. 640–652, 2015, doi: 10.1016/j. matdes.2015.07.086.

[163] R. E. White, "Applications of Electrochemistry and Nanotechnology in Biology and Medicine I" no. 52.

[164] Awad, S. H., & Qian, H. C. Deposition of duplex Al_2O_3/TiN coatings on aluminum alloys for tribological applications using a combined microplasma oxidation (MPO) and arc ion plating (AIP). (2006). *Wear*, *260*(1), 215-222.

[165] M. K. Dimah, F. D. Albeza, V. A. Borrás, and A. I. Muñoz, "Study of the biotribocorrosion behaviour of titanium biomedical alloys in simulated body fluids by electrochemical techniques," Wear, vol. 294, pp. 409-418, 2012.

[166] A. Amanov and S. Sasaki, "A study on the tribological characteristics of duplextreated Ti–6Al–4V alloy under oil-lubricated sliding conditions," Tribology International, vol. 64, pp. 155-163, 2013.

[167] N. Diomidis, S. Mischler, N. More, and M. Roy, "Tribo-electrochemical characterization of metallic biomaterials for total joint replacement," Acta biomaterialia, vol. 8, pp. 852-859, 2012.

[168] M. Runa, M. Mathew, and L. Rocha, "Tribocorrosion response of the Ti6Al4V alloys commonly used in femoral stems," Tribology International, vol. 68, pp. 85-93, 2013.

[169] M. Metikoš-Huković, A. Kwokal, and J. Piljac, "The influence of niobium and vanadium on passivity of titanium-based implants in physiological solution" Biomaterials, vol. 24, no. 21, pp. 37653775, 2003.

XRD Analysis:

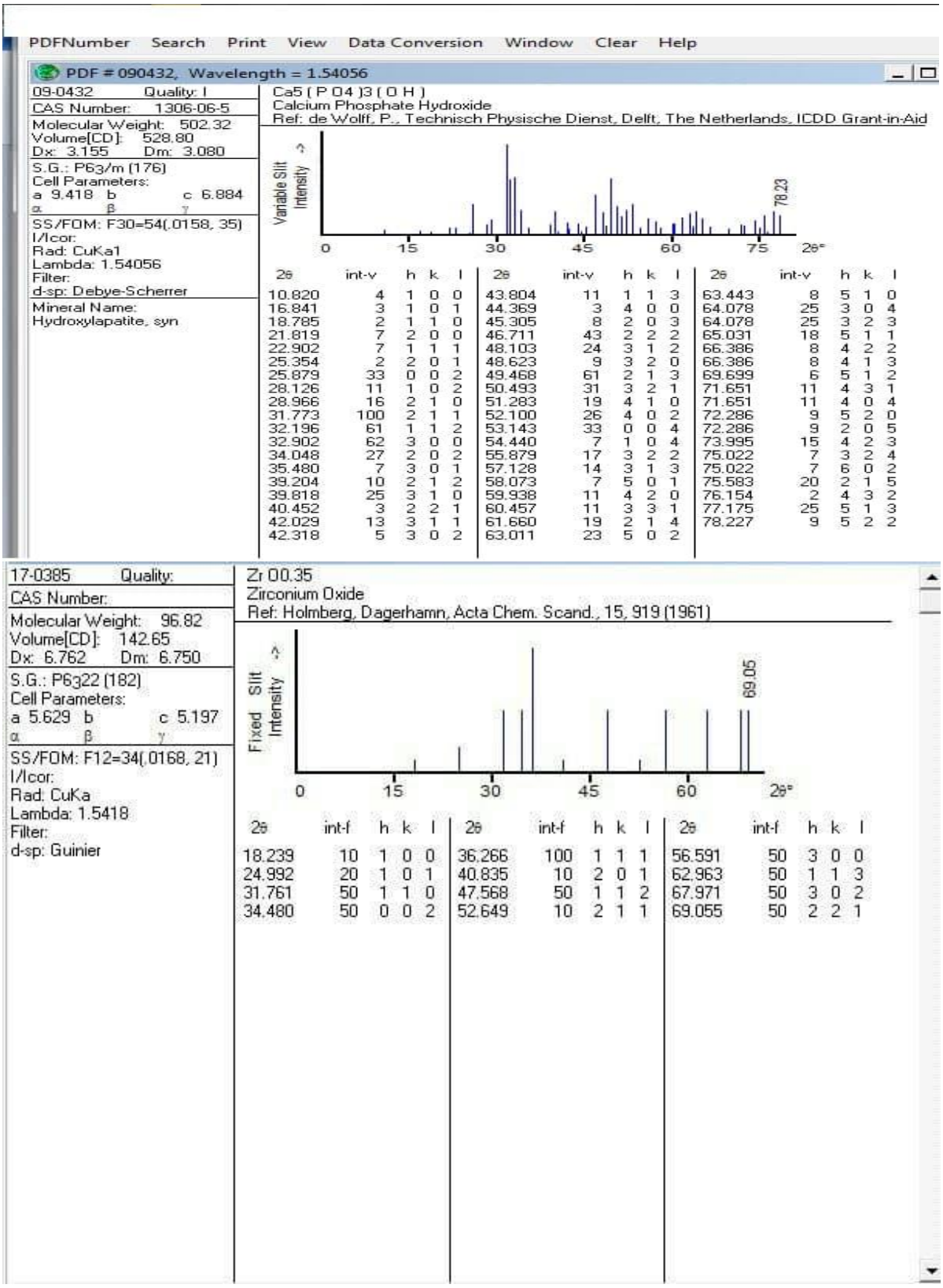

34-0657 Quality: C

CAS Number:

Molecular Weight: 91.22
Volume[CD]: 44.56
Dx: 6.798 Dm:

S.G.: Im3m (229)
Cell Parameters:
a 3.545 b c
α β γ

SS/FOM: F10=156(.0064, 10)
I/Icor:
Rad: CuKa1
Lambda: 1.5405
Filter:
d-sp: calculated

β-Zr
Zirconium
Ref: Ferguson, I., United Kingdom Atomic Energy Assoc.-TRG Report, 2438, 1 (1976)

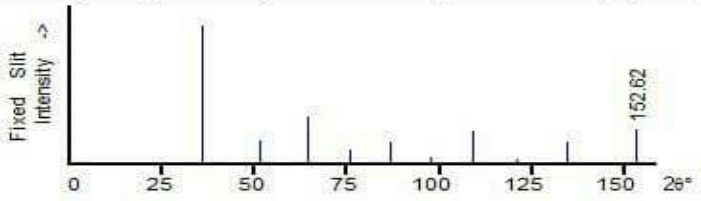

2θ	int-f	h	k	l	2θ	int-f	h	k	l	2θ	int-f	h	k	l
35.787	100	1	1	0	86.798	15	3	1	0	134.39	15	4	1	1
51.513	17	2	0	0	97.644	4	2	2	2	152.62	25	4	2	0
64.306	33	2	1	1	108.77	23	3	2	1					
75.832	10	2	2	0	120.70	3	4	0	0					

41-0017 Quality:

CAS Number:

Molecular Weight: 123.22
Volume[CD]: 120.13
Dx: 6.813 Dm:

S.G.:
Cell Parameters:
a 3.327 b 5.566 c 6.487
α β γ

SS/FOM: F15=3(0.132, 44)
I/Icor:
Rad: CuKa
Lambda: 1.5418
Filter:
d-sp: Debye-Scherrer

Zr O2
Zirconium Oxide
Ref: Devi, S., Ming, L., Manghnani, M., J. Am. Ceram. Soc., 70, C218 (1987)

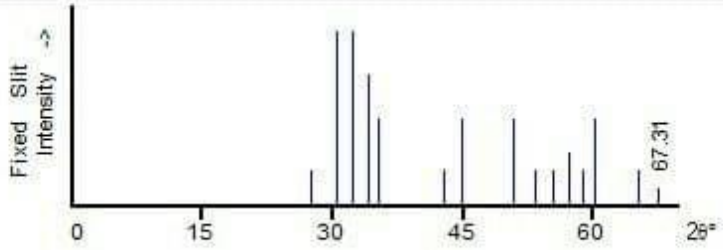

2θ	int-f	h	k	l	2θ	int-f	h	k	l	2θ	int-f	h	k	l
27.506	20	0	0	2	42.823	20	0	2	2	57.166	30	0	3	2
30.378	100	1	0	1	44.832	50	1	2	1	58.763	20	1	3	1
32.172	100	0	2	0	50.673	50	1	0	3	60.024	50	2	1	1
34.195	75	1	1	1	53.210	20	1	1	3	65.185	20	2	2	0
35.164	50	0	2	1	55.294	20	2	0	0	67.306	10	0	4	0

20-0684 Quality: C

CAS Number:

Molecular Weight: 107.22
Volume[CD]: 98.61
Dx: 7.222 Dm:

S.G.: Fm3m (225)
Cell Parameters:
a 4.62 b c
α β γ

SS/FOM: F11=257(.0039, 11)
I/Icor:
Rad: CuKa1
Lambda: 1.5405
Filter:
d-sp: calculated

Zr O
Zirconium Oxide
Ref: Natl. Bur. Stand. (U.S.) Monogr. 25, 5, 81 (1965)

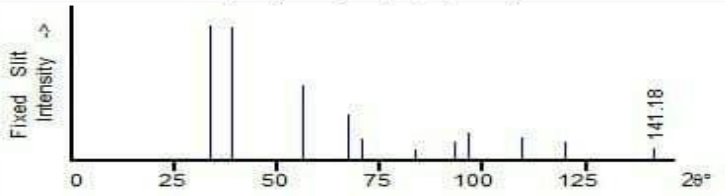

2θ	int-f	h	k	l	2θ	int-f	h	k	l	2θ	int-f	h	k	l
33.575	100	1	1	1	70.557	15	2	2	2	109.52	17	4	2	2
38.957	98	2	0	0	83.658	7	4	0	0	120.07	13	5	1	1
56.289	55	2	2	0	93.229	13	3	3	1	141.17	8	4	4	0
67.141	33	3	1	1	96.421	20	4	2	0					

17-0923 Quality:

CAS Number: 1314-23-4

Molecular Weight: 123.22
Volume[CD]: 137.63
Dx: 5.947 Dm:

S.G.: P$\bar{4}$m2 (115)
Cell Parameters:
a 5.12 b c 5.25
α β γ

SS/FOM: F23=3(0.152, 59)
I/Icor:
Rad: CuKa1
Lambda: 1.5405
Filter: Ni
d-sp:

Zr 02
Zirconium Oxide
Ref: U.S. Bureau of Mines, Open File Report

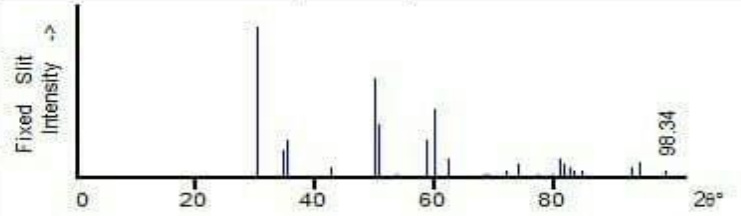

2θ	int-f	h	k	l	2θ	int-f	h	k	l	2θ	int-f	h	k	l
30.167	100	1	1	1	59.725	45	3	1	1	80.676	12	3	1	3
34.466	18	0	0	2	62.119	12	2	2	2	81.587	8	3	3	1
35.307	25	2	0	0	68.027	2	3	1	2	82.435	6	2	0	4
42.611	6	1	1	2	68.823	2	3	2	1	83.129	4			
49.785	65	2	0	2	71.904	4	0	0	4	84.375	4	4	2	0
50.373	35	2	2	0	73.928	8	4	0	0	92.763	6	2	2	4
53.546	2	2	2	1	77.323	2	1	1	4	94.026	10	0	0	5
58.559	25	1	1	3	79.549	2	3	3	0	98.341	4	3	1	4

22-1025 Quality:

CAS Number:

Molecular Weight: 289.66
Volume[CD]: 835.78
Dx: 6.906 Dm:

S.G.: R32 (155)
Cell Parameters:
a 5.563 b c 31.18
α β γ

SS/FOM: F16=2(0.214, 40)
I/Icor:
Rad: CuKa
Lambda: 1.5418
Filter:
d-sp:

Zr3 O
Zirconium Oxide
Ref: Dubertret, Lehr, C. R. Seances Acad. Sci., Ser. C, 268, 501 (1969)

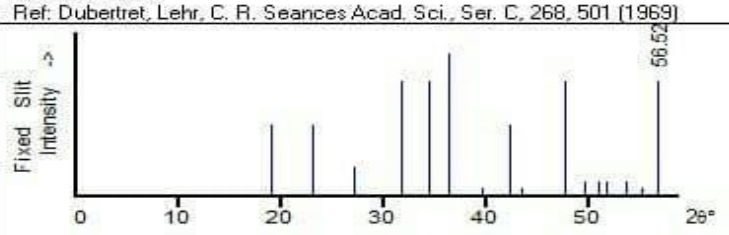

2θ	int-f	h	k	l	2θ	int-f	h	k	l	2θ	int-f	h	k	l
19.029	50	0	1	2	39.618	5	2	0	5	51.626	10	2	1	4
23.143	50	0	1	5	42.194	50	1	0	13	53.614	10	0	1	17
27.080	20	1	0	7	43.450	5	0	0	15	55.042	5	1	1	15
31.738	80	1	1	0	47.541	80	0	2	10	56.515	80	2	0	14
34.453	80	0	0	12	49.468	10	2	0	11					
36.236	100	1	1	6	50.824	10	1	0	16					

42-1164 Quality: *

CAS Number:

Molecular Weight: 123.22
Volume[CD]: 69.83
Dx: 5.861 Dm:

S.G.: $P4_2/nmc$ (137)
Cell Parameters:
a 3.64 b c 5.27
α β γ

SS/FOM: F30=253(.0030, 40)
I/Icor:
Rad: CuKa
Lambda: 1.5418
Filter:
d-sp: calculated

Zr O2
Zirconium Oxide
Ref: Teufer, G., Acta Crystallogr., 15, 1187 (1962)

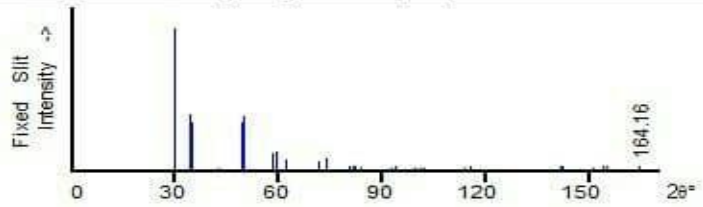

2θ	int-f	h	k	l	2θ	int-f	h	k	l	2θ	int-f	h	k	l
29.807	100	1	0	1	80.350	3	2	1	3	122.56	1	0	0	6
33.995	39	0	0	2	81.303	3	3	0	1	123.28	1	3	2	3
34.826	34	1	1	0	82.111	3	1	1	4	124.42	1	4	1	1
42.318	2	1	0	2	83.534	2	2	2	2	125.40	1	3	1	4
49.468	34	1	1	2	84.006	2	3	1	0	127.13	1	4	0	2
50.077	38	2	0	0	92.403	2	2	0	4	127.73	1	3	3	0
58.274	12	1	0	3	93.817	3	3	1	2	135.82	1	1	1	6
59.374	13	2	1	1	99.078	2	1	0	5	141.53	3	3	3	2
61.912	7	2	0	2	100.99	2	3	0	3	142.31	3	4	2	0
67.581	<1	2	1	2	101.95	2	3	2	1	150.95	2	3	0	5
71.557	6	0	0	4	113.59	2	2	2	4	153.71	3	2	0	6
73.526	8	2	2	0	115.65	3	4	0	0	155.12	3	4	1	3
76.895	<1	1	0	4	121.07	1	2	1	5	164.15	3	4	2	2

37-0031 Quality:

CAS Number:

Molecular Weight: 123.22
Volume[CD]: 104.02
Dx: 5.901 Dm:

S.G.:
Cell Parameters:
a 3.643 b c 9.050
α β γ

SS/FOM: F 7=3(0.096, 27)
I/Icor:
Rad:
Lambda:
Filter:
d-sp:

Zr O2
Zirconium Oxide
Ref: Hasegawa, H., J. Mater. Sci. Lett., 2, 91 (1983)

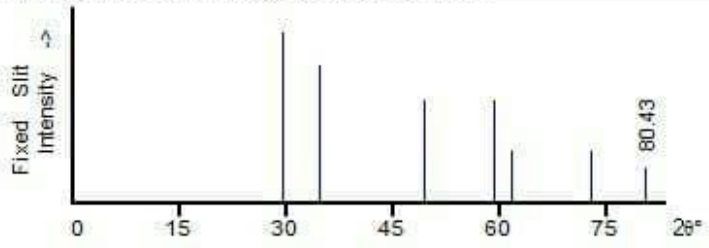

2θ	int-f	h	k	l	2θ	int-f	h	k	l	2θ	int-f	h	k	l
29.715	100	0	0	3	59.219	60	[1	1	3]	80.431	20	1	0	7
34.631	80	0	1	2	61.660	30	0	0	6	80.431	20	2	1	0
49.611	60	1	0	4	73.064	30	0	2	4					

الخلاصة

يمتلك الزركونيوم وسبائكه أعلى درجات التوافق الحيوي وذات سميه قليله مقارنة مع المعادن الأخرى المستخدمة في جسم الإنسان. ولكن يمتلك مقاومة بلى و صلاده منخفضة . افضل الحلول تتم بترسيب طلاء على السطح , يتم تحسينها بعدة طرق مثل الانوده حيث تعتبر معالجة جيده ومثيرة للاهتمام قادرة على منح سبائك الزركونيوم خصائص ميكانيكية عالية على السطح مثل(الصلاده ومقاومة البلى). اما تقنية أكسدة القوس الصغير (MAO) هي طريقة كيميائية-كهروكيميائية غير تقليدية متقدمة وفعالة لتشكيل طبقه طلاء ذات سمك وصلاده عاليه على سبائك الزركونيوم تمتاز بمقاومة ممتازة للتآكل.

في هذا العمل تم إجراء العديد من المحاولات لتحسين السطح من خلال الطلاء بعملية الأنودة وعملية MAO ، وعمليه الدمج من العمليتين السابقتين حيث تم تصنيع منظومه طلاء محليًا تتكون من مجهز طاقة بجهد (٠-٥٠٠) فولت وتيار (٠-٨) أمبير. أجريت عده اختبارات لتقييم كفاءة Zr705 قبل وبعد الطلاء ، مثل حيود الأشعة السينية ، الفحص المجهري الإلكتروني ، اختبار الصلاده ، اختبار البلى ، اختبار الالتصاقيه ، سمك الطلاء ، التبلل ، اختبار التآكل ،اختبار اطلاق الايونات في محلول هانك واختبار المضاد للبكتيريا.المحلول المستخدم في عملية الأنودة هو (١ مل / لتر من حامض الفوسفوريك مع ٠.٨ غرام / لتر من فلوريد الصوديوم) مع وبدون إضافة هيدروكسيبتايت بنسب (٢.٥، ٥، و ٨) غرام/لتر. بفولتيات (١٠-٣٠) فولت ، والوقت (٤-٦٠) دقيقة.

اظهرت نتائج عمليه الانوده صلاده مرتفعه قيمتها (٢٧٠) HV عند (٣٠ فولت، ٣٠دقيقه، و ٨ غرام /لترهيدروكسيبتايت) وقل معدل البلى الى (١٠.١ × ١٠$^{-٨}$ جم / م) ومعدل التآكل (0.743 × 10^{-6}) في محلول هانك وزداد سمك الطبقة الى (١٨)ميكرومتر.

اما في عمليه MAO تم العمل في ظروف مختلفة بجهد كهربائي (١٠٠-٢٠٠) فولت ، وزمن (٥-١٥) دقيقة. تم استخدام محلول (١٤ جم / لتر هيدروكسيد البوتاسيوم ، ١٤ غرام/ لتر فوسفات الصوديوم ، ١٤ غرام / لتر سيليكات الصوديوم ، و ٢ غرام / لتر من فلوريد الصوديوم) مع وبدون إضافة هيدروكسيباتيت (٢.٥ ، ٥ ، ٨) غرام/ لتر. ظهرت النتائج عند (٢٠٠فولت ، ١٠ دقيقه ، و٨ غرام/لترHA) صلاده عالية بلغت (٣٤٧.٥٩) HV ومعدل بلى (٤.٥ × ١٠$^{-٨}$ جم / م) ومعدل التآكل (0.454 × 10^{-6} mpy) في محلول هانك مع زيادة سماكة الطبقه الى (٤٤) ميكرومتر.

تم إجراء التحسين الفعلي عن طريق عملية دمج بين أفضل الظروف لعمليات الانوده و MAO اظهرت النتائج زياده في الصلاده بعد الطلاء من (١٦٤ إلى ٤٨٣.٦) HV ، بمعدل بلى (٢.٥ × ١٠-٨ غرام / لتر) ، ومعدل تآكل (0.137 × 10-6 mpy) في محلول هانك وازداد سمك الطبقة الى (٥٦.١) ميكرومتر.و كمية انطلاق ايون الزركونيوم في محلول هانك كانت أقل مما كانت عليه العينات بدون الطلاء والتي تساوي (٠.٠٢٢٩) جزء من المليون للعينة الغير مطلية ، وأفضل العينات للانوده وال MAO على التوالي كانت (٠.٠٢١٧ ، و ٠.٠٢٠٩) جزء من المليون ، اما لعمليه الدمج كانت قيمه انطلاق الايون (٠.٠١٩٣) جزء من المليون. و يتميز طلاء MAO والطلاء المدمج بتأثير قوي ضد البكتيريا ويمنع نموها.

جمهوريه العراقية
وزارة التعليم العالي والبحث العلمي
جامعة بابل
كلية هندسة المواد
قسم هندسة المعادن

تحسين السطح لسبيكه Zr 705 بواسطه طلاءات ZrO_2 /HA باستخدام عمليات مزدوجه من الانوده والاكسده بالقوس المايكروي للتطبيقات الطبيه

اطروحة

مقدمة إلى قسم هندسة المعادن في كلية هندسة المواد/ جامعة بابل كجزء من متطلبات نيل درجة الدكتوراه فلسفة في هندسة المواد/ معادن

من قبل

ميسم عبود سلمان

بكالوريوس هندسه الميكانيك (٢٠١٢)
ماجستير هندسه الميكانيك (٢٠١٧)

يشرف عليها

أ.د. علي هوبي حليم **أ.د.سمير حامد عواد**

١٤٤٣ هـ **٢٠٢٢ م**